COVID-19 vaccines work. How will they change the world? p. 768

Thermoelectrics stabilized with disorder p. 830

Human impacts on freshwater fishes p. 835

Science

$15
19 FEBRUARY 2021
sciencemag.org

AAAS

MITOCHONDRIAL RIBOSOME

Active protein synthesis and membrane delivery in mitochondria p. 846

EMPOWER WITH EVIDENCE

AAAS | ANNUAL MEETING

Knowledge based on well-validated scientific discovery gives us the ability to transform our world. Over the last half-century, new discoveries from many different areas of science, technology, engineering, mathematics, and medicine have provided solutions to seemingly intractable problems. Research provides an unparalleled opportunity to explore and transform our world in all its complexity and mechanistic detail. It enables us to uncover fundamental aspects of how we relate to our world and to one another.

And yet, while the trajectory of the future will be defined by both the predictable and unexpected consequences of current scientific endeavors, the value of and trust in science have diminished. Science literacy, evidence-based decision making, science-based planning, and the use of validated knowledge to drive public policy are no longer universal societal aspirations. Engagement and communication must ensure that the value of science becomes accessible to all.

The 2022 AAAS Annual Meeting will feature groundbreaking trans- and multi-disciplinary research – not only to advance knowledge, but to understand and ultimately resolve many of the problems we face. The meeting will also highlight new initiatives in advocacy, education, and policy to address the challenges of rebuilding the public's trust and appreciation of science.

aaas.org/meetings | #AAASmtg

Apply for our exciting research Prize!

SCIENCE-PINS PRIZE FOR NEUROMODULATION

SCIENCE-PINS

$25, 000 Grand Prize!
Get published in *Science*!

The *Science*-PINS Prize is a highly competitive international prize that honors scientists for their excellent contributions to neuromodulation research. For purposes of the Prize, neuromodulation is any form of alteration of nerve activity through the delivery of physical (electrical, magnetic, or optical) stimulation to targeted sites of the nervous system with impications for translational medicine.

For full details, judging criteria and eligibility requirements, visit:

www.sciencemag.org/prizes/pins

Submission Deadline: 15 March 2021

Science AAAS

PINS 品驰

Science Translational Medicine AAAS

CONTENTS

19 FEBRUARY 2021 • VOLUME 371 • ISSUE 6531

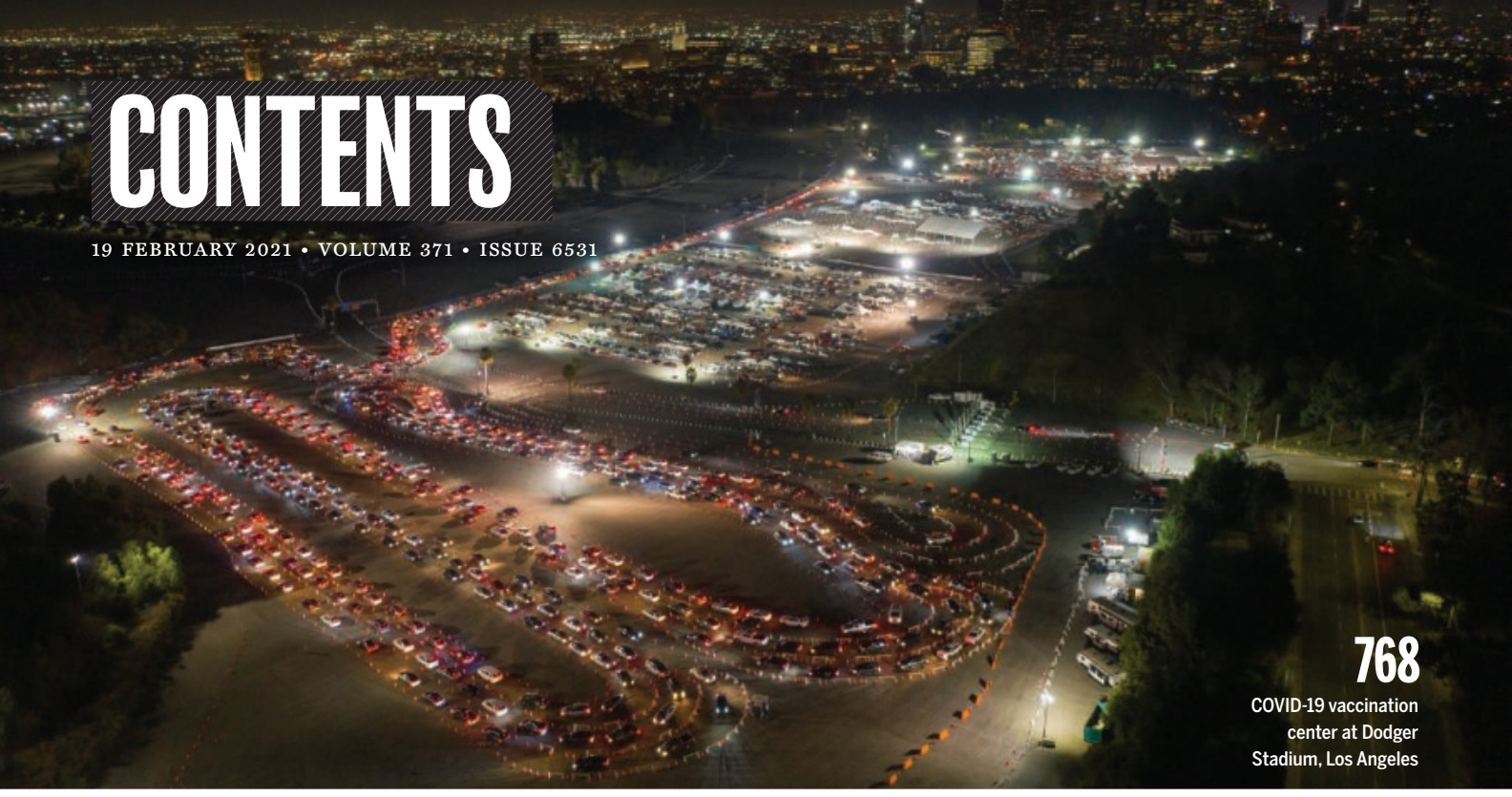

768
COVID-19 vaccination center at Dodger Stadium, Los Angeles

NEWS

IN BRIEF

760 News at a glance

IN DEPTH

762 Top German scientist fired after police raid of homes and offices
Reinhard Hüttl, head of earth science center and national academy official, faces allegations of financial crimes
By H. Feldwisch-Drentrup

763 France turns to citizens' panel to reduce vaccine skepticism
Panel advice on COVID-19 vaccines could counteract legacy of mistrust from past health scandals *By B. Casassus*

764 Deaths of health workers in Africa highlight vaccine inequity
Growing toll on fragile health systems prompts calls for rich countries to share their doses *By K. Kupferschmidt*

765 England's Stonehenge was erected in Wales first
Stones were set upright before being moved east *By A. Curry*

766 Kauri trees mark magnetic flip 42,000 years ago
Researchers say cosmic ray bombardment unleashed by weaker field drove climate shift *By P. Voosen*
RESEARCH ARTICLE p. 811

767 Media and aggression research retracted after scrutiny
Questioned psychology papers linger on in meta-analyses *By C. O'Grady*

FEATURES

768 The long road
Early signs suggest COVID-19 vaccines are having an impact, but questions abound about the path to normal
By J. Cohen
PODCAST

INSIGHTS

POLICY FORUM

774 We need a global science-policy body on chemicals and waste
Major gaps in current efforts limit policy responses *By Z. Wang* et al.

PERSPECTIVES

777 How many genetic changes create new species?
Speciation in plants and animals can involve differentiation across many genetic regions
By P. Nosil et al.

779 New genes from borrowed parts
Vertebrate genes acquire new capabilities by capturing parasitic genomic elements
By A. Wacholder and A.-R. Carvunis
RESEARCH ARTICLE p. 797

780 A masing ladder
A maser that amplifies emission of periodically modulated quantum states has uses in metrology *By R.-B. Liu*
SCIENCE ADVANCES RESEARCH ARTICLE BY M. JIANG *ET AL*. 10.1126/SCIADV.ABE0719

782 Re-engineering Botox
Botulinum neurotoxin is altered to recognize a different substrate *By P. Stenmark*
RESEARCH ARTICLE p. 803

783 The genetic underground of antibiotic resistance
The silent role and clinical relevance of metabolic mutations in antibiotic resistance begin to be unravelled *By M. Zampieri*
RESEARCH ARTICLE p. 799

784 Tissue regeneration: Reserve or reverse?
Stem cells recover from injury by tissue dedifferentiation, not from dedicated reserves *By R. A. Shivdasani* et al.

786 Emerging cell therapy for biliary diseases
Gallbladder organoids repair bile ducts in mouse and human liver
By S. N. T. Kurial and H. Willenbring
REPORT p. 839

BOOKS *ET AL.*

788 Portrait of a groundbreaking astronomer
A new biography paints a vivid picture of the life of dark matter pioneer Vera Rubin
By J. Behrman

PHOTO: BING GUAN/BLOOMBERG VIA GETTY IMAGES

789 Probing the genetic future of humanity
A bioethicist breaks down the first human germline genome editing experiment *By M. A. Goldman*

LETTERS

790 Protect and regulate China's oyster resources
By H. Yang et al.

790 CropLife International shares FAO's vision
By G. Di Tommaso

791 Lack of knowledge threatens beaked whales
By S. Li and M. Rosso

791 Errata

RESEARCH

IN BRIEF

793 From *Science* and other journals

REVIEW

796 Plant science
Plant evolution driven by interactions with symbiotic and pathogenic microbes
P.-M. Delaux and S. Schornack
REVIEW SUMMARY; FOR FULL TEXT: DOI.ORG/10.1126/SCIENCE.ABA6605

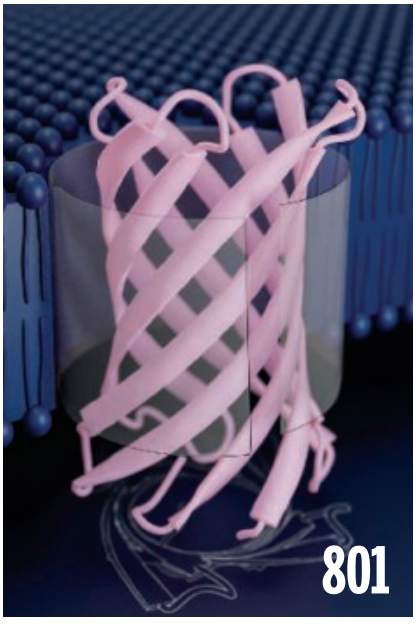

RESEARCH ARTICLES

797 Evolution
Recurrent evolution of vertebrate transcription factors by transposase capture *R. L. Cosby* et al.
RESEARCH ARTICLE SUMMARY; FOR FULL TEXT: DOI.ORG/10.1126/SCIENCE.ABC6405
PERSPECTIVE p. 779

798 Bacterial genomics
Microbial single-cell RNA sequencing by split-pool barcoding *A. Kuchina* et al.
RESEARCH ARTICLE SUMMARY; FOR FULL TEXT: DOI.ORG/10.1126/SCIENCE.ABA5257

799 Antibiotic resistance
Clinically relevant mutations in core metabolic genes confer antibiotic resistance
A. J. Lopatkin et al.
RESEARCH ARTICLE SUMMARY; FOR FULL TEXT: DOI.ORG/10.1126/SCIENCE.ABA0862
PERSPECTIVE p. 783

800 DNA origami
Absolute and arbitrary orientation of single-molecule shapes *A. Gopinath* et al.
RESEARCH ARTICLE SUMMARY; FOR FULL TEXT: DOI.ORG/10.1126/SCIENCE.ABD6179

801 Protein design
De novo design of transmembrane β barrels
A. A. Vorobieva et al.
RESEARCH ARTICLE SUMMARY; FOR FULL TEXT: DOI.ORG/10.1126/SCIENCE.ABC8182

802 Coronavirus
Inferring the effectiveness of government interventions against COVID-19
J. M. Brauner et al.
RESEARCH ARTICLE SUMMARY; FOR FULL TEXT: DOI.ORG/10.1126/SCIENCE.ABD9338

803 Protein engineering
Phage-assisted evolution of botulinum neurotoxin proteases with reprogrammed specificity *T. R. Blum* et al.
PERSPECTIVE p. 782

811 Paleoenvironment
A global environmental crisis 42,000 years ago *A. Cooper* et al.
NEWS STORY p. 766

818 Surface chemistry
Determining structural and chemical heterogeneities of surface species at the single-bond limit *J. Xu* et al.

823 Coronavirus
Broad and potent activity against SARS-like viruses by an engineered human monoclonal antibody *C. G. Rappazzo* et al.

REPORTS

830 Thermoelectrics
High-entropy-stabilized chalcogenides with high thermoelectric performance
B. Jiang et al.

835 Conservation
Human impacts on global freshwater fish biodiversity *G. Su* et al.

839 Tissue repair
Cholangiocyte organoids can repair bile ducts after transplantation in the human liver
F. Sampaziotis et al.
PERSPECTIVE p. 786

846 Mitoribosome
Mechanism of membrane-tethered mitochondrial protein synthesis
Y. Itoh et al.

850 Coronavirus
Prospective mapping of viral mutations that escape antibodies used to treat COVID-19
T. N. Starr et al.

DEPARTMENTS

759 Editorial
A universal coronavirus vaccine
By Wayne C. Koff and Seth F. Berkley

858 Working Life
Mentor as you'd want to be mentored
By Eric Wengert

ON THE COVER

Mitochondrial ribosomes, or mitoribosomes, are tethered to the mitochondrial inner membrane to facilitate insertion of synthesized proteins (bright yellow) encoded by the mitochondrial genome. A gating mechanism of the exit tunnel (cyan) enables protein delivery to the membrane insertase OXA1L (light brown). The relative positions shown here are from structural data of an intact translating human mitoribosome:OXA1L complex. See page 846. *Illustration: D. W. Nowakowski/N Molecular Systems, Inc.; Data: A. Amunts/Stockholm University*

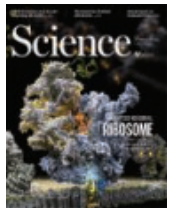

Science Staff 758
Science Careers 855

CREDIT: IAN HAYDON

SCIENCE (ISSN 0036-8075) is published weekly on Friday, except last week in December, by the American Association for the Advancement of Science, 1200 New York Avenue, NW, Washington, DC 20005. Periodicals mail postage (publication No. 484460) paid at Washington, DC, and additional mailing offices.

Copyright © 2021 by the American Association for the Advancement of Science. The title SCIENCE is a registered trademark of the AAAS.

Domestic individual membership, including subscription (12 months): $165 ($74 allocated to subscription). Domestic institutional subscription (51 issues): $2148; Foreign postage extra: Air assist delivery: $98. First class, airmail, student, and emeritus rates on request. Canadian rates with GST available upon request, GST #125488122. Publications Mail Agreement Number 1069624. **Printed in the U.S.A.**
Change of address: Allow 4 weeks, giving old and new addresses and 8-digit account number. **Postmaster:** Send change of address to AAAS, P.O. Box 96178, Washington, DC 20090–6178. **Single-copy sales:** $15 each plus shipping and handling available from backissues.sciencemag.org; bulk rate on request. **Authorization to reproduce** material for internal or personal use under circumstances not falling within the fair use provisions of the Copyright Act can be obtained through the Copyright Clearance Center (CCC), www.copyright.com. The identification code for *Science* is 0036-8075. *Science* is indexed in the *Reader's Guide to Periodical Literature* and in several specialized indexes.

Science AAAS

Editor-in-Chief Holden Thorp, hthorp@aaas.org

Executive Editor Monica M. Bradford

Editors, Research Valda Vinson, Jake S. Yeston **Editor, Insights** Lisa D. Chong

DEPUTY EDITORS Julia Fahrenkamp-Uppenbrink (UK), Stella M. Hurtley (UK), Phillip D. Szuromi, Sacha Vignieri **SR. EDITORIAL FELLOW** Andrew M. Sugden (UK) **SR. EDITORS** Gemma Alderton (UK), Caroline Ash (UK), Brent Grocholski, Pamela J. Hines, Di Jiang, Marc S. Lavine (Canada), Yevgeniya Nusinovich, Ian S. Osborne (UK), Beverly A. Purnell, L. Bryan Ray, H. Jesse Smith, Keith T. Smith (UK), Jelena Stajic, Peter Stern (UK), Valerie B. Thompson, Brad Wible, Laura M. Zahn **ASSOCIATE EDITORS** Michael A. Funk, Priscilla N. Kelly, Tage S. Rai, Seth Thomas Scanlon (UK), Yury V. Suleymanov **LETTERS EDITOR** Jennifer Sills **LEAD CONTENT PRODUCTION EDITORS** Harry Jach, Lauren Kmec **CONTENT PRODUCTION EDITORS** Amelia Beyna, Jeffrey E. Cook, Chris Filiatreau, Julia Katris, Nida Masiulis, Suzanne M. White **SR. EDITORIAL COORDINATORS** Carolyn Kyle, Beverly Shields **EDITORIAL COORDINATORS** Aneera Dobbins, Joi S. Granger, Jeffrey Hearn, Lisa Johnson, Maryrose Madrid, Ope Martins, Shannon McMahon, Jerry Richardson, Hilary Stewart (UK), Alana Warnke, Alice Whaley (UK), Anita Wynn **PUBLICATIONS ASSISTANTS** Jeremy Dow, Alexander Kief, Ronmel Navas, Brian White **EXECUTIVE ASSISTANT** Jessica Slater **ASI DIRECTOR, OPERATIONS** Janet Clements (UK) **ASI SR. OFFICE ADMINISTRATOR** Jessica Waldock (UK)

News Editor Tim Appenzeller

NEWS MANAGING EDITOR John Travis **INTERNATIONAL EDITOR** Martin Enserink **DEPUTY NEWS EDITORS** Elizabeth Culotta, Lila Guterman, David Grimm, Eric Hand (Europe), David Malakoff **SR. CORRESPONDENTS** Daniel Clery (UK), Jon Cohen, Jeffrey Mervis, Elizabeth Pennisi **ASSOCIATE EDITORS** Jeffrey Brainard, Catherine Matacic **NEWS REPORTERS** Adrian Cho, Jennifer Couzin-Frankel, Jocelyn Kaiser, Kelly Servick, Robert F. Service, Erik Stokstad, Paul Voosen, Meredith Wadman **INTERNS** Lucy Hicks, Cathleen O'Grady **CONTRIBUTING CORRESPONDENTS** Warren Cornwall, Andrew Curry (Berlin), Ann Gibbons, Sam Kean, Eli Kintisch, Kai Kupferschmidt (Berlin), Andrew Lawler, Mitch Leslie, Eliot Marshall, Virginia Morell, Dennis Normile (Shanghai), Elisabeth Pain (Careers), Charles Piller, Michael Price, Tania Rabesandratana (Barcelona), Joshua Sokol, Emily Underwood, Gretchen Vogel (Berlin), Lizzie Wade (Mexico City) **CAREERS** Donisha Adams, Rachel Bernstein (Editor), Katie Langin (Associate Editor) **COPY EDITORS** Julia Cole (Senior Copy Editor), Cyra Master (Copy Chief) **ADMINISTRATIVE SUPPORT** Meagan Weiland

Creative Director Beth Rakouskas

DESIGN MANAGING EDITOR Marcy Atarod **GRAPHICS MANAGING EDITOR** Alberto Cuadra **PHOTOGRAPHY MANAGING EDITOR** William Douthitt **WEB CONTENT STRATEGY MANAGER** Kara Estelle-Powers **DESIGN EDITOR** Chrystal Smith **DESIGNER** Christina Aycock **GRAPHICS EDITOR** Nirja Desai **INTERACTIVE GRAPHICS EDITOR** Kelly Franklin **SENIOR SCIENTIFIC ILLUSTRATORS** Valerie Altounian, Chris Bickel **SCIENTIFIC ILLUSTRATOR** Alice Kitterman **SENIOR GRAPHICS SPECIALISTS** Holly Bishop, Nathalie Cary **SENIOR PHOTO EDITOR** Emily Petersen **PHOTO EDITOR** Kaitlyn Dolan **WEB DESIGNER** Jennie Pajerowski

Chief Executive Officer and Executive Publisher Sudip Parikh

Publisher, Science Family of Journals Bill Moran

DIRECTOR, BUSINESS SYSTEMS AND FINANCIAL ANALYSIS Randy Yi **DIRECTOR, BUSINESS OPERATIONS & ANALYSIS** Eric Knott **DIRECTOR OF ANALYTICS** Enrique Gonzales **MANAGER, BUSINESS OPERATIONS** Jessica Tierney **SENIOR BUSINESS ANALYST** Cory Lipman, Meron Kebede **FINANCIAL ANALYST** Alexander Lee **ADVERTISING SYSTEM ADMINISTRATOR** Tina Burks **SENIOR SALES COORDINATOR** Shirley Young **DIGITAL/PRINT STRATEGY MANAGER** Jason Hillman **QUALITY TECHNICAL MANAGER** Marcus Spiegler **ASSISTANT MANAGER DIGITAL/PRINT** Rebecca Doshi **SENIOR CONTENT SPECIALISTS** Steve Forrester, Jacob Hedrick, Antoinette Hodal, Lori Murphy **PRODUCTION SPECIALIST** Kristin Wowk **DIGITAL PRODUCTION MANAGER** Lisa Stanford **CONTENT SPECIALIST** Kimberley Oster **ADVERTISING PRODUCTION OPERATIONS MANAGER** Deborah Tompkins **DESIGNER, CUSTOM PUBLISHING** Jeremy Huntsinger **SR. TRAFFIC ASSOCIATE** Christine Hall **SPECIAL PROJECTS ASSOCIATE** Sarah Dhere

ASSOCIATE DIRECTOR, BUSINESS DEVELOPMENT Justin Sawyers **GLOBAL MARKETING MANAGER** Allison Pritchard **DIGITAL MARKETING MANAGER** Aimee Aponte **JOURNALS MARKETING MANAGER** Shawana Arnold **MARKETING ASSOCIATES** Tori Velasquez, Mike Romano, Ashley Hylton **DIGITAL MARKETING SPECIALIST** Asleigh Rojanavongse **SENIOR DESIGNER** Kim Huynh

DIRECTOR AND SENIOR EDITOR, CUSTOM PUBLISHING Sean Sanders **ASSISTANT EDITOR, CUSTOM PUBLISHING** Jackie Oberst

DIRECTOR, PRODUCT & PUBLISHING DEVELOPMENT Chris Reid **DIRECTOR, BUSINESS STRATEGY AND PORTFOLIO MANAGEMENT** Sarah Whalen **ASSOCIATE DIRECTOR, PRODUCT MANAGMENT** Kris Bishop **PRODUCT DEVELOPMENT MANAGER** Scott Chernoff **PUBLISHING TECHNOLOGY MANAGER** Michael Di Natale **SR. PRODUCT ASSOCIATE** Robert Koepke **SPJ ASSOCIATE** Samantha Bruno Fuller

DIRECTOR, INSTITUTIONAL LICENSING Iquo Edim **ASSOCIATE DIRECTOR, RESEARCH & DEVELOPMENT** Elisabeth Leonard **MARKETING MANAGER** Kess Knight **SENIOR INSTITUTIONAL LICENSING MANAGER** Ryan Rexroth **INSTITUTIONAL LICENSING MANAGER** Marco Castellan **MANAGER, AGENT RELATIONS & CUSTOMER SUCCESS** Judy Lillibridge **SENIOR OPERATIONS ANALYST** Lana Guz **FULFILLMENT COORDINATOR** Melody Stringer **SALES COORDINATOR** Josh Haverlock

DIRECTOR, GLOBAL SALES Tracy Holmes **US EAST COAST AND MID WEST SALES** Stephanie O'Connor **US WEST COAST SALES** Lynne Stickrod **US SALES MANAGER, SCIENCE CAREERS** Claudia Paulsen-Young **US SALES REP, SCIENCE CAREERS** Tracy Anderson **ASSOCIATE DIRECTOR, ROW** Roger Goncalves **SALES REP, ROW** Sarah Lelarge **SALES ADMIN ASSISTANT, ROW** Bryony Cousins **DIRECTOR OF GLOBAL COLLABORATION AND ACADEMIC PUBLISHING RELATIONS, ASIA** Xiaoying Chu **ASSOCIATE DIRECTOR, INTERNATIONAL COLLABORATION** Grace Yao **SALES MANAGER** Danny Zhao **MARKETING MANAGER** Kilo Lan **ASCA CORPORATION, JAPAN** Kaoru Sasaki (Tokyo), Miyuki Tani (Osaka) **COLLABORATION/ CUSTOM PUBLICATIONS/JAPAN** Adarsh Sandhu

DIRECTOR, COPYRIGHT, LICENSING AND SPECIAL PROJECTS Emilie David **RIGHTS AND LICENSING COORDINATOR** Jessica Adams **RIGHTS AND PERMISSIONS ASSOCIATE** Elizabeth Sandler **CONTRACTS AND LICENSING ASSOCIATE** Lili Catlett

MAIN HEADQUARTERS
Science/AAAS
1200 New York Ave. NW
Washington, DC 20005

SCIENCE INTERNATIONAL
Clarendon House
Clarendon Road
Cambridge, CB2 8FH, UK

SCIENCE CHINA
Room 1004, Culture Square
No. 59 Zhongguancun St.
Haidian District, Beijing, 100872

SCIENCE JAPAN
ASCA Corporation
Sibaura TY Bldg. 4F, 1-14-5
Shibaura Minato-ku
Tokyo, 108-0073 Japan

EDITORIAL
science_editors@aaas.org

NEWS
science_news@aaas.org

INFORMATION FOR AUTHORS
sciencemag.org/authors/science-information-authors

REPRINTS AND PERMISSIONS
sciencemag.org/help/reprints-and-permissions

MEDIA CONTACTS
scipak@aaas.org

MULTIMEDIA CONTACTS
SciencePodcast@aaas.org
ScienceVideo@aaas.org

INSTITUTIONAL SALES AND SITE LICENSES
sciencemag.org/librarian

PRODUCT ADVERTISING & CUSTOM PUBLISHING
advertising.sciencemag.org/products-services
science_advertising@aaas.org

CLASSIFIED ADVERTISING
advertising.sciencemag.org/science-careers
advertise@sciencecareers.org

JOB POSTING CUSTOMER SERVICE
employers.sciencecareers.org
support@sciencecareers.org

MEMBERSHIP AND INDIVIDUAL SUBSCRIPTIONS
sciencemag.org/subscriptions

MEMBER BENEFITS
aaas.org/membercentral

AAAS BOARD OF DIRECTORS
CHAIR Steven Chu
PRESIDENT Claire M. Fraser
PRESIDENT-ELECT Susan G. Amara
TREASURER Carolyn N. Ainslie
CHIEF EXECUTIVE OFFICER
Sudip Parikh
BOARD Cynthia M. Beall
Rosina M. Bierbaum
Ann Bostrom
Stephen P.A. Fodor
S. James Gates, Jr.
Laura H. Greene
Kaye Husbands Fealing
Maria M. Klawe
Robert B. Millard
Alondra Nelson
William D. Provine

Science serves as a forum for discussion of important issues related to the advancement of science by publishing material on which a consensus has been reached as well as including the presentation of minority or conflicting points of view. Accordingly, all articles published in *Science*—including editorials, news and comment, and book reviews—are signed and reflect the individual views of the authors and not official points of view adopted by AAAS or the institutions with which the authors are affiliated.

BOARD OF REVIEWING EDITORS (Statistics board members indicated with **(S)**)

Takuzo Aida, *U. of Tokyo*
Leslie Aiello, *Wenner-Gren Foundation*
Deji Akinwande, *UT Austin*
Judith Allen, *U. of Manchester*
Marcella Alsan, *Harvard U.*
Sebastian Amigorena, *Institut Curie*
James Analytis, *UC Berkeley*
Trevor Archer, *NIEHS, NIH*
Paola Arlotta, *Harvard U.*
David Awschalom, *U. of Chicago*
Clare Baker, *U. of Cambridge*
Delia Baldassarri, *NYU*
Nenad Ban, *ETH Zürich*
Franz Bauer, *Pontificia U. Católica de Chile*
Ray H. Baughman, *UT Dallas*
Carlo Beenakker, *Leiden U.*
Yasmine Belkaid, *NIAID, NIH*
Philip Benfey, *Duke U.*
Kiros T. Berhane, *Columbia U.*
Bradley Bernstein, *Mass. General Hospital*
Joseph J. Berry, *NREL*
Alessandra Biffi, *Harvard Med.*
Chris Bowler, *École Normale Supérieure*
Ian Boyd, *U. of St. Andrews*
Emily Brodsky, *UC Santa Cruz*
Ron Brookmeyer, *UCLA* **(S)**
Christian Büchel, *UKE Hamburg*
Dennis Burton, *Scripps Res.*
Carter Tribley Butts, *UC Irvine*
György Buzsáki, *NYU School of Med.*
Mariana Byndloss, *Vanderbilt U. Med. Ctr*
Annmarie Carlton, *UC Irvine*
Nick Chater, *U. of Warwick*
Ling-Ling Chen, *SIBCB, CAS*
M. Keith Chen, *UCLA*
Zhijian Chen, *UT Southwestern Med. Ctr.*
Ib Chorkendorff, *Denmark TU*
James J. Collins, *MIT*
Robert Cook-Deegan, *Arizona State U.*
Virginia Cornish *Columbia U.*
Carolyn Coyne, *U. of Pitt.*
Roberta Croce, *VU Amsterdam*
Ismaila Dabo, *Penn State U.*
Jeff L. Dangl, *UNC*
Chiara Daraio, *Caltech*
Nicolas Dauphas, *U. of Chicago*
Christian Davenport, *U. of Michigan*
Frans de Waal, *Emory U.*
Claude Desplan, *NYU*
Sandra Díaz, *U. Nacional de Córdoba*
Ulrike Diebold, *TU Wien*
Stefanie Dimmeler, *Goethe-U. Frankfurt*
Hong Ding, *Inst. of Physics, CAS*
Dennis Discher, *UPenn*
Jennifer A. Doudna, *UC Berkeley*
Ruth Drdla-Schutting, *Med. U. Vienna*
Raissa M. D'Souza, *UC Davis*
Bruce Dunn, *UCLA*
William Dunphy, *Caltech*
Scott Edwards, *Harvard U.*
Todd Ehlers, *U. of Tübingen*
Jennifer Elisseeff, *Johns Hopkins U.*
Andrea Encalada, *U. San Francisco de Quito*
Nader Engheta, *U. of Penn.*
Karen Ersche, *U. of Cambridge*
Beate Escher, *UFZ & U. of Tübingen*
Barry Everitt, *U. of Cambridge*
Vanessa Ezenwa, *U. of Georgia*
Michael Feuer, *GWU*
Toren Finkel, *U. of Pitt. Med. Ctr.*
Gwenn Flowers, *Simon Fraser U.*
Peter Fratzl, *Max Planck Inst. Potsdam*
Elaine Fuchs, *Rockefeller U.*
Jay Gallagher, *U. of Wisconsin*
Daniel Geschwind, *UCLA*
Ramon Gonzalez, *U. of South Florida*
Sandra González-Bailón, *UPenn*
Elizabeth Grove, *U. of Chicago*
Nicolas Gruber, *ETH Zürich*
Hua Guo, *U. of New Mexico*
Taekjip Ha, *Johns Hopkins U.*
Sharon Hammes-Schiffer, *Yale U.*
Wolf-Dietrich Hardt, *ETH Zürich*
Louise Harra, *U. Coll. London*
Jian He, *Clemson U.*
Carl-Philipp Heisenberg, *IST Austria*
Ykä Helariutta, *U. of Cambridge*
Janet G. Hering, *Eawag*
Heather Hickman, *NIAID, NIH*
Hans Hilgenkamp, *U. of Twente*
Kai-Uwe Hinrichs, *U. of Bremen*
Deirdre Hollingsworth, *U. of Oxford*
Randall Hulet, *Rice U.*
Auke Ijspeert, *EPFL*
Akiko Iwasaki, *Yale U.*
Stephen Jackson, *USGS & U. of Arizona*
Erich Jarvis, *Rockefeller U.*
Peter Jonas, *IST Austria*
Matt Kaeberlein, *U. of Wash.*
William Kaelin Jr., *Dana-Farber Cancer Inst.*
Daniel Kammen, *UC Berkeley*
V. Narry Kim, *Seoul Nat. U.*
Robert Kingston, *Harvard Med.*
Nancy Knowlton, *Smithsonian Institution*
Etienne Koechlin, *École Normale Supérieure*
Alex L. Kolodkin, *Johns Hopkins U.*
Julija Krupic, *U. of Cambridge*
Gabriel Lander, *Scripps Res.* **(S)**
Mitchell A. Lazar, *UPenn*
Wendell Lim, *UCSF*
Luis Liz-Marzán, *CIC biomaGUNE*
Omar Lizardo, *UCLA*
Jonathan Losos, *Wash. U. in St. Louis*
Ke Lu, *Inst. of Metal Res., CAS*
Christian Lüscher, *U. of Geneva*
Jean Lynch-Stieglitz, *Georgia Inst. of Tech.*
David Lyons, *U. of Edinburgh*
Fabienne Mackay, *QIMR Berghofer*
Anne Magurran, *U. of St. Andrews*
Asifa Majid, *U. of York*
Oscar Marín, *King's Coll. London*
Charles Marshall, *UC Berkeley*
Christopher Marx, *U. of Idaho*
David Masopust, *U. of Minnesota*
Geraldine Masson, *CNRS*
Jason Matheny, *Georgetown U.*
Heidi McBride, *McGill U.*
C. Robertson McClung, *Dartmouth*
Rodrigo Medellín, *U. Nacional Autónoma de México*
Jane Memmott, *U. of Bristol*
C. Jessica Metcalf, *Princeton U.*
Baoxia Mi, *UC Berkeley*
Tom Misteli, *NCI, NIH*
Alison Motsinger-Reif, *NIEHS, NIH* **(S)**
Danielle Navarro, *U. of New South Wales*
Daniel Nettle, *Newcastle U.*
Daniel Neumark, *UC Berkeley*
Beatriz Noheda, *U. of Groningen*
Helga Nowotny, *Vienna Sci., Res. & Tech. Fund*
Rachel O'Reilly, *U. of Birmingham*
Pilar Ossorio, *U. of Wisconsin*
Andrew Oswald, *U. of Warwick*
Isabella Pagano, *Istituto Nazionale di Astrofisica*
Elizabeth Levy Paluck, *Princeton U.*
Jane Parker, *Max Planck Inst. Cologne*
Giovanni Parmigiani, *Dana-Farber Cancer Inst.* **(S)**
Daniel Pauly, *U. of British Columbia*
Samuel Pfaff, *Salk Inst.*
Julie Pfeiffer, *UT Southwestern Med. Ctr.*
Philip Phillips, *UIUC*
Matthieu Piel, *Institut Curie*
Kathrin Plath, *UCLA*
Martin Plenio, *Ulm U.*
Katherine Pollard, *UCSF*
Elvira Poloczanska, *Alfred-Wegener-Inst.*
Julia Pongratz, *Ludwig Maximilians U.*
Philippe Poulin, *CNRS*
Jonathan Pritchard, *Stanford U.*
Lei Stanley Qi, *Stanford U.*
Trevor Robbins, *U. of Cambridge*
Joeri Rogelj, *Imperial Coll. London*
Amy Rosenzweig, *Northwestern U.*
Mike Ryan, *UT Austin*
Miquel Salmeron, *Lawrence Berkeley Nat. Lab*
Nitin Samarth, *Penn State U.*
Erica Ollmann Saphire, *La Jolla Inst.*
Joachim Saur, *U. zu Köln*
Alexander Schier, *Harvard U.*
Wolfram Schlenker, *Columbia U.*
Susannah Scott, *UC Santa Barbara*
Anuj Shah, *U. of Chicago*
Vladimir Shalaev, *Purdue U.*
Jie Shan, *Cornell U.*
Beth Shapiro, *UC Santa Cruz*
Jay Shendure, *U. of Wash.*
Steve Sherwood, *U. of New South Wales*
Brian Shoichet, *UCSF*
Robert Siliciano, *JHU School of Med.*
Lucia Sivilotti, *U. Coll. London*
Alison Smith, *John Innes Centre*
Richard Smith, *UNC* **(S)**
Mark Smyth, *QIMR Berghofer*
John Speakman, *U. of Aberdeen*
Tara Spires-Jones, *U. of Edinburgh*
Allan C. Spradling, *Carnegie Institution for Sci.*
V. S. Subrahmanian, *Dartmouth*
Ira Tabas, *Columbia U.*
Eriko Takano, *U. of Manchester*
Patrick Tan, *Duke-NUS Med. School*
Sarah Teichmann, *Wellcome Sanger Inst.*
Rocio Titiunik, *Princeton U.*
Shubha Tole, *Tata Inst. of Fundamental Res.*
Kimani Toussaint, *Brown U.*
Wim van der Putten, *Netherlands Inst. of Ecology*
Reinhilde Veugelers, *KU Leuven*
Bert Vogelstein, *Johns Hopkins U.*
David Wallach, *Weizmann Inst.*
Jane-Ling Wang, *UC Davis* **(S)**
Jessica Ware, *Amer. Mus. of Natural Hist.*
David Waxman, *Fudan U.*
Chris Wikle, *U. of Missouri* **(S)**
Terrie Williams, *UC Santa Cruz*
Ian A. Wilson, *Scripps Res.* **(S)**
Yu Xie, *Princeton U.*
Jan Zaanen, *Leiden U.*
Kenneth Zaret, *UPenn School of Med.*
Bing Zhu, *Inst. of Biophysics, CAS*
Xiaowei Zhuang, *Harvard U.*
Maria Zuber, *MIT*

EDITORIAL

A universal coronavirus vaccine

Wayne C. Koff is chief executive officer of the Human Vaccines Project, New York, NY, USA. wkoff@humanvaccinesproject.org

Seth F. Berkley is chief executive officer of Gavi, The Vaccine Alliance, Geneva, Switzerland. sberkley@gavi.org

COVID-19 has already produced catastrophic social, economic, and public health consequences, with more than 107 million documented cases and 2.3 million deaths. Although this pandemic is far from over, we now have the tools to end it, with the largest and most rapid global deployment of vaccines under way. That we got this far so quickly is remarkable, but next time we might not be so lucky. More virulent and deadly coronaviruses are waiting in the wings. Thus, the world needs a universal coronavirus vaccine.

The speed with which safe and effective COVID-19 vaccines have been developed and made available is unprecedented, taking less than a year. However, if faced with a more virulent strain with a higher case fatality rate than severe acute respiratory syndrome coronavirus 2 (SARS-CoV-2), even this rapid time frame may not be enough to prevent a death toll on the scale of the 1918 influenza pandemic, which killed more than 50 million. Moreover, there is a continuing risk that the virus will mutate in ways that render existing COVID-19 vaccines less effective—as we've already seen for the B.1.351 variant first identified in South Africa—or even ineffective.

> "More virulent and deadly coronaviruses are waiting in the wings."

As with influenza, the case for a vaccine that protects all people against all forms of coronavirus is strong. SARS-CoV-2 belongs to a diverse group of viruses of which there are thousands capable of infecting a wide range of animals, from bats and pangolins to pigs and mink. SARS-CoV-1, which emerged in 2002, had a 10% fatality rate; Middle East respiratory syndrome coronavirus (MERS-CoV) in 2012 was 34% fatal.

The potential is increasing for other coronaviruses to jump species and cause more pandemics. The reasons are many. The animals that the viruses infect are ones that humans regularly come into contact with. Modern agricultural practices, viral evolution, and relentless human encroachment on the natural environment mean there is an increasing risk of people encountering previously isolated animal populations that harbor new strains with pandemic potential. With human migration, population growth, urbanization, rapid global travel, and climate change hastening the spread, it has never been easier for outbreaks to turn into epidemics and escalate into pandemics.

At the same time, the recent convergence of technological advances in biomedical, computing, and engineering sciences has ushered in a new era in antigen and vaccine discovery. High-performance supercomputing and machine learning, coupled with structural modeling, have the potential to greatly accelerate identification of common antigenic targets shared across coronaviruses. Databases of genetic sequences of animal isolates of coronaviruses can be used to model the evolutionary emergence of the viruses. Ongoing efforts to decode the principles of immunity in aging populations can enhance the effectiveness of vaccines for those most vulnerable. Collectively, studies now suggest that developing a universal coronavirus vaccine is scientifically feasible.

This must be a worldwide effort. A roadmap is needed to lay out the core scientific issues as well as a framework for funding and sharing of information, data, and resources. Early on, it will be essential to establish a global surveillance network for zoonotic coronaviruses like the World Health Organization's Global Influenza Surveillance and Response System or the United States Agency for International Development's PREDICT program (which was defunded last year). In addition, a global effort to identify coronavirus-specific broadly neutralizing antibodies is needed to facilitate cross-reactive coronavirus antigen discovery.

None of that can happen until all stakeholders, across governments, industry, academia, and nongovernmental organizations, recognize this as a global public health priority. With COVID-19, much of the groundwork has been laid. To wait until after this crisis passes could prove to be a missed opportunity. It is estimated that the current pandemic will end up costing between US$ 8 and 16 trillion globally, ~500 times more than would be required for preventing the next pandemic.

That is not to say that this will be easy, and a stepwise approach from COVID-19 to pan-coronavirus to universal coronavirus vaccines may be required. SARS-CoV-2 is rapidly adapting to humans, and other novel coronaviruses are mutating, recombining, and replicating in bats and other animal species, positioning to jump species sometime in the future. If we choose to wait for the next coronavirus to emerge, it may be too late, as it was with COVID-19. Creating the tools for preventing the next coronavirus pandemic is within our means and should be considered a global health priority. We can either invest now or pay substantially more later.

–Wayne C. Koff and Seth F. Berkley

10.1126/science.abh0447

$1.5 billion

NASA's savings estimate for its decision to launch the Europa Clipper probe to one of Jupiter's moons in 2024 on a commercial rocket instead of the larger Space Launch System, which has not yet flown. The commercial launch will delay the probe's arrival to 2030.

IN BRIEF

Edited by **Jeffrey Brainard**

THERAPEUTICS

Trial IDs second effective COVID-19 drug

The anti-inflammatory drug tocilizumab cut the death risk of people hospitalized with COVID-19, reduced their need for a mechanical ventilator, and shortened time spent in the hospital, investigators said last week. The results came from the United Kingdom's Recovery trial, the world's largest study of drugs to treat the disease. Tocilizumab is a monoclonal antibody that blocks the receptor for interleukin-6, a signaling molecule in the immune system. That dampens the immune response, which is often overactive in late-stage COVID-19. The mortality benefits spanned different ages, genders, and ethnicities. But at about £500 per treatment course in the United Kingdom, tocilizumab is 100 times more expensive than dexamethasone, a steroid that is the only other therapeutic shown to reduce deaths in severe cases of the disease. The cost raises questions once again about how to make sure populations across the world can benefit from scientific progress against COVID-19.

In-person teaching raised risks

COVID-19 | Keeping schools open in Sweden roughly doubled the risk that teachers would be diagnosed with the pandemic coronavirus in spring 2020, a study has found. It also raised the infection rate for their partners at home by 29% and for parents whose children attended in person by 17%, the authors reported on 11 February in the *Proceedings of the National Academy of Sciences*. Researchers in Sweden took advantage of their country's detailed health registry and the fact that schools through ninth grade never closed (they implemented extra hand washing but no mask requirements), while grades 10 to 12 were taught remotely from 18 March 2020 until the end of June. Comparing infection rates in teachers and parents of ninth versus 10th graders let the researchers examine the effects of keeping schools open on two otherwise very similar groups, making the study one of the most precise to examine the risks of in-person schooling. The researchers noted that more stringent protections likely would have lowered the risks even further. Other researchers had struggled to distinguish the effects of school-based virus transmission because schools tended to close in concert with other restrictions.

Ebola again in Guinea and Congo

INFECTIOUS DISEASES | New outbreaks of Ebola have been reported in Guinea and the Democratic Republic of the Congo (DRC), two countries that beat back previous large outbreaks. In Guinea, at least three people have died of the disease in a community near where the region's 2014–16 outbreak started. In the first suspected case, a nurse died on 28 January in the Gouécké area; at least six people who attended the funeral developed symptoms of Ebola, which testing confirmed on 11 February. One patient traveled to the capital city, Conakry, about 900 kilometers away, before being hospitalized—raising worries of possible widespread exposure. Meanwhile, vaccinations against the disease have begun in the DRC's North Kivu province, the center of a large outbreak from 2018 to June 2020. There, at least four people were infected this month, two of whom died. One was the wife of an Ebola survivor, and authorities are investigating whether sexual transmission played a role.

Vaccine claims get RFK Jr. banned

PUBLIC HEALTH | The social media service Instagram last week shut down the account of well-known antivaccine activist Robert Kennedy Jr., saying his account "repeatedly [shared] debunked claims about the coronavirus or vaccines." Two days earlier, Facebook, which owns Instagram, had issued a new policy saying it would take down accounts that repeatedly share such misinformation. Kennedy's Facebook account was still operating when *Science* went to press. In an online response to Instagram's action, Kennedy defended his statements as based on reliable sources.

Restored dish contacts Voyager 2

SPACE EXPLORATION | NASA is once again in command of Voyager 2, one of its two long-lived probes in interstellar space. In March 2020, the agency began to refurbish an aging 70-meter-wide radio antenna in Australia, the only dish—because of its size, power, and location in the Southern Hemisphere—capable of sending commands to the 43-year-old spacecraft. The work had prevented NASA from sending

The Deep Space Station 43 radio antenna in Canberra, Australia, prompted Voyager 2's call home.

PHOTO: NASA/CANBERRA DEEP SPACE COMMUNICATION COMPLEX

The Amazon's white-bellied spider monkey is particularly vulnerable to wildlife trafficking.

CONSERVATION

Hunting, trapping take big toll on biodiversity

Wildlife trafficking poses a profound threat to vulnerable species, even in protected areas, a study has found. In places where hunting and trapping have gone unchecked, populations of 133 animal species, some listed as endangered, declined by almost 65% overall, researchers report this week in *Nature Ecology & Evolution*. Even in guarded preserves and areas where hunting quotas are enforced, populations declined by more than one-third. The work, which synthesized the findings of 31 studies, is among the first meta-analyses of the wildlife trade. Sales of wild animals—both legal and illegal—are largely driven by foreign and domestic demand for bushmeat, pets, and traditional medicines. The study also exposed gaps in research on the wildlife trade. The 31 studies mostly focused on mammals, and none investigated amphibians, invertebrates, orchids, or cacti—organisms traded by the millions. Just four studies looked at Asian locales, Oscar Morton of the University of Sheffield and colleagues write. Filling in these gaps, other researchers say, could help reveal how trafficking's toll on biodiversity compares with other threats, such as habitat loss.

PHOTO: PETE OXFORD/MINDEN PICTURES

the probe instructions in an emergency. On 12 February, the antenna resumed continuous operation and signaled Voyager 2, now nearly 19 billion kilometers away—receiving a response 35 hours later.

Mammoth molar holds oldest DNA

PALEONTOLOGY | Scientists have sequenced the oldest samples of DNA, extracted from molars of mammoths that roamed Earth more than 1 million years ago. The previous record for oldest sequenced DNA was from a horse dated to about 700,000 years ago. (Researchers have inferred the sequence of much older genetic material by analyzing ancient proteins.) The molars belonged to three mammoths dug from the permafrost of northeastern Siberia, two of which, the DNA results suggested, were ancestral to woolly mammoths already known from eastern Eurasia. A third, previously dated by geological and molecular methods to about 1.2 million years ago, belonged to a previously unknown lineage. North America's Columbian mammoths were a hybrid of woolly mammoths and this newly described lineage, the authors report this week in *Nature*. Permafrost can preserve DNA remarkably well, in contrast to hot, humid environments that often degrade DNA more rapidly. The new findings raise hopes for the discovery of more DNA from other ancient high-latitude species.

'Planet Nine' evidence shrinks

ASTRONOMY | Claims for an unseen giant planet on the Solar System's frontier are looking shaky. Astronomers reported last week that the orbits of a handful of distant lumps of rock are not necessarily bunched together by the gravity of Planet Nine, as its proponents believe, but just seem clustered because that's where telescopes happened to be looking or were most sensitive. But advocates for Planet Nine, thought to have a mass as much as 10 times Earth's, aren't backing down. The debate may be settled by the Vera C. Rubin Observatory in Chile, which will avoid selection biases and is expected to discover many more of the rocky bodies when it debuts in 2023.

NEWSMAKER

WHO mission head in hot seat

"The politics was always in the room with us on the other side of the table," Peter Ben Embarek, an epidemiologist and food scientist, told *Science* about leading the World Health Organization's (WHO's) mission to Wuhan, China, earlier this year to meet with Chinese scientists and investigate the origins of the pandemic coronavirus. The WHO team has drawn criticism for saying at a news briefing it was "extremely unlikely" that SARS-CoV-2 originated in a Chinese laboratory, and for keeping open the possibility that it arrived in Wuhan on frozen food from another country—an explanation aggressively promoted by Chinese media. Ben Embarek defended the team's conclusions, telling *Science* that calling a lab escape "extremely unlikely is not the same as if it had been listed or assessed as impossible. We're not closing the door." The full interview is at http://scim.ag/EmbarekQA.

Reinhard Hüttl was dismissed last month by the German Research Centre for Geosciences.

PHOTO: DAVID AUSSERHOFER

IN DEPTH

SCIENTIFIC ETHICS

Top German scientist fired after police raid of homes and offices

Reinhard Hüttl, head of earth science center and national academy official, faces allegations of financial crimes

By **Hinnerk Feldwisch-Drentrup**

Reinhard Hüttl had risen to the very top of German science. The soil scientist was head of the German Research Centre for Geosciences (GFZ), where he commanded a staff of more than 1200 and a €95 million budget. He was vice president of acatech, Germany's engineering-focused national academy, and vice president of the nation's most prestigious state academy, the Berlin-Brandenburg Academy of Sciences and Humanities (BBAW). His advice even reached Chancellor Angela Merkel—for example as a government adviser with the Council on Bioeconomy.

That world has come crashing down. Last month, police raided Hüttl's homes and offices in Berlin and Potsdam on suspicion of fraud, breach of trust, and illegal acceptance of benefits by a public official—offenses that can be punished with fines or prison sentences. On 26 January, the GFZ board dismissed him, saying it "no longer sees any basis for a trustworthy cooperation." The Federal Ministry of Education and Research (BMBF), which finances the bulk of the GFZ budget, terminated his contract the same day.

Hüttl denies the allegations and has said he would sue BMBF for unlawful dismissal, although labor courts in Berlin and Potsdam said on 16 February that no lawsuits have been filed. Meanwhile, the high-profile case is turning heads in science policy circles across the nation. "Science is damaged severely if it is perceived to be led by interests and to be corrupt," says Klaus Gärditz, who specializes in science law at the University of Bonn.

The case is also raising questions about whether Germany's many science academies have adequate policies for avoiding conflicts of interest and disclosing financial ties. In German science, the boundaries of what is acceptable are not clear, says Peter Weingart, a sociologist of science at Bielefeld University and long-term BBAW colleague of Hüttl's. "The idea that members would declare conflicts of interest didn't occur to us." (Weingart adds that he believes the accusations against Hüttl—who stepped back from his BBAW vice presidency on 1 February—are unfounded.)

Hüttl's troubles began in October 2020, when GFZ revealed in a statement that an anonymous whistleblower had alleged that Hüttl had violated financial compliance rules. He was relieved from his duties "until further notice," and was banned from entering GFZ premises and using its resources. The center turned the case over to the Brandenburg state public prosecutor office responsible for fighting corruption, which says it is also investigating two other suspects. Hüttl, however, is the prime suspect.

The prosecutor's office has not yet decided whether to charge Hüttl, and declined to provide specific information about the case. But according to information in a search warrant, first reported in the German newspaper *Welt am Sonntag* and reviewed by *Science*, the possible crimes are diverse. Hüttl is alleged to have billed private trips and meals to GFZ, acatech, and the Centre for Energy Technology Brandenburg (CEBra), a research institute affiliated with the Brandenburg University of Technology Cottbus-Senftenberg, where Hüttl held a professorship. In a statement to *Science*, Hüttl says he doesn't currently have access to seized documents, but that he'll prove those allegations wrong.

The search warrant also alleges that Hüttl illegally accepted options on shares and reimbursements from Novihum Technologies, a German company seeking to make rich soil from brown coal, in return for help securing grant money for the company. The accusations are unfounded, Hüttl says.

A third set of allegations relates to two organizations linked to China's state-owned electrical grid, the Global Energy Interconnection Development and Cooperation Organization (GEIDCO) and the Global Energy Interconnection Research Institute (GEIRI), which both lobby for a green worldwide supergrid. The warrant alleges that GEIDCO or GEIRI paid for a private tourist trip to China for Hüttl, and paid $50,000 to CEBra annually since 2018, in return for Hüttl's influence and contacts. *Science* has seen a document Hüttl apparently sent to GEIDCO that lists 41 activities in 2019 as "contribution to GEIDCO," including meetings with China's ambassador to Germany, members of BMBF, and the Federal Ministry of the Interior.

In 2018, GEIDCO head Liu Zhenya, who was head of the state grid company for many years, was elected as a member of acatech. Hüttl and acatech didn't respond to questions about who nominated Liu to the academy.

Hüttl denies working for GEIDCO or GEIRI, and says the payments to CEBra were for a science project that will eventually publish results. "I did not draw benefits," he says. GEIDCO, GEIRI, and the state grid company did not reply to email inquiries. Acatech, CEBra, and Novihum declined to answer questions, referring to the ongoing investigation.

Public officials like Hüttl are allowed to do paid work on the side, but need permission from the institution where they are employed. Hüttl says GFZ was aware of his "diverse activities" and approved of them. But a BMBF spokesperson says it had no knowledge of Hüttl's activities for GEIDCO. Hüttl did not provide a list of his side jobs in response to a request from *Science*, even though he has publicly stressed the importance of transparency in the past. "Politics and the public expect—and can expect—freedom of thought, a high degree of interconnectedness, and transparency from us," Hüttl said at a 2010 event with Merkel.

Following Hüttl's resignation, BBAW says it will soon ask members a set of questions, modeled on U.S. national academy rules, to identify potential conflicts of interest. "I think that the model of self-reporting, used up to now, does not meet the standard anymore," says BBAW President Christoph Markschies, who took office with Hüttl in October 2020.

The affair may also lead to more scrutiny of conflicts relating to China. Recently, the United States has cracked down on foreign influence in science, even arresting researchers who failed to disclose funding from China. But European nations have largely ignored the issue. Sebastian Heilmann, a political scientist at the University of Trier, says European organizations should toughen up conditions for grants from countries like China, for example by requiring disclosure and setting clear rules for interactions. And research managers from publicly funded institutes shouldn't consult for Chinese state-owned organizations, says Asena Baykal, of the Global Public Policy Institute in Berlin, who studies cooperation with nondemocracies.

In the wake of the allegations, Hüttl has abandoned other positions. Acatech suspended him on his request, and he gave up his chairmanship of the European Council of Academies of Applied Sciences, Technologies and Engineering. But Hüttl remains on the supervisory board of the car manufacturer BMW. Earlier this month, he got a new job: leading EUREF Energy Innovation, a company developing hydrogen energy. On 3 February, the CEO of its parent company, real estate developer EUREF AG, put out a statement saying he was proud to have attracted a "renowned, excellent and active scientist." ■

Hinnerk Feldwisch-Drentrup is a journalist in Berlin.

SCIENCE AND SOCIETY

France turns to citizens' panel to reduce vaccine skepticism

Panel advice on COVID-19 vaccines could counteract legacy of mistrust from past health scandals

By **Barbara Casassus**

All across Europe, coronavirus vaccines are in scarce supply. But in France, they are also surprisingly unwanted: Recent polls suggest just 57% of the country intends to get vaccinated, whereas in the United Kingdom, 89% wants to get a shot for COVID-19.

With persistent, world-leading rates of vaccine skepticism, France is adopting a new tactic to boost trust. A 35-member citizens' vaccine panel, built from a random but demographically representative slice of the country, met for the first time last month in an effort to steer government strategy on COVID-19 vaccinations. The panel is one of an increasing number of citizen assemblies that have been set up across Europe to grapple with thorny questions at the intersection of science and society (*Science*, 30 October 2020, p. 518).

Science's COVID-19 reporting is supported by the Heising-Simons Foundation.

The panel's first advice is due in a progress report on 23 February. Alain Fischer, a pediatric immunologist at the College of France and president of the government's vaccine strategy board, hopes the group can identify the information the public wants and how it should be presented, so it can be "understood by everyone, regardless of their knowledge of vaccines." He also expects the panel to provide practical tips, such as how to provide vaccinations in remote rural areas. "Citizen panelists usually have a good grasp of the issues," he says. Some critics, however, say the government already receives plenty of citizens' input, and they question the need for the new body.

Heidi Larson, who directs the Vaccine Confidence Project at the London School of Hygiene & Tropical Medicine, says the memory of past health scandals accounts for some of the French wariness about vaccines. In the 1980s, HIV-contaminated blood transfusions are thought to have infected hundreds of people with hemophilia, while the antidiabetes drug Mediator may have killed hundreds of people before regulators finally took it off the market in 2009. "This is partly why the French people's default position is distrust," Larson says.

Her project's 2016 study of vaccine confidence showed France ranked last among 67 countries, with 41% of respondents saying they believed vaccines were unsafe. Larson says the findings helped the French government realize how big the problem was, and since then, trust in vaccines has risen a bit. Her project's latest polling, from December 2020, shows France fifth out of 32 nations for vaccine antipathy. "The French are incrementally more confident, but they are still at the low end in international comparisons," Larson says. The government has "made a significant effort in communication, but needs to focus more on the listening side of the dialogue."

Citizen groups offer a chance for this listening—or at least the appearance of it. Fischer notes how an earlier group contributed to the debate before parliament passed a law that, starting in 2018, boosted the number of required

Some experts say citizen advice helped counter the effect of French protests of an infant vaccination law.

PHOTO: SIPA/AP IMAGES

vaccinations for infants from three to 11. The group agreed the vaccinations were "indispensable," and, because immunity was dropping, they could be made mandatory, provided that pediatricians and the public were well informed, Fischer says. "There had been huge opposition to the idea," he says. "But 3 years later, protests are now barely a murmur and children are being inoculated as required."

The new vaccine panel is designed to be more than an ad hoc gathering. Its members match French society by age and education level and include a representative contingent of people with skeptical views of vaccines. Run by the Economic, Social and Environmental Council (CESE), an assembly of organizations from civil society, the panel can call for presentations by any experts it wants, and it will remain in business until the end of the vaccination campaign. It follows last year's 150-strong Citizens Climate Convention, which was also organized by CESE, and which generated dozens of recommendations, some of which will be included in a law expected to pass later this year. "We have certainly gained in notoriety," says CESE President Patrick Bernasconi.

To Cédric Villani, a mathematician and independent member of parliament, the panel is "just one too many." Already, says Villani, who is also president of the Parliamentary Office for Scientific and Technological Assessment, "There are about a dozen official bodies managing the COVID-19 pandemic in France, several of which have a citizen's component." But Larson says it is an important gesture. "Efforts to engage citizens should never be mocked."

Even without the efforts of the vaccine panel, French sentiment about vaccines appears to have shifted, at least for COVID-19. The latest figure for the proportion who intend to get vaccinated, 57%, is 17 points higher than it was in December 2020, according to an Ipsos poll.

But Pierre Verger, an epidemiologist, vaccine hesitancy specialist, and director of the Southeastern Health Regional Observatory in France, says skepticism still runs deep—even among the experts themselves. A recent unpublished survey of 1000 French doctors, conducted by Verger's observatory and the health ministry, suggests 25% are uncertain about or hostile to COVID-19 vaccines. "The media has gone overboard reporting that the French have changed their mind on vaccines," he says. "There has been an improvement, but not nearly as much as reports suggest." ■

Barbara Casassus is a journalist in France.

Mpilo Central Hospital in Bulawayo, Zimbabwe, one of 130 countries that don't have COVID-19 vaccines yet.

PHOTO: KB MPOFU/STRINGER/GETTY IMAGES

COVID-19

Deaths of health workers in Africa highlight vaccine inequity

Growing toll on fragile health systems prompts calls for rich countries to share their doses

By **Kai Kupferschmidt**

On 6 January, gastroenterologist Leolin Katsidzira received a troubling message from his colleague James Gita Hakim, a heart specialist and noted HIV/AIDS researcher. Hakim, chair of the department of medicine at the University of Zimbabwe, had fallen sick and had tested positive for COVID-19. He was admitted to a hospital in Harare 10 days later and moved to an intensive care unit (ICU) after his condition deteriorated. He died on 26 January.

It is a crushing loss to Zimbabwean medicine, Katsidzira says. "Don't forget: We have had a huge brain drain. So people like James are people who keep the system going," he adds. Scientists around the world mourned Hakim as well. He was "a unique research leader, a brilliant clinical scientist and mentor, humble, welcoming and empowering," wrote Melanie Abas, a collaborator at King's College London.

But Hakim's death also highlights a stark reality in the global response to the coronavirus pandemic. Countries in Europe, Asia, and the Americas have administered more than 175 million shots to protect people against COVID-19 since December 2020, with most countries giving priority to medical workers. But not a single country in sub-Saharan Africa has started immunizations—South Africa will be the first, this week—leaving health care workers dying in places where they are scarce to begin with.

The exact toll of COVID-19 among health workers is hard to gauge, but Hakim was one of several prominent doctors to succumb in recent weeks in Africa, which has suffered a second pandemic wave. Just 1 day before him, U.S. physician David Katzenstein, who had moved to Harare after his retirement and directed the Biomedical Research and Training Institute there, died from COVID-19 at the same hospital. Those losses stand for many others, says Robert Schooley, an infectious disease researcher at the University of California, San Diego, who worked with Hakim for many years. "We don't hear about a lot of the others who are laboring in the health care workforce behind them."

Neighboring Mozambique lost an anesthesiologist, a gastroenterologist, and a urologist in recent weeks, says parasitologist Emilia Noormahomed of Eduardo Mondlane University, as well as two young general care physicians. Several more are seriously ill. Such losses hit hard in Mozambique, which only has about eight doctors per 100,000 people, compared with almost 300 in the United States. "It will literally take an entire generation to rebuild" from

such losses, says Ashish Jha, dean of Brown University's School of Public Health.

Global inequities have existed since the start of the COVID-19 pandemic. ICUs, ventilators, and oxygen are scarce throughout the African continent, for instance. But in the early months, the basic public health measures required to control spread of the virus put countries more or less on an equal footing, says John Nkengasong, head of the Africa Centres for Disease Control and Prevention. And Africa has weathered the pandemic relatively well, in part because of its young population.

But now, the rollout of vaccines has put rich countries at a definitive advantage. Many have bet on several vaccines and signed contracts for enough doses to immunize their populations several times over, constraining supplies for the rest of the world. According to the World Health Organization (WHO), three-quarters of all vaccinations so far have happened in 10 countries that account for 60% of global gross domestic product; 130 countries have yet to administer a single dose. "I don't know why there isn't a massive clamor to do something about that," says Gavin Yamey of Duke University's Global Health Institute. "The world is on the brink of a catastrophic moral failure," Tedros Adhanom Ghebreyesus, the Ethiopian-born director-general of WHO, said in January. In a joint statement last week, he and UNICEF Executive Director Henrietta Fore called on governments that have vaccinated health workers and those at highest risk to share doses with other countries, and on vaccine manufacturers to allocate vaccines equitably.

> **"I don't know why there isn't a massive clamor to do something."**
> **Gavin Yamey**, Duke Global Health Institute

The equity gap could soon extend to COVID-19 therapeutics, as well. The first drug convincingly shown to cut the death rate from the virus, a steroid named dexamethasone, is cheap and used around the world; Hakim received it before he died. But tocilizumab, shown to further reduce mortality in a U.K. study released on 11 February, is an antibody that's about 100 times more expensive than dexamethasone and not widely available. "The [pandemic's] second wave, and potentially the third, is fought with a combination of public health measures and biomedical interventions, and that will increase the inequities," Nkengasong says.

Beyond the moral argument, there are sound economic and public health reasons to close the gap. Vaccinating those most at risk around the world would drive down hospitalizations and deaths everywhere sooner, allowing societies to reopen and economies to recover. It could also help reduce circulation of the virus globally, lowering the risk of new virus variants emerging.

WHO and other international organizations have worked to reduce the gap through the COVID-19 Vaccines Global Access (COVAX) Facility, a joint mechanism to procure billions of doses of several vaccines and distribute them to participating countries. It is beginning to pay off, albeit slowly: On Monday, WHO gave an emergency use listing to two versions of the AstraZeneca–University of Oxford vaccine, manufactured by the Serum Institute of India and SKBio, a South Korean company. COVAX expects to start supplying countries with these shots this month and to ship more than 300 million doses in the first half of the year, including 1.15 million to Zimbabwe and 2.43 million to Mozambique. It is also planning to distribute 1.2 million doses of the Pfizer-BioNTech vaccine.

Bruce Aylward, a senior adviser to Tedros, concedes the initial supply is only enough to cover a small part of many developing countries' populations. "But the reality is, we're going to get a lot more doses to a lot more people in a lot more places a lot faster than ever would have happened without the COVAX Facility," he says.

To secure more vaccine sooner, African countries have formed a vaccine acquisition task force that, with funding from mobile phone company MTN Group, has already bought 7 million doses of the AstraZeneca-Oxford vaccine. The first 1.5 million doses should be shipped to 19 countries on 22 February, allowing health care workers in those countries to be vaccinated by the end of that week. The overall aim is to vaccinate about 35% of the population in African countries before the end of the year and then another 25% next year, Nkengasong says. (Many Western countries hope to have their entire populations covered by this summer or fall.)

Schooley thinks the United States should take a more active role in protecting health care workers in countries such as Zimbabwe. The U.S. President's Emergency Plan for AIDS Relief, launched in 2003, has saved countless lives by providing more than $80 billion in the fight against HIV, he notes. "We have worked with our counterparts in sub-Saharan Africa for 20 years to try to help them build a more resilient health care infrastructure," Schooley says, "and we're sitting on our hands watching that be torn apart by the coronavirus." ■

ARCHAEOLOGY

England's Stonehenge was erected in Wales first

Stones were set upright before being moved east

By **Andrew Curry**

Around 3200 B.C.E., farmers in Wales's Preseli Hills built a great monument: They carved columns of dolerite, or bluestone, from a nearby quarry, then thrust them upright in a circle aligned with the Sun. Exactly what the circle meant to them remains a mystery. But new research reveals that several centuries later, their descendants took down many of the giant stones and hauled them 200 kilometers to the Salisbury Plain. There, they created what is still the world's most iconic prehistoric stone monument: Stonehenge.

The paper presents a "brilliant hypothesis" and "a very good argument Stonehenge is a dismantled stone circle from Wales," says Alison Sheridan, a curator emerita at the National Museum of Scotland.

Researchers had already traced Stonehenge's bluestones to Wales and even found where they were quarried. But activity at the quarries ended several centuries before the earliest construction at Stonehenge.

Then in 2017 and 2018, researchers led by University College London archaeologist Michael Parker Pearson excavated parts of an ancient monument in Wales called Waun Mawn, where a handful of toppled bluestones form a partial circle. The team found socket-shaped pits that, with the fallen bluestones, sketched out a circle 110 meters across—the same size as the outer earthen ditch of Stonehenge's original layout. As at Stonehenge, the circle's entrance was oriented to sunrise on the midsummer solstice.

Dating suggested the stones were erected between 3400 and 3200 B.C.E. and removed 300 or 400 years later, around when Stonehenge was first built, the team reported this week in *Antiquity*. "We're quite confident the reason they come down is they've gone to Stonehenge," Parker Pearson says. "They're bringing ancestral symbols as an act of unification." ■

EARTH SCIENCE

Kauri trees mark magnetic flip 42,000 years ago

Researchers say cosmic ray bombardment unleashed by weaker field drove climate shift

By **Paul Voosen**

Several years ago, workers breaking ground for a power plant in New Zealand unearthed a record of a lost time: a 60-ton trunk from a kauri tree, the largest tree species in New Zealand. The tree, which grew 42,000 years ago, was preserved in a bog and its rings spanned 1700 years, capturing a tumultuous time when the world was turned upside down—at least magnetically speaking.

Radiocarbon levels in this and several other pieces of wood chart a surge in radiation from space, as Earth's protective magnetic field weakened and its poles flipped, a team of scientists reports on p. 811. By modeling the effect of this radiation on the atmosphere, the team suggests Earth's climate briefly shifted, perhaps contributing to the disappearance of large mammals in Australia and Neanderthals in Europe. "We're only scratching the surface of what geomagnetic change has done," says Alan Cooper, an ancient DNA researcher at the South Australian Museum and one of the lead authors of the study.

Radiocarbon from a 42,000-year-old kauri tree in New Zealand helped unravel Earth's last magnetic upheaval.

The study not only nails in fine detail the timing and magnitude of the magnetic swap, the most recent in Earth's history, but is also among the first to make a credible, though speculative, case that these flips can affect the global climate, says Quentin Simon, a paleomagnetist at the European Center for Research and Teaching in Environmental Geoscience in Aix-en-Provence, France. But some paleoclimate scientists are skeptical of the team's broader claims, saying other records show few traces of climate upheaval.

Earth's magnetic field is created by the flow of molten iron in the outer core, which is prone to chaotic swings that not only weaken the field, but also cause the poles to wander and sometimes flip entirely. The magnetic orientations of minerals in rock record long-lasting reversals, but can't capture the details of a flip lasting hundreds of years, like the one 42,000 years ago.

Radioactive carbon-14, however, can mark these shorter fluctuations. The isotope is produced when cosmic rays—charged particles from outer space—slip past the magnetic field and strike the atmosphere. It is taken up by living things, and its specific half-life makes it a standard clock. The team used radiocarbon to date the kauri wood by lining it up with accurate, but coarse, radiocarbon cave records from China. And by measuring finer carbon-14 changes in the rings, they tracked how its production varied over 40-year intervals, as the magnetic field ebbed and surged. "It's just amazing you can do this back 42,000 years ago," says Lawrence Edwards, a geochemist at the University of Minnesota, Twin Cities, who worked on the Chinese cave records.

Spikes in radiocarbon indicated the magnetic field weakened to some 6% of its present day strength by 41,500 years ago. At that point the poles flipped and the field recovered some strength, before crashing and flipping back 500 years later. Cooper notes that not only was Earth's cosmic ray shield down; the Sun's was, too. Evidence from ice cores suggests that, around this same time, the Sun was experiencing several "grand minima"—episodes of low magnetic activity. The resulting cosmic ray assault charged the atmosphere to a level that would have knocked out today's power grid and created aurorae in the subtropics, Cooper says. "What happens when the atmosphere is that ionized?" he asks. "God only knows." (The paper is the first Cooper has led since he was fired in 2019 from the University of Adelaide following allegations that he bullied staff and students; Cooper has denied the allegations.)

To explore the consequences, the team ran a climate model, which suggested the cosmic ray bombardment would have eroded the ozone layer, reducing the heat it normally captures from ultraviolet rays. The high altitude cooling would have changed wind flows, which in turn may have led to "drastic changes" on the surface, including a warmer North America and cooler Europe, says Marina Friedel, a team member and doctoral student in stratospheric chemistry at ETH Zurich.

This is where other scientists say the study gets too speculative. Ice cores from Greenland and Antarctica that span the past 100,000 years capture stark temperature swings every few thousand years. But they show no shifts 42,000 years ago. A few Pacific Ocean records do show swings. But even if the shift occurred mostly in the tropics, as Cooper and colleagues suggest, it should be seen in the ice, says Anders Svensson, a glaciologist at the University of Copenhagen. "We just don't see that."

The study team goes further to argue that a climate shift could account for a spate of curious events 42,000 years ago. Most notably, large mammals in Australia went extinct around that time. Neanderthals vanished from Europe, and elaborate cave paintings began to appear in Europe and Asia. Still, neither milestone in human evolution lines up well with the flip 42,000 years ago, and neither was sudden, says Thomas Higham, an archaeologist and radiocarbon expert at the University of Oxford. Linking them to the field reversal, he says, "seems to me to be pushing the evidence too far." ■

PHOTO: JONATHAN PALMER

Do violent movies like *Sin City* lead to aggression? Retracted studies have muddied the debate.

PHOTO: AF ARCHIVE/ALAMY STOCK PHOTO

RESEARCH INTEGRITY

Media and aggression research retracted after scrutiny

Questioned psychology papers linger on in meta-analyses

By **Cathleen O'Grady**

As Samuel West combed through a paper that found a link between watching cartoon violence and aggression in children, he noticed something odd about the study participants. There were more than 3000—an unusually large number—and they were all 10 years old. "It was just too perfect," says West, a Ph.D. student in social psychology at Virginia Commonwealth University.

Yet West added the 2019 study, published in *Aggressive Behavior* and led by psychologist Qian Zhang of Southwest University of Chongqing, to his meta-analysis after a reviewer asked him to cast a wider net. West didn't feel his vague misgivings could justify excluding it from the study pool. But after *Aggressive Behavior* published West's meta-analysis last year, he was startled to find that the journal was investigating Zhang's paper while his own was under review.

It is just one of many papers of Zhang's that have recently been called into question, casting a shadow on research into the controversial question of whether violent entertainment fosters violent behavior. Zhang denies any wrongdoing, but two papers have been retracted. Others live on in journals and meta-analyses—a "major problem" for a field with conflicting results and entrenched camps, says Amy Orben, a cognitive scientist at the University of Cambridge who studies media and behavior. And not just for the ivory tower, she says: The research shapes media warning labels and decisions by parents and health professionals.

The investigations were triggered by Illinois State University psychologist Joe Hilgard, who published a blog post last month cataloging his concerns about Zhang's work. Hilgard was initially impressed when he came across a 2018 paper of Zhang's in *Youth & Society*, another study with 3000 subjects. "I was like, holy smokes!" he says. The study found some teenagers were more aggressive after playing violent video games. Given the huge sample size, it had the potential to be a "powerful chunk of evidence," Hilgard says.

But he found the paper's statistics mathematically impossible. Zhang and his coauthors reported high levels of statistical significance for their finding, but the reported differences in the effects of violent games versus nonviolent games were too small for that high statistical significance to be possible. Hilgard alerted Zhang and the journal, and Zhang submitted a correction. Hilgard says that made the statistics seem more plausible, but they were still incorrect.

Hilgard says he found problems in other papers of Zhang's, such as nearly identical results reported in three different papers. He emailed Zhang and asked to see his data, but he says Zhang refused. Hilgard then contacted Dorothy Espelage, a psychologist at the University of North Carolina, Chapel Hill, and co-author with Zhang on multiple papers. She told Hilgard that Zhang had refused to send her the data, too. It was only after Hilgard asked Southwest University to investigate that Zhang sent Hilgard data for a *Youth & Society* paper on movie violence.

But the data were odd, Hilgard says, and missing features normally found in similar experiments. He sent his findings to Zhang's university, which said it found problems, but not fraud, with Zhang's data, and that Zhang was "deficient in statistical knowledge and research methods." Dissatisfied with the response, Hilgard sent his observations to all the journals involved.

Marc Zimmerman, a psychologist at the University of Michigan, Ann Arbor, and the editor of *Youth & Society*, says Hilgard's email came a week after another source questioned Zhang's data. Two months later, in December 2019, the journal retracted Zhang's two papers. Without both whistleblower reports, Zimmerman says he might not have acted so promptly or decisively. "No journal editor wants to publish wrong data," he says, "but it's a serious accusation."

In an email to *Science*, Zhang denies any misconduct, and says "there is never just one 'right' way to look at the data." He says Hilgard, who is skeptical of the link between violent games and aggression, is "trying to make his name based just on claiming that everyone else does bad research." But Jay Hull, a psychologist at Dartmouth College whose work shows a link between violent video games and aggression, agrees with Hilgard's concerns about Zhang's work. More generally, Hull is worried about a "science that's built on shifting sands."

Other journals, including *Aggressive Behavior*, have not retracted any of Zhang's research, even though Espelage supported a retraction of the *Aggressive Behavior* paper on which she was a co-author. Craig Anderson, a psychologist at Iowa State University and editor-in-chief at *Aggressive Behavior*, declined to comment on the record. The paper's results will live on within West's meta-analysis, leaving him unsure how to correct his own work. It's "profoundly frustrating," West says.

Zhang's recent papers avoid the red flags Hilgard has complained about. But Hilgard isn't satisfied. The delays and lack of action, he says, make him "really anxious about how hard it's going to be to detect data that is flawed in more subtle ways." ■

FEATURES

THE LONG ROAD

Early signs suggest COVID-19 vaccines are having an impact, but questions abound about the path to normal

By **Jon Cohen**, *in San Diego*

Twenty days into the new year, cars were entering a parking lot bumper-to-bumper in the shadow of Petco Park, home of the San Diego Padres baseball team. Arms waving, attendants directed the cars into three lines, which split into four more, and yelled as though the first pitch had already been thrown. "I'm going to load you up, I'm sending you 10, you can stack them!" one attendant hollered to another.

But the Padres don't play in January.

Instead, Petco Park was home field for this city's drive-thru COVID-19 vaccinations. For 9 days straight, health workers there had been injecting about 5000 people between 7 a.m. and 7 p.m. Run by infectious disease clinician Shira Abeles of UC San Diego Health—dubbed the "vaccine czar" by the 300 people she manages at the Petco operation—it is the city's largest vaccination site, focusing on health care workers and anyone 75 or older. Cars moved through stations where workers checked people in, injected them, and then watched them for at least 15 minutes to make sure they didn't have immediate side effects.

The traffic flow was slow but steady—and no one honked. Above their masks, the visitors' eyes were smiling. If vaccine hesitancy

PHOTO: BING GUAN/BLOOMBERG VIA GETTY IMAGES

The parking lot at Dodger Stadium in Los Angeles serves as a drive-thru COVID-19 vaccine site open into the night.

PHOTO: AMIR LEVY/GETTY IMAGES

has an opposite, this was it.

By the end of January, nearly 100 million people around the world had received COVID-19 vaccines, and more than 1 million were getting shots each day in the United States and China. The effort was lagging in Europe, and staggering global inequities remain. The World Health Organization noted on 5 February that 75% of vaccinations have occurred in 10 countries. About 130 countries had yet to inject anyone with a COVID-19 vaccine. Still, the vaccines, shown in clinical trials to have efficacies of up to 95% against symptomatic disease, have finally given the world the prospect of an escape from COVID-19's long siege. "There is so much hope," Abeles says.

Now, as vaccination campaigns gain speed, a raft of pressing questions have arisen: Does being immunized mean you won't spread the virus? When will the campaigns begin to curb the pandemic and allow daily life to return to normal? And what do the new variants of SARS-CoV-2, able to spread faster or evade immune responses, mean for the promise of vaccines? "The reality here is this virus is evolving," says Lawrence Corey, a virologist at the University of Washington, Seattle, who co-leads the U.S. government–supported network that tests COVID-19 vaccines.

Still, answers are emerging.

How soon will there be an impact?

One month into the U.S. vaccination campaign, Abeles thinks she has seen its effect already. Beginning in mid-December 2020 some 11,000 UC San Diego Health employees began to receive the Pfizer-BioNTech or the Moderna vaccine, both of which contain messenger RNA (mRNA) that directs the body's cells to make the surface protein from SARS-CoV-2, spike, to trigger an immune response. Despite reports of health care workers hesitant to get the vaccines, 96% of Abeles's colleagues accepted the shots. Each week, those employees are tested for SARS-CoV-2, which exploded in San Diego county starting in December, even if they are feeling healthy.

At the peak, UC San Diego Health was detecting 20 to 30 infections each day in employees, many asymptomatic. By the third week in January, the number had fallen to just a handful. Abeles emphasizes that the evidence is far from conclusive, but says "we are extremely hopeful" that the link between the drop and the mass vaccination is real.

More compelling, if still preliminary, evidence comes from Israel, home to the world's most aggressive and best studied immunization campaign so far. A country of 9 million people, Israel has universal health care provided mainly through four HMOs with excellent electronic medical records. The Israeli government negotiated with Pfizer to rapidly roll out its mRNA shots in exchange for sharing data about their impact with the company. Between 19 December and 4 February, 39% of Israelis had received at least one dose of the vaccine. Per capita, that is far higher coverage than in any country other than the similarly small United Arab Emirates (36%).

Nationally, COVID-19 cases and hospitalizations appear to be dropping faster among people 60 or older, the first to receive the vaccines, than among the 40- to 60-year-old segment. And in a 1 February press release, the Maccabi Research and Innovation Center—an arm of one of the four HMOs—noted it had tracked 132,015 of its members over age 60 who had received a vaccine dose in the first 9 days of the immunization campaign. Diagnosed SARS-CoV-2 infections in that group peaked about 10 days after immunizations began. By day 28, when most people had received their second, booster dose, diagnoses had fallen by two-thirds, and COVID-19–related hospitalization had dropped from a daily high of seven people to one. In the general population, the team notes, reported cases dropped much more slowly.

That finding constitutes "persuasive evidence of real-world benefit of vaccination, especially since prior behavioral restrictions

Israel has vaccinated more of its population than any country—and has already seen encouraging drops in COVID-19 cases, hospitalizations, and deaths.

in Israel did not seem to selectively protect those over 60," says Roby Bhattacharyya, an infectious disease specialist at Massachusetts General Hospital.

In the United States, people living in long-term care facilities, most of them elderly, and facilities' staff were put at the front of the line for vaccines. Those residents account for about 40% of the country's COVID-19 deaths, so the impact of vaccinations on their hospitalization and mortality will probably be seen "within a month or two, certainly," says Ira Longini, a biostatistician at the University of Florida (UF).

The effect may have already become visible. COVID-19 cases have been dropping nationwide since December, including at nursing homes. Interventions other than vaccines explain some of the fall. But a county-level comparison of facilities that got their first shots from 18 to 27 December and those that didn't showed the drop in daily cases was more than twice as large in the earlier vaccinated facilities (a 48% decline versus 21%).

Blunting COVID-19 cases nationwide is a long game, however, especially in a country such as the United States, where the vaccine rollout has not been as fast or uniform as in Israel. "We have a big country. We have a lot of transmission," Longini says. "I don't think we'll see a big impact on numbers of cases" from vaccines until the summer.

Will vaccination stop you from spreading the virus?

If vaccines created what's known as sterilizing immunity all the time, no vaccinated person would transmit the virus. Vaccinated grandparents could safely play with their unimmunized grandchildren. Countries could welcome visitors who had proof of vaccination with little fear of introducing new viral variants or reigniting outbreaks.

That level of assurance is a tall order. Few vaccines, for any infectious diseases, create sterilizing immunity—even the most effective ones. The inactivated poliovirus vaccine developed by Jonas Salk did little to block infection or transmission of the virus, yet it powerfully prevented paralytic polio. By 1961, 6 years after it was licensed, only 54% of the U.S. population had received the vaccine, yet paralytic polio cases had dropped by more than 90%.

For practical reasons, the recent COVID-19 vaccine efficacy trials evaluated mainly the frequency of symptomatic disease, typically detected after participants feel sick and get a virus test. It's tougher to identify all SARS-CoV-2 infections, which remain invisible if they don't cause symptoms. Yet models suggest asymptomatic cases account for about half of transmission, so tracking them among vaccine recipients is key. "There are easy ways to look at transmission and hard ways," says Ruth Karron, who runs the Johns Hopkins University Center for Immunization Research.

One approach, says John Mascola, who heads the Vaccine Research Center at the National Institute of Allergy and Infectious Diseases (NIAID), is to ask: "If you're vaccinated, could you have the virus in your nose and shed it?" That's how researchers studying the AstraZeneca–University of Oxford vaccine recently tried to get at transmission. In a U.K. efficacy trial of that vaccine, participants did weekly nasal swabs at home. Results showed vaccination reduced asymptomatic infections by 49.3%. The data suggest, but do not prove, that the vaccine stymies viral spread; misleading news coverage claimed the vaccine had cut transmission by two-thirds. Moderna has also reported a similar decline in asymptomatic infections after just one dose of its mRNA vaccine in a subset of its large efficacy trial, which found overall that the vaccine had 94% efficacy against mild disease.

Several COVID-19 vaccine studies have opted for a simpler, if less precise, look at the issue. They took repeated blood samples from people in both the placebo and vaccinated groups at different time points. The trials tested for antibodies against the viral N protein, which are triggered by infection but not by most vaccines. If the placebo group has more positive N antibody tests than the vaccinated group, that would suggest the vaccine had cut asymptomatic infections—and therefore transmission. No group has yet reported results from those "serosurveys."

Early data from Israel indicate vaccinated people who nevertheless became infected with SARS-CoV-2 have reduced levels of virus, which may make them less contagious. A research team from the Maccabi group and the Israel Institute of Technology measured viral loads in nasal samples taken from more than 1000 people who became infected between 12 to 28 days after their first dose, the period in which immunity begins to build. The amount of virus found was significantly less than in a similar group of unvaccinated, infected Israelis, the group reported on 8 February in a preprint on bioRxiv.

Myron Cohen, an infectious disease clinician at the University of North Carolina, Chapel Hill, and colleagues at the COVID-19 Prevention Network have a proposal at NIAID to study the question in college students. One group would receive the vaccine immediately and a control population would get it weeks later. Both groups of students would swab their noses daily to assess whether there are differences in the rate of asymptomatic SARS-CoV-2 infections and levels of the virus. Withholding vaccine would be ethically dodgy if doses were plentiful, but most college students are still not eligible for vaccination, and they are less likely to develop serious COVID-19 than older adults. Cohen is confident the trial will receive the necessary ethical approvals.

Knowing whether vaccines stop transmission may not matter to government officials. "In the next 6 months, we're probably going to have a menu of vaccines and each is going to have characteristics related to the cold chain, number of doses required, reactogenicity, and efficacy," Karron notes. "We're going to make policy decisions about use based on all of those characteristics. I don't think that some superimprecise measure of transmission is going to be one of the things that goes into our calculus."

But Cohen contends that the difficult studies to evaluate whether immunized people spread the virus are worth doing. "Unless we answer this question, we are a masked society. We need to address this to become maskless."

When will we get back to normal?

That depends on the definition of normal. To many people now, it means herd immunity, in which a high percentage of a population has either been vaccinated or naturally infected, leaving too few susceptible hosts for a virus to continue to spread. "It's such a clean, beautiful concept, the tipping point idea, that if we can just get there, the virus will go away, and then we can just go about our business as if it's gone," Longini says. "It's kind of a pie-in-the-sky concept that's very, very attractive."

The idea of herd immunity, a term imported from livestock veterinarians, has become more beguiling as huge swaths of populations in parts of the world recover from SARS-CoV-2 infections, leaving them with some degree of immunity. In India, for example, serosurveys have found antibodies to the virus in about half of people in the city of Delhi and the entire state of Karnataka. And though no one is claiming this meets the herd immu-

A nursing home resident in Greece thanks a social worker after receiving a COVID-19 vaccine.

PHOTO: REUTERS/ALKIS KONSTANTINIDIS

nity threshold, new cases have recently dropped precipitously.

Still unclear is what percentage of a population needs to be vaccinated or recovered from COVID-19 before herd immunity kicks in. Early predictions were between 60% and 70% and then rose as high as 90%—but that's all based on modeling or even guesswork. Anthony Fauci, who heads NIAID, has been taken to task for changing his own estimates. Recently on CNN, Fauci acknowledged that: "I think we all have to be honest and humble. Nobody really knows for sure."

Recent developments have been sobering. The COVID-19 vaccines rolling out are highly effective against hospitalization and death, but their success against mild and moderate symptoms plummets when faced with viral variants that can evade vaccine-triggered antibodies. And herd immunity, even if it emerged, could easily fade as immunity waned or new variants arose.

Yet there is growing recognition that even if widespread vaccination can't halt the spread of the virus, it promises a major step back toward normal. Preventing severe disease and death in the elderly and people with comorbidities such as obesity and hypertension—the most vulnerable—is still a resounding victory over the virus, many epidemiologists say.

Large swaths of the population might still become infected and develop minor disease or asymptomatic infections. That prospect worries some scientists and clinicians, who note that even mild cases can lead to the "long COVID" phenomenon of lingering symptoms. Hospitals, though, will not become overwhelmed with emergency cases and deaths will become increasingly rare.

To Corey, those metrics are the most relevant. "When will the ICU use and all of this decant so that we're at the point where, yes, we can sort of tolerate this?" he asks.

"We're not going to shut down this virus and end transmission," agrees Nicole Lurie, an adviser to the Coalition for Epidemic Preparedness Innovations. "We have to make a decision as a society about how much of this we can and want to live with." Society lives with influenza, after all, which remains endemic despite a vaccine. But Lurie stresses that flu is not an appealing model. It kills to 60,000 people per year in the United States alone—a toll she would not want to accept from COVID-19.

Still, immunologist Brigitte Autran, a member of France's Scientific Committee on COVID-19 Vaccines, says herd immunity isn't needed to bring back normalcy. "The first goal is to have individual protection, and by summing the individual protections, to have a protection of the society that will allow countries to come back to almost real, true lives."

How much of a threat do viral mutants pose to immunity?

That concern quickly moved from the theoretical to the real world when multicountry studies recently revealed several vaccines were least effective against symptomatic COVID-19 in South Africa. That's where 95% of infections now stem from a viral variant that in test tube studies could dodge antibodies against the viral spike protein. Novavax's protein-based vaccine went from 89.3% protection in the United Kingdom, where the variant is rare, to 49.4% in South Africa. And South Africa even halted its planned rollout of the AstraZeneca-Oxford vaccine, which consists of a harmless viral "vector" carrying the gene for the spike protein, after a small trial there indicated the vaccine had 22% efficacy.

Still, the vaccine-triggered immune responses may retain plenty of muscle, enough to prevent serious symptoms. A third vaccine, from Johnson & Johnson, also fell short against mild disease in South Africa, but it prevented almost all severe disease—with no hospitalizations or deaths. (The AstraZeneca-Oxford and Novavax studies were too small to address impact on severe disease.)

One explanation could be that the level of key spike antibodies, those capable of "neutralizing" SARS-CoV-2's infectivity, jumped so high after vaccination that there was a cushion: Even though several labs reported that the variant in South Africa reduced the impact of the vaccine-induced antibodies by up to ninefold, if those immune fighters rise to high enough levels they may still pack enough punch to thwart serious disease.

Other arms of the immune system less affected by the mutations in the variant likely contribute to protection. Pfizer and BioNTech have shown their mRNA vaccine triggers a steep increase in key T cells. One set, which carries the CD8 receptor, targets and destroys cells that SARS-CoV-2 manages to infect. Underscoring the importance of those cells, Pfizer and BioNTech found that even though neutralizing antibody levels triggered by their vaccine were minimal in the 21 days between the first and second doses, it still gave 52.4% protection against disease during that period. "Vaccine-induced T cell responses are important for COVID-19 vaccines, particularly for resistant variants that might partially evade neutralizing antibodies," suggests Dan Barouch of Harvard Medical School, whose lab has documented the importance of CD8+ cells for protecting monkeys from coronavirus reinfection.

Mixing and matching COVID-19 vaccines may also boost both antibody and T cell responses to higher levels, creating bigger cushions. Studies of various combinations have begun.

Will the variants change the course of the pandemic?

That's the realm of modelers like Longini. Often, they restrict their analyses to tight geographical areas, which makes it easier to amass high-quality data and to account for variables that can alter outcomes. So Longini and Thomas Hladish, also at UF, created a model for their home state that extrapolates from actual case numbers for COVID-19 and assumes a rapid rollout, starting with people older than 65, of vaccines that are 60% effective at preventing infection. Assuming the virus doesn't change, they found that a vaccination campaign reaching half the population would slash symptomatic disease and death by 30% by August.

Surprisingly, their Florida model shows COVID-19 cases would steadily decline even without vaccination. That's because the state's reproductive number for SARS-CoV-2—how many other people each COVID-19 case infects—has dropped below 1. "It's mostly masking, social distancing, and the slow buildup of natural immunity in the population," Longini says. Indeed, as in many U.S. states, Florida's cases began to drop steeply in January.

But that decline could quickly reverse if a mutant strain takes off that's 50% more infectious, such as the B.1.1.7 variant strain that exploded first in the United Kingdom and has come to the United States, including Florida. "We will have a much bigger epidemic that starts happening now," Longini says. But with more viral spread, the impact of vaccination would be bigger, averting twice as many symptomatic cases and deaths.

Modeler Natasha Martin and her team at the University of California, San Diego, have looked at the interplay of variants and vaccines in an even smaller area: their home county. Sequencing of COVID-19 cases in San Diego county has shown the highly transmissible B.1.1.7 variant has a 5% prevalence so far—10 times higher than recently estimated for the nation. Martin's model shows that if the variant takes over, as many researchers expect, aggressive vaccination campaigns over the next 3 months will still cut case numbers in half. But if the county drops its guard and people become lax about prevention efforts, COVID-19 cases will triple even with rapid vaccination. "We are at a critical moment in the epidemic, where our progress in terms of declining cases could quickly be reversed as the B.1.1.7 strain expands," Martin says. "We have the tools we need to fight the spread of this virus: masking, social distancing, vaccination. Now is the time to vaccinate as many people as fast as we can, and double down on masking and distancing."

How quickly can we tailor vaccines to the new variants?

Vaccine developers proved in 2020 that they can move from concept to candidate vaccine, ready to test in people, in as little as 2 months. Changing the genetic code used in an mRNA or vector-based vaccine, or making a new inactivated-virus preparation, should be at least as fast. (A genetically engineered protein, such as the Novavax vaccine, takes longer.)

But by far the biggest time sink and expense for getting COVID-19 vaccines into use were the large-scale efficacy trials, which took about 4 months. Would those need to be repeated for each updated vaccine? No, says Peter Marks, who heads the vaccine division at the U.S. Food and Drug Administration. All the agency would likely require, he says, is a "modest size" study in humans showing the immune responses elicited by the new vaccine resemble those triggered by the original and are likely to be protective.

Flu vaccines, after all, are updated yearly to keep up with the ever-morphing influenza virus and are quickly approved. Makers can pop out components from the old vaccine and replace them with new ones. Regulators require minimal evidence about the revised product—often just animal studies showing it performs as well as last year's model.

But with COVID-19 vaccines, no one knows which immune responses correlate with protection. Many vaccine experts assume neutralizing antibodies to the spike protein are the most important driver of protection. To prove that, however, researchers need to compare immune responses between vaccinated people infected by viruses that "broke through" their protection and vaccinated people who did not become infected. A more in-depth "sieve" analysis of breakthrough cases refines the correlates of protection by looking at the genetics of the variants that break through. Those studies are underway, but the Moderna and Pfizer-BioNTech vaccines, the first approved, worked so well that it was difficult to figure out the protective immune responses. "There weren't that many vaccinated, infected people," explains Mascola, who is helping coordinate the analyses.

Still, Marks says he anticipates that by the time makers of vaccines formulate new preparations to combat variants and test them in small human studies, the key immune responses will have become clear. "We may well have the correlate confirmed by March when it is really needed," he says. That could open the way for rapid approval and rollout of boosters designed to keep up with the evolving virus—and ensure that any hard-won progress against the pandemic isn't undone. ■

Vaccines versus variant

Models suggest the impact of COVID-19 vaccinations in San Diego will be blunted by the fast-spreading B.1.1.7 variant, which already accounts for 5% of SARS-CoV-2 infections there. If other prevention efforts are relaxed, a surge of cases will swamp the gains from vaccination.

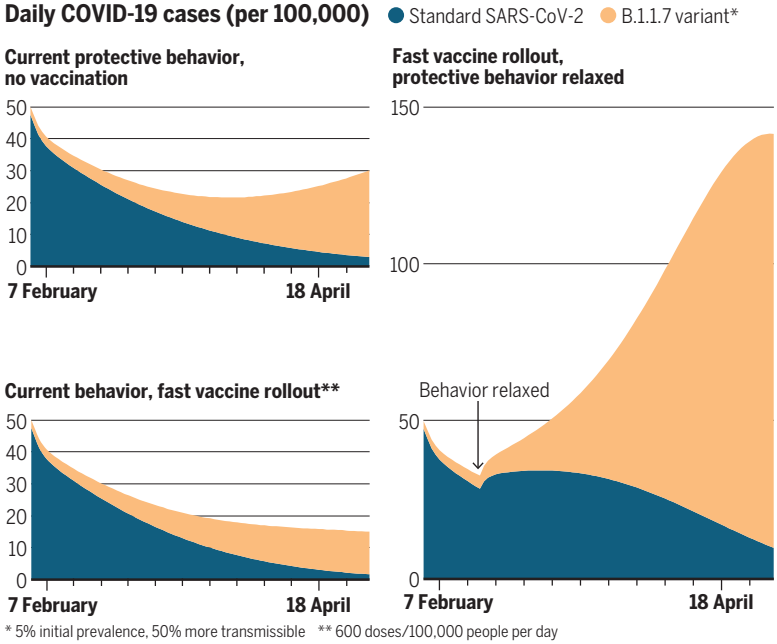

* 5% initial prevalence, 50% more transmissible ** 600 doses/100,000 people per day

CREDITS: (GRAPHIC) N. DESAI/*SCIENCE*; (DATA) KRISTIAN ANDERSEN/SCRIPPS RESEARCH INSTITUTE; NATASHA MARTIN/UC SAN DIEGO

eppendorf & Science

PRIZE FOR NEURO BIOLOGY

2020 Winner
Christopher Zimmerman, Ph.D.
Princeton Neuroscience Institute
For research on thirst and drinking behavior

Application Deadline
June 15, 2021

Now It's Your Turn!

Eppendorf & Science Prize for Neurobiology
The annual Eppendorf & Science Prize for Neurobiology is an international prize which honors young scientists for their outstanding contributions to neurobiological research based on methods of molecular and cell biology. The winner and finalists are selected by a committee of independent scientists, chaired by *Science*'s Senior Editor, Dr. Peter Stern. If you are 35 years of age or younger and doing great research, now is the time to apply for this prize.

As the Grand Prize Winner, you could be next to receive
> Prize money of US$25,000
> Publication of your work in *Science*
> Full support to attend the Prize Ceremony held in conjunction with the Annual Meeting of the Society for Neuroscience in the USA
> 10-year AAAS membership and online subscription to *Science*
> Complimentary products worth US$1,000 from Eppendorf
> An invitation to visit Eppendorf in Hamburg, Germany

It's easy to apply! Write a 1,000-word essay and tell the world about your work. Learn more at:

eppendorf.com/prize

eppendorf Science AAAS

AAAS® and Science® are registered trademarks of the American Association for the Advancement of Science, USA. Eppendorf® and the Eppendorf Brand Design are registered trademarks of Eppendorf AG, Germany. All rights reserved, including graphics and images. Copyright © 2021 by Eppendorf AG. Photography: Sameer A. Khan.

POLICY FORUM

ENVIRONMENTAL SCIENCE

We need a global science-policy body on chemicals and waste

Major gaps in current efforts limit policy responses

By **Zhanyun Wang[1], Rolf Altenburger[2,3], Thomas Backhaus[4], Adrian Covaci[5], Miriam L. Diamond[6,7], Joan O. Grimalt[8], Rainer Lohmann[9], Andreas Schäffer[3], Martin Scheringer[10,11], Henrik Selin[12], Anna Soehl[13], Noriyuki Suzuki[14]**

Many countries and regional political unions have regulatory and policy frameworks for managing chemicals and waste associated with human activities to minimize harms to human health and the environment. These frameworks are complemented and expanded by joint international action, particularly related to pollutants that undergo long-range transport via air, water, and biota; move across national borders through international trade of resources, products, and waste; or are present in many countries (*1*). Some progress has been made, but the Global Chemicals Outlook (GCO-II) from the United Nations Environment Programme (UNEP) (*1*) has called for "strengthen[ing] the science-policy interface and the use of science in monitoring progress, priority-setting, and policy-making throughout the life cycle of chemicals and waste." With the UN Environment Assembly (UNEA) soon meeting to discuss how to strengthen the science-policy interface on chemicals and waste (*2*), we analyze the landscape and outline recommendations for establishing an overarching body on chemicals and waste.

The world has seen a tremendous increase in the amount and variety of chemicals in use, with continuous growth expected; global chemical sales reached over US$5.6 trillion in 2017 and are projected to almost double by 2030 (*1*). Similar trends are also true for waste generation; for example, global plastic waste entering the ocean is estimated to increase from 4.8 to 12.7 million tonnes in 2010 to some 100 to 250 million tonnes by 2025 (*1*).

When chemicals and waste are poorly managed, not only are valuable resources lost, but chemical pollution can cause a wide range of adverse effects on human and ecosystem health at local, regional, and global levels. The latest Global Burden of Disease study estimated that exposure to lead and occupational exposure to 12 chemicals or groups of chemicals (a tiny fraction of the more than 100,000 chemicals in use) contributed to over 1.3 million premature human deaths in 2017 (*3*). Chemical pollution has also caused stratospheric ozone depletion, and it plays an important role in climate change (e.g., synthetic halogenated gases contributed over 10% of the global radiative forcing in 2011) (*4*) and ecosystem

PHOTO: BRIAN VAN DER BRUG/LOS ANGELES TIMES/GETTY IMAGES

Scientists conduct natural resource damage assessments in the aftermath of the oil spill in 2015 in Santa Barbara, California, informing policy-makers about planning and implementing restoration actions.

degradation (e.g., through the application of hazardous pesticides) (*1*).

For a large fraction of chemicals in use, substantial knowledge gaps hamper their sound management. Meanwhile, for those chemicals that are known as problematic or where there is emerging evidence of concern, control measures have often been limited (*1*). For example, although scientists have long raised concerns for widely used chemicals such as bisphenol A and some phthalates that they may act as endocrine-disrupting chemicals (and while informed action was taken in some countries and regions), they were identified by GCO-II in 2019 as issues with continued presence in many parts of the world, for potential joint action by the international community (*1*). Major gaps in the science-policy interface on chemicals and waste and how it keeps the international community up-to-date on scientific findings contribute to such delayed responses. This is particularly critical for developing countries, where national regulatory and policy frameworks are generally limited owing to a lack of capacity and accessibility of scientific information.

EXISTING SCIENCE-POLICY INTERACTIONS

The international community has a long history of taking concerted action on chemicals and waste. Much action happens through multilateral environmental agreements (MEAs) such as the Vienna Convention for the Protection of the Ozone Layer and its associated Montreal Protocol, the Basel Convention on the Control of Transboundary Movements of Hazardous Wastes and Their Disposal, and the Stockholm Convention on Persistent Organic Pollutants (POPs) (*5*). Other efforts are taken through individual or joint work programs by intergovernmental organizations such as UNEP, the World Health Organization (WHO), and the Food and Agriculture Organization (FAO) (*5*).

International chemicals and waste governance has greatly benefited from strong interactions between, and coproduction of, science and policy: Science informs policy developments, and policy incentivizes policy-relevant scientific research. An early example comes from the revelation by Svante Odén in the 1960s of links between sulfur dioxide emissions and acid rain in Europe. Odén's finding triggered a chain of science-policy interactions leading to the adoption of the Convention on Long-Range Transboundary Air Pollution (CLRTAP) (*6*). Science-policy coproduction has also been critical to the establishment of several other MEAs, including the Vienna Convention, the Montreal Protocol, and the Stockholm Convention, as well as the creation of the Arctic Monitoring and Assessment Programme (*5*).

To date, subsidiary science-policy interface bodies have been established under various MEAs and intergovernmental organizations to inform and support their work in specific areas related to chemicals and waste. For example, the POPs Review Committee was established under the Stockholm Convention for synthesizing scientific evidence of nominated chemicals and providing listing recommendations to the governing body of the convention [for more details on international chemicals and waste governance, the roles of science-policy interface bodies therein, and major current interface bodies, see the supplementary materials (SM)] (*5*, *7*). Although these bodies perform important roles in their respective areas, at least four critical gaps persist in the overall science-policy interface in international chemicals and waste governance (see fig. S1A and elaboration below; for more examples, see SM) (*7*, *8*). These gaps are highly problematic, particularly as scientific evidence regarding the environmental and human health concerns of chemicals and waste continues to grow.

FOUR MAJOR GAPS

First, there is a lack of coverage: The overall scope of existing interface bodies is limited and fragmented compared to the large and growing universe of chemicals and waste (*7*, *8*). Only a limited part of chemicals and waste is addressed by interface bodies under the global MEAs (e.g., POPs, mercury, ozone-depleting substances and replacements, and hazardous wastes). Interface bodies under global intergovernmental organizations may have wider scopes but are often constrained by the thematic domain of the host organization (e.g., environmental aspects under UNEP and human health aspects under WHO). Additional issues are addressed by regional and interregional interface bodies—e.g., atmospheric emissions of cadmium and lead under CLRTAP—yet these efforts remain inadequate in scope. Collectively, the lack of science-policy coverage of many issues related to chemicals and waste limits the international community's ability to identify and address issues of concern in a timely and informed way (*7*, *8*). In some cases, the lack of comprehensive scientific assessments has also provided space for intentional misrepresentation of scientific information due to conflicts of interest (*9*, *10*).

Second, there is a lack of horizon scanning and early warning mechanisms: Most existing interface bodies are not tasked, on a regular basis, with monitoring scientific developments and providing early warnings on risks related to chemicals and waste in their specific areas. Instead, many require external triggers to initiate work on specific issues. For example, the POPs Review Committee under the Stockholm Convention starts its assessments only after a party to the convention nominates a given chemical for potential control. Also, mechanisms for feeding informal early warnings by stakeholders into international governance processes are generally lacking. Consequently, the international community's ability to identify new issues for concerted action, even under existing MEAs, has been restricted. This is in sharp contrast to the rapid increase and diversification of chemicals and products in use and wastes, as well as the rapid generation of scientific findings, that demand constant vigilance and proactive assessment.

Third, there is a lack of bidirectional communication: Most interface bodies focus on informing policy-makers about scientific evidence on specific issues but take limited action to communicate policy developments and policy-relevant scientific questions back to the scientific community (*7*). Currently, policy needs for specific scientific evidence are often scattered over numerous documents under different MEAs and intergovernmental organizations, which are typically not read by, or accessible to, the scientific community, including funding agencies. This lack of policy-to-science communication restricts the scientific community from responding to policy needs with timely research.

Fourth, the wider scientific community is not sufficiently involved: Participation of scientists and practitioners (e.g., lawyers and physicians), particularly academics, in

[1]Institute of Environmental Engineering, ETH Zürich, 8093 Zurich, Switzerland. [2]Helmholtz Centre for Environmental Research UFZ, Permoserstrasse 15, Leipzig, Germany. [3]Institute for Environmental Research, RWTH Aachen University, Worringerweg 1, Aachen, Germany. [4]Department of Biological and Environmental Sciences, University of Gothenburg, Carl Skottsbergs Gata 22B, 40530, Gothenburg, Sweden. [5]Toxicological Centre, University of Antwerp, Universiteitsplein 1, 2610 Wilrijk, Belgium. [6]Department of Earth Sciences, University of Toronto, Toronto, Ontario, Canada. [7]School of the Environment, University of Toronto, Toronto, Ontario, Canada . [8]Department of Environmental Chemistry, IDAEA-CSIC, Barcelona, 08034, Spain. [9]Graduate School of Oceanography, University of Rhode Island, Narragansett, RI, USA.[10]Institute of Biogeochemistry and Pollutant Dynamics, ETH Zürich, 8092 Zürich, Switzerland. [11]RECETOX, Masaryk University, 625 00 Brno, Czech Republic. [12]Frederick S. Pardee School of Global Studies, Boston University, Boston, MA, USA.[13]International Panel on Chemical Pollution, 8092 Zürich, Switzerland. [14]Center for Health and Environmental Risk Research, National Institute for Environmental Studies, 16-2 Onogawa, Tsukuba, Ibaraki, Japan. Email: zhanyun.wang@ifu.baug.ethz.ch

science-policy interactions on chemicals and waste remains limited and often occurs in silos. This is partly due to the limited scopes of existing interface bodies in terms of the chemicals they cover and the mandates they have, and a lack of opportunities for scientists and practitioners to participate in their work. This inadequate engagement and participation reduces the visibility and importance of science-policy work and international chemicals and waste governance in general. Thus, for academics, work at the science-policy interface on chemicals and waste is most often neither recognized nor rewarded, in comparison to using their time to write another academic article (*11*). This further reduces participation.

Existing interface bodies may be improved in relation to gaps 2 to 4. However, such an approach is not efficient, as a number of international negotiations would need to take place under different MEAs and intergovernmental organizations to enact these changes; nor is it effective, as existing interface bodies would still be bounded by their specific scopes and mandates.

A WAY FORWARD

Against the backdrop of these four gaps, we support the establishment of an overarching international body to facilitate and foster broad bidirectional science-policy interactions on chemicals and waste (fig. S1B). It needs to have an inclusive scope that can cover all chemicals and waste while avoiding duplicating efforts of existing interface bodies (gap 1). For policy-makers, it would produce robust and authoritative scientific assessments, synthesizing the scientific basis and analyzing options for action. The assessments can be initiated through preagreed work programs, e.g., regular horizon scanning and early warning of new and emerging issues (gap 2), and per request by MEAs and governing bodies of intergovernmental organizations. It would also inform the scientific community in a timely fashion about international policy developments and highlight policy-relevant scientific questions, e.g., by presenting at major scientific conferences and informing research funding organizations (gap 3). This could, in turn, help to increase participation by the scientific community in its work (gap 4).

Although the exact institutional design of this body must emerge from an international negotiation process, four core characteristics warrant consideration to ensure its scientific credibility, political legitimacy, and policy salience—critical factors for its effectiveness (*7*, *12*). First, setting it up as an intergovernmental body—e.g., under the joint auspices of intergovernmental organizations, including UNEP and WHO—will ensure salience of its work program and government ownership of its scientific assessments. This arrangement is necessary to foster uptake in international and national policy-making (e.g., under MEAs or governing bodies of intergovernmental organizations). Stakeholders such as civil society organizations and industry can participate as observers, providing their expertise and knowledge.

Second, having a clear definition of roles and responsibilities, a strict conflict-of-interest policy, and a rigorous peer-review process (for examples, see SM) will be critical to an objective, independent, and transparent work process and to the credibility and legitimacy of this body and its work. Third, ensuring wide involvement of scientists and practitioners, with balanced and diverse representation of relevant disciplines of natural and social sciences, gender, and regions, will help provide comprehensive, authoritative, and widely usable assessments. At the same time, the body needs to organize its work in an agile and flexible manner—e.g., by having separate working groups on distinct issues. Fourth, active communication of its findings with policy-makers, the wider scientific community (including funding agencies), stakeholders, and the public will help raise overall awareness of, and participation in, sound management of chemicals and waste.

Overarching science-policy interface bodies are no strangers to the international community. The Intergovernmental Panel on Climate Change (IPCC) and the Intergovernmental Science-Policy Platform on Biodiversity and Ecosystem Services (IPBES) are two well-known and studied examples that provide holistic, balanced, and authoritative scientific assessments by thousands of scientists from different disciplines worldwide (*13*). The IPCC has played a critical role in informing international and national governance, and raising public awareness and urgency, about climate change. The IPBES is relatively new (established in 2012), but its impact on mainstreaming biodiversity and stimulating policy changes at various levels is evident (*14*). The wealth of knowledge and experience of IPCC, IPBES, and other interface bodies (see SM) offers important insights for designing an overarching science-policy interface body on chemicals and waste (although each thematic area and science-policy interface body has its own distinctive characteristics that need to be taken into consideration). For instance, the successful integration of natural scientific data, insights from social sciences, and local knowledge forms a strong basis for producing policy-relevant and usable information (*15*).

Not only can the overarching interface body on chemicals and waste learn from existing interface bodies, but it also may collaborate with them to conduct assessments that address multiple environmental and societal concerns in a synergistic manner. Setting up an overarching science-policy interface body on chemicals and waste will not solve all governance problems (e.g., a lack of effective national implementation and enforcement). However, it is a critical and necessary step toward strengthening informed policy-making for achieving the global sound management of chemicals and waste. ■

REFERENCES AND NOTES

1. United Nations Environment Programme, *Global Chemicals Outlook II - From Legacies to Innovative Solutions: Implementing the 2030 Agenda for Sustainable Development*; https://www.unenvironment.org/resources/report/global-chemicals-outlook-ii-legacies-innovative-solutions (2019).
2. United Nations Environment Programme, *Assessment of Options for Strengthening the Science-Policy Interface at the International Level for the Sound Management of Chemicals and Waste*, March 2020; https://wedocs.unep.org/bitstream/handle/20.500.11822/33808/OSSP.pdf?sequence=1&isAllowed=y (accessed 17 September 2020).
3. J. D. Stanaway *et al*., *Lancet* **392**, 1923 (2018).
4. G. Myhre *et al*., "Anthropogenic and Natural Radiative Forcing" in *Climate Change 2013: The Physical Science Basis. Contribution of Working Group I to the Fifth Assessment Report of the Intergovernmental Panel on Climate Change*, T. F. Stocker *et al.*, Eds. (Cambridge Univ. Press, 2013); www.ipcc.ch/site/assets/uploads/2018/02/WG1AR5_Chapter08_FINAL.pdf.
5. P. Wexler, J. van der Kolk, A. Mohapatra, R. Agarwal, Eds., *Chemicals, Environment, Health: A Global Management Perspective* (CRC Press, 2012), pp. 1–810.
6. P. Grennfelt *et al*., *Ambio* **49**, 849 (2020).
7. Z. Wang, I. Summerson, A. Lai, J. M. Boucher, M. Scheringer, *Strengthening the Science-Policy Interface in International Chemicals Governance: A Mapping and Gap Analysis*, Zenodo (2019); https://zenodo.org/record/2559189#.X3Tany1h3ao
8. M. Scheringer *et al*., *Environ. Sci. Pollut. Res. Int*. **13**, 432 (2006).
9. F. Lawrence, *Nature* **578**, 28 (2020).
10. M. Karlsson, *Sustainability* **11**, 4785 (2019).
11. G. G. Singh *et al*., *Front. Ecol. Environ*. **17**, 375 (2019).
12. D. W. Cash *et al*., *Proc. Natl. Acad. Sci. U.S.A*. **100**, 8086 (2003).
13. S. Beck, T. Forsyth, P. M. Kohler, M. Lahsen, M. Mahony, "The Making of Global Environmental Science and Politics" in *The Handbook of Science and Technology Studies*, C. Miller, L. Smith-Doerr, U. Felt, R. Fouché, Eds. (MIT Press, ed. 4, 2016).
14. M. H. Ruckelshaus *et al*., *Trends Ecol. Evol*. **35**, 407 (2020).
15. E. Löfmarck, R. Lidskog, *Environ. Sci. Policy* **69**, 22 (2017).

ACKNOWLEDGMENTS

The authors gratefully acknowledge G. White (Health Canada), M. Tschirren (Swiss Federal Office for the Environment), S. Sakai (Kyoto University), and S. T. Jahre (Norwegian Ministry of Climate and Environment) for helpful comments. The authors declare no competing interests. M.S. acknowledges financial support by the CETOCOEN PLUS project (CZ.02.1.01/0.0/0.0/15_003/0000469) of the Ministry of Education, Youth and Sports of the Czech Republic.

SUPPLEMENTARY MATERIALS

science.sciencemag.org/content/371/6531/774/suppl/DC1

10.1126/science.abe9090

A genetic region that controls coloration generates morphs of Midas cichlid fish, but speciation involves traits controlled by a number of different genes.

PHOTO: AD KONINGS

EVOLUTION

How many genetic changes create new species?

Speciation in plants and animals can involve differentiation across many genetic regions

By **Patrik Nosil[1,2], Jeffrey L. Feder[3], Zachariah Gompert[2]**

The formation of new species generates biodiversity and is often driven by evolution through natural selection. However, the number of genetic changes involved in speciation is largely unknown. Many theoretical models predict that if speciation occurs without geographic isolation, it will be driven by a small number of genes. The logic is that only the few genes that experience the strongest natural selection can overcome the homogenizing effect of genetic mixing (i.e., gene flow) to diverge between populations. However, empirical studies in plants and animals now suggest that speciation—even with gene flow—involves differentiation in surprisingly many genetic regions. This is thought possible because the effects of selection can become coupled across correlated genes such that the selection each gene experiences is much stronger than it would receive in isolation. Thus, the potential for genes to evolve collectively because of coupling may be a key to understanding speciation.

Over recent decades, major strides have been made in understanding the speciation process, which is characterized by the evolution of reproductive isolation (i.e., barriers to interbreeding) and eventually widespread differentiation across the genome. For example, it is now known that natural selection often drives speciation (*1*). Moreover, it has been shown that selection can stem from the ecological environment, as proposed by Darwin, or can occur within genomes through conflict and competition between genetic elements.

In contrast to improved knowledge of the role of selection in speciation, the genetic changes involved are less understood (*1*). Filling this gap in understanding is important because genetic details, such as the number of genes affected by selection and their genomic organization, can influence the dynamics by which new species form (*2*, *3*). For example, if only a few genes that are found together on the same chromosome drive speciation, the process could be highly constrained. By contrast, if many different genes and types of genetic changes drive speciation, the process may be more flexible, but less predictable (*3*). Although specific forms of reproductive isolation are

[1]Centre d'Ecologie Fonctionnelle et Evolutive, CNRS, EPHE, IRD, University Paul Valéry Montpellier 3, Montpellier, France. [2]Department of Biology, Utah State University, UT 84322, USA. [3]Department of Biological Sciences, University of Notre Dame, Notre Dame, IN 46556, USA.
Email: patrik.nosil@cefe.cnrs.fr

known to be controlled by many genes, the overall genome-wide architecture of differentiation during the active phases of speciation remains poorly understood (*1*).

A key consideration is whether geographic factors allow interbreeding between diverging populations (i.e., gene flow) (*2*–*5*). When divergence occurs with strong geographic isolation—for example between mountain ranges—independent populations can readily diverge in many genetic regions by the combination of natural selection and chance. The situation with gene flow is different. This is because gene flow acts as a homogenizing force that mixes genes between populations, keeping them similar and preventing them from diverging into separate species. For speciation to occur, natural selection must act in contrasting directions in different populations, to oppose this mixing effect and generate differences. Amounts of gene flow, and thus the selection required to counter them, form a continuum ranging from absent or low to high and can vary over time and space during the speciation process.

Theoretical models predict that speciation with high gene flow is promoted by concentrated genetic architectures comprising one or few genes of large effect (*2*–*4*). This allows these few genes to experience strong natural selection to overcome gene flow. That is, selection needs to be concentrated on a few regions, rather than being spread thin among many genes. For example, with a gene flow rate of 0.10 (10% of individuals are immigrants), divergence occurs more readily if two genes each experience a selection intensity of 0.20 each (20% difference in expected fitness, higher than the gene flow rate) than if 10 genes experience an intensity of 0.04 (weaker than gene flow). The total selection intensity of 0.40 is the same in these two cases, but per gene, selection is stronger than gene flow only in the former (*5*). Thus, models and some findings have led to the concept that speciation with gene flow is driven by a few, isolated genomic islands of divergence. The remainder of the genome is overwhelmed by gene flow and cannot diverge.

In contrast to these theoretical predictions, emerging data suggest that speciation with gene flow can involve many genetic regions. For example, population differentiation and reproductive isolation based on numerous regions across the genome have now been reported in systems diverging with gene flow, including insects (e.g., *Anopheles* mosquitoes, *Rhagoletis* flies, *Timema* stick insects) (*6*–*8*), fish (cichlids and stickleback) (*9*, *10*), and plants (sunflowers) (*11*), among others. Moreover, when divergence does occur in few genetic regions, this is often associated with discrete phenotypic morphs (as in mimetic butterflies) (*12*), rather than the strong reproductive isolation and genome-wide differentiation that characterize distinct species. In some cases, different outcomes have even been tied to variation in the genetic architecture of diverging traits. For example, differentiation in a genetic region controlling coloration generates morphs of Midas cichlid fish, but speciation and stable genome-wide differentiation involve traits controlled by a greater number of genes, such as jaw morphology and body shape (*9*). Thus, divergence in polygenic traits and multiple genetic regions seems key to progress toward speciation in some systems (see the figure).

Genetic changes that differentiate morphs and species

Patterns illustrate when few versus many genetic regions differentiate taxa. Black lines above the *x* axis represent two different chromosomes; the *y* axis represents the strength of genotype-phenotype association or the degree of population-genetic differentiation, represented by the orange traces.

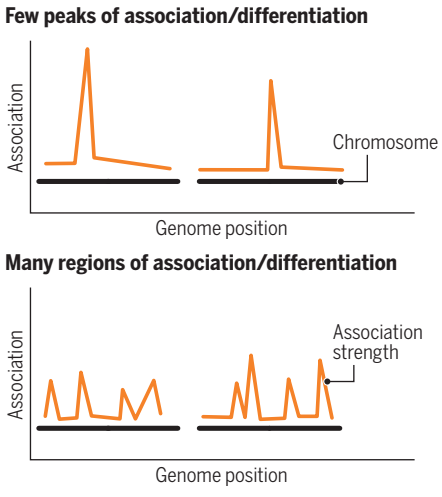

Given that models predict that speciation with gene flow will involve few genes, can these recent empirical findings be reconciled with theory? The answer is yes, but this requires a look at a different body of theory, focused on geographic clines, which describes how allele frequencies change over space. This theory was largely developed in the 1980s by Nick Barton and colleagues to understand the dynamics of hybrid zones between species (*13*). The models show how statistical associations between different genetic regions (called "linkage disequilibrium") can cause selection on one genetic region to be transferred to other correlated genetic regions. In essence, selection spills over, through association, from one genetic region to others. In this manner, the effects of selection can spread and become coupled across the genome, rather than being isolated to single genes (*4*, *13*). Such coupling means that the total selection that each genetic region experiences is much stronger than the direct selection it experiences in isolation. Thus, numerous genetic regions can evolve collectively as a unit to overcome gene flow (*4*).

Notably, the geographic configuration of populations can change during the speciation process, as species ranges expand and contract over time. This means that gene flow itself can be dynamic and change over time. Rather than occurring entirely in the presence or absence of gene flow, speciation likely involves periods of each. In turn, this can result in episodic hybridization, with diverse implications for evolution. For example, periods of geographic isolation might allow a pool of standing genetic variation to build up, including in structural features such as chromosomal inversions, which kick-starts the coupling process and later aids divergence with gene flow (*4*, *14*). Moreover, occasional bouts of gene flow can play a creative role in evolution by allowing for introgression of genes that facilitate adaptation, as reported in tropical butterflies (*12*), cichlids (*14*), sunflowers (*11*), and Darwin's finches (*15*). Thus, gene flow can have creative as well as homogenizing effects, and speciation likely reflects a balance between these effects.

Ideas concerning few versus many genes driving speciation are not in conflict. This is exemplified by *Helianthus* sunflowers (*11*) and *Rhagoletis* flies (*7*). In both systems, differentiation occurs genome-wide on many chromosomes but is accentuated in regions of reduced recombination, such as those harboring inversions. Thus, even with widespread genomic differentiation, by no means do all genetic regions always diverge equally; those under strong selection or experiencing low recombination may diverge more readily. Moreover, interactions between genes can amplify how strongly genes cause reproductive isolation, again making some genes more critical for speciation than others. Indeed, even speciation involving many genetic regions likely involves a finite number of building blocks, which can be combined in different ways to create diversity, as reported in sunflowers (*11*) and cichlids (*14*).

Despite this emerging evidence for the potential importance of genomic coupling in speciation, much work remains to be done. For example, almost all studies to date are purely correlational and often not highly replicated. Thus, experiments are needed to

GRAPHIC: N. DESAI/*SCIENCE*

test causal effects of differentiated regions on reproductive isolation and coupling, as are larger studies examining numerous taxon pairs. Such experiments could comprise experimental evolution studies in the lab or field transplants in the wild. Moreover, natural history and molecular studies, including those using ancient DNA, are required to establish whether divergence really occurred with gene flow. This is critical because false inference of gene flow could lead to erroneous evidence for coupling, because numerous genetic regions diverge between isolated populations through other processes (*5*). Moreover, genome assembly errors, particularly in regions of low recombination, could lead to a single genetic region being falsely inferred as multiple regions of differentiation. Nonetheless, initial evidence points to coupling as a consideration for understanding speciation. In turn, this suggests that sets of genes might exhibit emergent properties not seen by individual genes, implying the potential for sudden tipping points in the ability for selection to overcome gene flow (*4*).

By combining theory and data, evolutionary biologists are now poised to better understand how new species are created. A large part of this understanding will involve discovering how the effects of genes and phenotypes become coupled to cause a transition from polymorphism or geographic variation within species to genome-wide differences between distinct species. A major outstanding question is the extent to which the microevolutionary process of coupling can explain broader macroevolutionary patterns of biodiversity, as observed in radiations such as those in cichlid fish (*9*, *14*). ■

REFERENCES AND NOTES

1. D. Schluter, *Science* **323**, 737 (2009).
2. S. Gavrilets, *Fitness Landscapes and the Origin of Species* (Princeton Univ. Press, 2004).
3. S. Yeaman, M. C. Whitlock, *Evolution* **65**, 1897 (2011).
4. S. M. Flaxman, A. C. Wacholder, J. L. Feder, P. Nosil, *Mol. Ecol.* **23**, 4074 (2014).
5. T. E. Cruickshank, M. W. Hahn, *Mol. Ecol.* **23**, 3133 (2014).
6. M. K. N. Lawniczak *et al.*, *Science* **330**, 512 (2010).
7. A. P. Michel *et al.*, *Proc. Natl. Acad. Sci. U.S.A.* **107**, 9724 (2010).
8. R. Riesch *et al.*, *Nat. Ecol. Evol.* **1**, 82 (2017).
9. A. F. Kautt *et al.*, *Nature* **588**, 106 (2020).
10. F. C. Jones *et al.*, *Nature* **484**, 55 (2012).
11. M. Todesco *et al.*, *Nature* **584**, 602 (2020).
12. N. B. Edelman *et al.*, *Science* **366**, 594 (2019).
13. N. H. Barton, *Evolution* **37**, 454 (1983).
14. M. D. McGee *et al.*, *Nature* **586**, 75 (2020).
15. S. Lamichhaney *et al.*, *Science* **359**, 224 (2018).

ACKNOWLEDGMENTS

The work was funded by a grant from the European Research Council (EE-Dynamics 770826, https://erc.europa.eu/) to P.N., from NSF (DEB-1638997) and the U.S. Department of Agriculture–National Institute of Food and Agriculture program (2015-67013-23289) to J.L.F., and from the NSF (DEB 1844941) to Z.G. We thank D. Schluter for ongoing discussions concerning evolutionary genetics.

10.1126/science.abf6671

GRAPHIC: N.CARY/*SCIENCE* FROM A. WACHOLDER AND A.-R. CARVUNIS

GENETICS

New genes from borrowed parts

Vertebrate genes acquire new capabilities by capturing parasitic genomic elements

By **Aaron Wacholder**[1,2] *and* **Anne-Ruxandra Carvunis**[1,2]

The vast phenotypic diversity of life is in part a consequence of a continual process of genetic innovation. New genes, with distinct structures and capabilities, emerge regularly throughout evolutionary history. Making use of genomics technologies, researchers are beginning to form an understanding of the details of the processes by which new genes arise. On page 797 of this issue, Cosby *et al.* (*1*) provide clarity for one such process. Transposons are parasitic genomic elements that replicate by inserting copies of themselves in the host genome. Cosby *et al.* report how vertebrate genes have captured DNA transposon domains, generating new genes that encode new fusion proteins with distinct domain architectures. Fusion of transposon domains with host genes appears to be frequent, with 94 fusion events identified over tetrapod evolution. Transposon domain capture may be a common source of new genes and molecular innovation across the tree of life.

Cosby *et al.* expand on and generalize previous work that has characterized a small sample of host-transposon fusion proteins (*2*–*4*). For example, the mammalian gene *GTF2IRD2* (GTF2I repeat domain containing 2) (*2*), implicated in the rare genetic disorder Williams-Beuren syndrome, was previously discovered to be a carboxyl-terminal fusion of an ancestral transcription factor with a transposon domain. By using large-scale genomic comparison, Cosby *et al.* were able to reconstruct the general process by which DNA transposon domains are captured by host genes. Some DNA transposon families have been highly successful at replicating within tetrapod genomes, inserting themselves in proximity with numerous host genes. Capture occurs through exon shuffling: An exon from the transposon is spliced into the transcript of a nearby host gene, usually making use of the native splice sites within the transposon. The fusion product emerges initially as an alternative splice isoform to the main prefusion product and then becomes the dominant isoform through DNA sequence changes over evolutionary time.

DNA transposons appear especially well-suited for generating transcription factors through exon-shuffling. DNA transposons encode transposases that must recognize and bind to the transposon itself to replicate it. Cosby *et al.* found that most domains captured from DNA transposons perform this self-recognition role. Thus, the captured DNA-binding domains in

Origins of new protein-coding genes

A gene can acquire new molecular capacities by capturing a domain from a transposon or from a different host gene. Fusion among host genes can similarly assemble preexisting domains into distinct combinations. Alternatively, a gene can evolve new molecular capacities through a series of major sequence changes. This can be facilitated by gene duplication, which creates a copy that can diversify. In de novo gene birth, a fully new gene evolves from a previously noncoding sequence.

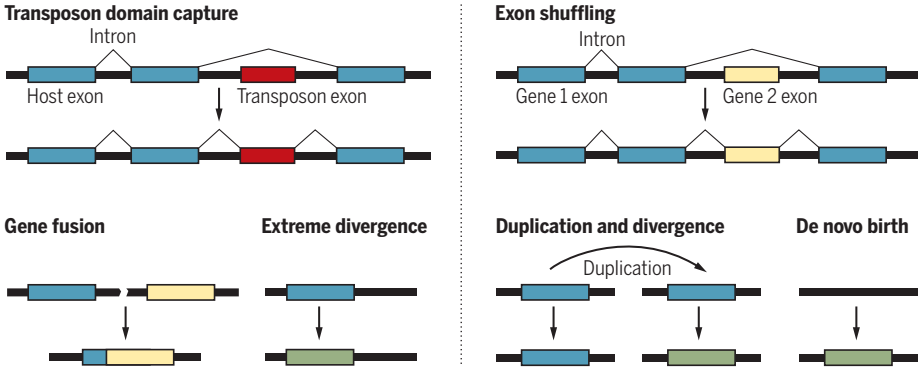

the fusion protein will initially bind to copies of the transposon itself. Because these copies are common throughout the genome after a period of successful transposon replication, the transposon family provides both DNA binding capacity to the new fusion protein and an initial set of binding sites throughout the genome. A skeleton of a regulatory subsystem is thus formed immediately, which can be further refined though coevolution of the fusion gene and the corresponding DNA-binding sites of the encoded fusion protein. In support of this model, Cosby *et al.* show that four recently evolved fusion proteins with captured transposon DNA-binding domains repress transcription of genes downstream of the transposon binding site. For example, the bat transcription factor KRABINER, a fusion with the DNA transposon *mariner*, binds both *mariner* and other sites throughout the genome, regulating hundreds of genes.

The study of Cosby *et al.* highlights the key role of transposons as drivers of genetic innovation. In addition to genes that originate as host-transposon fusions, full transposon genes can also be captured by the host. For example, the transposon-derived genes recombination activating gene 1 (*RAG1*) and *RAG2* are of central importance to adaptive immunity, generating antibody diversity through recombination (*5*). Studies have found that hundreds of human genes appear to be derived from transposons, as are an abundance of long noncoding RNAs (lncRNAs) and regulatory sites (*6*). Why is host capture of transposons so common? Although transposons themselves are "selfish" elements that can reproduce at the expense of the host, their replicative success brings with it the spread of raw material for potential innovation throughout the genome. This raw material is not random but is already capable of activities involved in transposon replication. DNA-binding activity encoded by the transposon can be directly incorporated in transcription factors, and transposon-derived genes can make use of translocation activity already present in the transposon ancestor to generate diversity-promoting genomic rearrangements in somatic cells.

Historically, the focus of much research on the generation of new genes has been on gene duplication followed by the diversification of these duplicates into distinct genes (*7*). However, many gene duplicates remain structurally similar to their parents. Cosby *et al.* demonstrate that transposon domain capture is a common mechanism by which entirely new capacities can be obtained in genes that were absent in the host parent, such as DNA-binding capacity. This is not specific to host-transposon interaction. Gene fusion and exon shuffling among host genes can similarly create new combinations of already-existing capacities (*8*). In contrast to this class of new gene-formation mechanisms, in which the innovation consists of rearranging functional domains in new contexts, the phenomenon of de novo gene birth from a nongenic sequence generates completely new domains and genes. Although once thought rare, well-characterized cases of de novo gene birth have now been reported in numerous taxa (*9*). New genes and domains can also arise through extreme divergence, in which a sequence evolves beyond recognition through a series of molecular changes (*10*).

"...transposon domain capture is a common mechanism by which entirely new capacities can be obtained in genes..."

A major open question is the relative contributions of these mechanisms (duplication and divergence, gene rearrangement, de novo birth, and extreme divergence) to gene formation and functional innovation (see the figure). Perhaps even more important will be to determine the distinct contexts in which these mechanisms contribute to innovation and how the mechanism of origin affects the type of molecular, physiological, and evolutionary impacts the newly created genes can have. Therefore, it is of great interest that Cosby *et al.* find that most domain capture events from transposons involve acquisition of DNA-binding domains and associated capabilities. ■

REFERENCES AND NOTES

1. R. L. Cosby *et al.*, *Science* **371**, eabc6405 (2021).
2. H. J. Tipney *et al.*, *Eur. J. Hum. Genet.* **12**, 551 (2004).
3. R. Cordaux, S. Udit, M. A. Batzer, C. Feschotte, *Proc. Natl. Acad. Sci. U.S.A.* **103**, 8101 (2006).
4. J. C. Newman, A. D. Bailey, H.-Y. Fan, T. Pavelitz, A. M. Weiner, *PLOS Genet.* **4**, e1000031 (2008).
5. A. Agrawal, Q. M. Eastman, D. G. Schatz, *Nature* **394**, 744 (1998).
6. I. A. Warren *et al.*, *Chrom. Res* **23**, 505 (2015).
7. J. S. Taylor, J. Raes, *Annu. Rev. Genet.* **38**, 615 (2004).
8. L. Patthy, *Gene* **238**, 103 (1999).
9. S. B. Van Oss, A.-R. Carvunis, *PLOS Genet.* **15**, e1008160 (2019).
10. N. Vakirlis, A.-R. Carvunis, A. McLysaght, *eLife* **9**, e53500 (2020).

[1]Department of Computational and Systems Biology, School of Medicine, University of Pittsburgh, Pittsburgh, PA, USA. [2]Pittsburgh Center for Evolutionary Biology and Medicine, School of Medicine, University of Pittsburgh, Pittsburgh, PA, USA. Email: anc201@pitt.edu

10.1126/science.abf8493

PHYSICS

A masing ladder

A maser that amplifies emission of periodically modulated quantum states has uses in metrology

By **Ren-Bao Liu**[1,2]

Masers, the precedent and radio-frequency (rf) counterpart of lasers, have many applications in metrology, communication, and spectroscopy. Jiang *et al.* (*1*) demonstrate a new type of maser in which rf radiation is amplified by stimulated emission from transitions between periodically modulated quantum states, called Floquet states (*2*), unlike a conventional maser, which uses transitions between stationary quantum states. The Floquet maser presents a phase-locked frequency comb equally spaced by the modulation frequency. With a modulating signal at a low frequency (1 to 100 mHz) converted to maser emission at high transition frequencies (~10 Hz) of ultranarrow spectral linewidth (<0.3 mHz), the authors overcome the low-frequency noise problem in metrology and show that subpicotesla sensitivity of magnetometry is achievable. Conceivable applications of this work include precision clocks and detection of ultralight dark-matter particles such as axions.

The quantum emitters used are the nuclear spins associated with xenon-129 (^{129}Xe) nuclei, whose quantum states have long lifetimes (~14 s). A static magnetic field splits the quantum states of the nuclear spins into the upper and lower energy levels (see the figure). The periodic modulation of the magnetic field can be viewed as what would result from a magnet mounted onto an oscillator. The spins in the upper or lower levels, which point upward or downward, would be attracted or repulsed by the magnet and in turn offset the oscillator in the opposite direction. In quantum mechanics, the offset oscillator has a ladder of equally spaced energy levels, corresponding to the upper and the lower ladders of Floquet states.

Jiang *et al.* optically pump the ^{129}Xe spins to achieve population inversion (the up-

[1]Department of Physics, The Chinese University of Hong Kong, Shatin, New Territories, Hong Kong, China. [2]Hong Kong Institute of Quantum Information Science and Technology, The Chinese University of Hong Kong, Shatin, New Territories, Hong Kong, China. Email: rbliu@phy.cuhk.edu.hk

Floquet-state ladders

Jiang *et al*. created a maser that amplifies emission of periodically modulated quantum states (Floquet states). They converted low-frequency (1 to 100 mHz) signals into maser emission at ~10 Hz with ultranarrow spectral linewidth (<0.3 mHz) to create a phase-locked frequency comb.

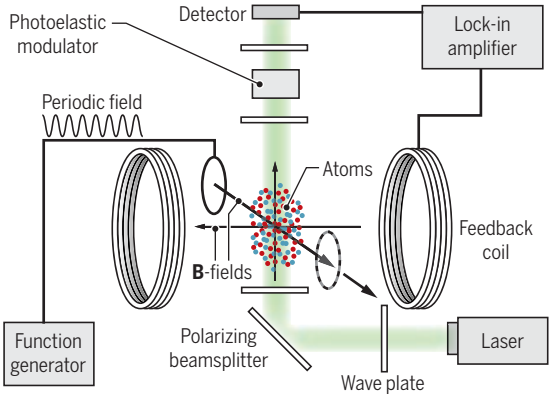

Experimental schematic
A low-frequency periodically modulated magnetic (**B**) field is applied to the nuclear spins of xenon-129, which are optically detected through spin exchange with rubidium-87 atoms. The spin-transition signals are amplified and used to drive coils that create a second feedback magnetic field.

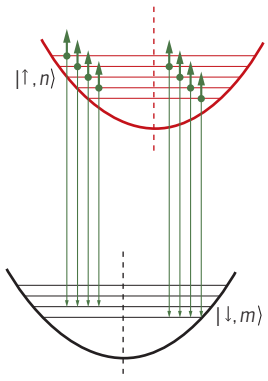

State splitting
The magnetic field creates upper (*n*) and lower (*m*) ladders of periodically modulated quantum states, or Floquet states.

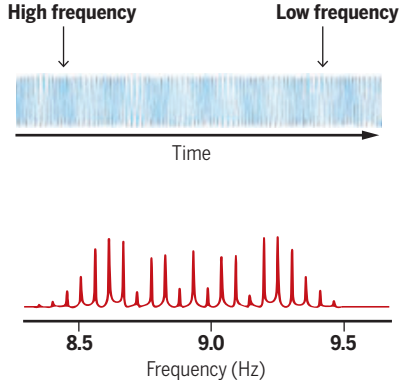

A low-frequency comb
The oscillation frequency of the masing (radio-frequency emission) periodically changes over time. Its Fourier transform (red) creates a phase-locked millihertz frequency comb.

per ladder becomes more populated than the lower one) so that the radiation by the ^{129}Xe spins is amplified by stimulated emission. The ^{129}Xe nuclear spins emit photons coherently and collectively, by the so-called superradiance process (*3*), and in turn undergo coherent precession. In the experiment, the spin precession is monitored through spin-exchange collisions with optically pumped rubidium-87 atoms, and then the signal is amplified and fed back to the spins by a pair of coils. The gain by the stimulated emission and the feedback amplification enables masing between the Floquet states, which results in equally spaced, phase-locked sharp spectral lines.

Transitions between Floquet states are also the basis of two other important and extremely nonlinear optical phenomena. High-harmonic generation (HHG) occurs when a system driven by a strong laser radiates at large integer multiples of the driving frequency (*4*, *5*). HHG has applications in coherent x-ray spectroscopy as well as attosecond and even zeptosecond ultrafast optics (*5*). High-order sideband generation (HSG) occurs when a system driven by a strong low-frequency field and excited by a weak high-frequency laser emits sidebands of the weak laser separated by integer multiples of the driving frequency (*6*, *7*). HSG may be used for high-speed optical communication (*6*). Both HHG and HSG are platforms that can be used to study extreme strong-field physics (*5*, *7*). The Floquet maser resembles the HSG but has two new features, collective coherence (superradiance) (*3*) and gain. New physics and applications are expected from the study of HHG and HSG in gain media that exhibit collective quantum coherence.

The Floquet maser is closely related to another innovation in lasers, quantum amplification of superradiant emission of radiation, or QASER (*8*). The idea is to drive atoms by a strong low-frequency laser so that the atoms are in Floquet states that contain a small, periodically oscillating mixture between the upper and lower levels. When the population oscillation in the Floquet states is resonant with the superradiance-induced oscillation between the emission and absorption of photons, radiation at the atomic transition frequency (which is much larger than the driving frequency) can be amplified without population inversion. If realized, QASER will be useful for achieving extreme high-frequency lasers, such as gamma-ray lasers.

The Floquet maser demonstrated by Jiang *et al*., although still at the rf waveband, already has a few key elements of QASER, in particular, the superradiance and the Floquet states. Nonetheless, some important modifications are needed to demonstrate the idea of QASER. It will be relatively straightforward to reconfigure the geometry and polarization of the driving field to achieve coherent population oscillation needed for QASER. The nontrivial missing piece is that the feedback amplification in the Floquet maser is not quantum and is unfeasible for QASER in the gamma-ray frequency band. Further theoretical and experimental investigations can show whether the Floquet maser could be sustained with only quantum amplification in place.

The Floquet maser demonstrated by Jiang *et al*. provides a new platform for studying exotic temporal phenomena in quantum many-body systems (*9*–*12*). An outstanding example is time crystals (*11*, *12*), wherein the Floquet states of a periodically driven quantum system undergo a spontaneous symmetry breaking so that the system oscillates at a fractional frequency of the driving field. It would be interesting to study time crystals in the presence of quantum amplification, the interplay with a Floquet maser, or even mutual excitation of a time crystal and a Floquet maser. The Floquet maser and the versions of it yet to come provide a ladder to high-frequency, high-precision metrology applications and a platform for studying quantum phenomena. ■

REFERENCES AND NOTES

1. M. Jiang, H. Su, Z. Wu, X. Peng, D. Budker, *Sci. Adv.* **7**, eabe0719 (2021).
2. J. H. Shirley, *Phys. Rev.* **138** (4B), B979 (1965).
3. R. H. Dicke, *Phys. Rev.* **93**, 99 (1954).
4. M. Ferray *et al*., *J. Phys. B* **21**, L31 (1988).
5. P. B. Corkum, F. Krausz, *Nat. Phys.* **3**, 381 (2007).
6. B. Zaks, R. B. Liu, M. S. Sherwin, *Nature* **483**, 580 (2012).
7. H. B. Banks *et al*., *Phys. Rev. X* **7**, 041042 (2017).
8. A. Svidzinsky, L. Yuan, M. O. Scully, *Phys. Rev. X* **3**, 041001 (2013).
9. N. H. Lindner, G. Refael, V. Galitski, *Nat. Phys.* **7**, 490 (2011).
10. D.-W. Wang, H. Cai, L. Yuan, S.-Y. Zhu, R.-B. Liu, *Optica* **2**, 712 (2015).
11. J. Zhang *et al*., *Nature* **543**, 217 (2017).
12. S. Choi *et al*., *Nature* **543**, 221 (2017).

ACKNOWLEDGMENTS

R.-B.L. is supported by the Hong Kong Research Grants Council.

10.1126/science.abg1081

GRAPHIC: C. BICKEL/*SCIENCE*

SYNTHETIC BIOLOGY

Re-engineering Botox

Botulinum neurotoxin is altered to recognize a different substrate

By **Pål Stenmark**[1,2]

Some of the most toxic substances known are the botulinum neurotoxins. The most well-known member of this toxin family is Botulinum neurotoxin A1, famously known as Botox. Botulinum neurotoxins are large proteins that target neurons and block the release of synaptic vesicles at nerve terminals, causing paralysis (*1*, *2*). Yet despite their extreme toxicity, botulinum neurotoxins are used therapeutically and cosmetically. Expanding their potential beyond their natural substrates has been limited by the lack of tools to master the complex substrate specificity of the protease domains of these toxins. On page 803 of this issue, Blum *et al.* (*3*) describe a phage-assisted evolution approach to control the substrate specificities of the toxin's protease domains. This may lead to new therapeutics, targeting diseases that previously have been inaccessible to treatment.

Botulinum neurotoxins can cause the deadly disease botulism, which is often associated with the consumption of incorrectly canned food. The disease is also caused by toxin released from the bacteria *Clostridium botulinum* that have colonized the intestine of infants. The toxins are also possible bioterrorism agents (*4*). Despite being one of the most toxic compounds known, with median lethal dose values of only a few nanograms per kilo, botulinum neurotoxins are used therapeutically, mainly to dampen or inactivate specific muscles. The number of applications for the neurotoxins is rapidly increasing, and there are now more than 100 medical conditions for which the toxins are applied (*5*–*7*).

The toxins have an exquisite design, containing three domains with different tasks each. The binding domain directs the toxin to the correct cells (binding receptors on neurons), and the translocation domain moves the protease domain across the membrane into the cell (*1*, *2*, *8*, *9*). The spearheads of the botulinum neurotoxins are the light-chain protease domains, which cleave distinct SNARE [soluble NSF attachment protein (SNAP) receptor] proteins within the neuron (*1*, *2*, *10*, *11*). The protease domain recognizes its SNARE substrate through extensive interactions and several exosites (secondary substrate-binding sites on the toxin), elegantly explaining the high substrate specificity (*9*, *12*).

The SNARE proteins are key players in membrane vesicle fusion (*13*). Cleavage of the SNARE proteins stops the vesicle fusion events needed for the release of synaptic vesicles that contain the neurotransmitter acetylcholine at the neuromuscular junction, severing the connection between the nerve and the muscle.

Progress is being made in the ability to engineer the receptor interactions and cell specificity of the toxins (*14*). To master the substrate specificity of the protease domain of the toxins, Blum *et al.* developed a variant of phage-assisted continuous evolution that facilitates simultaneous negative and positive selection for specific protease activities. Briefly, the technique relies on coupling the desired properties of the protease domain to the infectivity of a bacteriophage and allowing it to rapidly evolve over many generations.

"The possibilities that are opened up by the method developed by Blum *et al.* have enormous potential..."

Decreasing the specificity and thereby widening the substrate specificity of proteases has been demonstrated previously. However, the beauty of the method described by Blum *et al.* is the possibility to select for a certain substrate at the same time as selecting against another. The authors demonstrate this by evolving botulinum neurotoxin serotype X, a recently discovered botulinum neurotoxin that naturally has multiple substrates (*15*). Blum *et al.* engineered the toxin to cleave one of its substrates efficiently while having no activity toward others. Another of the key advances by Blum *et al.* is the ability to evolve activity toward completely new substrates, as they show by evolving botulinum neurotoxin E toward a non-SNARE target.

The possibilities that are opened up by the method developed by Blum *et al.* have enormous potential in many fields. The protease domains of the toxins could be evolved to cleave specific proteins involved in the sensation of pain. Or, one could envision evolving activity specifically toward a mutated oncogene while sparing the proto-oncogene, targeting cancer cells while sparing other cells.

There are many other proteases for which the redirection of substrate specificities could have great potential. For example, the technique from Blum *et al.* could be used to refine and alter the specificities of other proteases that are being developed for treating cardiovascular disease, digestive disorders, inflammation, cystic fibrosis, retinal disorders, and other medical conditions. The method could also be used to develop highly specific proteases for use as research tools, similar to how botulinum neurotoxins are used to study vesicle fusion.

Many challenges remain before we can access the full potential of the botulinum neurotoxins and other proteases. However, the findings of Blum *et al.* open up new fields of research with the potential to develop therapeutics and target diseases that previously have been inaccessible. ■

[1]Department of Biochemistry and Biophysics, Stockholm University, Stockholm, Sweden. [2]Department of Experimental Medical Science, Lund University, Lund, Sweden. Email: stenmark@dbb.su.se

REFERENCES AND NOTES

1. M. Dong, G. Masuyer, P. Stenmark, *Annu. Rev. Biochem.* **88**, 811 (2019).
2. M. Montal, *Annu. Rev. Biochem.* **79**, 591 (2010).
3. T. R. Blum *et al.*, *Science* **371**, 803 (2021).
4. S. S. Arnon *et al.*, Working Group on Civilian Biodefense, *JAMA* **285**, 1059 (2001).
5. J. Jankovic *et al.*, *Botulinum Toxin E-Book: Therapeutic Clinical Practice and Science* (Elsevier Health Sciences, 2009).
6. D. Truong, D. Dressler, M. Hallett, C. Zachary, *Manual of Botulinum Toxin Therapy* (Cambridge Univ. Press, 2014).
7. M. Pirazzini, O. Rossetto, R. Eleopra, C. Montecucco, *Pharmacol. Rev.* **69**, 200 (2017).
8. D. B. Lacy, W. Tepp, A. C. Cohen, B. R. DasGupta, R. C. Stevens, *Nat. Struct. Biol.* **5**, 898 (1998).
9. M. A. Breidenbach, A. T. Brunger, *Nature* **432**, 925 (2004).
10. J. Blasi *et al.*, *Nature* **365**, 160 (1993).
11. G. Schiavo *et al.*, *Nature* **359**, 832 (1992).
12. O. Rossetto *et al.*, *Nature* **372**, 415 (1994).
13. T. C. Südhof, J. E. Rothman, *Science* **323**, 474 (2009).
14. M. Elliott *et al.*, *Sci. Adv.* **5**, eaau7196 (2019).
15. S. Zhang *et al.*, *Nat. Commun.* **8**, 14130 (2017).

ACKNOWLEDGMENTS

I thank the Swedish Research Council (2018-03406), the Swedish Cancer Society (20 1287), and the Novo Nordisk Foundation (NNF20OC0064789) for financial support. I thank J. Davies for discussions.

10.1126/science.abg3535

MICROBIOLOGY

The genetic underground of antibiotic resistance

The silent role and clinical relevance of metabolic mutations in antibiotic resistance begin to be unravelled

By **Mattia Zampieri**

Metabolism has mostly been studied for its role in providing building blocks and energy to sustain cell duplication. Previously unexplored roles of metabolism in signaling and regulation have now been unveiled. Mounting evidence suggests a fundamental role of microbial metabolism in mediating the short-term (*1*, *2*) and long-term responses to antimicrobial agents (*3*), opening possibilities for combination therapies that could hamper the evolution of antibiotic resistance (*4*–*6*). Given their impact on bacterial growth, indirect effects of antibiotic treatment on metabolism were to be expected. But there are also common and drug-specific metabolic changes that are independent from growth inhibition and can play an important role in antibiotic lethality (*1*, *5*, *6*). If metabolism plays a key role in mediating antibiotic response and drug toxicity, does metabolism have a role in antibiotic resistance? On page 799 of this issue, Lopatkin *et al.* (*7*) reveal the interplay between metabolism and antibiotic resistance in clinically relevant pathogens.

By analyzing a library of 7243 *Escherichia coli* genomes, Lopatkin *et al.* observed that in clinical strains isolated from human patients, mutations that map to core metabolic functions were as frequent as well-known resistance mutations (*8*), such as those affecting the drug target. However, the authors showed that these metabolic mutations are observed significantly less frequently in traditional in vitro evolution experiments that select for antibiotic resistance.

Because a mutation conferring antibiotic resistance may exhibit different fitness costs depending on the environmental conditions, evolutionary trajectories to antibiotic resistance can be influenced by the nutritional compositions of the environment and treatment regimens (*2*–*4*). Additionally, the sequence of solutions adopted to evolve antibiotic resistance can be radically different if bacteria are continuously exposed to a high dosage of the antibiotic or if selection is applied by intermittent antibiotic exposure (*2*). Therefore, Lopatkin *et al.* asked whether, in contrast to classical approaches that rely on growth-dependent selection, in vitro evolution protocols that maximize metabolic adaptation may be more representative of genetic selection for antibiotic resistance in vivo.

Lopatkin *et al.* first used a traditional protocol for evolution of antibiotic-resistant *E. coli*: serial passages of populations continuously challenged with an increasing concentration of three representative bactericidal drugs that target protein synthesis (streptomycin), DNA replication (ciprofloxacin), and cell wall biosynthesis (carbenicillin). They found larger genetic variability by sequencing entire populations versus isolated clones, emphasizing how clonal analysis can mask the role of relatively infrequent, but potentially equally relevant, mutations. Many of the high-frequency mutations were consistent with classical resistance mechanisms (*8*), such as mutations in drug targets or regulators of multidrug response genes. Notably, although at low frequency, many more mutations in metabolic genes were found at the population level than at the clonal level, suggesting that an underlying diverse genetic network of mutations directly impinging on metabolism could play a more important role than previously anticipated in mediating the evolution of resistance to antibiotics.

Lopatkin *et al.* suspected that in classical experimental evolution, constant exposure to antibiotics creates a strong selective pressure for growth-related processes and possibly masks the importance of mutated metabolic genes in conferring protection from antibiotic-induced stress. To test whether frequency of metabolic mutations throughout the evolution of antibiotic resistance could be increased, the authors cycled *E. coli* cells between 1 hour of antibiotic treatment per day and 22 hours of growth without antibiotics. Metabolic activity during treatment was modulated by increasing the temperature 1°C higher every day for 10 days, starting at 20°C (low metabolic activity). As a result of this new protocol, metabolic mutations now dominated the genetic changes in the emerging strains. Moreover, metabolic mutations were not just a consequence of the cycling between growing and nongrowing conditions but were exclusively associated with exposure to antibiotics. The same metabolic mutations were found to be common between strains resistant to different antibiotics, reflecting the potential relevance of modulating metabolism as a general adaptive strategy against antibiotic-mediated stress.

These findings raised the question of whether metabolic mutations are necessary to facilitate evolution of resistance (*2*) and/or sufficient to acquire antibiotic resistance. Lopatkin *et al.* showed that on average, metabolic mutations alone can confer mild, but measurable, antibiotic resistance, suggesting that increased survival is unlikely a result of increased tolerance—that is, the ability to survive antibiotic exposure for a longer time. For example, although in wild-type *E. coli* carbenicillin induced a strong up-regulation of enzymes in the tricarboxylic acid cycle—

Metabolic protection from antibiotics

Genetic diversity in antibiotic-resistant populations of *Escherichia coli* result from convergent paths to antibiotic resistance. These paths also involve various mutations in metabolic genes that can fulfill a common task: shielding bacterial metabolism from the effects of antibiotic treatment.

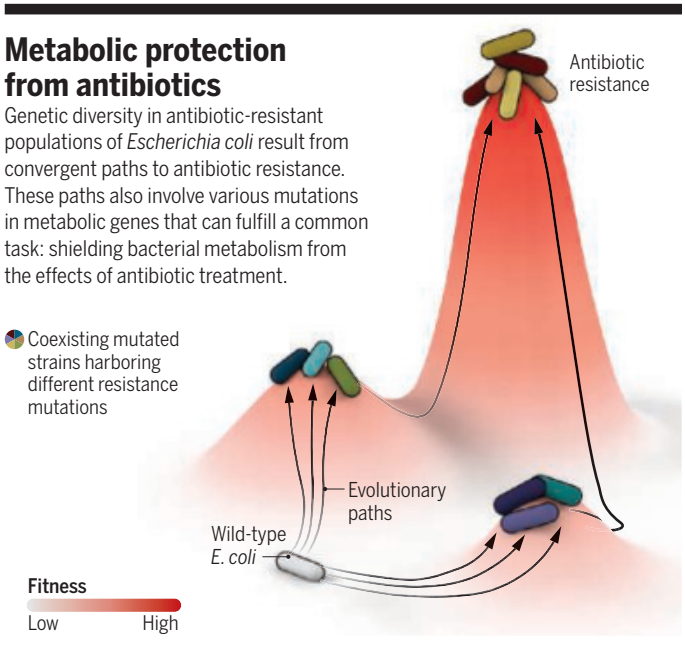

GRAPHIC: V. ALTOUNIAN/*SCIENCE*

ETH Zurich, Zurich, Switzerland.
Email: zampieri@imsb.biol.ethz.ch

which is responsible for converting organic fuel molecules (e.g., glucose) and oxygen into carbon dioxide, water, and energy—a mutation in one of these enzymes, the 2-oxoglutarate dehydrogenase enzyme (*sucA*), is sufficient to not only abolish this up-regulation but also confer carbenicillin resistance. These findings reinforce that antibiotic efficacy is intimately linked to the cell's metabolic state.

These analyses suggest that rewiring of central metabolism may be a general strategy to acquire antibiotic resistance, but the scope of metabolic changes resulting from these mutations remains to be systematically unraveled. One hypothesis emerging from this study is that different metabolic mutations can converge to similar adaptive changes and provide resistance to antibiotics with largely different modes of action. Hence, although individually at lower frequency than classical resistance mutations, it is possible that different metabolic mutations can play the same role in mediating antibiotic resistance (see the figure).

Advances in technologies that enable the monitoring of dynamic metabolic changes in response to genetic and environmental perturbations combined with computational models of cellular metabolism will help researchers to investigate the common scope of diverse metabolic mutations in antibiotic resistance (*3*, *5*, *9*, *10*). Predicting how mutations affect the metabolic state of cells, alter drug action, and ultimately shape the fitness landscape of resistance mutations will be of paramount importance to leverage this understanding in the optimization of treatment regimens and the discovery of new drugs and combination therapies. Small molecules that interfere with respiratory and fermentative metabolism might improve the killing efficacy of classical antibiotics (*4*, *11*) and hamper the evolution of resistance by changing the fitness landscape of antibiotic resistance (*3*, *5*, *6*). From the data and analysis presented by Lopatkin *et al.*, mechanisms by which pathogenic bacteria can become resistant in vivo can be unraveled. ■

REFERENCES AND NOTES

1. P. Belenky *et al.*, *Cell Rep.* **13**, 968 (2015).
2. O. Fridman, A. Goldberg, I. Ronin, N. Shoresh, N. Q. Balaban, *Nature* **513**, 418 (2014).
3. M. Zampieri *et al.*, *Mol. Syst. Biol.* **13**, 917 (2017).
4. S. Meylan *et al.*, *Cell Chem. Biol.* **24**, 195 (2017).
5. A. I. Campos, M. Zampieri, *Mol. Cell* **74**, 1291 (2019).
6. M. Vestergaard *et al.*, *mBio* **8**, e01114 (2017).
7. A. J. Lopatkin *et al.*, *Science* **371**, eaba0862 (2021).
8. I. Yelin, R. Kishony, *Cell* **172**, 1136 (2018).
9. E. S. Kavvas, L. Yang, J. M. Monk, D. Heckmann, B. O. Palsson, *Nat. Commun.* **11**, 2580 (2020).
10. Y. Hart *et al.*, *Nat. Methods* **12**, 233 (2015).
11. Y. Shan *et al.*, *mBio* **8**, e02267 (2017).

ACKNOWLEDGMENTS

I thank V. Chubukov and K. Ortmayr for helpful feedback.

10.1126/science.abf7922

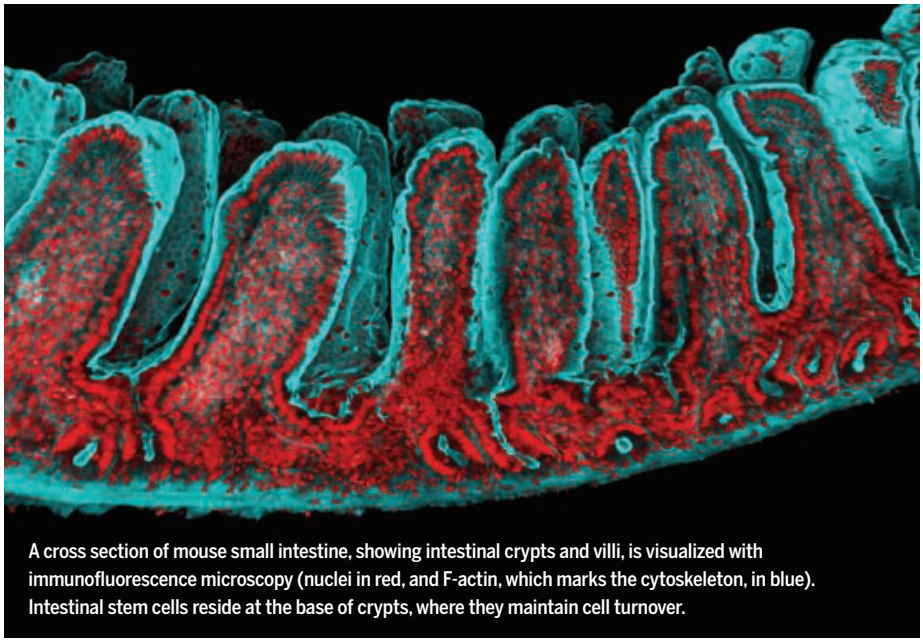

A cross section of mouse small intestine, showing intestinal crypts and villi, is visualized with immunofluorescence microscopy (nuclei in red, and F-actin, which marks the cytoskeleton, in blue). Intestinal stem cells reside at the base of crypts, where they maintain cell turnover.

PHOTO: FLORIJN DEKKERS AND ANNE RIOS

STEM CELLS

Tissue regeneration: Reserve or reverse?

Stem cells recover from injury by tissue dedifferentiation, not from dedicated reserves

By **Ramesh A. Shivdasani[1,2,3], Hans Clevers[4,5,6], Frederic J. de Sauvage[7]**

Tissues with high intrinsic turnover, such as the skin and intestinal lining, rely on resident stem cells, which generate all native cell types. Intestinal stem cells (ISCs) are highly sensitive to damage, although they recover quickly. It is unclear whether this recovery (i.e., regeneration) occurs from less sensitive pools of "reserve" stem cells (*1*) or whether ISC progeny undergo "reverse" differentiation into stem cells (*2*). Recent studies in diverse organs highlight that dedifferentiation of specified cell types is a pervasive and dominant means for tissue regeneration. The findings have broad implications because all tissues experience some cell attrition over a lifetime, and knowing how tissues replenish those losses may help in preventing or treating organ failure. Moreover, it remains unclear whether incomplete differentiation, a common feature of cancer, reflects normal tissue plasticity, and it is unclear whether stem cells that arise by dedifferentiation may spawn cancers.

ISCs expressing leucine-rich repeat–containing G protein–coupled receptor 5 (*Lgr5*) lie at the bottom of small bowel crypts (*3*). In the course of homeostatic tissue turnover, their immediate progeny adopt alternative enterocyte or secretory fates, then fill the crypts with replicating progenitors that migrate away from ISCs. Cell division ceases at the crypt tops, where postmitotic cells begin a 3- to 5-day journey along intestinal villi. When ISCs sustain irreparable damage, some source in the crypt must regenerate new ISCs. Other adult epithelia—such as airways, prostate, and liver—are organized differently from the intestine and from each other (see the figure). These epithelia also restore cells lost by damage or attrition, even though at rest they turn over at least a hundred times more slowly than the intestinal lining.

[1]Department of Medical Oncology and Center for Functional Cancer Epigenetics, Dana-Farber Cancer Institute, Boston, MA, USA. [2]Department of Medicine, Brigham and Women's Hospital and Harvard Medical School, Boston, MA, USA. [3]Harvard Stem Cell Institute, Cambridge, MA, USA. [4]Hubrecht Institute, Utrecht, Netherlands. [5]Royal Netherlands Academy of Arts and Sciences (KNAW), Utrecht, Netherlands. [6]University Medical Center Utrecht, Utrecht, Netherlands. [7]Department of Molecular Oncology, Genentech, South San Francisco, CA, USA. Email: ramesh_shivdasani@dfci.harvard.edu

Airway epithelial structure varies from trachea to small bronchioles, and distinct progenitors in different segments produce assorted secretory and ciliated cell types. In the lining of human and mouse upper airways, flat basal cells lie beneath a layer of columnar differentiated cells and adjacent to submucosal myoepithelial glands. Stem cell activity in normal tissue turnover maps to a subpopulation of keratin 5 (*Krt5*)–expressing basal cells (*4*). The trachea and bronchi are vulnerable to diverse injuries, including targeted destruction of Krt5$^+$ stem cells and pervasive mucosal damage from noxious inhalants or viruses.

Adult human and mouse prostate glands also contain columnar luminal and flat KRT5$^+$ basal cells. Distinct unipotent progenitors maintain both populations, and castration induces massive luminal cell loss. Androgen reexposure restores prostate mass within weeks, which implies the presence of castration-resistant progenitors. However, an unequivocal stem cell pool has not been identified. The liver also has notable regenerative abilities after chemical or surgical injury. The emerging consensus is that this organ lacks a dedicated stem cell compartment and recovers from damage through dedifferentiation of mature hepatocytes and biliary cells (*5*, *6*).

Stem cell activity in vivo is demonstrated most persuasively by introducing into a tissue a permanent color or fluorescent label whose expression depends on Cre recombinase–mediated excision of a STOP cassette. When Cre activity is restricted to stem cells, all the progeny of those cells exclusively carry the label. ISCs and tracheal stem cells were thus identified because targeted Cre activity in LGR5$^+$ or KRT5$^+$ mouse cells labeled the respective full lineages (*3*, *4*). Investigation of tissue regeneration requires ablation of a stem cell compartment, followed by tracking of the restored ability to produce sufficient numbers of all native stem cell progeny. The canon of tissue repair rests heavily on such lineage-tracing experiments, but one limitation is that Cre recombinase is not often confined to a single defined cell type. This challenge lies at the heart of competing models for tissue recovery after lethal cell injuries.

Dividing cells take up labels such as [^{3}H]thymidine or fluorescent histone 2B and shed these labels as they replicate further or their daughters die. In the intestine, however, rare cells located near the fourth tier from the crypt base retain [^{3}H]thymidine for weeks. Given once-popular ideas that stem cells must be few in number and retain one "immortal" DNA strand when they replicate, +4 label-retaining cells (LRCs) were described as ISCs. In support of that idea, lineage tracing from *Bmi1*, a locus thought to be restricted to nonreplicating +4 LRCs, elicited an ISC-like response in vivo (*7*).

To reconcile the evidence for ISC properties in both LGR5$^+$ crypt base columnar cells (CBCs) and +4 LRCs, researchers postulated that abundant CBCs serve as frontline ISCs, whereas the smaller +4 LRC population contains dedicated reserves. Indeed, intestinal turnover is unperturbed when LGR5$^+$ CBCs are ablated because other crypt cells' progeny continue to repopulate villi and an LGR5$^+$ ISC compartment is soon restored (*1*). Multiple candidate markers of +4 LRCs that regenerate ISCs after injury have been proposed (*8*). Although these cells are too few to explain the typical scale and speed of ISC restoration, the prospect of two stem cell pools carried the additional allure of a sound adaptive strategy in a tissue that requires continuous self-renewal.

ISC differentiation is, however, not strictly unidirectional. Cre expression in absorptive or secretory cell types tags those cells selectively, but upon ablation of LGR5$^+$ CBCs, the label appears throughout (*9*). These observations imply that differentiated daughter cells have reverted into ISCs. Moreover, *Bmi1* expression was found to mark differentiated crypt endocrine cells (*10*), and putative +4 markers are expressed in many crypt cells including LGR5$^+$ CBCs. Accordingly, when Cre is expressed from these loci, the traced lineage might simply reflect CBC activity in resting animals and reverse differentiation of crypt cells after ISC ablation. But is dedifferentiation a rare and physiologically inconsequential event or the predominant mode of stem cell recovery? Dedifferentiation may obviate the need to invoke a dedicated reserve population, or it is possible that ISC recovery may reflect both dedifferentiation and contributions from a reserve stem cell population.

To investigate these issues, researchers activated a fluorescent label in LGR5$^+$ CBCs and waited for this label to pass into progeny cells before ablating CBCs (*11*). Thus, only the CBCs that recover by dedifferentiation should be labeled, and any cells arising from reserve ISCs should not. Nearly every restored crypt and CBC was fluorescent, with substantial contributions from both enterocytes and secretory cells (*11*). Cells captured early in the restorative process coexpressed mature-cell and ISC genes, which is compatible with recovery by dedifferentiation. Another study found that damaged ISCs are reconstituted wholly by the progeny of LGR5$^+$ CBCs (*8*). Thus, dedifferentiation would seem to be the principal mode of ISC regeneration, and prior conclusions about +4 ISCs likely reflect unselective Cre expression.

Stem cells in homeostasis and recovery

Physiologic cell turnover and recovery from injury occur from different cellular sources in diverse epithelia (intestine, upper airway, and prostate gland). Homeostatic turnover is driven by the stem cell pool, and tissue restoration from injury occurs through transient expansion and dedifferentiation of specified mature cells.

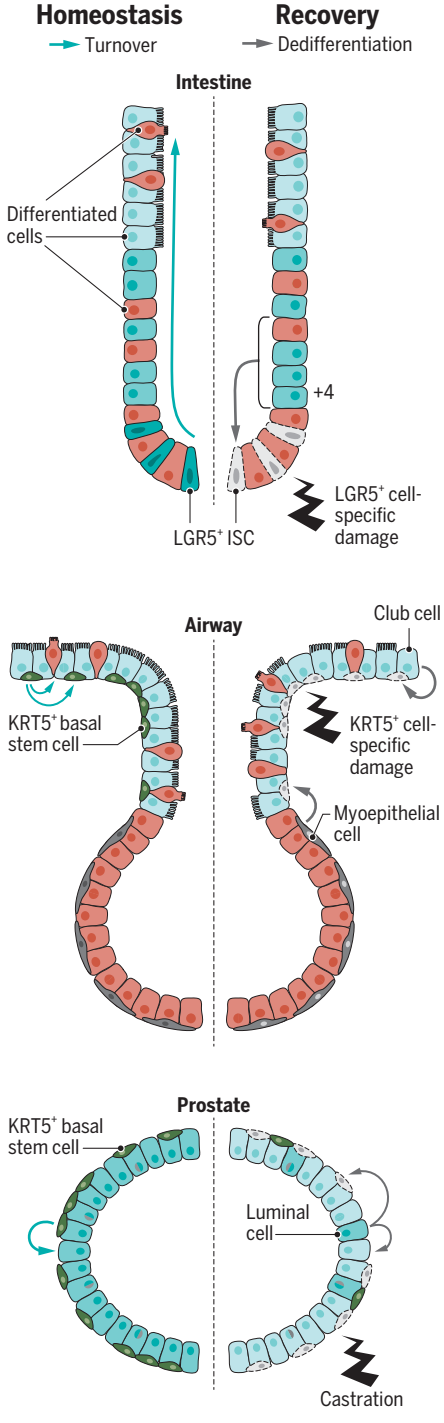

ISC, intestinal stem cell; KRT5, keratin 5; LGR5, leucine-rich repeat–containing G protein–coupled receptor 5.

GRAPHIC: KELLIE HOLSKI/*SCIENCE*

Different tissues might deploy distinct regenerative strategies, and recent studies in mouse airway, prostate, intestinal, and liver epithelia provide insightful lessons. After ablation of KRT5$^+$ airway stem cells, specified secretory and club cell precursors were found to undergo clonal multilineage expansion and accounted for up to 10% of restored KRT5$^+$ cells in vivo (*12*). Chemical or viral damage was subsequently reported to induce migration and dedifferentiation of submucosal gland myoepithelial cells into the basal layer to reconstitute the surface lining, including KRT5$^+$ stem cells (*13*). Thus, dedifferentiation into native stem cells occurs upon injury to both airway and intestinal linings in mice.

Single-cell RNA sequencing (scRNA-seq) analysis of mouse prostate glands recently revealed distinct gene expression profiles in ~3% of luminal cells, which are more clonogenic than others, express putative stem cell markers, and hence qualify as a pool enriched for native stem-like cells (*14*). After androgen reexposure following castration, however, the scale and distribution of cell replication and the location of restored clones were incompatible with an origin wholly within that small pool. Rather, the principal source of gland reconstitution in vivo, including new KRT5$^+$ basal cells, was the dominant population of differentiated luminal cells (*14*). These observations parallel those in the liver, where recovery of organ mass after tissue injury occurs by renewed proliferation of mature resting hepatocytes (*5*), abetted by expansion of bile duct cells that transdifferentiate into hepatocytes (*6*). Cell plasticity is thus widespread, whether tissues have or lack native stem cell compartments.

Reverse differentiation in the intestine, airways, and prostate gland was generally observed after near-total elimination of resident stem or luminal cells, an extreme and artificial condition. However, several observations suggest that this dedifferentiation reflects a physiologic process designed to maintain a proper cell census. Contact with a single KRT5$^+$ airway stem cell prevents secretory and club cell dedifferentiation in vitro (*12*), and tracheal submucosal glands exhibit limited stem cell activity even in the absence of injury (*13*). Live imaging of intestinal crypts reveals continuous and stochastic exit from and reentry into the ISC compartment (*15*), implying that barriers for differentiation or dedifferentiation are inherently low. However, the primary purpose of dedifferentiating airway, intestinal, liver, and prostate cells is not to enable tissue recovery. Therefore, they should be regarded as facultative stem cells; that is, they have other physiologic functions and realize a latent stem cell capacity only under duress.

This distinction from "reserve" stem cells is not merely semantic. Emphasis in regenerative therapy research belongs on any cell population with restorative potential; in vivo findings now direct attention away from putative reserve cells and toward dedifferentiation as a common means for tissue recovery. The absence of dedicated reserves and the inherent cellular ability to toggle between stem and differentiated states also inform cancer biology. Because mutations realize oncogenic potential only in long-lived cells, both frontline and reserve stem cells represent candidate sources of cancer, in contrast to differentiated cells, which are generally short-lived. However, oncogenic mutations that arise in differentiated cells could become fixed upon dedifferentiation, thus enabling tumor development.

Notably, stem cell properties and interconversion with their progeny are not stereotypic. ISCs divide daily into two identical daughters, whereas hematopoietic stem cell replication is infrequent and asymmetric. Severe loss of blood stem cells does not elicit substantial dedifferentiation and is rescued only by adoptive stem cell transfer. Immature secretory precursors dedifferentiate more readily than terminally mature airway cells (*12*), whereas fully differentiated cells fuel liver and prostate regeneration. Cell plasticity in each case is determined by local signals. Unknown factors from KRT5$^+$ tracheal stem cells, for example, suppress secretory cell dedifferentiation (*12*), and specific factors secreted from the prostate mesenchyme stimulate luminal cell dedifferentiation (*14*). The intestinal mesenchyme probably senses ISC attrition to trigger tissue recovery, but the spatial and molecular determinants remain unknown. Outstanding challenges are to identify the signaling pathways that ensure a stable cell census and to harness diverse regenerative responses to ameliorate acute tissue injuries or prevent organ failure. Knowing the cellular basis for stem cell recovery in different contexts brings us closer to those goals. ■

REFERENCES AND NOTES

1. H. Tian *et al.*, *Nature* **478**, 255 (2011).
2. J. H. van Es *et al.*, *Nat. Cell Biol.* **14**, 1099 (2012).
3. N. Barker *et al.*, *Nature* **449**, 1003 (2007).
4. J. R. Rock *et al.*, *Proc. Natl. Acad. Sci. U.S.A.* **106**, 12771 (2009).
5. B. D. Tarlow *et al.*, *Cell Stem Cell* **15**, 605 (2014).
6. A. Raven *et al.*, *Nature* **547**, 350 (2017).
7. E. Sangiorgi, M. R. Capecchi, *Nat. Genet.* **40**, 915 (2008).
8. A. Ayyaz *et al.*, *Nature* **569**, 121 (2019).
9. S. J. Buczacki *et al.*, *Nature* **495**, 65 (2013).
10. K. S. Yan *et al.*, *Cell Stem Cell* **21**, 78 (2017).
11. K. Murata *et al.*, *Cell Stem Cell* **26**, 377 (2020).
12. P. R. Tata *et al.*, *Nature* **503**, 218 (2013).
13. T. J. Lynch *et al.*, *Cell Stem Cell* **22**, 653 (2018).
14. W. R. Karthaus *et al.*, *Science* **368**, 497 (2020).
15. L. Ritsma *et al.*, *Nature* **507**, 362 (2014).

10.1126/science.abb6848

CELL THERAPY

Emerging cell therapy for biliary diseases

Gallbladder organoids repair bile ducts in mouse and human liver

By **Simone N. T. Kurial**[1] *and* **Holger Willenbring**[1,2,3]

Cell therapy has potential as an alternative to liver transplantation. The liver cell therapy field has been focused on diseases affecting hepatocytes, which provide most of the liver's metabolic and synthetic functions (*1*). Less attention has been paid to biliary diseases affecting cholangiocytes, the cells that form the biliary tree. This system consists of intrahepatic and extrahepatic bile ducts and the gallbladder, and drains bile into the intestine. Because bile is toxic when it accumulates in the liver, biliary diseases can lead to liver fibrosis and failure, necessitating liver transplantation (*2*). Despite progress in bioengineering bile ducts for treating extrahepatic biliary diseases (*3*), few studies have explored cell therapy for diseases affecting intrahepatic bile ducts. Still, evidence is accumulating that supports the feasibility of cell therapy for intrahepatic biliary diseases, and on page 839 of this issue, Sampaziotis *et al.* (*4*) provide the most definitive example to date.

Cell therapy for intrahepatic biliary diseases requires repopulating large stretches of injured bile ducts or forming new ones. As in any emerging field, distinct approaches have been taken to meet these requirements, varying in the source of transplanted cells, recipient characteristics, and route of cell delivery (see the table). Most studies have used primary cells, including expandable cells isolated from the extrahepatic part of the human biliary tree by two-dimensional or organoid culture (*4, 5*). In culture, these cells lose regional specification but maintain core cholangiocyte identity; after engraftment in the liver, they acquire intrahepatic cholangiocyte

[1]Eli and Edythe Broad Center of Regeneration Medicine and Stem Cell Research, University of California San Francisco, San Francisco, CA, USA. [2]Department of Surgery, Division of Transplant Surgery, University of California San Francisco, San Francisco, CA, USA. [3]Liver Center, University of California San Francisco, San Francisco, CA, USA. Email: holger.willenbring@ucsf.edu

differentiation, reflecting cell plasticity (*4*) or, as an alternative explanation, stem or progenitor (stem/progenitor) cell identity (*5*). Fetal liver stem/progenitor cells isolated from rats also give rise to intrahepatic cholangiocytes upon transplantation, which is consistent with their role as precursors of cholangiocytes and hepatocytes in development (*6*). In light of this lineage relationship, it is perhaps not surprising that transplanted hepatocytes can generate intrahepatic cholangiocytes by transdifferentiation, a plasticity that is conserved between mice (*7*), rats (*8*), and humans (*9*).

Evidence also supports the potential of reprogrammed cells for therapy of intrahepatic biliary diseases, including cells functioning as bipotential liver stem/progenitor cells. Such cells can be generated from mouse embryonic fibroblasts (MEFs) and human umbilical vein or peripheral blood–derived endothelial cells by the overexpression of hepatic transcription factors (*10, 11*) or from rat hepatocytes by treatment with small molecules that target signaling pathways involved in cell differentiation and proliferation (*12*). In addition, cholangiocytes generated by directed differentiation of human induced pluripotent stem cells (iPSCs) have been shown to engraft in intrahepatic bile ducts (*13*).

These diverse cell types have been tested by transplantation into equally diverse recipients, ranging from uninjured mice to mice lacking all intrahepatic bile ducts. The animal models of human biliary diseases used to develop cell therapies can be distinguished as two groups on the basis of underlying mechanism and severity: Models of intrahepatic cholangiocyte deficiency—absence caused by genetic mutation as in human Alagille syndrome (ALGS) (*7*) or loss caused by the biliary toxin 4,4′-methylenedianiline (MDA) (*4*)—have a very acute and severe phenotype. In addition, protocols are available to model cholestasis, a more chronic condition that leads to expansion of the intrahepatic biliary tree—referred to as ductular reaction in humans (*2*)—and liver fibrosis. For this, bile drainage is blocked by extrahepatic bile duct ligation (BDL) (*6*) or formation of porphyrin crystals in intrahepatic bile ducts triggered by the chemical 3,5-diethoxycarbonyl-1,4-dihydrocollidine (DDC) (*10*).

In cholangiocyte-deficiency mouse models, extensive contribution of transplanted hepatocytes or gallbladder organoids to intrahepatic bile ducts was observed, which highlighted postengraftment proliferation as a factor determining the efficiency of cell therapy (*4, 7*). Moreover, generation of intrahepatic cholangiocytes by specification of gallbladder organoids and, even more so, transdifferentiation of hepatocytes revealed the instructive power of probiliary signaling in severe biliary diseases. In addition, transplanted hepatocytes formed intrahepatic bile ducts in the mouse model of ALGS without preexisting bile ducts serving as scaffolds, which illustrated the remodeling capacity of the liver (*7*). Survival of mice treated with MDA and transplanted with gallbladder organoids, but not mice transplanted with mesenchymal stem cells or freshly isolated gallbladder cholangiocytes, established therapeutic efficacy of the repopulated bile ducts (*4*).

For cell delivery to the liver, most studies have relied on injection into the spleen, which leads to distribution through the portal vein and is therefore equivalent to direct portal vein injection, the most commonly used route in clinical trials of hepatocyte transplantation (*1*). In addition, retrograde injection into the biliary tree through the gallbladder or an extrahepatic bile duct, a procedure resembling clinically practiced endoscopic retrograde cholangiopancreatography, was effective in engrafting iPSC-derived cholangiocytes and gallbladder organoids in intrahepatic bile ducts (*4, 13*).

The collective evidence provided by these studies supports the feasibility of cell therapy for intrahepatic biliary diseases. Clearly, more research is needed to address knowledge gaps related to engraftment efficiency and therapeutic efficacy of the tested cell types, as well as their safety. However, it is encouraging that, in the setting of biliary disease, injured liver provides a conducive environment for cell therapy by promoting cholangiocyte differentiation, proliferation, and tubulogenesis. Moreover, most of the tested cell types meet important criteria for clinical translation: Gallbladder organoids and reprogrammed cells can be efficiently expanded in vitro and facilitate autologous transplantation that bypasses complications of immune suppression. Hepatocytes can be expanded in animal models (*14*), and allogeneic cells can be protected from immune rejection by gene editing (*15*). In addition, development of biliary cell therapy can build on established routes of cell delivery. In the most recent advance, Sampaziotis *et al*. show that gallbladder organoids engraft in human livers maintained by normothermic machine perfusion and provide cholangiocyte function (*4*), which brings cell therapy for intrahepatic biliary diseases a step closer to clinical translation. ■

Principal approaches

Cell therapy for intrahepatic biliary diseases comprises three different routes.

CELLS	RECIPIENTS	REPOPULATION LOCATION AND EXTENT
Intrahepatic route		
Human extrahepatic biliary tree stem/progenitor cells	Uninjured	Various size ducts; 12.7 ± 5.5% (0.5 M, 30 d) (*5*)
Intraductal route		
Human gallbladder organoids	MDA	Various size ducts; 25–55% (90 d) (*4*)
	NMP	Terminal duct branches; 40–85%* (10 M, 100 h) (*4*)
Human iPSC-derived cholangiocytes	Uninjured	Various size ducts (*13*)
Intrasplenic route		
Mouse hepatocytes	ALGS	Various size ducts; 78.3 ± 13.9% (1 M, 121 d) (*7*)
Rat fetal liver stem/progenitor cells	BDL	Smaller ducts, ductular reaction (*6*)
Rat hepatocyte-derived induced liver stem/progenitor cells	Hepatocyte injury	Various size ducts (*12*)
MEF-derived induced liver stem/progenitor cells	DDC	Large ducts only; 1.44 ± 0.41% (1 M, 3 w) (*10*)

Intrahepatic route is based on direct injection into the liver tissue. Recipients are mice except NMP (human liver) and BDL (rats). Information on repopulation is given where available, including number of transplanted cells and time of analysis (M, million; h, hours; d, days; w, weeks). MDA, 4,4′-methylenedianiline; NMP, normothermic machine perfusion; ALGS, Alagille syndrome; BDL, bile duct ligation; MEF, mouse embryonic fibroblast; DDC, 3,5-diethoxycarbonyl-1,4-dihydrocollidine.
*In region of localized delivery.

REFERENCES AND NOTES

1. M. P. Nguyen *et al*., *Expert Rev. Gastroenterol. Hepatol*. **14**, 185 (2020).
2. J. M. Banales *et al*., *Nat. Rev. Gastroenterol. Hepatol*. **16**, 269 (2019).
3. Z. Wang, J. Faria, L. Penning, R. Masereeuw, B. Spee, *Tissue Eng. Part C Methods* (2020). 10.1089/ten.TEC.2020.0283
4. F. Sampaziotis *et al*., *Science* **371**, 839 (2021).
5. V. Cardinale *et al*., *Hepatology* **54**, 2159 (2011).
6. M. I. Yovchev, E. J. Lee, W. Rodriguez-Silva, J. Locker, M. Oertel, *Hepatol. Commun*. **3**, 1137 (2019).
7. J. R. Schaub *et al*., *Nature* **557**, 247 (2018).
8. G. K. Michalopoulos, L. Barua, W. C. Bowen, *Hepatology* **41**, 535 (2005).
9. B. D. Tarlow *et al*., *Cell Stem Cell* **15**, 605 (2014).
10. B. Yu *et al*., *Cell Stem Cell* **13**, 328 (2013).
11. H. Inada *et al*., *Nat. Commun*. **11**, 5292 (2020).
12. T. Katsuda *et al*., *Cell Stem Cell* **20**, 41 (2017).
13. T. M. De Assuncao *et al*., *Lab. Invest*. **95**, 684 (2015).
14. H. Azuma *et al*., *Nat. Biotechnol*. **25**, 903 (2007).
15. T. Deuse *et al*., *Nat. Biotechnol*. **37**, 252 (2019).

ACKNOWLEDGMENTS

The authors are funded by the National Institutes of Health (F31 DK126419, R01 DK107553, R01 AA026578, UH3 DK120004, and P30 DK026743). H.W. is a cofounder and advisory board member of Ambys Medicines.

10.1126/science.abg3179

BOOKS *et al.*

SCIENCE LIVES

Portrait of a groundbreaking astronomer

A new biography paints a vivid picture of the life of dark matter pioneer Vera Rubin

Fourteen-year-old Rubin makes adjustments to her homemade telescope.

By **Joanna Behrman**

Vera Rubin would not have called herself the discoverer of dark matter. In fact, she once tried to prevent a press release from even including the word "discovery," instead suggesting that the National Science Foundation's press team write that her observations "provided convincing evidence." It is, after all, rare that any topic has only a single devoted researcher and unlikely that a scientific discovery of such magnitude would be made in the absence of a support network of contributors, despite what many biographies would have readers believe.

Unlike such tomes, Jacqueline and Simon Mitton's *Vera Rubin* offers a thoughtful and nuanced chronicle of the famed astronomer's life that neither overinflates nor diminishes the importance of her contributions. The Mittons' book is the first full-length biography of Rubin, whose work on the rotational velocity of galaxies went a long way toward establishing the existence of dark matter.

To achieve their remarkable portrait, the authors draw on Rubin's extensive correspondence, which she saved throughout her life; on marginalia scribbled on research papers; on interviews; and on other archival documents, all of which have only recently become available to researchers. The Mittons also use their own expertise in astronomy to explain Rubin's findings and their significance.

Rubin (née Cooper) was born in Philadelphia, Pennsylvania, on 23 July 1928 to Pete and Rose Cooper, both immigrants from Eastern Europe who met while employed at the Bell Telephone Company. When the family moved to Washington, D.C., in 1938, Rubin slept in a bed by a window, which sparked a lifelong interest in the night sky. In her free time, she built a telescope and photographed star trails, but her experience with formal education was less than rosy. Rubin enjoyed her math and English classes—every essay she wrote for the latter was related to astronomy—but her high school physics teacher ignored the female students and lauded male scientists, while implying that the achievements of female scientists, such as Marie Curie, relied more on diligence than on brilliance. Rubin later described the physics labs as "a nightmare."

Rubin's passion for astronomy inspired her to attend Vassar College, which had a small observatory and a tradition of training female astronomers. (Maria Mitchell had been a professor there.) She largely avoided physics classes, focusing instead on astronomy. During the summers, she returned to D.C., where she worked at the U.S. Naval Research Laboratory.

Vera married Bob Rubin shortly after graduation, rejecting an offer to attend graduate school at Harvard in favor of pursuing a master's degree at Cornell University, where Bob was finishing his Ph.D. in physics. She would complete her own doctorate at Georgetown University in 1954. The authors emphasize the personal support network provided by Bob and by Vera's parents that made it possible for her to continue her work in astronomy as the young family grew to include four children.

Mitton and Mitton outline the extensive professional network within which Rubin worked, describing her relationships with various mentors, with co-workers at the Carnegie Institution, and with the larger astronomy community. In doing so, they frame her story within a longer history of humanity's study of galaxies, offering readers a fresh perspective on the history of astronomy in the 20th century. Readers learn, for example, how advances in imaging technologies affected deep field astronomy.

Rubin was a woman in a male-dominated field, and her story is replete with instances of subtle and overt sexism: A Cornell professor burdened her with his grunt work, Princeton University refused her graduate application, and major observatories lacked quarters and bathroom facilities for women. As her status within astronomy grew, so did her efforts to change the field.

Vera Rubin: A Life
Jacqueline Mitton and Simon Mitton
Harvard University Press, 2021. 320 pp.

Whether admonishing societies with all-male conference lineups or advocating for the use of gender-neutral language, many of the issues Rubin struggled against persist, but her perseverance will likely resonate with many readers. "As long as the problems of 'Women in…' are women's problems," she wrote in 1996 to the National Academy of Sciences, "I doubt that they will improve. It has to be everyone's problem."

Rubin, who died on 25 December 2016, "once claimed that she neither knew nor cared what role history would assign to her… If other astronomers found her observations 'irresistible,' it was the highest compliment she could wish for," conclude the Mittons. "And they certainly did." ■

The reviewer is at the Center for History of Physics, American Institute of Physics, College Park, MD 20740, USA. Email: jbehrman@aip.org

10.1126/science.abg1818

PHOTO: COURTESY CARNEGIE INSTITUTION FOR SCIENCE DEPARTMENT OF TERRESTRIAL MAGNETISM ARCHIVES

MEDICAL ETHICS

Probing the genetic future of humanity

A bioethicist breaks down the first human germline genome editing experiment

By **Michael A. Goldman**

On 25 November 2018, He Jiankui, a biophysicist at Southern University of Science and Technology in Shenzhen, China, announced that his laboratory had pulled off a previously unthinkable achievement: the successful modification of the germline genome of two living humans. Two children, female fraternal twins known by the pseudonyms Lulu and Nana, had been born with altered copies of the C-C motif chemokine receptor 5 (*CCR5*) gene, having been subjected to a CRISPR-Cas9–based genome editing protocol. The purported purpose of this feat was to protect the children from contracting human immunodeficiency virus (HIV). Packed with facts and analysis, Henry Greely's *CRISPR People* examines what He did, explains why Greely believes it was wrong, describes the world's reaction, and details what we can and should do about work like this in the future.

Greely draws a parallel between the birth of Lulu and Nana and the 1996 birth of Dolly, the cloned sheep, noting that in both instances, the respective breakthroughs underlying each achievement were unimaginable right up until they were attained. Before Dolly, we could clone frogs with some success, but mammalian biparental reproduction just could not be replaced. And then, suddenly, it had been done.

The scientific feasibility of He's experiment was not necessarily in question. We had known for some time that human eggs could undergo in vitro fertilization, for example, and that the resulting embryos could be genetically manipulated. What we did not know was that someone would ignore the consensus of every major scientific and medical organization and forge ahead with an experiment in humans. And then, someone did just that.

"I stand by the comments I made to the press just after the news broke [of the twins' birth]," writes Greely. "[T]he experiment was 'criminally reckless' as well as 'grossly premature, and deeply unethical.'" Citing the Nuremberg Code and the Helsinki Declaration, he argues that the risk-benefit ratio for such an experiment is simply too high.

CCR5 Δ32, the naturally occurring *CCR5* mutation that He sought to replicate in his experiment, is a 32–base pair deletion in the coding sequence of the gene, an alteration that produces a nonfunctional protein. Such mutations afford significant, although incomplete, protection against HIV infection in individuals with two copies of the deletion. But He's experiment did not replicate the natural variant: One twin had two different mutations, and the other had one normal copy of CCR5 and one copy containing a different mutation.

He Jiankui went public with his startling claim in November 2018.

Even had He succeeded, Greely notes that HIV transmission can occur via non-CCR5-mediated pathways, that there are potential side effects of the CRISPR editing process, and that some benefits are conferred by wild-type CCR5. Furthermore, the CCR5 Δ32 mutation may increase one's risk of death from influenza (*1*), which is a more likely cause of death in China than HIV infection.

"Evolution has been working toward optimizing the human genome for 3.85 billion years. Do we really think that some small group of human genome tinkerers could do better without all sorts of unintended consequences?" summarized Francis Collins in 2015 (*2*). Greely appears to feel similarly, although he does not go so far as supporting a total ban on such technologies. "I think this argument cannot be based directly on the consequences of human germline genome editing but instead must be founded on the belief that such a procedure is inherently wrong," he writes. "I accept that people may hold such a position, but I do not see how they can hold it consistently with acceptance of a great deal of modern life, modern medicine, and modern reproduction."

Trained as an attorney, Greely is among today's best thinkers in the field of bioethics. His writing is straightforward, conversational, and technically accurate. What it does not, and perhaps cannot, provide is a simple answer to the complex questions posed by human genome editing. Indeed, his penchant for considering every argument and counterargument precludes a simple conclusion or a straightforward way of assessing similar ethical dilemmas that we will no doubt be faced with in the future. Meanwhile, readers seeking a broader view of the genome editing landscape may wish to consult Kevin Davies's *Editing Humanity: The CRISPR Revolution and the New Era of Genome Editing* (*3*). Nevertheless, with *CRISPR People*, Greely provides an exquisite view of the wide-ranging issues at play in this particular case. ■

CRISPR People: The Science and Ethics of Editing Humans
Henry T. Greely
MIT Press, 2021. 400 pp.

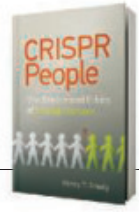

The reviewer is at the Department of Biology, San Francisco State University, San Francisco, CA 94132, USA. Email: goldman@sfsu.edu

PHOTO: KIN CHEUNG/AP IMAGES

REFERENCES AND NOTES

1. A. Falcon *et al.*, *J. Gen. Virol.* **96**, 2074 (2015).
2. P. Skerrett, "Experts debate: Are we playing with fire when we edit human genes?," STAT News, 17 November 2015; www.statnews.com/2015/11/17/gene-editing-embryo-crispr/.
3. K. Davies, *Editing Humanity: The CRISPR Revolution and the New Era of Genome Editing* (Pegasus, 2020).

10.1126/science.abg0509

LETTERS

China's declining oyster reefs provide valuable ecosystem services.

Edited by **Jennifer Sills**

Protect and regulate China's oyster resources

China has at least 30 oyster species (*1*), all of which provide valuable ecosystem services. Oysters' filter feeding habit reduces suspended particles and nutrients. One hectare of oyster reef can clean a volume of water equivalent to nearly 15 Olympic swimming pools daily (*2*). Oysters' excrement can stimulate denitrification by removing nitrogenous organic matter, helping to mitigate eutrophication (*3*). Natural oyster reefs provide habitat for many species, enhancing biodiversity and increasing fisheries. Oyster reefs can reduce impacts of waves caused by hurricanes and typhoons, stabilizing shorelines (*4*). Despite their ecological importance, 85% of oyster reefs globally have been degraded since the 19th century by overharvesting, coastal development, water pollution, and disease (*4*). China's oyster reefs, especially those in Tianjin and Jiangsu (*5*, *6*), have been seriously damaged during recent decades. Urgent action by Chinese authorities is required to protect these crucial species.

Extensive degradation of natural oyster reefs has been accompanied by rapid development of oyster aquaculture, driven by high profitability (*7*). China's oyster farming accounts for more than 80% of global production and covers more than 1400 km^2 (*8*). However, fewer than 10% of oyster farmers have aquaculture licenses or permits (*9*). Poor water-quality management within large aquaculture developments contaminates oysters with heavy metals, organohalogens, and viruses (*10*). Very high concentrations of cadmium, lead, inorganic arsenic, and polychlorinated biphenyl now occur in oysters in southern China, posing carcinogenic risks (*10*).

China should address the threats to natural oyster reefs by providing stronger protection, ceasing inappropriate coastal development, and reducing water contamination. Effective regulation of aquaculture must include exclusion of polluted waters and stringent depuration procedures. The Restorative Aquaculture Opportunity Index should be used to identify areas for oyster aquaculture (*11*). Finally, China can help protect oyster reefs as well as other kinds of aquatic life by promoting sustainable prawn-fish-shellfish-algae polyculture instead of single-species aquaculture (*12*).

Hong Yang[1,2]*, Mingguo Ma[1], Julian R. Thompson[3], Roger J. Flower[3]
[1]Chongqing Jinfo Mountain Karst Ecosystem National Observation and Research Station, School of Geographical Sciences, Southwest University, Chongqing 400715, China. [2]Department of Geography and Environmental Science, University of Reading, Reading RG6 6AB, UK. [3]Department of Geography, University College London, London, WC1E 6BT, UK.
*Corresponding author.
Email: hongyanghy@gmail.com

REFERENCES AND NOTES

1. X. M. Guo, C. Li, H. Y. Wang, Z. Xu, *J. Shellfish Res.* **37**, 755 (2018).
2. L. D. Coen *et al.*, *Mar. Ecol. Prog. Ser.* **341**, 303 (2007).
3. M. L. Kellogg, M. J. Brush, L. Kellogg, M. Brush, "An updated model for estimating the TMDL-related benefits of oyster reef restoration" (Virginia Institute of Marine Science, 2018).
4. M. W. Beck *et al.*, *Bioscience* **61**, 107 (2011).
5. W. Quan *et al.*, *Acta Ecol. Sin.* **36**, 7749 (2016).
6. W. Sun *et al.*, *Hebei Fishery* **249**, 23 (2014).
7. J. A. Fitzsimons *et al.*, *Conserv. Sci. Pract.* **2**, 10.1111/csp2.198 (2020).
8. Fishery Bureau of the Ministry of Agriculture of the People's Republic of China, "China fishery statistical yearbook 2019" (China Agriculture Press, 2020) [in Chinese].
9. H. Li *et al.*, *Mar. Sci.* **41**, 125 (2017).
10. H. Liu *et al.*, *J. Shanghai Ocean Univ.* **26**, 921 (2017).
11. S. J. Theuerkauf *et al.*, *PLOS One* **14**, 10.1371/journal.pone.0222282 (2019).
12. D. C. Little *et al.* *Aquaculture* **493**, 338 (2018).

10.1126/science.abg8656

CropLife International shares FAO's vision

In their Letter "Stay true to integrated pest management" (8 January 2021, p. 133), K. Wyckhuys *et al.* point to the essential role of checks and balances in the context of CropLife International's recently agreed partnership with the UN's Food and Agriculture Organization (FAO). However, we disagree with their assertion that the FAO and CropLife International have contrasting visions of integrated pest management (IPM). CropLife International fully supports the FAO definition of IPM,

PHOTO: CHUNYIP WONG/GETTY IMAGES

which is a fundamental element of the International Code of Conduct on Pesticide Management (*1*). The IPM objective is "careful consideration of all available pest control techniques and subsequent integration of appropriate measures that discourage the development of pest populations and keep pesticides and other interventions to levels that are economically justified and reduce or minimize risks to human and animal health and/or the environment." [(*1*), p. 4] Supporting FAO's Code of Conduct on Pesticide Management is a condition of membership for CropLife International, and IPM is a core stewardship activity promoted by CropLife International to farmers globally.

FAO has had great success in reducing pesticide use in Bangladesh, India, and Vietnam, as cited by Wyckhuys *et al.* (*2*), but these are not the only countries where improvements have been made. A recent study conducted by Phillips McDougal shows that the average application rates per hectare of modern pesticides are down by 95% since 1960, and there has been a substantial reduction in their acute toxicity (*3*). This is in large part due to the industry's development of more effective crop protection products and technologies (*4*) in combination with farmers' efforts to support optimized pesticide use in the framework of IPM. CropLife International also forms long-term partnerships with organizations such as GIZ (*5*), who value our expertise in training farmers on IPM and the responsible use of pesticides.

We recognize the challenges that humankind faces in making agriculture more sustainable without compromising yields. Digital and precision farming are already contributing to further optimization, and their deployment will need to be accelerated to achieve the sustainable intensification that we need to avoid further agricultural encroachment of habitats and biodiversity loss (*6*). Innovation, shared knowledge, and partnership will all be invaluable to improving the sustainability of the agri-food system. This is the rationale for our collaboration with FAO and indeed all of our partnerships and alliances.

Giulia Di Tommaso
President and CEO, CropLife International, Brussels 1050, Belgium.
Email: Giulia.DiTommaso@CropLife.org

REFERENCES AND NOTES

1. FAO, World Health Organization, *The International Code of Conduct on Pesticide Management* (2014); www.fao.org/3/I3604E/i3604e.pdf.
2. H. van den Berg, J. Jiggins, *World Dev.* **35**, 4 (2007).
3. Phillips McDougall, "Evolution of the crop protection industry since 1960" (2019).
4. E. Radcliffe, W. Hutchinson, R. Cancelado, *Integrated Pest Management: Concepts, Tactics, Strategies and Case Studies* (Cambridge University Press, 2009).
5. "Better Rice Initiative Asia—Promotion of Integrated Pest Management in Thailand" (GIZ, 2018).
6. M. Bacco, P. Barsocchi, E. Ferro, A. Gotta, R. Massimiliano, *Array* **3–4**, 100009 (2019).

10.1126/science.abg8056

Lack of knowledge threatens beaked whales

Beaked whales represent about one quarter of known extant cetacean species, but they are the least understood among large mammals. All known beaked whale species are listed on either Appendix I or II of the Convention on International Trade in Endangered Species of Wild Fauna and Flora (*1*). The recent discovery of a possible new species of beaked whale in Mexico (*2*) and the live sighting of a mysterious beaked whale identified as either *Mesoplodon hotaula* or *Mesoplodon ginkgodens* in the South China Sea (*3*) have highlighted how little we know about these whales.

Beaked whales are widely distributed in deep and offshore waters of all oceans, from the tropics to the polar region (*4*). However, research on most of these species is limited, with knowledge based largely on the examination of a few stranded individuals. Newly described mammal species have been shown to be disproportionately threatened (*5*), reinforcing concerns that species might be vanishing before they are known to science.

Beaked whales face an increasing number of threats and are believed to be particularly vulnerable to anthropogenic noise disturbances caused by geological and seismic surveying, military sonar, and naval traffic (*6–8*). The extensive use of air guns could have a cumulative impact on them (*9*). Beaked whales are likely particularly at risk in areas where their habitat is subject to seismic survey activity (*9*). The temporal and spatial association between multiple stranded beaked whales and naval exercises was first reported in the Mediterranean Sea in the early 1960s (*10*, *11*). The link between mid-frequency active sonar and stranded whales was demonstrated in the Bahamas in 2000 (*7*). Over the past 4 decades, many hundreds of beaked whales worldwide were stranded en masse (*10*). However, the lack of baseline data on beaked whale distribution, population size and structure, and life history impedes comprehensive assessment of potential population level impacts (*12*).

To properly protect the beaked whales, we must know more about them. Policymakers, conservationists, and scientists should work to facilitate research that will increase our knowledge about these elusive species. Financial support and personnel training will allow more data collection from poorly surveyed parts of the oceans, informing conservation action going forward.

Songhai Li[1,2,3,4]* and Massimiliano Rosso[5]
[1]Marine Mammal and Marine Bioacoustics Laboratory, Institute of Deep-Sea Science and Engineering, Chinese Academy of Sciences, Sanya, 572000, China. [2]Function Laboratory for Marine Fisheries Science and Food Production Processes, Qingdao National Laboratory for Marine Science and Technology, Qingdao, 266237, China. [3]Tropical Marine Science Institute, National University of Singapore, 119227, Singapore. [4]Center for Ocean Mega-Science, Chinese Academy of Sciences, Qingdao, 266071, China. [5]CIMA Research Foundation, Savona, 17100, Italy.
*Corresponding author. Email: lish@idsse.ac.cn

REFERENCES AND NOTES

1. Convention on International Trade in Endangered Species of Wild Fauna and Flora, "Appendices I, II, and III" (2020); https://cites.org/eng/app/appendices.php.
2. "Sea Shepherd research mission discovers possible new species of whale in Mexico" (Sea Shepherd, 2020); https://seashepherd.org/2020/12/08/sea-shepherd-research-mission-discovers-possible-new-species-of-whale-in-mexico/.
3. M. Rosso *et al.*, *Integrat. Zool.* 10.1111/1749-4877.12507 (2020).
4. C. D. MacLeod *et al.*, *J. Cetacean Res. Manag.* **7**, 271 (2006).
5. J. Schipper *et al.*, Science **322**, 225 (2008).
6. A. Frantzis, *Nature* **392**, 29 (1998).
7. T. M. Cox *et al.*, *J. Cetacean Res. Manag.* **7**, 117 (2006).
8. N. Aguilar Soto *et al.*, *Mar. Mamm. Sci.* **22**, 690 (2006).
9. M. Podestà *et al.*, *Adv. Mar. Biol.* **75**, 103 (2016).
10. M. Podestà *et al.*, *J. Cetacean Res. Manag.* **7**, 251 (2006).
11. A. Cañadas, G. Notarbartolo di Sciara, "*Ziphius cavirostris* (Mediterranean subpopulation)" (The IUCN Red List of Threatened Species, 2018).
12. S. K. Hooker *et al.*, *Front. Mar. Sci.* **5**, 514 (2019).

COMPETING INTERESTS

S.L. receives funding from the National Natural Science Foundation of China (41422604), "One Belt and One Road" Science and Technology Cooperation Special Program of the International Partnership Program of the Chinese Academy of Sciences (183446KYSB20200016), and the Key Deployment Project of Center for Ocean Mega-Science of the Chinese Academy of Sciences (COMS2020Q15).

10.1126/science.abg8922

ERRATA

Erratum for the Report "CRISPR-Cas12a target binding unleashes indiscriminate single-stranded DNase activity" by J. S. Chen *et al.,* *Science* **371**, eabh0317 (2021). Published online 19 February 2021; 10.1126/science.abh0317

Erratum for the Research Article "Recent global decline of CO_2 fertilization effects on vegetation photosynthesis" by S. Wang *et al.,* *Science* **371**, eabg8637 (2021). Published online 5 February 2021; 10.1126/science.abg8637

Erratum for the Report "Circadian rhythms in the absence of the clock gene *Bmal1*" by S. Ray *et al.,* *Science* **371**, eabg5409 (2021). Published online 29 January 2021; 10.1126/science.abg5409

NOMIS & Science
YOUNG EXPLORER AWARD

Research at the intersection of the social and life sciences

Unconventional. Interdisciplinary. Bold.

The newly launched **NOMIS & *Science* Young Explorer Award** recognizes bold, early-career researchers with an M.D., Ph.D., or M.D./Ph.D. who ask fundamental questions at the intersection of the social and life sciences. It is awarded to scientists who conduct research with an enthusiasm that catalyzes cross-disciplinary collaboration and who take risks to creatively address relevant and exciting questions.

Award winners will receive a cash prize of up to $15,000, and their essay submissions will be published in *Science*. They will also be invited to share their ideas with leading scientists in their respective fields at an award ceremony and to present their research to the NOMIS Board of Directors for potential future funding.

Apply by May 15, 2021
at www.sciencemag.org/nomis

Science
AAAS

NOMIS
FOUNDATION
Creating the Spark

RESEARCH

IN *SCIENCE* JOURNALS

Edited by **Michael Funk**

CONSERVATION

No waters left untouched

We are increasingly aware of human impacts on biodiversity across our planet, especially in terrestrial and marine systems. We know less about fresh waters, including large rivers. Su *et al*. looked across such systems globally, focusing on several key measures of fish biodiversity. They found that half of all river systems have been heavily affected by human activities, with only very large tropical river basins receiving the lowest levels of change. Fragmentation and non-native species have also led to the homogenization of rivers, with many now containing similar species and fewer specialized lineages. —SNV *Science*, this issue p. 835

Fish such as brook trout have contributed to phylogenetic dissimilarity in rivers in which they are introduced as exotic species.

PHOTO: OCEANPHOTO/ MINDEN PICTURES

SURFACE CHEMISTRY

Joint strategy for surface chemistry

Recent advances in the development of tip-based microscopy have led to angstrom-scale spatial resolution, but no technique provides univocal characterization of the structural and chemical heterogeneities of surface species. Using a model system of pentacene derivatives on the Ag(110) surface, Xu *et al.* show that the combination of scanning tunneling microscopy, atomic force microscopy, and tip-enhanced Raman scattering provides the electronic, structural, and chemical information sufficiently correlated for an unambiguous characterization of the different—but structurally similar—chemical species and their interaction with the metal surface with single-bond resolution. The proposed multitechnique approach could find wide application in fundamental studies of heterogeneous catalysis and surface chemistry in general. —YS

Science, this issue p. 818

SOFT ROBOTS

Walk this way

Pneumatic soft robots generally require an assortment of electronically controlled, bulky components such as pumps and valves to achieve legged locomotion. Drotman *et al.* simplified the design of walking soft robots by using fluidic circuits, rather than electronic circuits, to achieve locomotion. Specifically, a soft ring oscillator produces movement by generating rhythmic motions analogous to biological central pattern generator neural circuits found in nature. —MML

Sci. Robot. **6**, eaay2627 (2021).

THERMOELECTRICS

Distorted thermal properties

Thermoelectric devices can convert waste heat into electricity, providing one path for improving energy efficiency. Jiang *et al.* leveraged entropy engineering to synthesize a single-phase high-entropy alloy with attractive thermoelectric properties. By increasing the number of elements in the alloy, the resulting disorder helps to stabilize against breakdown into multiple phases. The disordered and distorted crystal lattice suppresses thermal transport while maintaining the electrical properties, which boosts the heat-conversion efficiency of the material. —BG

Science, this issue p. 830

CORONAVIRUS

Targeting sarbecoviruses

As we continue to battle the COVID-19 pandemic, we must confront the possibility of new pathogenic coronaviruses emerging in humans in the future. With this in mind, Rappazzo *et al.* isolated antibodies from a survivor of the 2003 severe acute respiratory syndrome coronavirus (SARS-CoV), used yeast display libraries to introduce diversity into these

antibodies, and then screened for binding to SARS-CoV-2. One of the affinity-matured progeny strongly neutralized SARS-CoV-2, SARS-CoV, and two SARS-related viruses from bats. In addition, this antibody bound to the receptor-binding domains from a panel of sarbecoviruses, suggesting broader activity, and provided protection against SARS-CoV and SARS-CoV-2 in mouse models. —VV

Science, this issue p. 823

CORONAVIRUS

Mapping antibody escape in SARS-CoV-2

Several antibodies are in use or under development as therapies to treat COVID-19. As new severe acute respiratory syndrome coronavirus 2 (SARS-CoV-2) variants emerge, it is important to predict whether they will remain susceptible to antibody treatment. Starr *et al.* used a yeast library that covers all mutations to the SARS-CoV-2 receptor-binding domain that do not strongly disrupt binding to the host receptor (ACE2) and mapped how these mutations affect binding to three leading anti–SARS-CoV-2 antibodies. The maps identify mutations that escape antibody binding, including a single mutation that escapes both antibodies in the Regeneron antibody cocktail. Many of the mutations that escape single antibodies are circulating in the human population. —VV

Science, this issue p. 850

MITORIBOSOME

Making the energy makers

Within a mitochondrion, the powerhouse of eukaryotic cells, synthesis of the specialized transmembrane proteins of the electron transport chain is performed by dedicated mitoribosomes. The mechanism by which mitoribosomes couple protein synthesis with membrane insertion is poorly understood. Itoh *et al.* determined structures of the human mitoribosome during nascent chain synthesis while bound to its membrane insertase. These structures revealed a series of coordinated conformational changes within the polypeptide exit tunnel. The gating mechanism offers a fundamental molecular insight into how membrane proteins are synthesized in human mitochondria. —DJ

Science, this issue p. 846

PALEOENVIRONMENT

Reversing the field

Do terrestrial geomagnetic field reversals have an effect on Earth's climate? Cooper *et al.* created a precisely dated radiocarbon record around the time of the Laschamps geomagnetic reversal about 41,000 years ago from the rings of New Zealand swamp kauri trees. This record reveals a substantial increase in the carbon-14 content of the atmosphere culminating during the period of weakening magnetic field strength preceding the polarity switch. The authors modeled the consequences of this event and concluded that the geomagnetic field minimum caused substantial changes in atmospheric ozone concentration that drove synchronous global climate and environmental shifts. —HJS

Science, this issue p. 811

NEUROSCIENCE

No ligand needed for learning

In addition to its role in stimulating appetite, the hormone ghrelin and its receptor, GHS-R1a, are implicated in cognition. Ribeiro *et al.* found a role for ghrelin-independent GHS-R1a signaling in learning in mice. Treating mice with an inverse agonist of GHS-R1a impaired spatial and contextual memory formation. Thus, the use of ghrelin receptor–blocking therapies, which have been proposed for treating metabolic disorders, acromegaly, cancer, and alcoholism, may also have cognitive side effects. —LKF

Sci. Signal. **14**, eabb1953 (2021).

IN OTHER JOURNALS

Edited by **Caroline Ash** *and* **Jesse Smith**

BEHAVIOR

Free trade between species

The use of tokens as a bartering tool in nonhuman primate studies has taught us much about the willingness of nonhuman primates to engage in economic transactions. The question of whether it reflects a phenomenon that might emerge in natural conditions has received less attention. Long-tailed macaques (*Macaca fascicularis*) living in a Balinese temple regularly steal visitors' possessions and then barter for food with humans anxious to regain their belongings. Leca *et al.* discovered that they preferentially steal items of high value (for example, digital devices and wallets) over those with low value (for example, empty bags or hairpins) because higher-value food rewards tend to be offered for items that humans value more. The ability to identify high-value objects increases with age and experience, as does the macaques' skill as thieves. The animals in this group have been stealing and trading for more than 30 years, suggesting that the practice is culturally transmitted. —SNV

Philos. Trans. R. Soc. London Ser. B **376**, 20190677 (2021).

Macaques have learned to barter for food with humans to return stolen possessions according to how highly an object is valued.

PHOTO: DBIMAGES/ALAMY STOCK PHOTO

CATALYSIS

Cagey hydrosilylation

Platinum-catalyzed hydrosilylation is applied at a vast scale to produce carbon-silicon bonds underlying certain stretchy polymers, lubricants, adhesives, and coatings. Pan *et al.* report that surrounding the platinum with a molecular cage can boost its activity and enhance its selectivity. Specifically, they used copper ions to template assembly of hexaphenylbenzene-based panels into a porous shell and then swapped out the copper for platinum. The caged catalyst was highly selective toward unencumbered carbon sites and also proved compatible with carbonyl and epoxide functionality. —JSY

Nat. Commun. 10.1038/s41467-020-20233-w (2021).

REGENERATION

Stem cells relieve pressure

In glaucoma, intraocular pressure damages innervation from the eye, resulting in irreversible blindness. The most common form of glaucoma is primary open-angle glaucoma (POAG), characterized by deterioration of the trabecular meshwork (TM) cells that encircles the base of the cornea. When Xiong *et al.* transplanted exogenous human trabecular meshwork stem cells (TMSCs) into a POAG mouse model, aqueous humor drained normally, intraocular pressed was reduced and the function of the retinal ganglion cells was preserved. TMSC transplantation also increased TM cellularity and promoted myocilin secretion, which reduced endoplasmic reticulum stress in the cells. These signs of TM tissue repair show promise for use of stem cells in the development of clinical treatments for glaucoma. —BAP

eLife **10**, e63677 (2021).

MICROBIOLOGY

Wash in, wash out, repeat

Just as floods can temporarily displace human communities, intense rain periodically brings disturbances to aquatic habitats. To study these cycles of disturbance and recovery, Shabarova *et al.* compared physical and chemical features with microbial community dynamics in Jiřická Pond in the Czech Republic. Water inflow from extreme rain events caused a rapid disturbance, including washout of larger microorganisms, influx of nutrients, and introduction of virus-like particles. However, four well-defined phases of succession returned the pond to its original state by about 2 weeks after the disturbance. —MAF

Nat. Microbiol. 10.1038/s41564-020-00852-1 (2021).

EXOPLANETS

A six-planet system with resonant orbits

Orbital migration during planet formation can produce resonant chains of orbits that are simple multiples of each other. Studying such multiplanet systems provides information on the formation process. Leleu **et al.** used transit and radial velocity data to investigate a candidate multiple-planet system, TOI-178. They found six planets there, which had looked like three in the initial observations because some of the orbits were simple multiples of each other. Analysis of the extended dataset showed that five of the six planets are in a resonant chain. The planets are all between Earth and Neptune size and are on short orbits with high surface temperatures. —KTS

Astron. Astrophys. 10.1051/0004-6361/202039767 (2021).

STRUCTURAL VIROLOGY

A role for cholesterol in Ebola virus

The 2013–2016 Ebola epidemic in West Africa caused terrible disease and more than 10,000 deaths. The only protein on the surface of this virus is the glycoprotein (GP), which comprises the GP1 and GP2 domains. After binding to a host protein, GP1 is unclamped from GP2, and GP2 initiates membrane fusion that implicates cholesterol. Lee *et al.* show that cholesterol interacts with glycine residues in the transmembrane domain of GP2. Mutation of a key glycine reduced membrane fusion using GP2 embedded in viral membrane surrogates and reduced cell entry of virus-like particles. Such particles produced from cells treated with cholesterol-lowering statins also showed impaired cell entry. Biophysical studies suggest that cholesterol affects the structure of GP2 and that this in turn may affect the efficiency of membrane fusion. —VV

Nat. Struct. Mol. Biol. 10.1038/s41594-020-00548-4 (2021).

PARASITE GENOMES

Moving genes through parasitism

Plants that parasitize other plants include species such as mistletoe and members of the endophytic family Rafflesiaceae, which have the largest flowers of any plant but no other recognizable external structures. The impact of extreme host dependency usually results in genome streamlining. Cai *et al.* assembled the genome of the parasitic Rafflesia *Sapria himalayana*, hosts of which include members of the grape family. This parasite shows rapid genome evolution that has resulted in extensive gene loss in the chloroplast and photosynthetic machinery but retention of key genes for other organs. Unexpectedly, it has gained extensive repeat regions, resulting in a substantially larger genome than its closest free-living relatives, which may reflect horizontal gene transfer occurring during ancestral host associations. —LMZ *Curr. Biol.* 10.1016/j.cub.2020.12.045 (2021).

Flowering *Sapria himalayana*, which, despite being an endoparasite and completely dependent on its vine host, has a surprisingly large genome.

PHOTO: PHICHAKLIM1/ISTOCKPHOTO

REVIEW SUMMARY

PLANT SCIENCE

Plant evolution driven by interactions with symbiotic and pathogenic microbes

Pierre-Marc Delaux* and Sebastian Schornack*

BACKGROUND: Microbial interactions have shaped plant diversity in terrestrial ecosystems. By forming mutually beneficial symbioses, microbes helped plants colonize land more than 450 million years ago. In parallel, omnipresent pathogens led to the emergence of innovative defense strategies. The evolution of plant-microbe interactions encompasses ancient conserved gene modules, recurrent concepts, and the fast-paced emergence of lineage-specific innovations. Microbes form communities on the surface or inside plant tissues and organs, and most intimately, microbes live within single plant cells. Intracellular colonization is established and controlled in part by plant genes that underpin general cell processes and defense mechanisms. To benefit from microbes, plants also evolved genetic modules for symbiosis support. These modules have been maintained despite the risk of getting hijacked by pathogens.

ADVANCES: The hundreds of land plant and algal genomes that are now available enable genome-wide comparisons of gene families associated with plant immunity and symbiosis. Reconstruction of gene phylogenies and large-scale comparative phylogenomic approaches have revealed an ancient subset of genes co-evolving with the widespread arbuscular mycorrhiza symbiosis, the most ancient plant intracellular symbiosis, and with other types of more recently evolved intracellular symbioses in vascular and nonvascular plants. Intercellular symbiotic interactions formed with cyanobacteria or ectomycorrhizal fungi seem to repeatedly evolve through convergent, but not necessarily genetically conserved, mechanisms. Phylogenetic analyses revealed occurrence of candidate disease-resistance genes in green algae, as well as orthologs of flowering plant genes involved in symbiosis signaling and sensing microbial patterns. Yet, more research is needed to understand their functional conservation.

The extent to which conserved symbiosis genes also fulfill often opposing roles during pathogen-plant interactions is being explored through studies of pathogen infections in plants capable of supporting symbiotic relationships. The development of plant-microbe systems in genetically tractable species covering the diversity of land plant lineages—including angiosperms and bryophytes, such as the liverwort *Marchantia polymorpha*—makes it possible to test hypotheses that emerge from phylogenetic analyses, linking genetic and functional conservation across land plants. Studies in bryophytes illustrate the range of possibilities for pathogen management: ancient genes, such as membrane receptors that perceive fungus-derived chitin; pathways with bryophyte clade–specific components, such as phenylpropanoid-derived auronidin stress metabolites; and jasmonate-like hormonal signaling for immunity.

OUTLOOK: Only a few plant-microbe interactions have been studied in depth, and those in only a few land plant lineages. Future investigations of interactions occurring across the diversity of plants may unravel new types of symbiotic or pathogenic interactions. The occurrence of microbe-sensing genes in streptophyte algae, harboring the closest algal relative to land plants, suggest the existence of overlooked and potentially ancient symbiotic associations. Genetically tractable plant-microbe model systems in diverse streptophyte algae, hornworts, liverworts, ferns, and the so far unsampled diversity of seed plants will enable dissection of the spectrum of molecular mechanisms that regulate the breadth of interactions occurring in plants. The actual function of the symbiotic genes present in bryophyte genomes also remains to be determined. Furthermore, our understanding of plant-microbe interactions will be enriched by more often combining evolutionary concepts with mechanistic studies. More efforts are needed to decipher the molecular changes that have enabled the emergence of new interactions, signaling pathways, and enzymatic specificities to support symbiosis and to protect against pathogens. Microbes manipulate plant processes, and complementary microbial studies are key to gaining a complete picture of plant-microbe evolution. Knowing the rules of engagement between distantly related plants and their microbes then helps genetic transplantation approaches into crops and the orthogonal engineering of bioprocesses aimed at achieving quantitative resistance against pathogens, improving phosphate uptake, or establishing nitrogen-fixing associations for efficient use in sustainable agriculture. ■

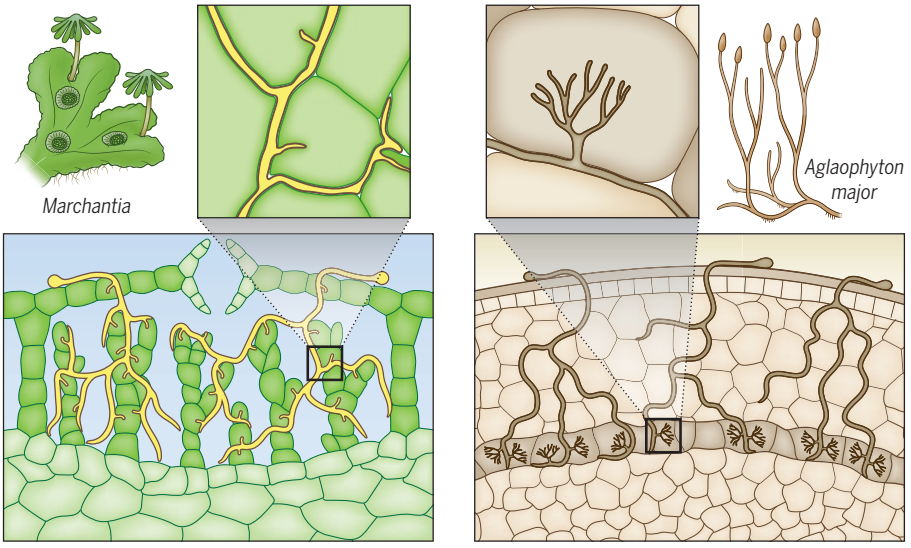

Ancient friends and recent enemies shape plant evolution. Some pathogens such as oomycetes are able to infect a wide range of extant plant lineages, including bryophytes (left), and plant pathogen interactions often evolve at a fast pace. By contrast, some symbiotic interactions that look exactly as they do today can be found in the most ancient land plant fossils, here depicted as an illustration of the Rhynie chert fossil plant *Aglaophyton major* (right). Still, both types of plant-microbe interactions feature evolutionarily ancient as well as rapidly evolving aspects. Extending plant-microbe studies across diverse groups of plant lineages has enriched our understanding of these processes and their evolution.

The list of author affiliations is available in the full article online.
*Corresponding author. Email: pierre-marc.delaux@lrsv.ups-tlse.fr (P.-M.D.); sebastian.schornack@slcu.cam.ac.uk (S.S.)
Cite this article as P.-M. Delaux and S. Schornack, *Science* **371**, eaba6605 (2021). DOI: 10.1126/science.aba6605

READ THE FULL ARTICLE AT
https://doi.org/10.1126/science.aba6605

RESEARCH ARTICLE SUMMARY

EVOLUTION

Recurrent evolution of vertebrate transcription factors by transposase capture

Rachel L. Cosby, Julius Judd, Ruiling Zhang*, Alan Zhong*, Nathaniel Garry, Ellen J. Pritham, Cédric Feschotte†

INTRODUCTION: How novel protein architectures evolve remains poorly understood. The rearrangement of domains with preexisting functions into new composite architectures through exon shuffling is a powerful path to form genes encoding proteins with novel functionalities. Although exon shuffling is thought to account for the evolution of many protein structures, the source of new exons and splice sites as well as the mechanisms by which they become assimilated have been scarcely characterized. In this work, we investigate the contribution of DNA transposons to the formation of novel protein-coding genes through exon shuffling during vertebrate evolution.

RATIONALE: DNA transposons are widespread mobile elements encoding transposase proteins that promote their selfish replication in host genomes. Transposases typically contain DNA binding and catalytic nuclease domains, which may be repurposed for cellular functions. By inserting functional domains into new genomic contexts, transposase sequences can generate host-transposase fusion (HTF) genes through alternative splicing. Several genes with critical developmental functions, such the *Pax* transcription factors, are thought to have been born through this process. However, the mechanism by which transposase domains are captured to generate HTFs, how common this process is, and the functions of most known HTF genes remain unclear.

RESULTS: We used comparative genomics to survey all tetrapod genomes with available gene models (596) for putative HTFs. We identified 106 distinct HTFs derived from 94 independent fusion events over the course of ~300 million years of evolution. We found that most HTFs evolved through the alternative splicing of host domains to transposase proteins using splice sites provided by the transposon. The transposase domains of all HTFs analyzed (81) are evolving under purifying selection, which suggests that they have been maintained for organismal function. The domain composition of HTF proteins indicates that most of them consist of transposase DNA binding domains fused to host domains that are predicted to function in transcriptional and/or chromatin regulation, especially the repressive Krüppel-associated box (KRAB) domain (involved in ~30% of all HTFs), which suggests that many HTFs function as transcriptional regulators. Supporting this hypothesis, we show that four independently evolved KRAB-transposase fusion proteins repress gene expression in a sequence-specific manner in reporter assays. Furthermore, loss of function, rescue, and regulatory genomics experiments in bat cells revealed that the bat-specific KRABINER fusion protein binds hundreds of cognate transposons genome-wide and controls a large network of genes and cis-regulatory elements.

CONCLUSION: Our findings confirm that exon shuffling is a major evolutionary force generating genetic novelty. We provide evidence that DNA transposons promote exon shuffling by inserting transposase domains in new genomic contexts. This process provides a plausible path for the emergence of several ancient transcription factors with important developmental functions. By illustrating how a transcription factor and its dispersed binding sites can emerge simultaneously from a single transposon family, our results bolster the view that transposons are key players in the evolution of gene regulatory networks. ■

The list of author affiliations is available in the full article online.
*These authors contributed equally to this work.
†Corresponding author. Email: cf458@cornell.edu
Cite this article as R. L. Cosby *et al.*, *Science* **371**, eabc6405 (2021). DOI: 10.1126/science.abc6405

READ THE FULL ARTICLE AT
https://doi.org/10.1126/science.abc6405

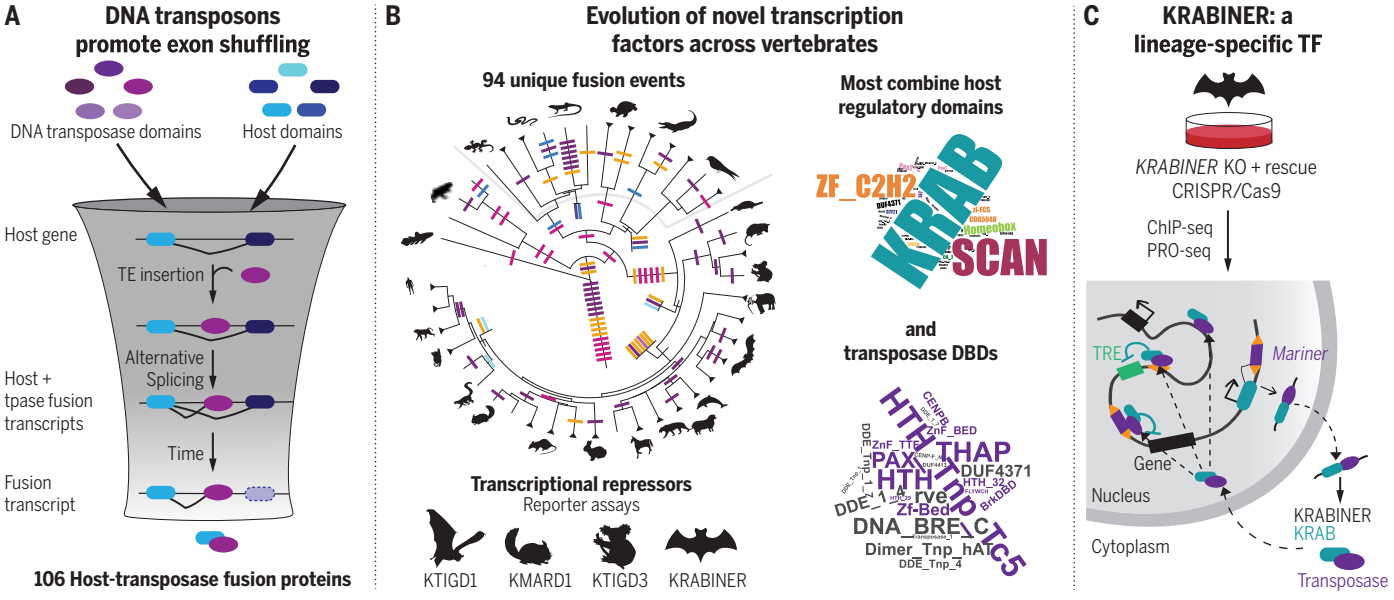

Transposase capture contributes to the evolution of transcription factors by combining DNA transposase and host domains. (**A**) Model for how transposase capture occurs. (**B**) Abundance and characteristics of identified HTFs. (**C**) Summary of KRABINER's role as a transcription factor (TF) in bat cells. TE, transposable element; tpase, transposase; DBDs, DNA binding domains; KO, knockout; ChIP-seq, chromatin immunoprecipitation sequencing; PRO-seq, precision run-on sequencing; TRE, transcribed regulatory element.

RESEARCH ARTICLE SUMMARY

BACTERIAL GENOMICS

Microbial single-cell RNA sequencing by split-pool barcoding

Anna Kuchina*, Leandra M. Brettner*, Luana Paleologu, Charles M. Roco, Alexander B. Rosenberg, Alberto Carignano, Ryan Kibler, Matthew Hirano, R. William DePaolo, Georg Seelig†

INTRODUCTION: Bacteria heterogeneously activate gene expression programs in response to environmental changes, stress, and other stimuli. Such behavior may serve as a bet-hedging strategy and is essential for population growth and survival. Because bet-hedging programs are often activated only in a small fraction of cells, their unbiased discovery and characterization remains challenging. High-throughput single-cell RNA sequencing (scRNA-seq) has become ubiquitous for analyzing cell types and states in eukaryotes, but existing methods are not easily adapted to bacteria. Given the need for bacterial scRNA-seq, we developed microSPLiT (microbial split-pool ligation transcriptomics), a low-cost and high-throughput approach tailored to microbes. microSPLiT labels the cellular origin of RNA through combinatorial barcoding and uses only basic laboratory equipment to profile tens of thousands of cells in a single experiment. microSPLiT overcomes challenges specific to bacteria such as their low mRNA content, diversity in cell size, and cell wall architecture.

RATIONALE: The lack of single-cell resolution in bacterial RNA sequencing is a severe limitation, considering that even isogenic bacteria frequently exhibit functional subpopulations essential for fitness and survival. Gene expression heterogeneities are likely magnified in natural environments where microbes are exposed to complex chemical, physical, and biological factors, but to date, such functional variation remains obscured. Functional subpopulations may be rare and hard to culture, making their analysis challenging with existing fluorescence-based single-cell methods.

RESULTS: In a species-mixing experiment performed with Gram-negative *Escherichia coli* and Gram-positive *Bacillus subtilis*, microSPLiT detected on average 235 unique transcripts per cell in *E. coli* and 397 in *B. subtilis*. MicroSPLiT reliably distinguished heat-shocked from non–heat-shocked bacteria by expression of classical heat shock genes, demonstrating its ability to detect differential gene expression in mixed populations. We applied microSPLiT to >25,000 *B. subtilis* cells grown in rich media and sampled across the growth curve [optical density (OD) 0.5 to 6.0]. MicroSPLiT provided a comprehensive view of carbon utilization across all growth stages, detecting a surprising subpopulation associated with myo-inositol catabolism at intermediate ODs. Single-cell microscopy confirmed heterogeneous expression of the myo-inositol uptake and utilization operons. MicroSPLiT also identified gene expression programs associated with a range of bacterial lifestyles and stress responses. Our data revealed a rare subpopulation of less than 0.2% of all cells associated with prophage activation and another subpopulation of around 2% of cells in a state of competence. Gene expression within these clusters was in close agreement with prior reports on competence and prophage activation.

CONCLUSION: We developed a high-throughput bacterial scRNA-seq method and applied it to characterize *B. subtilis* growth in rich media. Our analysis revealed several heterogeneously activated gene expression programs, even though exponential growth is not typically associated with cellular heterogeneity. We were able to detect subpopulations of cells as rare as 0.142%, pointing to microSPLiT's potential to uncover physiologically relevant rare cell states that are hard to study by bulk or low-throughput methods. The same microSPLiT protocol worked reliably for a mix of Gram-negative and Gram-positive model bacteria; we expect that this versatility together with the scalability inherent to combinatorial barcoding will make microSPLiT a powerful tool for the investigation of complex natural and engineered microbial communities. ■

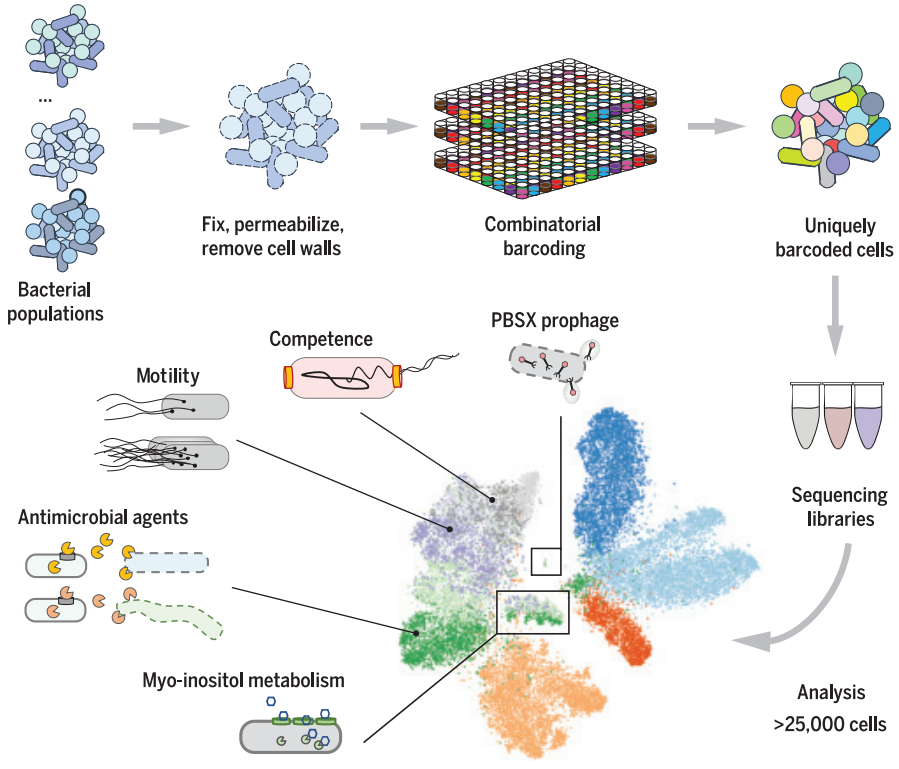

MicroSPLiT uncovers transcriptional states in bacterial populations. MicroSPLiT is a scRNA-seq method for bacteria that uses combinatorial barcoding to label bacterial RNA by cell of origin; the steps in the process are shown. In an experiment performed with >25,000 *B. subtilis* cells sampled along a growth curve from early exponential to early stationary phase, microSPLiT uncovered a wide range of developmental and metabolic gene expression programs, including rare cell states associated with competence, prophage activation, and myo-inositol metabolism.

The list of author affiliations is available in the full article online.
*These authors contributed equally to this work.
†Corresponding author. Email: gseelig@uw.edu
Cite this article as A. Kuchina *et al.*, *Science* 371, eaba5257 (2021). DOI: 10.1126/science.aba5257

READ THE FULL ARTICLE AT
https://doi.org/10.1126/science.aba5257

RESEARCH ARTICLE SUMMARY

ANTIBIOTIC RESISTANCE

Clinically relevant mutations in core metabolic genes confer antibiotic resistance

Allison J. Lopatkin, Sarah C. Bening, Abigail L. Manson, Jonathan M. Stokes, Michael A. Kohanski, Ahmed H. Badran, Ashlee M. Earl, Nicole J. Cheney, Jason H. Yang, James J. Collins*

INTRODUCTION: Despite the complexity of antibiotic lethality, canonical mechanisms of resistance are generally grouped into three broad categories: target modification, drug inactivation, and drug transport. Although metabolism has been shown to actively contribute to antibiotic lethality, antibiotic resistance mutations are infrequently identified in metabolic genes, and metabolic dysregulation is not a commonly cited mechanism of antibiotic resistance. One explanation is that previous approaches provide a limited view of the antibiotic resistance landscape. Indeed, laboratory evolutions paired with sequencing candidate genes and/or a small number of clonal isolates per condition highlight mutations that are either expected, or repeatedly occur, at high frequency. Moreover, antibiotic-mediated effects on bacterial metabolism involve numerous, complex, and coordinated biomolecular networks, which makes it challenging to predict candidates of likely resistance a priori. Additionally, the diversity of involved pathways increases the number of possible evolutionary outcomes, which reduces the likelihood for convergent mutations, and thus would be readily missed using previous methods. As a result, genetic mechanisms of antibiotic resistance related to metabolism are significantly understudied.

RATIONALE: The importance of population-level analyses for understanding the evolutionary landscape in response to drug treatment is becoming increasingly recognized. Low-frequency mutants make up most genetic diversity within a population, and in many cases, beneficial mutations may drift to extinction before becoming established. This is particularly relevant for genes involved in cellular metabolism, in which the diverse array of metabolic pathways can lead to a myriad of potential evolutionary outcomes compared with canonical drug targets. As such, we sought to use a more comprehensive view afforded by both population and clonal analyses to elucidate metabolic aspects of antibiotic resistance. Moreover, considering these constraints, typical laboratory evolution protocols and their analysis methods are not optimized to detect mutations in metabolism-related genes. Constant antibiotic exposure imposes growth-dependent selection, and a lack of metabolic-specific selection pressure further minimizes the likelihood of enriching for metabolic-specific pathways and processes. Thus, we reasoned that maximizing metabolic rather than growth adaptation would allow us to shift these dynamics and further tease out antibiotic-specific metabolic variants.

RESULTS: We sequenced and analyzed *Escherichia coli* adapted to three representative antibiotics at increasingly heightened metabolic states. Doing so revealed a variety of underappreciated noncanonical genes, such as those related to central carbon and energy metabolism, which are implicated in antibiotic resistance. These mutations in metabolic genes often arose in multiple independent populations and/or in response to more than one drug. Several of the identified metabolism-specific mutations are overrepresented in the genomes of >3500 clinical *E. coli* pathogens at levels similar to, and in some cases greater than, known resistance mutations indicating their clinical relevance. To evaluate whether these metabolic mutations confer resistance, we chose a representative subset of both genes related to metabolism and classic resistance on the basis of their prevalence and clinical significance. We expressed the wild-type and mutant variants of each gene from a medium-copy plasmid introduced into the corresponding chromosomal knockout strain. In all cases, metabolic mutations increased the minimum inhibitory concentration to at least one, and in many cases more than one, of the antibiotics. Finally, phenotypic and genotypic analyses of one representative mutation in the 2-oxoglutarate dehydrogenase (sucA) enzyme provides a preliminary picture of how altered metabolism gives rise to antibiotic resistance: Lower basal respiration prevents antibiotic-mediated induction of tricarboxylic acid cycle activity, thereby avoiding metabolic toxicity and minimizing lethality.

CONCLUSION: Our findings that metabolic mutations arise in response to antibiotic treatment, and that these mutations confer resistance and are highly prevalent in clinical pathogens, suggests that the three general antibiotic resistance categories may not be as representative, nor the mechanisms as comprehensive, as previously thought. Indeed, metabolic adaptation may represent a separate class of resistance mechanisms beyond conferring tolerance, whereby cells also alter their metabolic response to mitigate downstream toxic aspects of antibiotic lethality. ■

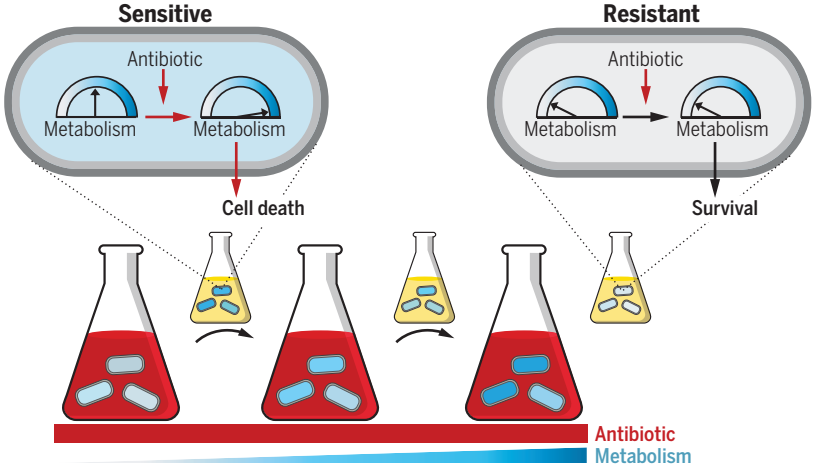

Altered metabolic state confers antibiotic resistance. Cells were exposed to high antibiotic concentrations (red) for short durations under incrementally increasing metabolic states (blue), separated by rounds of drug-free growth (small flasks). Left to right indicates evolutionary time. Initially, antibiotic-mediated metabolic stimulation partially contributes to cell lethality (sensitive cell). Evolved cells acquire resistance caused by decreased basal metabolic activity that avoids antibiotic-mediated stimulation and subsequent lethality (resistant cell).

The list of author affiliations is available in the full article online.
*Corresponding author. Email: jimjc@mit.edu
Cite this article as: A. J. Lopatkin *et al.*, *Science* **371**, eaba0862 (2021). DOI: 10.1126/science.aba0862

READ THE FULL ARTICLE AT
https://doi.org/10.1126/science.aba0862

RESEARCH ARTICLE SUMMARY

DNA ORIGAMI

Absolute and arbitrary orientation of single-molecule shapes

Ashwin Gopinath*, Chris Thachuk, Anya Mitskovets, Harry A. Atwater, David Kirkpatrick, Paul W. K. Rothemund*

INTRODUCTION: Molecular and particulate nanodevices such as carbon nanotubes and semiconductor nanowires exhibit properties that are difficult to achieve with conventional silicon microfabrication. Unfortunately, most such devices must be synthesized or processed in solution. To combine nanodevices into larger circuits, or simply to connect them with the macroscopic world, scientists use a range of directed self-assembly techniques to deposit them at specific locations on microfabricated chips. Many such methods work well with spherical devices for which orientation is irrelevant. For linear wire-like devices, flow or field alignment works for applications involving a single global orientation. However, a general solution for multiple orientations or less symmetric devices (e.g., diodes or transistors) has remained elusive.

RATIONALE: Single-molecule DNA origami shapes can simultaneously act as templates to create nanodevices and as adaptors to integrate them onto chips. With 200 attachment sites just 5 nm apart, origami can organize any material that can be linked to DNA; for example, carbon nanotube crosses have been templated to yield field-effect transistors. With ~100-nm outlines, origami are large enough that shape-matched binding sites can be written at arbitrary positions on chips using electron-beam lithography. Our prior work used equilateral triangles that stuck to binding sites in six degenerate orientations. Here, we asked whether origami shapes could provide both absolute orientation (to uniquely orient asymmetric devices) and arbitrary orientation (to independently orient each device). Success depended on finding a suitably asymmetric shape.

RESULTS: To break up-down symmetry and to ensure that each shape was deposited right-side up, we added adhesion-decreasing single-stranded DNAs to one side of each origami. The binding of asymmetric right triangles to shape-matched sites gave orientation distributions consistent with strong kinetic trapping, as predicted by the volumes of basins of attraction around local minima. This motivated the design of a "small moon" shape whose energy landscape has a single minimum. Fluorescent molecular dipoles fixed to small moons served as model nanodevices and allowed us to measure variability in orientation (±3.2°) by polarization microscopy. Large-scale integration was demonstrated by an array of 3456 small moons in 12 orientations, which we used as a fluorescence polarimeter to indicate excitation polarization. The utility of orientation for optimizing device performance was shown by aligning fluorescent dipoles within microfabricated optical cavities, which showed a factor of 4.5 increase in emission.

CONCLUSION: Control over optical dipole orientation may enable metal nanorod metasurfaces at visible wavelengths, optimized coupling of emitters to nanoantennas, lumped nanocircuits, and coherence effects between small numbers of emitters. Still, these applications and the devices we present do not demonstrate the full power of the small moons: Dipolar devices can rotate 180° and still function. Completely asymmetric nanodevices requiring absolute orientation (e.g., molecular bipolar junction transistors) have yet to be developed; now that orientation can be controlled, there is motivation to invent them. In the meantime, the wiring of existing devices into circuits may be greatly simplified. ■

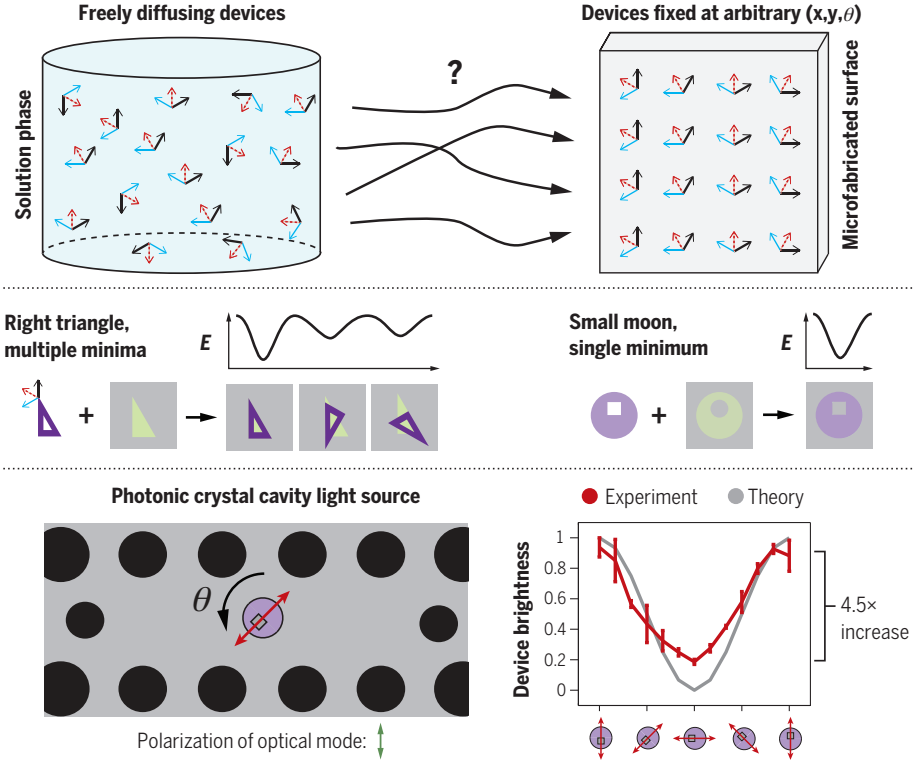

Directed self-assembly of asymmetric DNA origami shapes enables orientation-controlled integration of chemically synthesized nanodevices with conventionally fabricated microdevices. Top: How can one transfer thousands of nanodevices to a surface and fix each with its own orientation independent of the others? Middle left: Naïvely, an asymmetric right triangle (dark purple) carrying a device could orient the device by sticking to a surface binding site (green) of the same shape. But such triangles often bind incorrectly because there are multiple minima in the energy landscape (*E*). Middle right: The landscape for a disk with an offset hole (small moon, light purple) has a single minimum; thus, a small moon binds its site with a unique orientation. Bottom: The intensity of light emitted by a photonic crystal cavity microdevice (left) can be optimized (right) when small moons are used to align fluorescent molecule nanodevices (red arrow) with the polarization of the cavity mode.

The list of author affiliations is available in the full article online.
*Corresponding author. Email: agopi@mit.edu (A.G.); pwkr@dna.caltech.edu (P.W.K.R.)
Cite this article as A. Gopinath *et al.*, *Science* **371**, eabd6179 (2021). DOI: 10.1126/science.abd6179

READ THE FULL ARTICLE AT
https://doi.org/10.1126/science.abd6179

RESEARCH ARTICLE SUMMARY

PROTEIN DESIGN

De novo design of transmembrane β barrels

Anastassia A. Vorobieva, Paul White*, Binyong Liang*, Jim E. Horne, Asim K. Bera, Cameron M. Chow, Stacey Gerben, Sinduja Marx, Alex Kang, Alyssa Q. Stiving, Sophie R. Harvey, Dagan C. Marx, G. Nasir Khan, Karen G. Fleming, Vicki H. Wysocki, David J. Brockwell, Lukas K. Tamm, Sheena E. Radford, David Baker†

INTRODUCTION: Despite their key biological roles, only a few proteins that fold into lipid membranes have been designed de novo. A class of membrane proteins—transmembrane β barrels (TMBs)—forms a continuous sheet that closes on itself in lipid membranes. In addition to the challenge of designing β-sheet proteins, which are prone to misfolding and aggregation if folding is not properly controlled, the computational design of TMBs is complicated by limited understanding of TMB folding. As a result, no TMB has been designed de novo to date.

Although the folding of TMBs in vivo is catalyzed by the β-barrel assembly machinery (BAM), many TMBs can also fold spontaneously in synthetic membranes to form stable pores, making them attractive for biotechnology and single-molecule analytical applications. Hence, de novo design of TMBs has potential both for understanding the determinants of TMB folding and membrane insertion and for the custom engineering of TMB nanopores.

RATIONALE: We used de novo protein design to distill key principles of TMB folding through several design-build-test cycles. We iterated between hypothesis formulation, its implementation into computational design methods, and experimental characterization of the resulting proteins. To focus on the fundamental principles of TMB folding in the absence of complications due to interactions with chaperones and BAM in vivo, we focused on the challenge of de novo design of eight-stranded TMBs, which can fold and assemble into synthetic lipid membranes.

RESULTS: We used a combination of purely geometric models and explicit Rosetta protein structure simulations to determine the constraints that β-strand connectivity and membrane embedding place on the TMB architecture. Through a series of design-build-test cycles, we found that, unlike almost all other classes of proteins, locally destabilizing sequences are critical for expression and folding of TMBs, and that the β-turns that translocate through the bilayer during folding have to be destabilized to enable correct assembly in the membrane. Our results suggest that premature formation of β hairpins may result in off-target β-sheet structures that compete with proper membrane insertion and folding, and hence the β hairpins of TMBs must be designed such that they are only transiently formed prior to membrane insertion, when the protein is in an aqueous environment. In the hydrophobic environment of the lipid bilayer, the full TMB can assemble because the membrane-facing nonpolar residues, which would tend to cluster nonspecifically in an aqueous environment, instead make favorable interactions with the lipids. As the TMB assembles, the β hairpins are stabilized by interactions with the neighboring β strands.

Using computational methods that incorporate the above insights, we designed TMB sequences that successfully fold and assemble into both detergent micelles and lipid bilayers. Two of the designs were highly stable and could fold into liposomes more rapidly and reversibly than the transmembrane domain of the model outer membrane protein A (tOmpA) of *Escherichia coli*. A nuclear magnetic resonance solution structure and a high-resolution crystal structure for two different designs closely match the design models, showing that the TMB design method developed here can generate new structures with atomic-level accuracy.

CONCLUSION: This study elucidates key principles for de novo design of transmembrane β barrels, ranging from constraints on β-barrel architecture and β-hairpin design, as well as local and global sequence features. Our designs provide starting points for the bottom-up elucidation of the molecular mechanisms underlying TMB folding and interactions with the cellular outer membrane folding and insertion machinery. More generally, our work demonstrates that TMBs can be designed with atomic-level accuracy and opens the door to custom design of nanopores tailored for applications such as single-molecule sensing and sequencing. ■

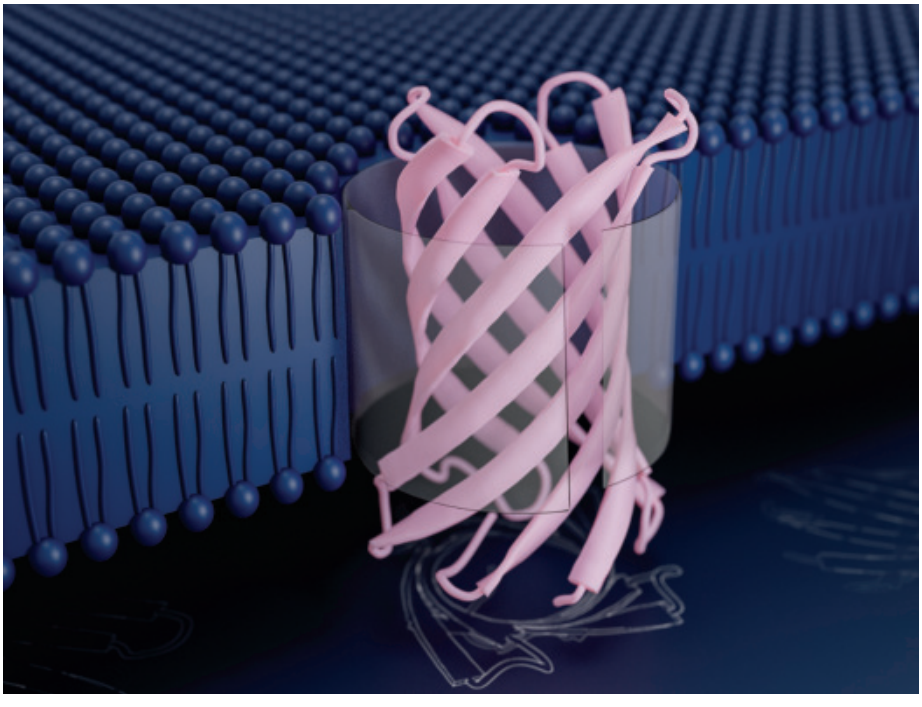

CREDIT: IAN HAYDON.

De novo–designed eight-stranded transmembrane β barrels fold spontaneously and reversibly into synthetic lipid membranes. The illustration shows the crystal structure of the protein TMB2.17 designed in this study, which adopts a structure identical to the design model.

The list of author affiliations is available in the full article online.
*These authors contributed equally to this work.
†Corresponding author. Email: dabaker@uw.edu
Cite this article as A. A. Vorobieva *et al.*, *Science* 371, eabc8182 (2021). DOI: 10.1126/science.abc8182

READ THE FULL ARTICLE AT
https://doi.org/10.1126/science.abc8182

RESEARCH ARTICLE SUMMARY

CORONAVIRUS

Inferring the effectiveness of government interventions against COVID-19

Jan M. Brauner*†, Sören Mindermann*†, Mrinank Sharma*†, David Johnston, John Salvatier, Tomáš Gavenčiak, Anna B. Stephenson, Gavin Leech, George Altman, Vladimir Mikulik, Alexander John Norman, Joshua Teperowski Monrad, Tamay Besiroglu, Hong Ge, Meghan A. Hartwick, Yee Whye Teh, Leonid Chindelevitch‡, Yarin Gal‡, Jan Kulveit‡

INTRODUCTION: Governments across the world have implemented a wide range of nonpharmaceutical interventions (NPIs) to mitigate the spread of severe acute respiratory syndrome coronavirus 2 (SARS-CoV-2). Given the increasing death toll of the pandemic and the social cost of some interventions, it is critical to understand their relative effectiveness. By considering the effects that interventions had on transmission during the first wave of the outbreak, governments can make more-informed decisions about how to control the pandemic.

RATIONALE: Rigorously studying the effectiveness of individual interventions poses considerable methodological challenges. Simulation studies can explore scenarios, but they make strong assumptions that may be difficult to validate. Data-driven, cross-country modeling comparing the timing of national interventions to the subsequent numbers of cases or deaths is a promising alternative approach. We have collected chronological data on the implementation of several interventions in 41 countries between January and the end of May 2020, using independent double entry by researchers to ensure high data quality. Because countries deployed different combinations of interventions in different orders and with different outcomes, it is possible to disentangle the effect of individual interventions. We estimate the effectiveness of specific interventions with a Bayesian hierarchical model by linking intervention implementation dates to national case and death counts. We partially pool NPI effectiveness to allow for country-specific NPI effects. Our model also accounts for uncertainty in key epidemiological parameters, such as the average delay from infection to death. However, intervention effectiveness estimates should only be used for policy-making if they are robust across a range of modeling choices. We therefore support the results with extensive empirical validation, including 11 sensitivity analyses under 206 experimental conditions. In these analyses, we show how results change when we vary the data, the epidemiological parameters, or the model structure or when we account for confounders.

RESULTS: While exact intervention effectiveness estimates varied with modeling assumptions, broader trends in the results were highly consistent across experimental conditions. To describe these trends, we categorized intervention effect sizes as small, moderate, or large, corresponding to posterior median reductions in the reproduction number R of <17.5%, between 17.5 and 35%, and >35%, respectively. Across all experimental conditions, all interventions could robustly be placed in one or two of these categories. Closing both schools and universities was consistently highly effective at reducing transmission at the advent of the pandemic. Banning gatherings was effective, with a large effect size for limiting gatherings to 10 people or less, a moderate-to-large effect for 100 people or less, and a small-to-moderate effect for 1000 people or less. Targeted closures of face-to-face businesses with a high risk of infection, such as restaurants, bars, and nightclubs, had a small-to-moderate effect. Closing most nonessential businesses delivering personal services was only somewhat more effective (moderate effect). When these interventions were already in place, issuing a stay-at-home order had only a small additional effect. These results indicate that, by using effective interventions, some countries could control the epidemic while avoiding stay-at-home orders.

CONCLUSION: We estimated the effects of nonpharmaceutical interventions on COVID-19 transmission in 41 countries during the first wave of the pandemic. Some interventions were robustly more effective than others. This work may provide insights into which areas of public life require additional interventions to be able to maintain activity despite the pandemic. However, because of the limitations inherent in observational study designs, our estimates should not be seen as final but rather as a contribution to a diverse body of evidence, alongside other retrospective studies, simulation studies, and experimental trials. ■

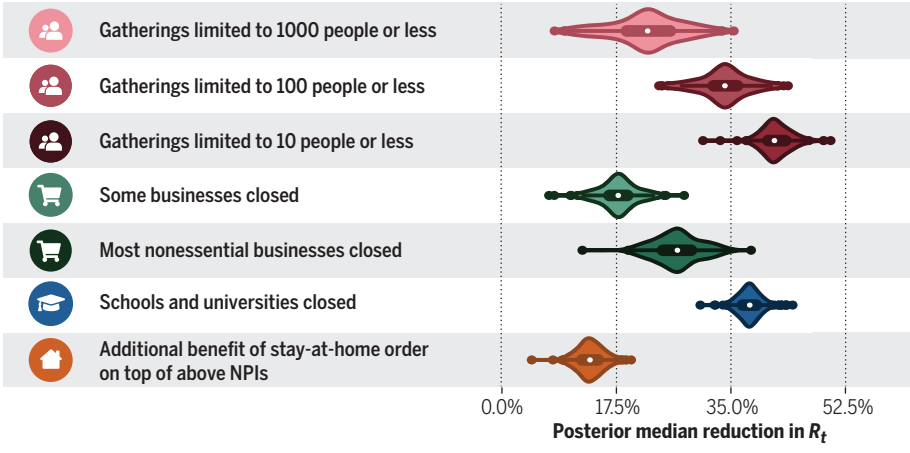

Median intervention effectiveness estimates across a suite of 206 analyses with different epidemiological parameters, data, and modeling assumptions. Bayesian inference using a semimechanistic hierarchical model with observed national case and death data across 41 countries between January and May 2020 is used to infer the effectiveness of several nonpharmaceutical interventions. Although precise effectiveness estimates depend on the assumed data and parameters, there are clear trends across the experimental conditions. Violins show kernel density estimates of the posterior median effectiveness across the sensitivity analysis. R_t, instantaneous reproduction number.

The list of author affiliations is available in the full article online.
*Corresponding author. Email: jan.brauner@cs.ox.ac.uk (J.M.B.); soren.mindermann@cs.ox.ac.uk (S.M.); mrinank@robots.ox.ac.uk (M.S.)
†These authors contributed equally to this work.
‡These authors contributed equally to this work.
This is an open-access article distributed under the terms of the Creative Commons Attribution license (https://creativecommons.org/licenses/by/4.0/), which permits unrestricted use, distribution, and reproduction in any medium, provided the original work is properly cited.
Cite this article as J. M. Brauner *et al.*, *Science* 371, eabd9338 (2021). DOI: 10.1126/science.abd9338

READ THE FULL ARTICLE AT
https://doi.org/10.1126/science.abd9338

RESEARCH ARTICLES

PROTEIN ENGINEERING

Phage-assisted evolution of botulinum neurotoxin proteases with reprogrammed specificity

Travis R. Blum[1,2,3], Hao Liu[4,5], Michael S. Packer[1,2,3], Xiaozhe Xiong[4,5], Pyung-Gang Lee[4,5], Sicai Zhang[4,5], Michelle Richter[1,2,3], George Minasov[6], Karla J. F. Satchell[6], Min Dong[4,5]*, David R. Liu[1,2,3]*

Although bespoke, sequence-specific proteases have the potential to advance biotechnology and medicine, generation of proteases with tailor-made cleavage specificities remains a major challenge. We developed a phage-assisted protease evolution system with simultaneous positive and negative selection and applied it to three botulinum neurotoxin (BoNT) light-chain proteases. We evolved BoNT/X protease into separate variants that preferentially cleave vesicle-associated membrane protein 4 (VAMP4) and Ykt6, evolved BoNT/F protease to selectively cleave the non-native substrate VAMP7, and evolved BoNT/E protease to cleave phosphatase and tensin homolog (PTEN) but not any natural BoNT protease substrate in neurons. The evolved proteases display large changes in specificity (218- to >11,000,000-fold) and can retain their ability to form holotoxins that self-deliver into primary neurons. These findings establish a versatile platform for reprogramming proteases to selectively cleave new targets of therapeutic interest.

The ability of proteases to cleave protein targets with high efficiency and specificity enables them to play important roles in biology, biotechnology, and medicine (*1*). Applications of proteases could be greatly expanded by the ability to reprogram them to selectively cleave new targets for which no known protease exists. Although proteases have been engineered or evolved for increased stability (*2*), solvent tolerance (*3*), inhibitor resistance (*4*, *5*), activity (*6*–*8*), and altered specificity (*9*–*15*), reports of successfully changing substrate specificity beyond a single amino acid in the primary peptide recognition sequence are rare (*16*–*19*). Moreover, the laboratory evolution of proteins to accept new substrates commonly results in substrate promiscuity (*19*–*27*). Although negative selections during protease evolution have reduced off-target activity for single amino acid substrate changes (*28*–*33*), the limits of directed evolution's ability to extensively reprogram proteases away from their original substrates to achieve highly specific cleavage of a new target remain largely untested.

Many pathogens have evolved proteases that cleave proteins with exquisite specificity to precisely modulate host cell functions. These proteases, exemplified by botulinum neurotoxins (BoNTs), have proven to be powerful therapeutic agents. BoNTs are a family of bacterial toxins with seven major serotypes (BoNT/A to BoNT/G). Each BoNT consists of a heavy chain (HC; ~100 kDa) and a light chain (LC; ~50 kDa) connected through a disulfide bond (*34*, *35*). The HC serves as a delivery vehicle, containing both receptor binding and membrane translocation domains, whereas the LC is a zinc-dependent metalloprotease. BoNT HCs mediate entry into the neuronal cytosol, where disulfide bond reduction releases the LC. Known substrates of BoNT LCs are all members of the SNARE protein family, which mediates membrane fusion in eukaryotic cells (*36*). The LCs target and selectively cleave SNARE proteins essential for synaptic vesicle exocytosis. BoNT/A, BoNT/C, and BoNT/E cleave the 25-kDa synaptosome-associated protein (SNAP-25); BoNT/B, BoNT/D, BoNT/F, and BoNT/G cleave vesicle-associated membrane proteins 1, 2, and 3 (VAMP1, VAMP2, and VAMP3); and BoNT/C also cleaves Syntaxin-1. Cleavage of these proteins blocks synaptic vesicle exocytosis, causing muscle paralysis. BoNTs are commonly known for their cosmetic applications, but they have also been used as important therapeutic proteins for over 30 years to treat many other conditions (*35*).

The exquisite selectivity of BoNT LC proteases is critical for their therapeutic application. Past efforts to engineer BoNT LCs have expanded their ability to cleave homologous SNARE proteins but have been unable to retarget these proteases to selectively cleave proteins that differ even modestly from their native substrates. For example, engineered BoNT/A and BoNT/E proteases cleave SNAP-23 but retain activity on SNAP-25 (*37*, *38*). Because of their high specificity and dependence on multiple exosites and conformational changes to mediate substrate recognition and cleavage (*39*, *40*), the prospect of reprograming BoNT proteases to cleave proteins beyond SNARE family members has seemed out of reach.

Although several systems for protease evolution have been reported (*41*), phage-assisted continuous evolution (PACE) is especially well-suited to address this challenge, as PACE continuously diversifies and selects gene variants with desired properties ~100-fold faster than stepwise protein evolution methods (*5*, *19*, *21*–*24*, *42*–*50*). We recently reported a PACE selection for protein cleavage (*5*) and used the selection to evolve tobacco etch virus (TEV) proteases that cleave a sequence in human interleukin-23 (*19*). Because this PACE system did not enable selection against off-target cleavage activity, the evolved TEV protease maintained strong activity on its native substrate (*19*). A platform to generate highly selective proteases that avoid such promiscuity has been a long-standing goal (*51*, *52*). Here, we developed a simultaneous PACE positive and negative selection system and used it to reprogram the substrate specificity of three BoNT LC proteases, yielding four proteases with high specificity for their new targets. These results establish a system to rapidly evolve a class of clinical proteases to preferentially cleave non-native targets.

Results

Development of a phage-assisted evolution negative selection for proteases

PACE uses a modified M13 bacteriophage that encodes an evolving gene of interest in place of *gIII*, which encodes a protein (pIII) essential for phage replication. During PACE, *gIII* is encoded on an accessory plasmid (AP) in *Escherichia coli* host cells, and its expression is made dependent on the activity of interest (*24*, *50*). To evolve proteases in PACE, we use a protease-activated RNA polymerase (PAP), an autoinhibited T7 (or T7 variant) RNA polymerase (RNAP) expressed in host cells as a fusion with its native inhibitor T7 lysozyme (enLys) (Fig. 1A) (*5*). The linker between T7 RNAP and T7 lysozyme contains the proteolysis target sequence of interest. Cleavage of the target sequence releases T7 lysozyme, restoring T7 RNAP activity and triggering expression of *gIII*, which is under control of the T7 promoter (Fig. 1A). Propagating phage are continuously diluted by fresh host cells and are continuously mutated by induction of a host cell mutagenesis plasmid (*44*).

We first verified that LC proteases from BoNT/E, BoNT/F, and the recently discovered BoNT-like toxin BoNT/X (*34*, *53*, *54*) could

[1]Merkin Institute of Transformative Technologies in Healthcare, Broad Institute of Harvard and MIT, Cambridge, MA 02142, USA. [2]Department of Chemistry and Chemical Biology, Harvard University, Cambridge, MA 02138, USA. [3]Howard Hughes Medical Institute, Harvard University, Cambridge, MA 02138, USA. [4]Department of Urology, Boston Children's Hospital, Boston, MA 02115, USA. [5]Department of Microbiology and Department of Surgery, Harvard Medical School, Boston, MA 02115, USA. [6]Department of Microbiology-Immunology, Northwestern University Feinberg School of Medicine, Chicago, IL 60611, USA.
*Corresponding author. Email: min.dong@childrens.harvard.edu (M.D.); liu@chemistry.harvard.edu (D.R.L.)

perform proteolytic activation of T7-PAPs containing minimized substrate fragments, resulting in luciferase expression. We observed that all three proteases are functional when expressed in *E. coli* and activate T7-PAP in a manner consistent with their native cleavage specificities (figs. S1 and S2).

Next, we developed a PACE negative selection that impedes the propagation of phage encoding proteases with off-target cleavage activities. We previously evolved a T7-RNA polymerase variant with high selectivity for the T3 promoter (T3′-RNAP) (*21*). We converted T3′-RNAP, which remains inhibited by tethered T7 lysozyme, into a protease-activated T3′ polymerase (T3′-PAP) that supports positive selection through transcription of *gIII* in response to on-target cleavage (Fig. 1A). We then used a T7-PAP containing an off-target substrate to construct a negative selection in which off-target cleavage drives expression of

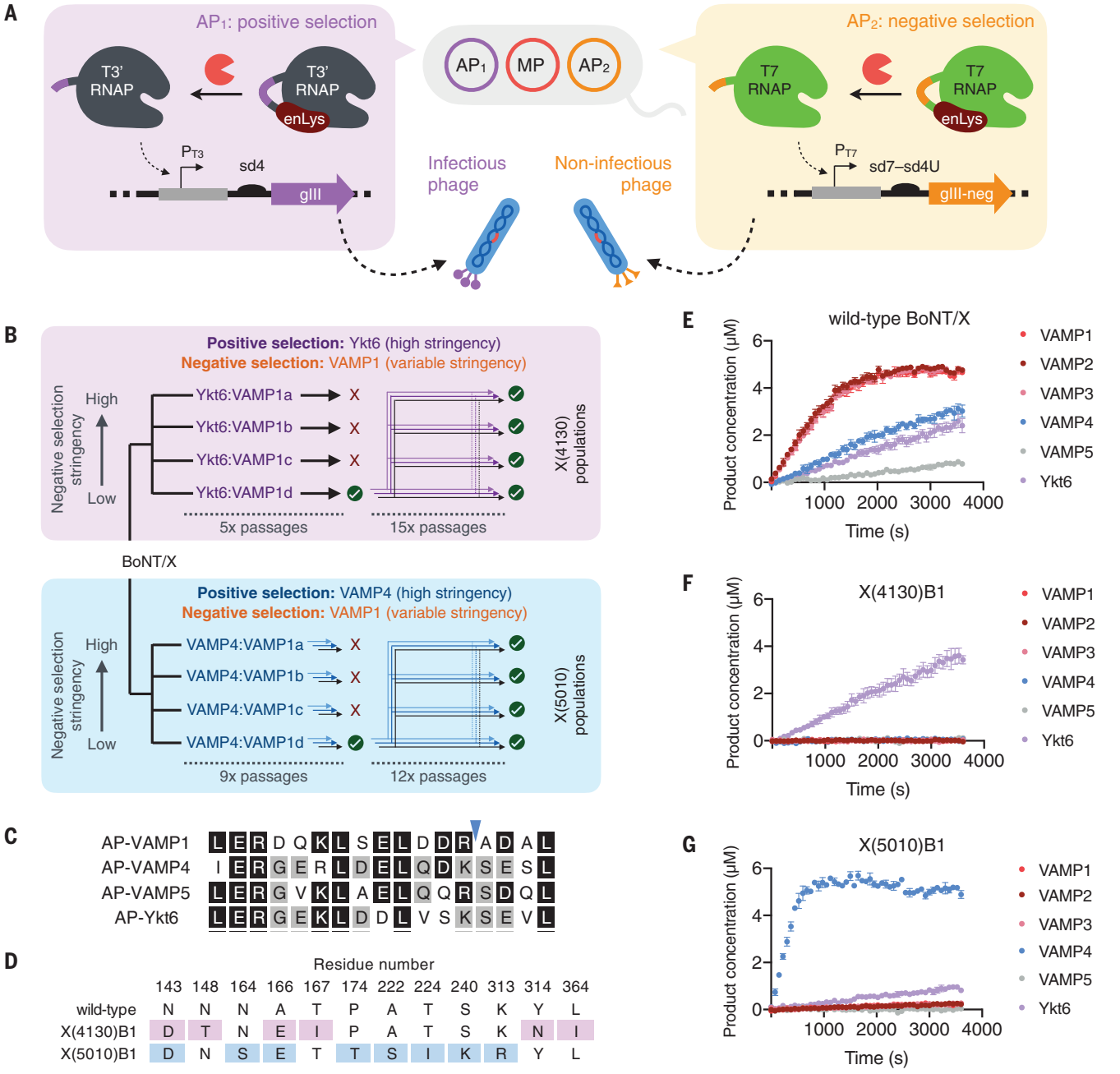

Fig. 1. Phage-assisted protease positive and negative selection systems and their application to BoNT/X LC proteases. (**A**) Schematic of the PACE and PANCE dual positive and negative selection for proteolysis. (**B**) Summary of the strategy for stepwise evolution of a Ykt6-selective and a VAMP4-selective protease from promiscuous wild-type BoNT/X LC protease. (**C**) Four major substrates of wild-type BoNT/X protease, with the cleavage position indicated by the blue wedge. Positions in VAMP4, VAMP5, and Ykt6 identical to VAMP1 are in black, while positions in VAMP5 and Ykt6 identical to VAMP4 are in gray. Residue abbreviations: A, alanine; C, cysteine; D, aspartic acid; E, glutamic acid; F, phenylalanine; G, glycine; H, histidine; I, isoleucine; K, lysine; L, leucine; M, methionine; N, asparagine; P, proline; Q, glutamine; R, arginine; S, serine; T, threonine; V, valine; Y, tyrosine. (**D**) Selected Ykt6-selective and VAMP4-selective BoNT/X protease variants. (**E** to **G**) Representative kinetic traces showing cleavage activity of wild-type BoNT/X protease, X(4130)B1 protease, and X(5101)B1 protease on the six major BoNT/X substrates. Reactions in (E) to (G) were performed at 37°C with 2.5 nM protease and 5 μM substrate.

gIII-neg, which encodes a dominant-negative pIII variant that suppresses phage replication (*21*), from the T7 promoter (Fig. 1A). Negative selection stringency can be tuned using ribosome binding site variants to control translation rates of pIII-neg in different host strains.

To enable greater control of selection pressure when needed, we performed simultaneous positive and negative selection using phage-assisted noncontinuous evolution (PANCE) (*23*, *46*–*48*), in which phage are periodically, rather than continuously, diluted into media containing fresh host cells. PANCE is conducted in 96-well plates and offers reduced selection stringency in a high-throughput format. PANCE allows parallel protease evolution experiments over a range of negative selection stringencies, while simultaneously maintaining high-stringency positive selection in all hosts.

Dual selection PANCE evolves a Ykt6-selective BoNT/X protease

We started with BoNT/X, which is different from other BoNT family proteases in that it cleaves not only VAMP1, -2, and -3 but also VAMP4 and -5 and Ykt6 (*53*, *54*). Whereas BoNT/X in principle could serve as a powerful tool to investigate the roles of VAMP4 and Ykt6 in cells, its substrate promiscuity impedes this possibility. To explore whether the selectivity of BoNT/X protease can be improved using dual selection PANCE, we generated a phage-encoded library of mutant BoNT/X LC protease genes through propagation in host strains with the mutagenic plasmid MP6 (*44*) and inoculated this library into host strains each supporting high-stringency positive selection for Ykt6 cleavage alongside negative selection against VAMP1 cleavage at various selection stringencies (Fig. 1, B, top, and C). Initial passages supported phage survival only at low stringency, enriching the mutation Ala^{166}→Glu (A166E). BoNT/X proteases containing A166E [for example, X(3206)A14] showed increased, though incomplete, preference for Ykt6 over VAMP1 (fig. S2). We then subjected the A166E-enriched population to additional PANCE in triplicate using the same set of host strains for 15 passages (Fig. 1B and fig. S3), resulting in phage persistence even at high stringency under high dilution. The final BoNT/X variants converged on distinct combinations of mutations, with substitutions at N143, T167, and L364 independently enriched in all three replicates (table S1). We observed a large apparent increase in Ykt6 selectivity in isolated variants (fig. S2), and we characterized in depth the clone BoNT/X(4130)B1 (Fig. 1D).

Purified X(4130)B1 protease (fig. S4) showed large increases in selectivity for Ykt6 over other native 60-mer substrate fragments when assayed in vitro (Fig. 1, E and F) (*55*, *56*). X(4130)B1 also showed reduced activity on not only VAMP1 but also other VAMP family substrates, despite the fact that no other VAMP homolog was the target of negative selection (Fig. 1F). Overall, evolved X(4130)B1 showed 1.5-fold-higher activity on Ykt6 and 700-fold-lower activity on VAMP1, -2, or -3 relative to wild-type BoNT/X LC, representing a total evolved protease selectivity change of 1060-fold. These findings establish that negative selection protease PANCE can evolve variants of a promiscuous BoNT protease with greatly improved substrate selectivity.

Reversion analysis of X(4130)B1 demonstrated that A166E and T167I were responsible for

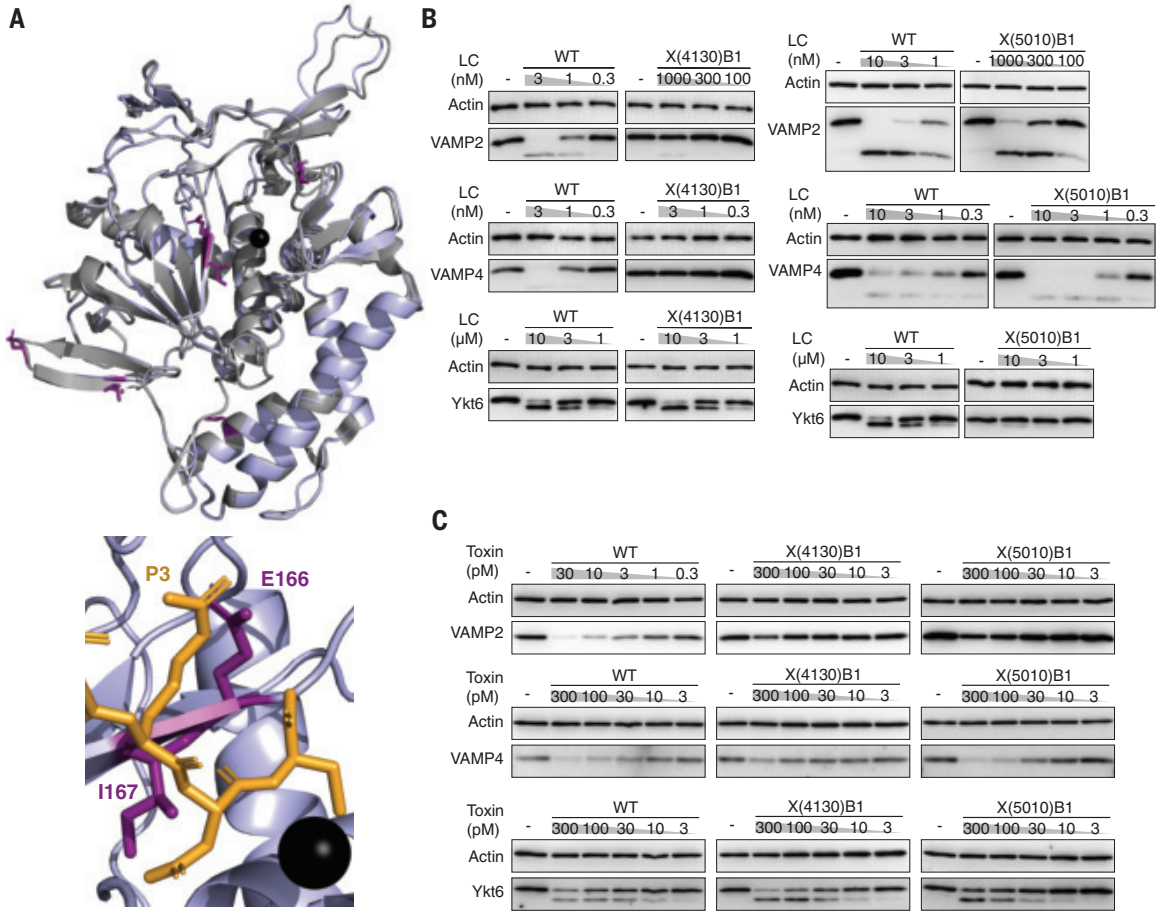

Fig. 2. Evolved BoNT protease structure, activity, and holotoxin compatibility in human cell lysates and in primary cortical neurons. (**A**, top) Superposition of the 1.8-Å resolution x-ray crystal structure of evolved X(4130)B1 (light blue) with the wild-type BoNT/X LC (gray; PDB 6F4E). Mutated residues in X(4130)B1 are shown in purple, with the active site zinc shown as a black sphere. (Bottom) Superposition of a BoNT/F LC-bound VAMP2 mimic (orange; from PDB 3FIE) and the crystal structure of X(4130)B1 (light blue), showing the close proximity of the P3 Arg (orange) to E166 and I167 (purple). The active site zinc is shown as a black sphere. (**B**) Evaluation of X(4130)B1 and X(5010)B1 activities on full-length substrates in human HEK293T cell lysates by immunoblotting. Actin served as a loading control. (**C**) Evolved LC protease delivery and activity as chimeric BoNT holotoxins (*53*) added to cultured rat cortical neurons. Neurons were treated with the indicated concentrations of holotoxin for 16 hours. Cleavage on endogenous VAMP2, VAMP4, and Ykt6 was detected by immunoblotting analysis of neuron lysates. WT, wild type; LC, light chain.

much of the selectivity for Ykt6 over VAMP1 (fig. S5). We further obtained x-ray diffraction–quality crystals of X(4130)B1 protease and solved a 1.8-Å resolution crystal structure (Fig. 2A and table S2) (PDB code 7KZ7). The fold of BoNT/X(4130)B1 is largely unchanged from that of wild-type BoNT/X LC (PDB code 6F47; root mean square deviation of 0.42 Å) (*54*). The E166 mutation places a negatively charged Glu side chain across the active site cleft from the catalytic zinc cofactor. The structure of the related BoNT/F protease bound to a VAMP2 substrate mimic (*40*) suggests that E166 may interact with the substrate's P3 residue (Fig. 2A). We speculate that the A166E mutation electrostatically repels the anionic P3 residue (D66) in VAMP1, while tolerating the neutral P3 amino acid (V171) in Ykt6, thereby contributing to Ykt6 selectivity.

Negative selection PANCE to evolve a VAMP4-selective BoNT/X protease

Next, we applied the protease negative selection to evolve BoNT/X LC into a VAMP4-selective protease that rejects VAMP1 (Fig. 1B, bottom). We began with PANCE in triplicate, again using a mutagenized population of wild-type BoNT/X LC phage, and observed phage titers drop rapidly at all stringencies, necessitating mutagenic drift at passage 5. After this rediversification, phage began to persist at low dilution factors and under the lowest negative selection stringency. Phage isolated after nine total passages converged on distinct sets of mutations between replicates, with mutations at N143, N164, P174, and S240 enriching across multiple populations. These proteases showed increased selectivity for VAMP4 over VAMP1 in the bacterial luciferase assay (fig. S6), although they also showed high apparent activity on Ykt6, likely because positions of divergence between VAMP1 and VAMP4 are mostly conserved between VAMP4 and Ykt6 (Fig. 1C).

We reinitiated PANCE using the same host strains to improve the partially VAMP4-selective phage. After 12 passages, clones from the highest stringency conditions in all three replicates (Fig. 1B and fig. S7) independently converged on mutations T224I and S240K (table S3). The replicate that evolved the clones with the highest selectivity also converged on the A166E mutation present in the Ykt6-selective X(4130). Because VAMP4 similarly lacks a negatively charged P3 Asp, these results support the hypothesis that the A166E mutation provides selectivity against VAMP1.

When evaluated by luciferase assay, all variants from the final PANCE passage showed very high apparent selectivity for VAMP4 over VAMP1 (fig. S8). As with the X(4130)B1 protease, we observed selectivity for VAMP4 over all other natural BoNT/X substrates, including VAMP5 and Ykt6, in several X(5010) protease variants (fig. S8). Protease BoNT/X(5010)B1, which contained eight mutations relative to wild-type BoNT/X protease, exhibited the highest selectivity for VAMP4 over all other BoNT/X substrates (Fig. 1G) and was characterized further. X(5010)B1 contained mutations in the substrate-binding cleft that may contribute to selectivity, including A166E, N164S, P174T, and S240K (fig. S9). Isolated X(5010)B1 protease (fig. S4) showed an 85-fold reduction in catalytic efficiency [the rate of turnover of the protease and its affinity to the substrate (the k_{cat}/K_M ratio)] for VAMP1 and a 2.5-fold increase in k_{cat}/K_M for VAMP4, resulting in an overall k_{cat}/K_M change of 218-fold compared with wild-type BoNT/X protease. Additional analysis revealed that X(5010)B1's preference for VAMP4 over VAMP5 improved >6-fold, and the preference for VAMP4 over Ykt6 increased 2.8-fold (Fig. 1G). These outcomes establish the ability of the PANCE dual positive and negative selection system to evolve selective proteases.

Biological evaluation of evolved BoNT/X proteases

To further validate the selectivity and activity of the evolved BoNT/X proteases on full-length substrates, we incubated purified proteases with lysate from human embryonic kidney (HEK) 293T cells expressing full-length VAMP2, VAMP4, or Ykt6. In HEK293T cell lysates, X(4130)B1 and X(5010)B1 each cleave their respective targets with selectivities consistent with their activity in vitro relative to wild-type BoNT/X protease (Figs. 1, F and G, and 2B).

To test if the evolved proteases remain compatible with native BoNT holotoxin delivery machinery, we incorporated proteases X(4130)B1 and X(5010)B1 into a hybrid holotoxin consisting of the evolved BoNT/X proteases linked to the BoNT/X translocation domain (H_N) and conjugated to the BoNT/A receptor binding domain (H_C) via sortase-mediated ligation (*53*). This process generated chimeric holotoxins containing X(4130)B1 or X(5010)B1 as their LCs (fig. S10). Both of these evolved protease holotoxins showed potent self-delivery and efficient cleavage of their intended intracellular targets at picomolar concentrations in cultured rat cortical neurons (Fig. 2C). Moreover, the evolved protease holotoxins show dramatically reduced (~100-fold lower) cleavage of their native target VAMP2, indicating that the large activity and selectivity changes evolved during PANCE in bacteria also manifest in neurons. These findings establish that the dual selection protease evolution platform can generate reprogrammed BoNT proteases that support assembly into holotoxins, intracellular delivery into neurons, and selective activity on their chosen targets in mammalian cells.

Evolution of BoNT protease activity on a noncanonical SNARE substrate

We next challenged the dual selection system to reprogram a BoNT protease to cleave a novel SNARE target not known to be processed by any native BoNT protease. We chose to evolve BoNT/F LC protease because of the availability of structural (*40*) and structure–activity relationship (*57*) data. We selected the longin-SNARE VAMP7 as the target because of its role in trafficking, secretion, and autophagy (*58*). VAMP7 poses a challenge as a new target because of its limited homology (40% identity) with VAMP1, -2, and -3 across the protease recognition site (Fig. 3A, bottom) (*57*), and no BoNT proteases have been reported to cleave VAMP7.

We designed a positive-selection evolutionary trajectory for BoNT/F protease starting from VAMP1(T29–R88) and ending with VAMP7(K121–R180) (table S4). The trajectory passes through five intermediate substrates that serve as evolutionary stepping stones (Fig. 3A). We first evolved tolerance of the D59G mutation in VAMP1 (stepping stone F1, or SS.F1), which is known to prevent cleavage by BoNT/F (*57*). We then divided the surviving phage into three replicate populations that were subjected to PACE on the remaining stepping stones in parallel to preserve access to diverse solutions (*42*). We added substrate mutations L56A (SS.F2), Q60E (SS.F3), and K61R (SS.F4) before challenging the surviving phage on SS.F7, which contained seven mutations as well as substrate termini from VAMP7 (Fig. 3A, bottom). Surviving phage were ultimately evolved in host cells harboring a T7-PAP containing VAMP7(K121–R180). The resulting replicate populations were pooled and then competed in a PACE experiment with a high-stringency VAMP7 AP, yielding the genotypes in table S5.

The overall PACE campaign consisted of 795 hours of PACE in the longest linear path, requiring phage to survive an average total dilution of ~10^{240}-fold. The resulting proteases (Fig. 3B) exhibited high apparent cleavage activity on the VAMP7 selection substrate (Fig. 3C). Clone F(3041)B6, with 16 mutations relative to wild-type BoNT/F protease, showed ≥18-fold-improved activity on VAMP7 in vitro, which was constrained by the detection limit of VAMP7 cleavage by wild-type BoNT/F (fig. S11). These efforts demonstrated the possibility of evolving a BoNT protease that cleaves a protein outside the known substrate portfolio of natural BoNTs.

Consistent with prior efforts to reprogram proteases (*19*), the VAMP7-cleaving BoNT/F variants maintained activity on the native VAMP1 substrate (fig. S12). We therefore applied the dual selection system to reduce activity on VAMP1 while maintaining activity on VAMP7. Starting with the F(3041) population,

we initiated PANCE in separate replicates at four negative selection stringencies (Fig. 3A). Initially, phage persisted only in hosts containing the two lowest-stringency negative selection VAMP1 APs. After periodic reinfection into high-stringency negative selection host cells, the evolving phage eventually accessed solutions capable of robust propagation at 10-fold-higher dilution levels than initial passages (fig. S13). After 15 total passages, we evaluated clones (table S6) surviving at the highest negative selection stringency in a luciferase assay (Fig. 3C). These assays suggested variants evolved greatly reduced activity on VAMP1 while maintaining VAMP7 activity. Based on activity, selectivity, and protein production levels, we selected BoNT/F(3230)A3 for in-depth characterization.

Purification and in vitro assessment confirmed that F(3230)A3 protease cleaves the target VAMP7 sequence (figs. S4 and S14), with only trace cleavage of VAMP1 (Fig. 3D). Because the activity of wild-type BoNT/F on VAMP7 was too low to determine the k_{cat}/K_M, turnover frequency ($k_{cat,app}$) at 5 mM substrate was used to compare selectivity between evolved and wild-type BoNT/F proteases. The evolved F(3230)A3 protease cleaved VAMP1 (T29–R88) with a $k_{cat,app}$ of 1.6×10^{-4} s^{-1} and VAMP7 with a $k_{cat,app}$ of 7.7×10^{-3} s^{-1}. By contrast, wild-type BoNT/F protease cleaved VAMP1 with a $k_{cat,app}$ of 1.1 s^{-1} and VAMP7 with a $k_{cat,app}$ of $<1.5 \times 10^{-4}$ s^{-1}. Thus, the total selectivity change of evolved F(3230)A3 favoring VAMP7 (≥51-fold) and disfavoring VAMP1 (6800-fold) is $\geq 3.5 \times 10^{5}$–fold.

To illuminate the role of individual mutations, we separately reverted each of the 21 mutations in F(3230)A3 and assessed their relative VAMP1 and VAMP7 cleavage activities in a luciferase assay (fig. S15). None of the individual reversion mutants recovered meaningful VAMP1 activity, demonstrating that the origins of selectivity cannot be attributed to any single mutation. Several reversions (H72Y, A106V, N148S, P158A, Y166S, H184N, G200E, I224S, and L240R) reduced apparent VAMP7 activity, suggesting that

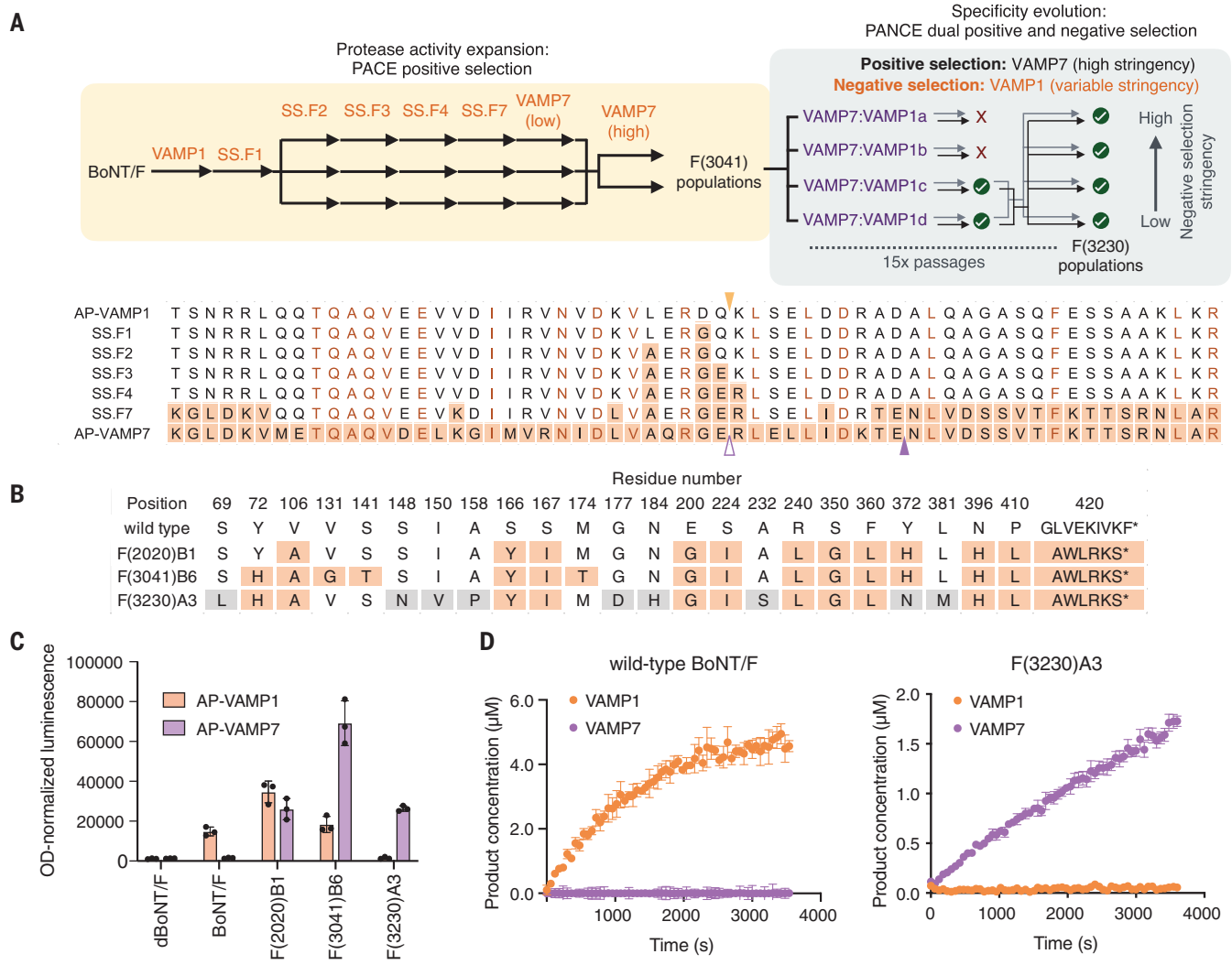

Fig. 3. Phage-assisted evolution of a VAMP7-selective BoNT protease. (**A**, top) Summary of the strategy for stepwise evolution of a VAMP7-cleaving protease from BoNT/F LC protease, followed by dual positive and negative selection for evolving VAMP7 selectivity from promiscuous variants. (Bottom) Substrates used during the evolution of a VAMP7-selective protease from a VAMP1-cleaving protease. The orange wedge shows the wild-type BoNT/F cleavage site. The predicted (hollow) and actual (filled) purple wedges show VAMP7 cleavage sites of the evolved F(3230)A3 protease. (**B**) Selected variants from evolution of VAMP7-selective BoNT/F proteases. Mutations in gray were enriched during negative selection. (**C**) Apparent protease activity by luciferase assay for selected clones from various stages of BoNT/F evolution dBoNT/F is an inactive BoNT/F protease mutant. (**D**) Comparison of wild-type BoNT/F protease (left) and evolved F(3230)A3 protease (right) activity on VAMP1 and VAMP7. Assays were performed using proteases containing an N-terminal maltose-binding protein (MBP) tag under standard assay conditions at 37°C with 5 μM substrate and either 2.5 nM BoNT/F or 50 nM F(3230)A3.

they are important either for VAMP7 activity or for expression in *E. coli*. Four reversion mutations increased apparent VAMP7 activity: S232A, G350S, M381L, and L410P. When these four reversions were combined, VAMP1 off-target cleavage activity increased markedly (fig. S16). These results are consistent with the complex nature of BoNT protease substrate recognition and processing, which are driven by exosite binding interactions as well as conformational reorientation (*39*, *40*).

BoNT/F(3230)A3 also demonstrated ≥20-fold selectivity for VAMP7 over all eight related VAMP family members (table S7). Although the basis of this broad selectivity is not clear, we determined by mass spectrometry that F(3230)A3 cleaved VAMP7 not between E152 and R153, as anticipated, but instead 10 residues C-terminal, after E162 (Fig. 3A, bottom, and fig. S17). This region of VAMP7 contains several residues, including L156, I158, T161, and N163, that are minimally conserved among the eight other VAMP family proteins. To test whether this cleavage site shift contributes to specificity for VAMP7, we generated chimeric VAMP7-VAMP1 substrates with substituted corresponding VAMP7 residues into VAMP1 at positions E64, D66, A69, and A71 (fig. S18). None of the resulting

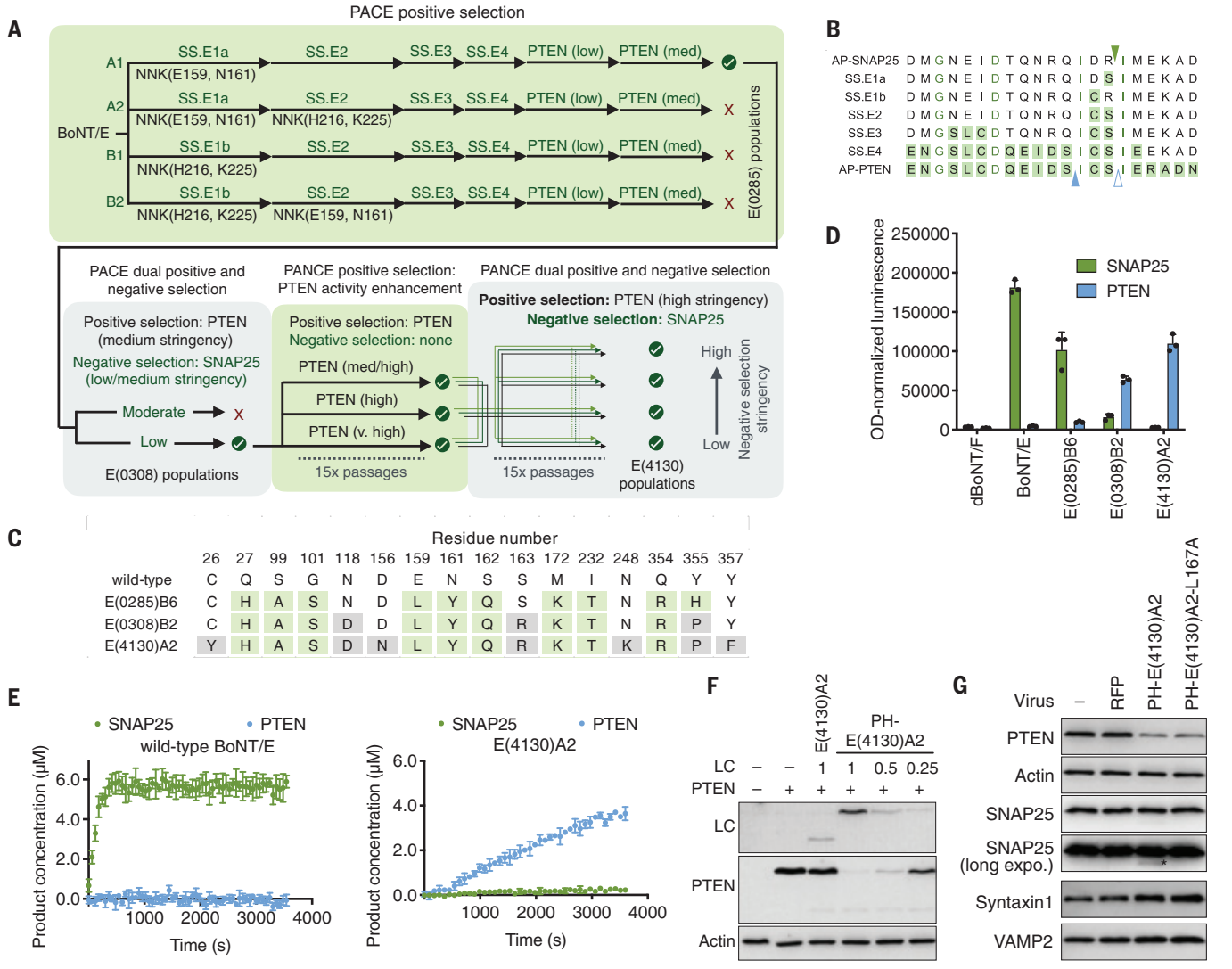

Fig. 4. Phage-assisted evolution of a BoNT protease that selectively cleaves PTEN, a non-SNARE protein. (**A**) Strategy for stepwise evolution of a PTEN-cleaving protease from wild-type SNAP-25–cleaving BoNT/E LC protease. (**B**) Protease cleavage substrates used during the evolution of a PTEN-selective protease. (**C**) Selected variants from the evolution of a PTEN-selective BoNT/E protease. Mutations in green were enriched during the positive selection, and mutations in gray were enriched during negative selection. (**D**) Apparent protease activity by luciferase assay of clones from BoNT/E evolution. (**E**) Comparison of wild-type BoNT/E LC (left) and E(4130)A2 protease (right) activity on SNAP-25 and PTEN. Assays were performed under standard conditions at 37°C using 5 μM substrate and 10 nM protease. (**F**) Evaluation of full-length PTEN cleavage in cells. FLAG-tagged full-length PTEN was coexpressed with either hemagglutinin (HA)-tagged E(4130)A2 or HA-tagged PH-E(4130)A2 in HEK293 cells. PH-E(4130)A2 contains an N-terminal pleckstrin homology (PH) domain fused to E(4130)A2. Cell lysates were analyzed by immunoblotting, detecting PTEN (via FLAG-tag) and E(4130)A2 (via HA tag). Actin served as a loading control. Numbers indicate the ratio of the BoNT LC and PTEN substrate plasmids. (**G**) PTEN and SNARE protein cleavage in cultured rat cortical neurons transduced with lentivirus expressing RFP (red fluorescent protein, a negative control), PH-E(4130)A2 protease, or the PH-E(4130)A2(L167A) protease. Neuron lysates were analyzed by immunoblotting, detecting endogenous PTEN, SNAP-25, VAMP2, and Syntaxin 1. Actin served as a loading control. The asterisk marks the minor cleavage of SNAP-25 by PH-E(4130)A2 detected with long exposure time (Long expo.), which was not observed for PH-E(4130)A2(L167A).

individual VAMP1 mutants were competent substrates for F(3230)A3, but the combination of all four substitutions yielded a substrate that was cleaved by evolved F(3230)A3 (fig. S18). These findings suggest that PACE led to recognition of an optimal VAMP7 sequence that diverges from other VAMP homologs to survive the dual selection, resulting in broad specificity among other VAMP proteins.

Evolution of BoNT proteases that selectively cleave a non-SNARE target

To further challenge this protease evolution platform, we sought to generate BoNT proteases that selectively cleave a target unrelated to SNARE proteins. We selected BoNT/E protease for this purpose, which natively targets SNAP-25. Interactions between BoNT/E and SNAP-25 residues G168 (P13), D172 (P9), I178 (P3), and I181 (P1′) are known important substrate recognition elements (*59*). We performed a protein BLAST search for targets that preserved these residues with similar spacing, with no restrictions on the 16 remaining positions across a 20-residue sequence query. We manually reviewed the resulting candidates for target sequence accessibility with available structural data and for potential biomedical impact. This evaluation identified phosphatase and tensin homolog (PTEN) as an attractive target. PTEN plays a number of critical roles in cellular signaling (*60*, *61*) and has been a target of long-standing interest in regenerative medicine. Recent reports suggest that PTEN knockdown can stimulate nerve regeneration after injury (*62*). PTEN is not a SNARE protein and shares only 4 of 21 residues with SNAP-25 flanking the anticipated proteolysis site. The evolution of a BoNT protease that selectively cleaves PTEN thus represents a formidable challenge.

Integrating the lessons from the campaigns described above, we pursued parallel evolutionary trajectories toward a PTEN-cleaving BoNT/E variant (Fig. 4A and table S8). Trajectory A began by challenging proteases to recognize the P1 site R180S mutation (SS.E1a), starting from phage containing NNK codon randomization at E159 and N161 in BoNT/E. Survivors of PACE on SS.E1a were then challenged to cleave a stepping stone substrate containing the D179C+R180S double mutant (SS.E2) either with continuous mutagenesis (trajectory A1) or with NNK codon randomization of H216 and K225 prior to inoculation (trajectory A2). Trajectory B began with the P2 site D179C mutation (SS.E1b), and PACE experiments were inoculated with BoNT/E phage carrying NNK codon libraries at H216 and K225. This initial PACE stage was also followed by selection on the D179C+R180S double mutant (SS.E2), either directly (trajectory B1) or with NNK codon randomization of E159 and N161 (trajectory B2) (Fig. 4A).

These PACE trajectories each converged on distinct genotypes. We evolved the resulting populations separately on four additional evolutionary stepping stones before selection on the final PTEN target sequence (Fig. 4, A and B). These intermediate substrates first incorporated PTEN residues S294 to C296 in place of the SNAP-25 residues N169 to I171 (SS.E3), then replaced the entire N-terminal SNAP-25 D166–Q177 with PTEN residues E291 to S302 (SS.E4). Last, all lineages were challenged with PACE on PTEN E291–N311 (AP-PTEN) at low and then moderate stringency (Fig. 4A). Surviving phage originated from a single lineage (trajectory A1), which strongly enriched 10 consensus mutations relative to wild-type BoNT/E protease (Fig. 4C). In luciferase assays, the consensus clone E(0285)B6 demonstrated clear but weak PTEN cleavage activity (Fig. 4D and fig. S19). As expected given the absence of negative selection, this evolved protease retained high activity on its native SNAP-25 substrate.

Next, we performed low-stringency dual positive and negative selection PACE to reduce activity on SNAP-25 and improve activity on PTEN. These experiments evolved BoNT/E protease variants such as E(0308)B2 (Fig. 4C), with improved, but incomplete, selectivity (Fig. 4D). After rediversifying the protease populations across 15 passages of positive selection PANCE on PTEN (Fig. 4A, middle bottom), we performed an additional 15 PANCE passages of dual positive and negative selection (Fig. 4A and fig. S20). After passage 15, phage from the host cells containing the highest-stringency negative selection APs (table S9) converged on additional mutations C26Y, D156N, N248K, and Y357F (Fig. 4C). The consensus clone BoNT/E(4130)A2 carried 16 total mutations compared with wild-type BoNT/E protease, with 7 mutations arising during negative selection. This E(4130)A2 protease demonstrated high apparent activity on the PTEN substrate with nearly undetectable activity on SNAP-25 in luciferase assays (Fig. 4D). Reversion analysis (fig. S21) revealed that E159L, N161Y, S162Q, and S163R contribute to PTEN cleavage activity.

Isolation and in vitro kinetic assessment of E(4130)A2 (fig. S4) confirmed high activity levels on PTEN and low activity on SNAP-25. E(4130)A2 protease efficiently cleaved the target PTEN sequence, which is not detectably cleaved by wild-type BoNT/E protease, with a measured improvement in k_{cat} of >18,300-fold, which was constrained by the assay's limit of detection (Fig. 4E). When combined with 606-fold reduced cleavage of the endogenous SNAP-25 substrate (Fig. 4E), E(4130)A2 exhibited an overall $\geq 1.1 \times 10^7$–fold change in substrate selectivity. This large change in selectivity was driven primarily by a much higher k_{cat} for PTEN, which increased from $<3.2 \times 10^{-5}$ s^{-1} for wild-type BoNT/E protease to 0.59 s^{-1} for E(4130)A2, rather than by an impaired K_M for SNAP-25 (fig. S22). Selectivity through k_{cat} rather than K_M is consistent with host cells producing a large excess of off-target SNAP-25 substrate relative to the on-target substrate during the negative selection. At high concentrations of SNAP-25, BoNT/E variants that evolve impaired K_M for SNAP-25 likely gain little fitness compared to variants that evolve impaired k_{cat} for SNAP-25. Adjusting the concentrations of substrates (PAPs) could modify the selection in ways that favor improvements in selectivity that are K_M-driven.

Interestingly, the E(4130)A2 cleavage site in PTEN was determined by mass spectrometry to occur after PTEN residue S302 (fig. S23), three residues N-terminal from our predicted cleavage position. This cleavage position preserves key amino acid identity between SNAP-25 and PTEN at P1′, P2, and P3, which is apparently preferred over predicted cleavage site preservation at P1′, P3, P9, and P13 (Fig. 4B). Consistent with the cleavage site shift during the evolution of BoNT/F(3230)A3, positional flexibility during protease evolution may contribute to the acquisition of selective activity on new targets. Collectively, these results demonstrate the feasibility of evolving BoNT proteases that cleave non-SNARE targets.

Last, we assessed E(4130)A2 in mammalian cells. We cotransfected plasmids encoding the protease and PTEN into HEK293T cells. Although weak cleavage of PTEN was detected, most PTEN was not cleaved in cells (Fig. 4F), potentially because PTEN is localized to plasma membranes, whereas BoNT/E LC is known to remain cytosolic (*63*). To localize the evolved protease to plasma membranes, we fused to the N terminus of E(4130)A2, a plextrin homology (PH) domain from protein kinase C (*64*). Coexpression of this PH-E(4130)A2 protease with full-length PTEN resulted in efficient cleavage in HEK293T cells (Fig. 4F). Expression of either E(4130)A2 or PH-E(4130)A2 resulted in no loss of viability (fig. S24), an important additional indicator of selectivity.

We also transduced rat cortical neurons with lentivirus encoding PH-E(4130)A2 and then examined cleavage of both endogenous PTEN and SNAP-25 by Western blotting. The transduced cells showed substantial cleavage of endogenous PTEN, with minimal off-target cleavage of the native BoNT/E substrate SNAP-25 (Fig. 4G). This selectivity was further enhanced by introducing the L167A mutation, which is known to disrupt an exosite binding interaction and decrease SNAP-25 cleavage by BoNT/E protease (*65*) (Fig. 4G). Other endogenous SNARE proteins, such as VAMP2 and Syntaxin 1, were not cleaved by PH-E(4130)A2 (Fig. 4G). These results confirm

that evolved BoNT proteases emerging from dual selection PACE can support efficient and selective proteolysis of a non-SNARE target in mammalian cells.

Discussion

BoNTs are powerful agents for mediating intracellular proteolysis, but attempts to extend their application beyond their small set of native SNARE protein targets has been a long-standing challenge. Here, we developed and applied a dual selection PACE system to evolve four BoNT protease variants that selectively cleave both native (Ykt6 and VAMP4) and non-native (VAMP7 and PTEN) substrates. The efficiency of phage-assisted evolution enables complex fitness landscapes to be quickly navigated using parallel trajectories and carefully controlled positive and negative selection stringencies. This system makes practical the evolution of proteases over hundreds of generations of mutation, selection, and replication. Varying additional selection parameters such as substrate concentration and PAP efficiency could in principle generate proteases with additional desired properties.

Our findings establish that BoNT proteases may be far more evolutionarily malleable than their high natural target specificity would suggest. The evolved F(3230)A3 and E(4130)A2 proteases cleave new substrates that share limited homology with their native substrates. The known exosite dependence of BoNT proteases may facilitate reprogramming their specificities, as their extended enzyme–substrate interface provides a large surface over which new contacts can evolve while maintaining interactions required for catalysis.

Though extended substrate recognition may contribute evolutionary plasticity and selectivity in BoNT proteases, we found a structurally homologous five–amino acid stretch of BoNT protease active sites (residues 164 to 168 in BoNT/F, 159 to 163 in BoNT/E, and 164 to 168 in BoNT/X) that carried at least two mutations in each of the evolved proteases characterized in depth in this study (fig. S25). The comparatively high frequency of mutations in this region across all four evolved proteases suggests that diversifying this region of BoNT proteases may be especially productive for future BoNT reprogramming efforts.

The ability to potently deliver their protease domains to the cytosol of susceptible cells is a remarkable feature of BoNTs. It is encouraging that evolved BoNT proteases can retain compatibility with translocation machinery in BoNT HCs to form functional holotoxins. Efforts to engineer BoNT HCs to support self-delivery to various cell and tissue types (*66*) raise the intriguing possibility of developing evolved BoNTs for tissue-specific delivery of reprogrammed proteases that selectively manipulate target intracellular proteins.

REFERENCES AND NOTES

1. Q. Li, L. Yi, P. Marek, B. L. Iverson, *FEBS Lett.* **587**, 1155–1163 (2013).
2. H. Zhao, F. H. Arnold, *Protein Eng. Des. Sel.* **12**, 47–53 (1999).
3. L. You, F. H. Arnold, *Protein Eng.* **9**, 77–83 (1996).
4. E. L. Madison, E. J. Goldsmith, R. D. Gerard, M. J. Gething, J. F. Sambrook, *Nature* **339**, 721–724 (1989).
5. B. C. Dickinson, M. S. Packer, A. H. Badran, D. R. Liu, *Nat. Commun.* **5**, 5352 (2014).
6. S. W. Meister, N. M. Hendrikse, J. Löfblom, *Biol. Chem.* **400**, 405–415 (2019).
7. M. I. Sanchez, A. Y. Ting, *Nat. Methods* **17**, 167–174 (2020).
8. G. A. Allen *et al*., *Arterioscler. Thromb. Vasc. Biol.* **27**, 683–689 (2007).
9. S. Sellamuthu *et al*., *Biochem. Biophys. Res. Commun.* **371**, 122–126 (2008).
10. D. T. Tran, V. J. Cavett, V. Q. Dang, H. L. Torres, B. M. Paegel, *Proc. Natl. Acad. Sci. U.S.A.* **113**, 14686–14691 (2016).
11. S. S. Sidhu, T. J. Borgford, *J. Mol. Biol.* **257**, 233–245 (1996).
12. C. Renicke, R. Spadaccini, C. Taxis, *PLOS ONE* **8**, e67915 (2013).
13. K. D. Verhoeven, O. C. Altstadt, S. N. Savinov, *Appl. Biochem. Biotechnol.* **166**, 1340–1354 (2012).
14. Y. C. Lin *et al*., *J. Virol.* **74**, 4710–4720 (2000).
15. T. W. Ridky *et al*., *J. Biol. Chem.* **271**, 10538–10544 (1996).
16. S. Sellamuthu *et al*., *PLOS ONE* **6**, e22554 (2011).
17. J. L. Guerrero, M. A. O'Malley, P. S. Daugherty, *ACS Chem. Biol.* **11**, 961–970 (2016).
18. M. E. Hill *et al*., *ACS Chem. Biol.* **11**, 1603–1612 (2016).
19. M. S. Packer, H. A. Rees, D. R. Liu, *Nat. Commun.* **8**, 956 (2017).
20. B. M. Dorr, H. O. Ham, C. An, E. L. Chaikof, D. R. Liu, *Proc. Natl. Acad. Sci. U.S.A.* **111**, 13343–13348 (2014).
21. J. C. Carlson, A. H. Badran, D. A. Guggiana-Nilo, D. R. Liu, *Nat. Chem. Biol.* **10**, 216–222 (2014).
22. A. H. Badran *et al*., *Nature* **533**, 58–63 (2016).
23. J. H. Hu *et al*., *Nature* **556**, 57–63 (2018).
24. K. M. Esvelt, J. C. Carlson, D. R. Liu, *Nature* **472**, 499–503 (2011).
25. S. W. Santoro, L. Wang, B. Herberich, D. S. King, P. G. Schultz, *Nat. Biotechnol.* **20**, 1044–1048 (2002).
26. K. B. Levin *et al*., *Nat. Struct. Mol. Biol.* **16**, 1049–1055 (2009).
27. H. Renata, Z. J. Wang, F. H. Arnold, *Angew. Chem. Int. Ed.* **54**, 3351–3367 (2015).
28. Z. M. Carrico, K. L. Strobel, M. E. Atreya, D. S. Clark, M. B. Francis, *Biotechnol. Bioeng.* **113**, 1187–1193 (2016).
29. N. Varadarajan, J. Gam, M. J. Olsen, G. Georgiou, B. L. Iverson, *Proc. Natl. Acad. Sci. U.S.A.* **102**, 6855–6860 (2005).
30. N. Varadarajan, S. Rodriguez, B. Y. Hwang, G. Georgiou, B. L. Iverson, *Nat. Chem. Biol.* **4**, 290–294 (2008).
31. L. Yi *et al*., *Proc. Natl. Acad. Sci. U.S.A.* **110**, 7229–7234 (2013).
32. N. Varadarajan, G. Georgiou, B. L. Iverson, *Angew. Chem. Int. Ed.* **47**, 7861–7863 (2008).
33. B. Ramesh *et al*., *ACS Chem. Biol.* **14**, 2616–2628 (2019).
34. M. Dong, G. Masuyer, P. Stenmark, *Annu. Rev. Biochem.* **88**, 811–837 (2019).
35. M. Pirazzini, O. Rossetto, R. Eleopra, C. Montecucco, *Pharmacol. Rev.* **69**, 200–235 (2017).
36. T. C. Südhof, J. E. Rothman, *Science* **323**, 474–477 (2009).
37. S. Chen, J. T. Barbieri, *Proc. Natl. Acad. Sci. U.S.A.* **106**, 9180–9184 (2009).
38. T. Binz *et al*., *Toxicon* **156**, S10 (2018).
39. M. A. Breidenbach, A. T. Brunger, *Nature* **432**, 925–929 (2004).
40. R. Agarwal, J. J. Schmidt, R. G. Stafford, S. Swaminathan, *Nat. Struct. Mol. Biol.* **16**, 789–794 (2009).
41. J. L. Guerrero, P. S. Daugherty, M. A. O'Malley, *Biotechnol. Bioeng.* **114**, 33–38 (2017).
42. B. C. Dickinson, A. M. Leconte, B. Allen, K. M. Esvelt, D. R. Liu, *Proc. Natl. Acad. Sci. U.S.A.* **110**, 9007–9012 (2013).
43. B. P. Hubbard *et al*., *Nat. Methods* **12**, 939–942 (2015).
44. A. H. Badran, D. R. Liu, *Nat. Commun.* **6**, 8425 (2015).
45. D. I. Bryson *et al*., *Nat. Chem. Biol.* **13**, 1253–1260 (2017).
46. T. B. Roth, B. M. Woolston, G. Stephanopoulos, D. R. Liu, *ACS Synth. Biol.* **8**, 796–806 (2019).
47. M. F. Richter *et al*., *Nat. Biotechnol.* **38**, 883–891 (2020).
48. S. M. Miller *et al*., *Nat. Biotechnol.* **38**, 471–481 (2020).
49. B. W. Thuronyi *et al*., *Nat. Biotechnol.* **37**, 1070–1079 (2019).
50. S. M. Miller, T. Wang, D. R. Liu, *Nat. Protoc.* **15**, 4101–4127 (2020).
51. G. Masuyer, J. A. Chaddock, K. A. Foster, K. R. Acharya, *Annu. Rev. Pharmacol. Toxicol.* **54**, 27–51 (2014).
52. F. Keith, C. John, *Toxins (Basel)* **2**, 2795–2815 (2010).
53. S. Zhang *et al*., *Nat. Commun.* **8**, 14130 (2017).
54. G. Masuyer *et al*., *Sci. Rep.* **8**, 4518 (2018).
55. D. R. Ruge *et al*., *Anal. Biochem.* **411**, 200–209 (2011).
56. M. Dong, W. H. Tepp, E. A. Johnson, E. R. Chapman, *Proc. Natl. Acad. Sci. U.S.A.* **101**, 14701–14706 (2004).
57. S. Sikorra, T. Henke, T. Galli, T. Binz, *J. Biol. Chem.* **283**, 21145–21152 (2008).
58. F. Daste, T. Galli, D. Tareste, *J. Cell Sci.* **128**, 4263–4272 (2015).
59. S. Chen, J. T. Barbieri, *J. Biol. Chem.* **281**, 10906–10911 (2006).
60. Y. R. Lee, M. Chen, P. P. Pandolfi, *Nat. Rev. Mol. Cell Biol.* **19**, 547–562 (2018).
61. C. A. Worby, J. E. Dixon, *Annu. Rev. Biochem.* **83**, 641–669 (2014).
62. K. Liu *et al*., *Nat. Neurosci.* **13**, 1075–1081 (2010).
63. E. Fernández-Salas *et al*., *Proc. Natl. Acad. Sci. U.S.A.* **101**, 3208–3213 (2004).
64. J. Chen, Z. J. Chen, *Nature* **564**, 71–76 (2018).
65. S. Chen, J. T. Barbieri, *J. Biol. Chem.* **282**, 25540–25547 (2007).
66. A. Pickett, K. Perrow, *Toxins (Basel)* **3**, 63–81 (2011).

ACKNOWLEDGMENTS

We thank A. Kupinski, V. Tripathi, S. Donald, M. Beard, and K. Foster for contributions to research design. We thank A. Viera for contributions during manuscript preparation and T. Wang for helpful discussions. **Funding:** This work was supported by U.S. NIH grants R01EB027793, R01EB022376, R35GM118062, R01NS080833, R01AI132387, R01AI139087, R21NS106159, and HHSN272201700060C, the Burroughs Wellcome Fund, the Howard Hughes Medical Institute, and Ipsen Bioinnovation. T.R.B. is a Ruth L. Kirchstein National Research Service Award Postdoctoral Fellow (F32 GM122261-03). This research used the Advanced Photon Source, operated for the DOE Office of Science by Argonne National Laboratory (DE-AC02-06CH11357) and LS-CAT Sector 21, supported by the Michigan Economic Development Corporation and the Michigan Technology Tri-Corridor (085P1000817). **Author contributions:** T.R.B. designed the research, performed experiments, analyzed data, and wrote the manuscript. H.L. designed and performed mammalian cell and delivery experiments. M.S.P. and M.R. assisted in research design, experiments, and data analysis for BoNT/E evolution. P.-G.L. produced sortase-ligated toxins and assisted with analysis on cultured neurons. X.X., S.Z., G.M., and K.J.F.S. performed crystallization and structure determination. M.D. and D.R.L. designed and supervised the research and wrote the manuscript. **Competing interests:** The authors have filed patent applications on the evolved proteases, PACE, and related improvements. K.J.F.S. holds a patent on a different protease targeting cancer signaling. All other authors declare no competing interests. **Data and materials availability:** Plasmids used in this study are available from Addgene. The atomic coordinates and structure factors (code 7KZ7) have been deposited in the Protein Data Bank (http://wwpdb.org).

SUPPLEMENTARY MATERIALS

science.sciencemag.org/content/371/6531/803/suppl/DC1
Materials and Methods
Figs. S1 to S25
Tables S1 to S9
References (*67*–*73*)
MDAR Reproducibility Checklist

5 November 2020; accepted 24 December 2020
10.1126/science.abf5972

PALEOENVIRONMENT

A global environmental crisis 42,000 years ago

Alan Cooper[1,2]*†, Chris S. M. Turney[3]*†, Jonathan Palmer[3], Alan Hogg[4], Matt McGlone[5], Janet Wilmshurst[5,6], Andrew M. Lorrey[7], Timothy J. Heaton[8], James M. Russell[9], Ken McCracken[10], Julien G. Anet[11], Eugene Rozanov[12,13,14], Marina Friedel[12], Ivo Suter[15], Thomas Peter[12], Raimund Muscheler[16], Florian Adolphi[17], Anthony Dosseto[18], J. Tyler Faith[19], Pavla Fenwick[20], Christopher J. Fogwill[21], Konrad Hughen[22], Mathew Lipson[23], Jiabo Liu[24], Norbert Nowaczyk[25], Eleanor Rainsley[21], Christopher Bronk Ramsey[26], Paolo Sebastianelli[27], Yassine Souilmi[28], Janelle Stevenson[29,30], Zoë Thomas[3], Raymond Tobler[28], Roland Zech[31]

Geological archives record multiple reversals of Earth's magnetic poles, but the global impacts of these events, if any, remain unclear. Uncertain radiocarbon calibration has limited investigation of the potential effects of the last major magnetic inversion, known as the Laschamps Excursion [41 to 42 thousand years ago (ka)]. We use ancient New Zealand kauri trees (*Agathis australis*) to develop a detailed record of atmospheric radiocarbon levels across the Laschamps Excursion. We precisely characterize the geomagnetic reversal and perform global chemistry-climate modeling and detailed radiocarbon dating of paleoenvironmental records to investigate impacts. We find that geomagnetic field minima ~42 ka, in combination with Grand Solar Minima, caused substantial changes in atmospheric ozone concentration and circulation, driving synchronous global climate shifts that caused major environmental changes, extinction events, and transformations in the archaeological record.

Over the recent past, Earth's magnetic field has steadily weakened (~9% in the past 170 years), and this, along with the current rapid movement of the magnetic North Pole, has increased speculation that a field reversal may be imminent (*1*, *2*). The estimated economic impacts of such a reversal have focused on the increased exposure to extreme solar storms, with multibillion-dollar daily loss estimates (*3*) likely to be conservative. One of the best opportunities to study the impacts of extreme changes in Earth's magnetic field is the Laschamps Excursion (hereafter Laschamps)—a recent, relatively short-duration (<1000 year) reversal ~41 thousand years ago (ka) (*4*). Sedimentary and volcanic deposits indicate a weakening of the magnetic field intensity to <28% of current levels during the reversed phase of the Laschamps and, notably, as little as 0 to 6% during the preceding transition as polarity switched (Fig. 1 and supplementary materials) (*1*, *2*, *5*).

Studies of Greenland ice cores have failed to reveal marked impacts in high-latitude paleoclimate associated with Laschamps (*5*, *6*), and this observation has underpinned the current view that there is no relationship between geomagnetic reversals and climate or environmental changes. However, the markedly increased levels of solar and cosmic radiation reaching Earth's atmosphere because of the weakened geomagnetic field are likely to have increased atmospheric ionization and decreased stratospheric ozone levels, potentially generating regional climatic impacts, particularly in lower latitudes (*7*–*9*). In this regard, it is notable that many environmental records around the Pacific Basin appear to detail a major (and often sustained) change in behavior ~40 to 42 ka, including local glacial maxima in Australasia and the Andes (*7*, *10*), long-term shifts in atmospheric circulation patterns (*11*, *12*), and continent-wide aridification and megafaunal extinction in Australia (*4*, *13*–*16*). The same period in North America saw the rapid, pronounced expansion of the Laurentide Ice Sheet (LIS) from a local minimum close to 42 ka (*17*–*19*). Many of these records document a long-term phase shift into a glacial state that persisted until the transition into the Holocene (~11.6 ka), in direct contrast to the Atlantic Basin records of millennial-scale abrupt and extreme changes associated with stadial-interstadial events.

Although the Pacific Basin environmental changes appear broadly coincident with the Laschamps, the lack of knowledge about the exact timing and duration of the geomagnetic excursion has greatly limited the ability to examine whether it played any role. In addition, chronological uncertainties are complicated in radiocarbon-dated terrestrial and marine records around the Laschamps because of the elevated production of ^{14}C and ^{10}Be, cosmogenic radionuclides resulting from the substantial increase in high-energy cosmic radiation reaching the upper atmosphere. The high ^{10}Be flux has been well described from Greenland and Antarctic ice core records (*6*, *20*, *21*), which reveal synchronous century-long ^{10}Be peaks across the Laschamps that appear to reflect a series of pronounced Grand Solar Minima (GSM; prolonged periods of low solar activity similar to the Spörer and Maunder Minima: 1410 to 1540 CE and 1645 to 1715 CE), with unknown climate impacts (*20*, *21*). By contrast, the associated atmospheric ^{14}C changes remain poorly constrained (*22*), preventing precise calibration (*23*).

Radiocarbon changes across the Laschamps

In this study, we performed detailed radiocarbon analyses of ancient kauri (*Agathis australis*) trees preserved in northern New Zealand wetlands (*24*) to generate a contiguous reconstruction of atmospheric ^{14}C across the Laschamps (see supplementary materials). We compared a series of radiocarbon measurements across multiple kauri trunk cross sections to identify variations in atmospheric radiocarbon at a highly resolved level. A 1700-year record from a tree recovered from Ngāwhā, Northland, is

[1]South Australian Museum, Adelaide, SA 5000, Australia. [2]BlueSky Genetics, PO Box 287, Adelaide, SA 5137, Australia. [3]Chronos ^{14}Carbon-Cycle Facility, and Earth and Sustainability Science Research Centre, University of New South Wales, Sydney, NSW 2052, Australia. [4]Radiocarbon Dating Laboratory, University of Waikato, Hamilton 3240, New Zealand. [5]Landcare Research, PO Box 69040, Lincoln, New Zealand. [6]School of Environment, University of Auckland, Private Bag 92019, Auckland 1142, New Zealand. [7]National Institute of Water and Atmospheric Research Ltd, Auckland 1010, New Zealand. [8]School of Mathematics and Statistics, University of Sheffield, Sheffield S3 7RH, UK. [9]Department of Geological Sciences, Brown University, Providence, RI 02912, USA. [10]University of New South Wales, Sydney, NSW 2052, Australia. [11]Zurich University of Applied Sciences, Centre for Aviation, 8401 Winterthur, Switzerland. [12]Institute for Atmospheric and Climatic Science, ETH Zurich, 8006 Zurich, Switzerland. [13]Physikalisch-Meteorologisches Observatorium Davos and World Radiation Center, 7260 Davos, Switzerland. [14]Department of Physics of Earth, Faculty of Physics, St. Petersburg State University, St. Petersburg 198504, Russia. [15]Swiss Federal Laboratories for Materials Science and Technology (Empa), 8600 Dübendorf, Switzerland. [16]Department of Geology, Quaternary Sciences, Lund University, 22362 Lund, Sweden. [17]Alfred Wegener Institute, Helmholtz Centre for Polar and Marine Research, 27570 Bremerhaven, Germany. [18]Wollongong Isotope Geochronology Laboratory, School of Earth, Atmospheric and Life Sciences, University of Wollongong, Wollongong, NSW 2522, Australia. [19]Natural History Museum of Utah and Department of Anthropology, University of Utah, Salt Lake City, UT 84108, USA. [20]Gondwana Tree-Ring Laboratory, PO Box 14, Little River, Canterbury 7546, New Zealand. [21]School of Geography, Geology and the Environment, University of Keele, Keele, Staffordshire ST5 5BG, UK. [22]Department of Marine Chemistry and Geochemistry, Woods Hole Oceanographic Institution, Woods Hole, MA 02543, USA. [23]Centre of Excellence for Climate System Science, University of New South Wales, Sydney, NSW 2052, Australia. [24]Southern University of Science and Technology, Department of Ocean Science and Engineering, Shenzhen 518055, China. [25]Helmholtz Centre Potsdam, GFZ German Research Centre for Geosciences, Section 4.3, 14473 Potsdam, Germany. [26]Research Laboratory for Archaeology and the History of Art, School of Archaeology, University of Oxford, OX1 3TG, UK. [27]Faculty of Mathematics, Astronomy and Physics (FAMAF), National University of Cordoba, X5000HUA, Argentina. [28]Australian Centre for Ancient DNA, University of Adelaide, Adelaide, SA 5000, Australia. [29]Archaeology and Natural History, School of Culture History and Language, ANU College of Asia and the Pacific, Canberra, ACT 2601, Australia. [30]Australia ARC Centre of Excellence for Australian Biodiversity and Heritage, Australian National University, ACT 2601, Australia. [31]Institute of Geography, Friedrich-Schiller-University Jena, 07743 Jena, Germany.
*These authors contributed equally to this work.
†Corresponding author. Email: alan.cooper@blueskygenetics.com (A.C.); c.turney@unsw.edu.au (C.S.M.T.)

particularly important because it spans the period of greatest change in ^{14}C, including an apparent weakening of the magnetic field before the Laschamps. The growth of the Ngāwhā tree is relatively suppressed compared with both modern kauri and other late Pleistocene kauri, and there is a marked decrease in tree-ring width that coincides with the weakest phase of the geomagnetic field (supplementary materials). We spliced the kauri tree ^{14}C series into the radiocarbon dataset reported from the ^{230}Th-dated Hulu Cave speleothem (*22*) to provide an absolute (calendar) time scale (Fig. 1). Our 40-year–resolved reconstruction (Fig. 1) shows major changes in atmospheric radiocarbon before and during the Laschamps (*23*), closely matching reconstructions of the virtual geomagnetic pole [positions and geomagnetic intensity (*1*, *5*)]. A comparison of the kauri-Hulu ^{14}C with the paleomagnetic intensity data indicates that

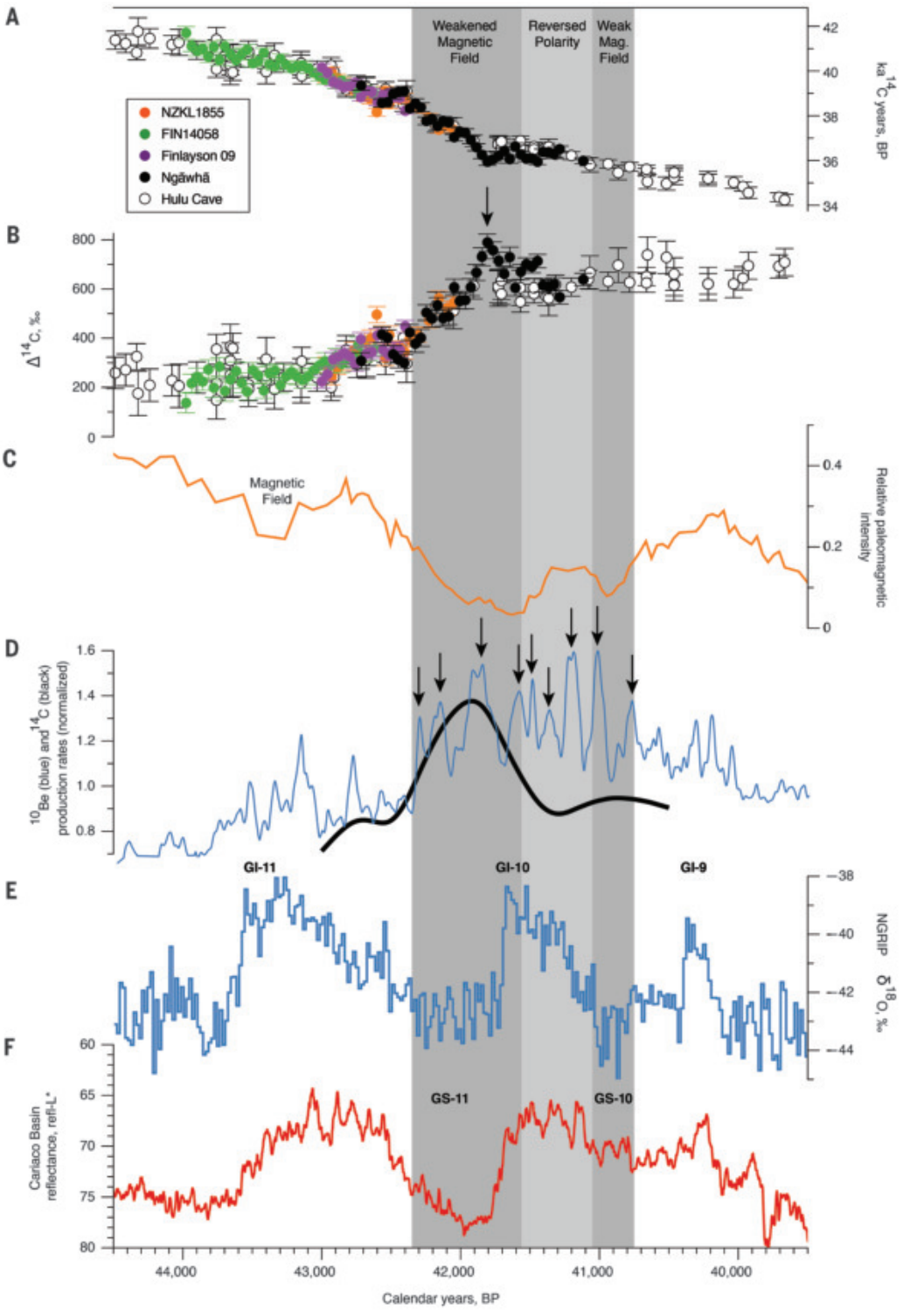

Fig. 1. Atmospheric radiocarbon changes across the Laschamps geomagnetic excursion and compared with key environmental datasets. (**A** and **B**) Kauri ^{14}C ages and $\Delta^{14}C$ values before and through the Laschamps (colored symbols) compared with Hulu Cave radiocarbon values (open symbols) (*22*). The arrow denotes the peak in $\Delta^{14}C$ coincident with a prominent GSM (see below). A short ^{14}C plateau 42.20 to 42.04 ka occurs around halfway through the steep rise in ^{14}C, which is consistent with Cariaco Basin (*40*) and demonstrates that this is a robust feature in the record. B.P., before present (1950 CE); Mag., magnetic. Error bars indicate 1σ. (**C**) Relative paleomagnetic intensity curve aligned to the Greenland ice core record reported from Black Sea sediments (*5*). (**D**) Normalized Greenland ^{10}Be flux (light blue line) (*20*) compared with modeled ^{14}C production rates from the kauri-Hulu dataset (thick black line). The amplified peaks in ^{10}Be during the weakened paleomagnetic field are consistent with increased ionizing radiation during GSM (arrows; see supplementary materials). (**E**) North Greenland Ice Core Project (NGRIP) $\delta^{18}O$ record reported on the GICC05 (+265 years) time scale B.P.; Greenland interstadial (warming) events 11 to 9 are shown (*41*), along with the weak Greenland stadial (GS-10), which may represent a local Greenland signal of abrupt cooling interrupting a larger interstadial event originally consisting of GI-10 and GI-9 (*29*, *30*). (**F**) Sediment total reflectance (refl-L*) measurements from Cariaco Basin (250-point running mean) showing the absence of a clear GS-10 signal (*30*). The reversed geomagnetic polarity (light-gray column) and flanking transition phases (dark gray) are indicated, with the latter being the weakest periods of Earth's magnetic field and closely coincident with GS-11 and GS-10.

the reversed phase of the geomagnetic field (and associated partial recovery) defining the Laschamps sensu stricto occurred at 41.56 to 41.05 ka (supplementary materials).

By modeling ^{14}C-production rates from our kauri Δ^{14}C record, it is possible to precisely align to the ice core time scale by using ^{10}Be records (*21*). Across this period, we infer that the Greenland ice core 2005 (GICC05) time scale is 265 years younger than the Hulu Cave time scale (95.4% range: 160 to 310 years) (Fig. 1 and fig. S15), which is considerably more precise than previous comparisons (*21*). Notably, the steep rise in Δ^{14}C commences at 42.35 ka, with a peak value of 782 per mil (‰) occurring at 41.8 ka, 300 years before the full Laschamps reversal. This is the highest atmospheric ^{14}C concentration yet reported of the pre-anthropogenic radiocarbon time scale (*22*, *23*, *25*) (see supplementary materials). The peak Δ^{14}C value reported here occurs during the most weakened phase of the geomagnetic field (*5*) and is associated with a prominent GSM recorded by ^{10}Be flux (*20*) (Fig. 1 and supplementary materials), when the weakened solar interplanetary magnetic field allowed enhanced input of galactic cosmic rays (GCRs) into the upper atmosphere. This kauri-Hulu record provides a precise radiocarbon calibration curve for this period, permitting a detailed recalibration of wider environmental changes to test synchrony between events while also enabling us to investigate the potential climate drivers during the Laschamps.

Global chemistry-climate modeling

To explore the impacts of a greatly weakened geomagnetic field on atmospheric ionization, chemistry, and dynamics, we undertook a series of simulations using a global chemistry-climate model, SOCOL-MPIOM (*8*) (see supplementary materials). First, the global conditions before the Laschamps were modeled by using modern values of the geomagnetic dipole moment (M) and average solar modulation potential (ϕ) of 800 MV (equivalent to the modern value). After a 398-year spin-up, three 72-year–long simulations (from which the last 60 years were used for analysis) were branched off to study the Laschamps and two additional solar states likely to influence atmospheric ionization: a reference run keeping M = 100% current and ϕ = 800 MV (experiment REF); the Laschamps with weakened geomagnetic field (M = 0% current, ϕ = 800 MV; experiment M0P800) (*2*); and a Laschamps weakened geomagnetic field plus GSM when the decreased geomagnetic field and the reduced solar modulation potential greatly increase the GCR ionization rate in Earth's atmosphere (M = 0% current, ϕ = 0 MV; experiment M0P0).

Although our simulation for the weakened magnetic field during the Laschamps (M0P800) showed modest but significant changes in atmospheric chemistry and climate (see supplementary materials), the scenario for Laschamps plus GSM (M0P0) showed greatly amplified

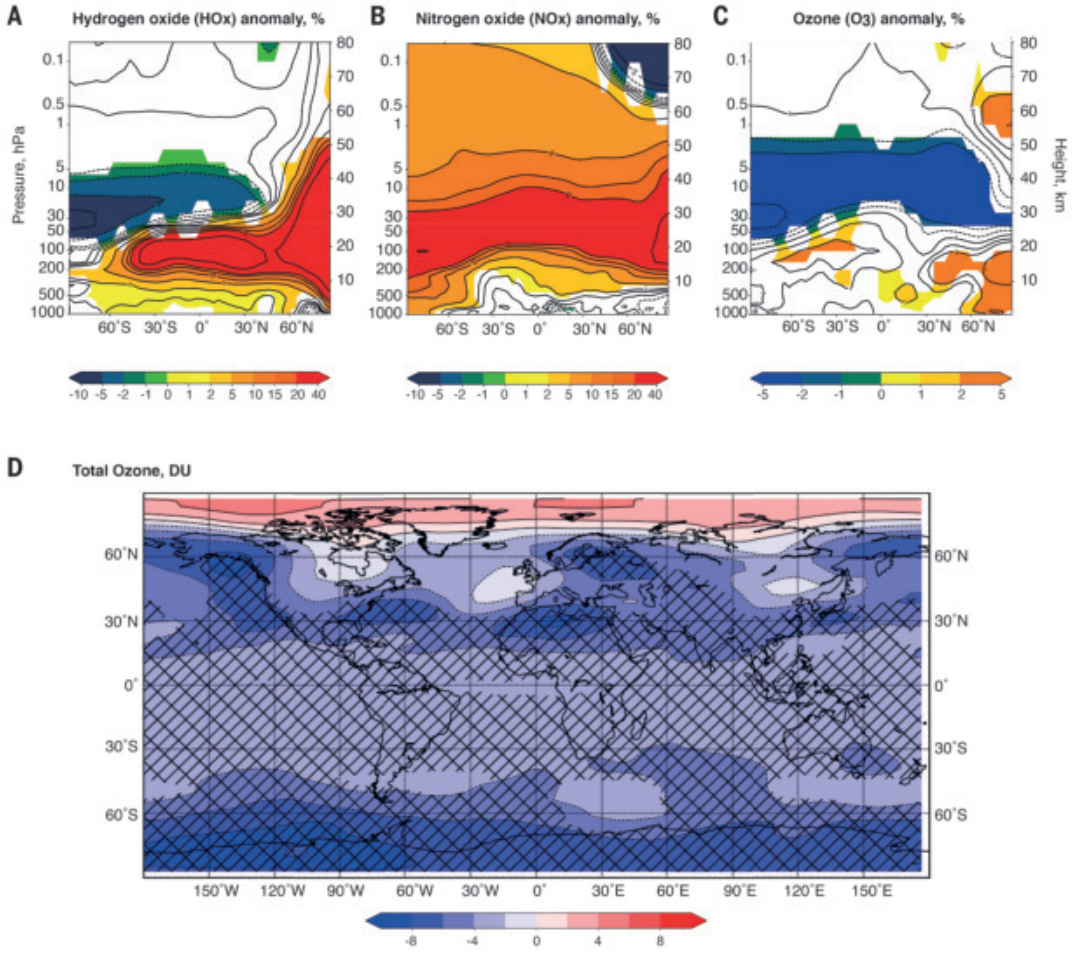

Fig. 2. The impact of a weakened geomagnetic field and GSM on global chemistry. (**A** to **C**) Simulated anomalies in boreal winter and austral summer (relative to experiment REF; December to February) atmospheric chemistry [HOx, NOx, and O_3 in (A), (B), and (C), respectively] for a weakened magnetic field during the Laschamps plus GSM (M = 0, ϕ = 0); colored areas denote 10% significance. (**D**) Total ozone column change [Dobson units (DU)]; hatched areas denote 10% significance level.

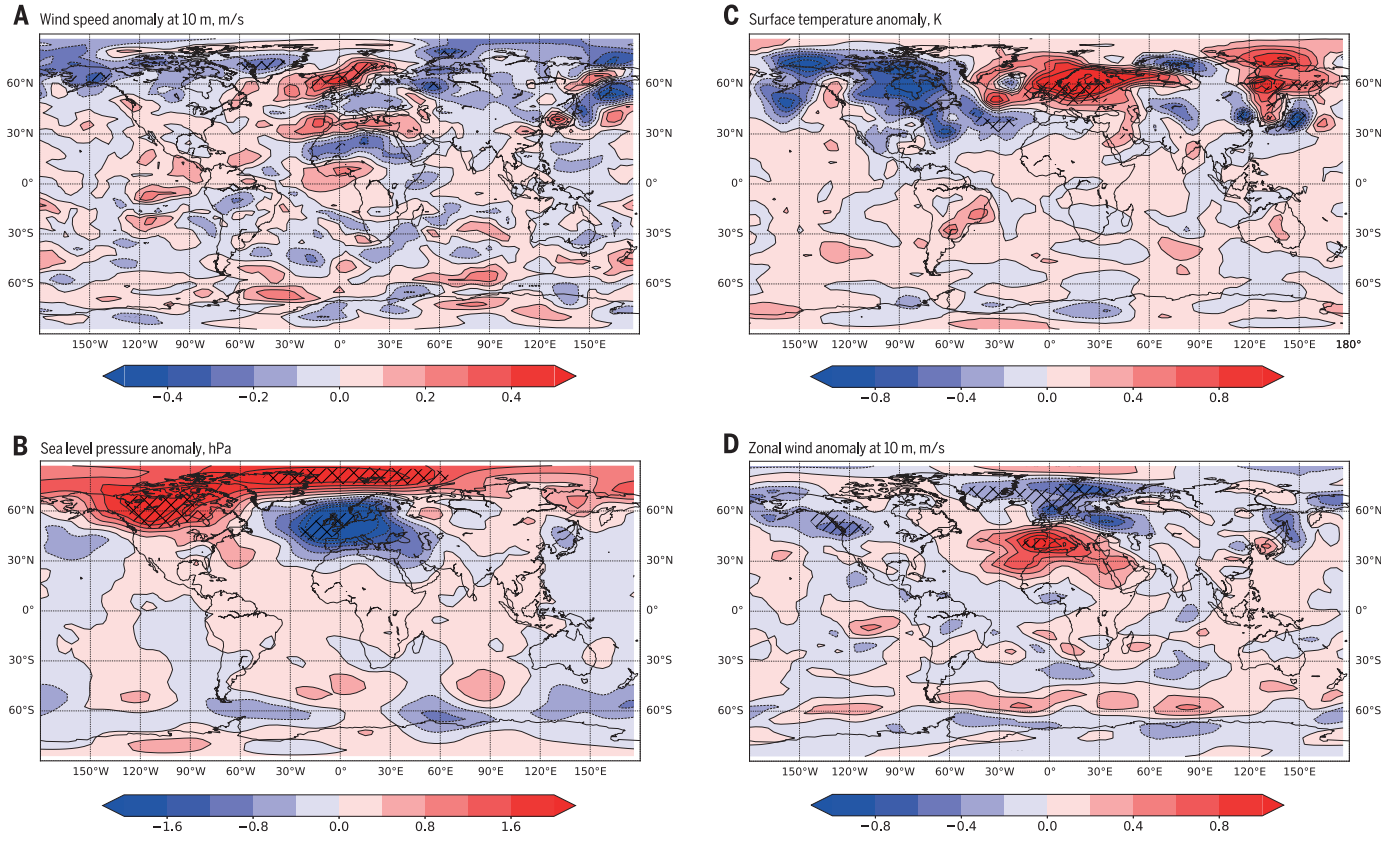

Fig. 3. The impact of a weakened geomagnetic field and GSM on global climate. (**A** to **D**) Simulated anomalies in boreal winter and austral summer (relative to experiment REF; December to February) wind speed at 10 m, sea-level pressure, surface temperature, and zonal wind [(A) to (D), respectively] for a weakened magnetic field during the Laschamps plus GSM (M = 0, ϕ = 0); hatched areas denote 10% significance level.

impacts, most notably during the boreal winter and austral summer (December to February) (Figs. 2 and 3 and figs. S18 to S30). Our results yield a large increase in atmospheric ionization from GCRs, resulting in an enhanced production of hydrogen and nitrogen oxides (HOx and NOx, respectively) (Fig. 2, A and B) (*8*) down to very low altitudes. The increased HOx and NOx concentrations influenced ozone levels over the entire atmosphere, decreasing the O_3 mixing ratio in the stratosphere (~5%) while increasing the O_3 mixing ratio in the troposphere, with the greatest changes observed over Antarctica (~5%) (Fig. 2, C and D).

We find that decreasing stratospheric O_3 concentrations had climatic impacts over the mid- to high latitudes in both hemispheres (Fig. 3). In the Northern Hemisphere, this changed the equator-to-pole temperature gradient, weakening the Arctic polar vortex and leading to a net warming effect in the lower polar stratosphere. We postulate that this positive temperature anomaly was further amplified by an increase in the Brewer-Dobson Circulation, which would have, among other effects, led to adiabatic warming of air masses sinking from upper to lower stratospheric heights. The reason for the increased Brewer-Dobson Circulation may originate from a wavier jet stream, reaching higher velocities at the Northern Hemisphere latitudes with the most pronounced orographic barriers and increasing gravity-wave production, which subsequently propagated vertically up through the atmospheric column (*26*). The lower atmosphere responded to those factors with sea-level pressure increases over the Arctic and North America and decreases over Western Europe, with parallel changes in surface temperature. These changes resemble a negative phase of the Arctic Oscillation (AO) and North Atlantic Oscillation (NAO), consistent with reanalysis studies (*27*). In the Southern Hemisphere, decreasing stratospheric O_3 appears to be associated with small changes in the mid-latitude airflow (Fig. 3) and subtropical precipitation patterns (see supplementary material) (*8*). Because the significance is <10%, an ensemble of longer model runs is required to confirm this finding.

Although previous studies have suggested that snowfall over Greenland is summer dominated during glacial conditions (*28*), the model predictions of pronounced boreal winter Arctic surface cooling are potentially important in the context of the Greenland ice core records spanning this period. It is notable that the two weakest phases of geomagnetic field strength during the Laschamps closely coincide with the cold Greenland stadials 11 (GS-11) and GS-10 (Fig. 1). Furthermore, GS-10 and the following brief interstadial GI-9 have a number of atypical features that have led to suggestions that they might represent the interruption of a single long warm interstadial (composed of GI-10 and GI-9, as seen in other records such as Cariaco Basin) (Fig. 1) by an abrupt cold phase, likely related to an expansion in North Atlantic sea-ice extent, which changed the climatic gradient between the mid-latitudes and Greenland (*29*, *30*) (supplementary materials). As a result, the climatic impacts of the Laschamps may have been obscured by the way they are represented in the Greenland ice core records.

Pacific climate and environmental impacts

In the Northern Hemisphere, it remains difficult to disentangle the similarly timed impacts of Laschamps from Greenland stadial-interstadial

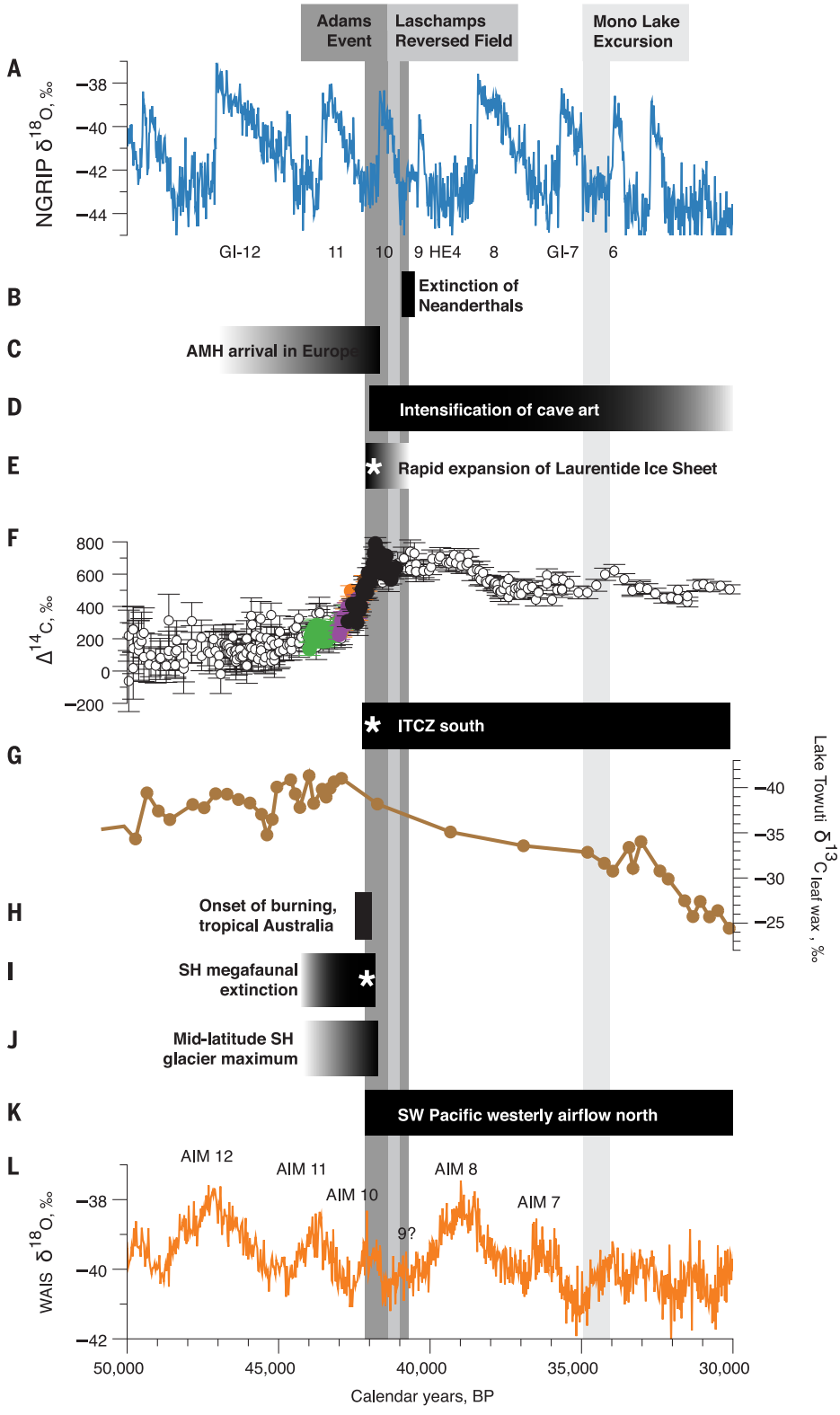

Fig. 4. Climatic and environmental changes across the 42 ka Adams Event. (**A**) NGRIP $\delta^{18}O$ (*41*). HE4 refers to Heinrich Event 4 within GS-9. (**B** and **C**) Neanderthal extinction in Europe (40.9 to 40.5 ka) recalibrated with the kauri-Hulu calibration curve (B) and arrival of AMHs in Europe (C) and development of Initial Upper Paleolithic cultures (*37*). (**D**) Early cave art and cave utilization across both Europe and Southeast Asia (*34*–*36*). (**E**) Rapid expansion of LIS after a minimum extent at 42 ka calendar B.P. that commenced immediately before or during the Laschamps (*17*–*19*). (**F**) Kauri and Hulu Cave $\Delta^{14}C$ values; colored solid circles denote individual trees (key in Fig. 1). Error bars indicate 1σ. (**G**) Migration south of the Intertropical Convergence Zone (ITCZ) as recorded by Lake Towuti $\delta^{13}C_{leaf\ wax}$ reported in this study (*11*). (**H**) Onset of burning in tropical Queensland, Australia (*15*). (**I**) Extinction of megafauna in Australia (and continental-wide aridification) (*13*, *14*) and faunal turnover in southern Africa (*42*). SH, Southern Hemisphere. (**J**) Local glacial maxima in the southwest Pacific (*7*, *10*) and the central Andes (*7*, *10*). (**K**) Migration of mid-latitude westerly airflow equatorward from Auckland Islands (*12*) and possible extinction of subantarctic plant species (fig. S6). (**L**) West Antarctic (WAIS) $\delta^{18}O$ (*41*). NGRIP and WAIS $\delta^{18}O$ values reported on the GICC05 (+265 years) time scale (*41*). AIM, Antarctic isotopic maximum events. The Laschamps is shown in three phases: the transition phases (dark gray) on either side of the reversed polarity (light gray). The Mono Lake Excursion (34.6 ka) is also shown (light gray column) (*1*). Asterisks denote evidence of geomagnetic alteration associated with the Laschamps, demonstrating synchronous change across many parts of the globe.

events, early glacial advances, and the expansion of anatomically modern humans (AMHs) (*4*, *31*). Therefore, to isolate the potential impacts of Laschamps from these confounding factors, we used the kauri-Hulu radiocarbon calibration curve to examine a transect of stratigraphically constrained sites in the Pacific (i.e., outside the Atlantic Ocean basin) from the subantarctic to the tropics (Fig. 4).

We used high-resolution radiocarbon dating to investigate Laschamps-aged sedimentary sequences at sites that record the behavior of both the Intertropical Convergence Zone (ITCZ) (Lake Towuti, Sulawesi) and mid-latitude Southern Hemisphere westerlies (subantarctic Auckland Islands). On the subantarctic Auckland Islands (50°S) (see supplementary materials), which currently

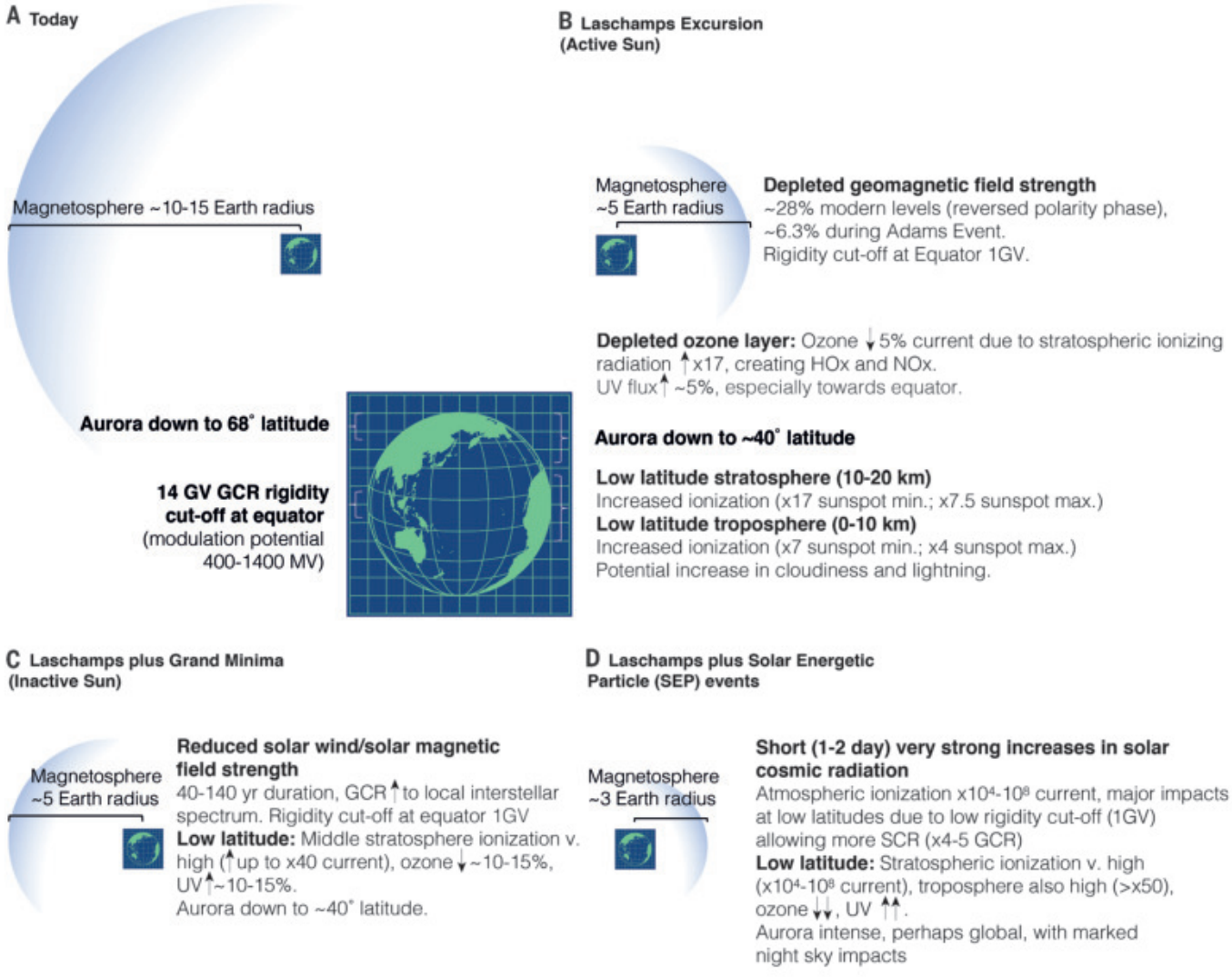

Fig. 5. Summarized potential impacts of different states of Earth's magnetic field and solar events. (**A** to **D**) Size of the magnetosphere, auroral extent, atmospheric ionization and associated chemistry and climate impacts for (A) today, (B) the Laschamps, (C) GSM during the Laschamps, and (D) major SEP events during the Laschamps (see supplementary materials). Upward arrows represent increase, and downward arrows represent decrease. max., maximum; min., minimum; SCR, solar cosmic radiation; GV, gigavolt; MV, megavolt.

sit under Southern Hemisphere mid-latitude westerly airflow (*12*), a lignite sedimentary horizon at Pillar Rock records a warm period from 54 to 42 ka within the last glaciation. Pollen records of *Dracophyllum* scrub grassland on this exposed cliff top and long-distance transport of lowland podocarp forest pollen from the New Zealand mainland indicate weaker westerly winds than now and mean annual temperatures within 1° to 1.5°C of those today (supplementary materials), interpreted to represent a period when the core of the Southern Hemisphere westerlies lay relatively poleward, delivering mid-latitude air masses over this sector of the Southern Ocean (*12*). A series of 12 contiguous ^{14}C ages reveals the upper stratigraphic boundary, marking a return to periglacial conditions that occurred at 42.23 ± 0.2 ka, coincident with the weakening of the magnetic field during the transition phase into the Laschamps (Fig. 1). The periglacial conditions lasted until the Holocene (*12*), suggesting pervasive and widespread cold conditions (associated with a strengthening or northward shift in the core westerly airflow) across this sector of the Southern Ocean.

In the equatorial west Pacific, Lake Towuti currently experiences a wet season from December to May as the ITCZ migrates southward (*11*). During the last glacial period, Lake Towuti preserves a marked and sustained shift in $\delta^{13}C_{leaf\ wax}$ to more positive values (interpreted as representing more arid conditions), which persisted until the Pleistocene-Holocene boundary (Fig. 4 and supplementary materials) (*11*). A comprehensive series of 13 new radiocarbon dates and sediment magnetic intensity minima suggest that the ITCZ shift occurred at 42.35 ± 0.2 ka, again during the geomagnetic transition phase into the Laschamps (fig. S11), precisely aligning to the westerly airflow shift recorded at Pillar Rock. The high level of precision on the ages obtained for the major climatic boundaries recorded in Lake Towuti and the Auckland Islands is only possible because of the contiguous series of radiocarbon dates from each sequence, which permit accurate alignment against the steep rise in atmospheric radiocarbon values across this period (Fig. 1).

The above changes are consistent with a wealth of observations that indicate major environmental changes around the Pacific

Basin at the time of the geomagnetic transition into the Laschamps. For instance, a northward movement of the Southern Hemisphere westerlies has been proposed to explain the local peak glacial advance in the arid southern-central Andes, sometime before 39 ka (Fig. 4) (*7*) and tentatively related to fluxes in cosmic radiation and the Laschamps (*8*). Maximum glacial advances are also observed in New Zealand ~42 ka (*10*), consistent with the climate modeling of enhanced southwesterly airflow over the mid-latitudes (Fig. 3C) (*8*). These broad-scale atmospheric circulation changes appear to have had far-reaching consequences. Within Australia, the peak megafaunal extinction phase is dated at ~42.1 ka, both in the mainland and Tasmania (Fig. 4) (*14*–*16*), and has generally been attributed to human action, although well after their initial arrival at least 50 ka (*14*, *16*, *32*). Instead, the megafaunal extinctions appear to be contemporaneous with a pronounced climatic phase shift to arid conditions that resulted in the loss of the large interior lakes and widespread change in vegetation patterns (*13*, *15*). At Lynch's Crater in northeast Australia, the shift in vegetation structure, accompanied by increased burning (*15*), has been recalibrated here at 41.91 ± 0.4 ka, overlapping with the climatic boundaries observed at Lake Towuti and the Auckland Islands. Likewise, sediments at the Lake Mungo site associate the timing of the loss of Australia's interior lakes and megafaunal extinction phase with a reported geomagnetic excursion ~42 ka (locally called the "Lake Mungo Excursion") (supplementary materials) (*13*). Similar signals of marked floral and faunal change also appear to exist on New Caledonia and as far afield as South Africa (see supplementary materials). Together, these records suggest that both a mid-latitude climatic shift and major extinction phases overlap with the geomagnetic transition leading into the Laschamps, implying an association between these events.

Our model simulations potentially provide important insights into the global nature of the changes observed around the time of the Laschamps. Although the immediate impacts associated with the geomagnetic transition were likely on the order of the duration (800 years), many of the above synchronous changes persisted for millennia. This implies that a threshold may have been passed in one or more Earth system components, effectively tipping into a different persistent state (Fig. 4). One possibility is that with Earth's orbital configuration moving toward a full glacial state and limited global ocean ventilation (see supplementary materials), the climate system may have been sensitive to a relatively short but extreme forcing around the time of the Laschamps. For instance, terrestrial and marine sedimentary records have revealed that the LIS expanded rapidly from a local minimum at 42 ka (*18*, *19*) in association with a magnetic reversal (*17*, *19*), with geological constraints and numerical models indicating that some parts of the ice sheet may have expanded >1000 km by ~39 to 37 ka (*18*). Although our model simulations do not suggest any major change in airflow over the equatorial and southern Pacific, we do find a substantially weakened polar vortex, most notably during the boreal winter (Fig. 3 and supplementary materials). The greatly reduced surface temperatures akin to a negative phase of the AO and NAO could potentially have created a positive feedback for ice sheet growth, reducing global sea levels. Recent work has suggested that a greatly expanded LIS would have reorganized atmospheric circulation across the wider Pacific Ocean (*11*). Such a hemisphere-wide response to abrupt forcing is consistent with the synchronous movement of the mid-latitude Southern Hemisphere westerlies determined from Pillar Rock and implied from glacial behavior in New Zealand, Australia, and the central Andes.

The Adams Transitional Geomagnetic Event and wider implications

Overall, the signals discussed above suggest that contemporaneous climatic and environmental impacts occurred across the mid- to lower latitudes ~42 ka, coincident with Earth's weakened geomagnetic field immediately preceding the reversed state of the Laschamps (Fig. 4). We describe this as the "Adams Transitional Geomagnetic Event" (hereafter "Adams Event"), named after the science writer Douglas Adams because of the timing (the number "42") and the associated range of extinctions (*33*). Previous studies may have failed to identify such a relationship between the Laschamps and climatic impacts because of the lack of temporal resolution and by focusing on the period of actual reversed geomagnetic field (41.5 to 41.1 ka) (*5*, *6*) rather than the preceding extended phase of much weaker geomagnetic field (42.4 to 41.5 ka).

The lowered geomagnetic field intensity during the Adams Event, together with major changes in the intensity of cosmic radiation, is estimated to have increased levels of atmospheric ionization and ultraviolet (UV) radiation, especially in equatorial and low latitudes (<40°), because of a 10-fold decrease in the cosmic ray cut-off rigidity (Fig. 5 and supplementary materials). During GSM, the ionization in the middle stratosphere and surface UV radiation levels are estimated to have been further heightened (up to 25 to 40% and 10 to 15% above current levels, respectively), after taking into account changes in the solar spectrum. Furthermore, these values are likely to be much greater during the short-lived solar energetic particle (SEP) events (Fig. 5 and supplementary materials). Although the relationship between increased atmospheric ionization and stratospheric and tropospheric cloudiness through cloud-seeding–type impacts remains uncertain, such impacts would be focused toward the lower latitudes (*9*), where the potential for lightning strikes could explain the increased records of charcoal observed around the Laschamps in Australia (*15*) and lack of relationship with archaeological signs of human activity (see supplementary materials).

The implications of this study are considerable. For instance, the Adams Event is very close in timing to the globally widespread appearance and increase in figurative cave art, red ochre handprints, and changing use of caves ~40 to 42 ka, e.g., in Europe and Island Southeast Asia (fig. S34 and supplementary materials) (*34*–*36*). This sudden behavioral shift in very different parts of the world is consistent with an increasing or changed use of caves during the Adams Event, potentially as shelter from the increase of ultraviolet B, potentially to harmful levels, during GSM or SEPs, which might also explain an increased use of red ochre sunscreen (*4*). Rather than the actual advent of figurative art, early cave art would therefore appear to represent the preservation of preexisting behaviors on a new medium (supplementary materials) (*36*). Other important archaeological boundaries during the wider Laschamps include the extinction of the Neanderthals (recalibrated here at 40.9 to 40.5 ka), along with the disappearance of some of the first European AMH cultures and the subsequent widespread appearance of the Aurignacian technocomplex (Fig. 4 and supplementary materials) (*4*, *31*, *37*).

The Adams Event appears to represent a major climatic, environmental, and archaeological boundary that has previously gone largely unrecognized. Furthermore, another well-known geomagnetic excursion in the recent past, Mono Lake (34 ka) (*1*), also appears to be marked by a distinct peak in the $\Delta^{14}C$ levels in the Hulu Cave stalagmite (Fig. 3) and aligns closely with a further latitudinal shift in the ITCZ as recorded in Lake Towuti, as well as a cluster of megafaunal extinctions in Eurasia (*38*) (supplementary materials). Importantly, geomagnetic transition phases can last substantially longer than during the Laschamps; for instance, the most recent full geomagnetic reversal, the Brunhes-Matuyama (at ~790 ka) (*39*) has a transition phase of ~20 ka, some 25 times longer than the Adams Event, with potentially far-reaching global climatic and evolutionary effects. The discovery that geomagnetic excursions can alter latitudinal temperature gradients through drastic increases in cosmic radiation and decreased ozone concentrations provides a new model for sudden paleoclimate

shifts. Overall, these findings raise important questions about the evolutionary impacts of geomagnetic reversals and excursions throughout the deeper geological record (*4*).

REFERENCES AND NOTES

1. C. Laj, H. Guillou, C. Kissel, *Earth Planet. Sci. Lett.* **387**, 184–197 (2014).
2. M. Brown, M. Korte, R. Holme, I. Wardinski, S. Gunnarson, *Proc. Natl. Acad. Sci. U.S.A.* **115**, 5111–5116 (2018).
3. E. J. Oughton, A. Skelton, R. B. Horne, A. W. P. Thomson, C. T. Gaunt, *Space Weather* **15**, 65–83 (2017).
4. J. E. T. Channell, L. Vigliotti, *Rev. Geophys.* **57**, 709–738 (2019).
5. J. Liu, N. R. Nowaczyk, S. Panovska, M. Korte, H. W. Arz, *J. Geophys. Res.* **125**, e2019JB019225 (2020).
6. G. Wagner, D. M. Livingstone, J. Masarik, R. Muscheler, J. Beer, *J. Geophys. Res.* **106**, 3381–3387 (2001).
7. R. Zech, J. Zech, C. Kull, P. W. Kubik, H. Veit, *Clim. Past* **7**, 41–46 (2011).
8. I. Suter, R. Zech, J. Anet, T. Peter, *Clim. Past* **10**, 1183–1194 (2014).
9. J. Kirkby *et al*., *Nature* **533**, 521–526 (2016).
10. P. D. Strand *et al*., *Quat. Sci. Rev.* **220**, 165–177 (2019).
11. J. M. Russell *et al*., *Proc. Natl. Acad. Sci. U.S.A.* **111**, 5100–5105 (2014).
12. E. Rainsley *et al*., *Clim. Past* **15**, 423–448 (2019).
13. J. M. Bowler *et al*., *Nature* **421**, 837–840 (2003).
14. F. Saltré *et al*., *Nat. Commun.* **7**, 10511 (2016).
15. S. Rule *et al*., *Science* **335**, 1483–1486 (2012).
16. C. S. M. Turney *et al*., *Proc. Natl. Acad. Sci. U.S.A.* **105**, 12150–12153 (2008).
17. H. W. Hill, B. P. Flower, T. M. Quinn, D. J. Hollander, T. P. Guilderson, *Paleoceanography* **21**, PA1006 (2006).
18. A. S. Dalton *et al*., *Geology* **47**, 111–114 (2019).
19. A. S. Dalton, S. A. Finkelstein, P. J. Barnett, S. L. Forman, *Quat. Sci. Rev.* **146**, 288–299 (2016).
20. G. M. Raisbeck *et al*., *Clim. Past* **13**, 217–229 (2017).
21. F. Adolphi *et al*., *Clim. Past* **14**, 1755–1781 (2018).
22. H. Cheng *et al*., *Science* **362**, 1293–1297 (2018).
23. R. A. Staff *et al*., *Earth Planet. Sci. Lett.* **520**, 1–9 (2019).
24. A. M. Lorrey *et al*., *Quat. Sci. Rev.* **183**, 124–139 (2018).
25. C. S. M. Turney *et al*., *Sci. Rep.* **8**, 3293 (2018).
26. K. Kodera, Y. Kuroda, *J. Geophys. Res.* **107**, ACL 5-1–ACL 5-12 (2002).
27. J. Kidston *et al*., *Nat. Geosci.* **8**, 433–440 (2015).
28. V. Masson-Delmotte *et al*., *Science* **309**, 118–121 (2005).
29. S. O. Rasmussen *et al*., *Quat. Sci. Rev.* **106**, 14–28 (2014).
30. G. Deplazes *et al*., *Nat. Geosci.* **6**, 213–217 (2013).
31. M. Staubwasser *et al*., *Proc. Natl. Acad. Sci. U.S.A.* **115**, 9116–9121 (2018).
32. J. F. O'Connell *et al*., *Proc. Natl. Acad. Sci. U.S.A.* **115**, 8482–8490 (2018).
33. D. Adams, M. Carwardine, *Last Chance to See* (Arrow Books, 2009).
34. A. W. Pike *et al*., *Science* **336**, 1409–1413 (2012).
35. S. O'Connor, R. Ono, C. Clarkson, *Science* **334**, 1117–1121 (2011).
36. M. Aubert *et al*., *Nature* **564**, 254–257 (2018).
37. J.-J. Hublin *et al*., *Nature* **581**, 299–302 (2020).
38. A. Cooper *et al*., *Science* **349**, 602–606 (2015).
39. B. S. Singer, B. R. Jicha, N. Mochizuki, R. S. Coe, *Sci. Adv.* **5**, eaaw4621 (2019).
40. K. Hughen *et al*., *Science* **303**, 202–207 (2004).
41. WAIS Divide Project Members, *Nature* **520**, 661–665 (2015).
42. J. T. Faith, *J. Hum. Evol.* **65**, 715–730 (2013).

ACKNOWLEDGMENTS

We thank Marble Hill Estate, Adelaide Hills, for hosting a research meeting in 2016 that helped initiate this project. We are grateful for the assistance of N. Parker at Nelson's Kaihu Kauri, Top Energy, and Ngāpuhi iwi for permission to obtain and analyze samples of the Ngāwhā tree. We would also like to thank B. Finlayson, R. Finlayson, K. Finlayson, and G. Beckham for providing access to the subfossil kauri. M. Guzowski kindly helped prepare the map used in Fig. 5. Many colleagues have provided valuable support and suggestions; L. Van Gelder, H. Cadd, S. Haberle, S. Haaland, T. Cooper, N. Golledge, and S. Fry. M. Thuerkow kindly provided the initial land surface dataset and ocean temperatures for the model simulations, and G. Chiodo provided support for the chemistry-climate modeling. We acknowledge ETH Zürich for use of the Euler Linux cluster and other computing facilities. We thank three anonymous reviewers whose comments improved the manuscript considerably. This work is dedicated to Douglas Adams and Roger Cooper. **Funding:** We thank the Australian Research Council for Discovery Grant and Laureate Fellowship support [DP170104665 and FL140100260 (A.C.) and FL100100195 (C.S.M.T.)], the University of Adelaide Environment Institute, the Australasian Antarctic Expedition 2013–2014 and *The Tiama*, the Royal Society of New Zealand Marsden Fund (contract MFP-NIW1803), NIWA, the University of Waikato, the Leverhulme Trust (RF-2019-140\9), the Russian Science Foundation (20-67-46016), and a Swiss National Science Foundation Ambizione grant (PZ00P2_180043). **Author contributions:** C.S.M.T. and A.C. designed the research; C.S.M.T., A.C., J.P., A.H., M.M., J.W., A.M.L., T.J.H., J.M.R., J.G.A., I.S., and P.F. performed the research; A.C., C.S.M.T., J.P., A.H., J.G.A., T.P., E.Ro., K.M., M.M., J.W., A.M.L., T.J.H., J.M.R., R.M., F.A., A.D., and I.S. analyzed the data; and A.C. and C.S.M.T. wrote the paper with input from all authors. **Competing interests:** The authors declare no competing interests. **Data and materials availability:** All data are available in the main text or the supplementary materials.

SUPPLEMENTARY MATERIALS

science.sciencemag.org/content/371/6531/811/suppl/DC1
Materials and Methods
Figs. S1 to S34
Tables S1 to S8
References (*43*–*175*)

24 March 2020; accepted 14 December 2020
10.1126/science.abb8677

SURFACE CHEMISTRY

Determining structural and chemical heterogeneities of surface species at the single-bond limit

Jiayu Xu*, Xiang Zhu*, Shijing Tan†, Yao Zhang, Bin Li, Yunzhe Tian, Huan Shan, Xuefeng Cui, Aidi Zhao, Zhenchao Dong, Jinlong Yang, Yi Luo, Bing Wang†, J. G. Hou†

The structure determination of surface species has long been a challenge because of their rich chemical heterogeneities. Modern tip-based microscopic techniques can resolve heterogeneities from their distinct electronic, geometric, and vibrational properties at the single-molecule level but with limited interpretation from each. Here, we combined scanning tunneling microscopy (STM), noncontact atomic force microscopy (AFM), and tip-enhanced Raman scattering (TERS) to characterize an assumed inactive system, pentacene on the Ag(110) surface. This enabled us to unambiguously correlate the structural and chemical heterogeneities of three pentacene-derivative species through specific carbon-hydrogen bond breaking. The joint STM-AFM-TERS strategy provides a comprehensive solution for determining chemical structures that are widely present in surface catalysis, on-surface synthesis, and two-dimensional materials.

When a molecule is adsorbed on a surface, the molecular structure often undergoes marked changes, resulting in different surface species formed from structural deformation, chemical bond breaking, and/or chemical bond formation (*1*–*3*). Identifying the structure or heterogeneity of surface species has been the central theme of surface science for decades (*4*–*7*), and requires precise characterization of chemical bonds within the molecule and with the substrate (*8*–*12*). Various state-of-the-art tip-based microscopic and spectroscopic techniques using sensitive measurements of electron, force, and photon have made the task achievable (*13*–*19*). In many cases, scanning tunneling microscopy (STM), scanning tunneling spectroscopy (STS), and noncontact atomic force microscopy (AFM) with a q-Plus probe were capable of resolving the static electronic structures and intramolecular geometries of surface species with high energy and spatial resolution (*20*–*25*). A known weakness of the above-mentioned technique is the lack of chemical sensitivity, which severely hinders its ability to determine the heterogeneities of the surface species. Fortunately, such a weakness can be effectively overcome by tip-enhanced Raman spectroscopy (TERS) (*16*, *19*, *26*–*30*). Using TERS, scanning Raman picoscopy (SRP) provides an optical means with single-bond resolution to fully map individual vibrational modes and visually construct the chemical structure of a single molecule (*31*). At this stage, the three techniques all reach Ångström-level resolution in real space. It can thus be anticipated that a combination of these techniques would provide a comprehensive means to interrogate heterogeneity of surface species.

As a first attempt, we chose pentacene ($C_{22}H_{14}$) on the Ag(110) surface as our model system. Pentacene has been frequently used as a benchmark system for characterizing the resolution and performance of STM and AFM (*21*, *24*, *32*–*35*) because of its high stability and planarity. Figure 1A shows STM images of an atomically resolved Ag(110) surface with adsorbed pentacene and CO molecules obtained at a low voltage bias of 60 mV. It can be seen

Hefei National Laboratory for Physical Sciences at the Microscale and Synergetic Innovation Center of Quantum Information and Quantum Physics, University of Science and Technology of China, Hefei, Anhui 230026, China.
*These authors contributed equally to this work.
†Corresponding author. Email: tansj@ustc.edu.cn (S.T.); bwang@ustc.edu.cn (B.W.); jghou@ustc.edu.cn (J.G.H.)

that the pentacene lies down with its long molecular axis parallel to the [001] direction and the central benzene ring over the hollow site of the Ag(110) surface (see fig. S1). At the imaging bias voltage of 0.1 V, the intact pentacene exhibits a rod-like feature (labeled as α) in an STM topographic image (Fig. 1B). However, by sequentially applying voltage pulses of 2.0 V over a molecule, two kinds of new species with different shapes were formed (Fig. 1, C and D): species β, with a slightly distorted dumbbell-like shape, and species γ, with a spindle-like shape. Pentacene and its derivative species showed strongly voltage-dependent contrast in STM topographies (fig. S2) and quite different electronic states in STS spectra (fig. S3). Our quantitative measurements indicated a bias-polarity–independent threshold value of ~1.5 to 1.6 V for the tip-induced transformations, which is consistent with the measured threshold voltage for tip-induced light emission from the nanocavity plasmon (fig. S4). This strongly suggests that plasmonic excitation is responsible for the transformations of pentacene (see the supplementary text). Nevertheless, the use of STM or STS alone cannot directly determine the actual chemical structures of the transformed species.

To further characterize the three species, we then used AFM with a CO-decorated tip (Fig. 1E and fig. S5, A to C). Dark halos, which are known to mainly arise from the Van der Waals attraction, were present at the periphery of all three species, and the inner molecular structures were resolved with atomic resolution originating from short-range Pauli repulsion (*21*, *22*, *34*). In this case, AFM gave more detailed structural information than STM. The uniform rod-like feature of α in STM was nonuniform in AFM, with two bright protrusions located around the C–H bonds of the central benzene ring. These two protrusions were markedly different from the flat contrast in previous AFM images of pentacene on Cu(111) or NaCl layers (*21*, *35*), implying that the center C atoms could interact with the Ag (110) surface specifically. Furthermore, from α to γ, the overall contrast at the central part became weaker, as can be seen clearly in the three-dimensional plot (fig. S6), which may imply a stereo-deformation of the molecular skeleton (*36*) associated with the collapse of the central ring toward the surface. At the same time, the apparent size of the benzene rings changed markedly from α to γ, as can be seen in the respective Laplace-filtered images (Fig. 1F). The central benzene ring in α appeared to be expanded along the long molecular axis, with a larger width than other rings in the line profiles (Fig. 1, G and H). Along with the absence of one protrusion in β and both protrusions in γ, the second and fourth benzene rings became much expanded by ~1 Å along the long molecular axis (Fig. 1H), and the ring feature for the central one was barely resolvable. From the image itself, the visual impression would lead to the conclusion that the β and γ species could undergo a large structural deformation. However, the fact that the total lengths of the three species remained nearly unchanged is a strong argument against this point of view (fig. S5, D to F), and is quite different from the charging-induced structural change of pentacene previously observed on the insulating NaCl surface because the entire molecular axis is elongated (*35*). The disappearance of the two protrusions and the size change of the benzene ring in the AFM images point to two possible sources of the transformation from α to γ: C–H bond breaking at the central benzene ring with skeleton deformation or the opening of the central benzene ring with atom rearrangements. Confirmation of either hypothesis requires knowledge of local chemical bonds.

Chemical bond information can be well characterized by TERS measurements because Raman signals are directly related to the vibrational motion of the bonds (*28*, *31*). Figure 2A shows the Raman spectra taken from species α, β, and γ when the tip was located around the middle and end sites (labeled by the corresponding crosses). It has been established that the C–H stretching mode of pentacene should appear alone in the high-wave-number

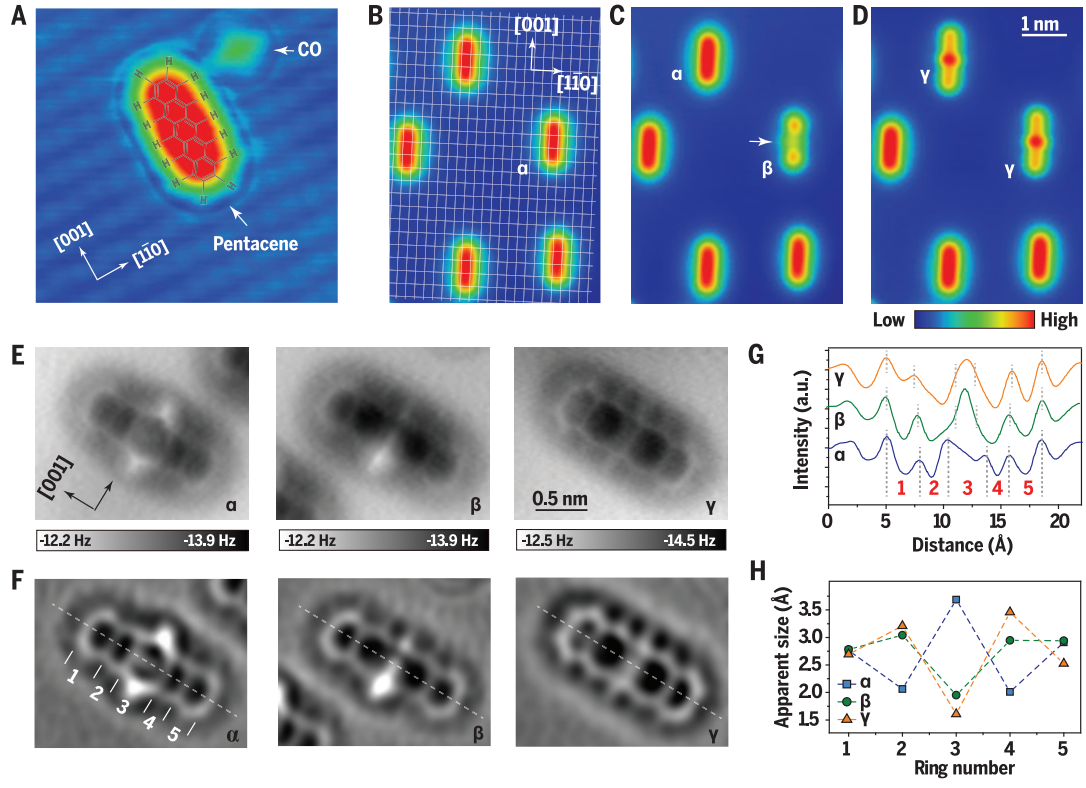

Fig. 1. Transformations of pentacene on the Ag(110) surface. (**A**) Atomically resolved Ag(110) surface with adsorbed pentacene and CO molecules. STM imaging conditions: 60 mV and 1000 pA with a CO-decorated tip. (**B** to **D**) STM topographic images of individually intact pentacene molecules (α) and the transformed species (β and γ) classified according to shape. The middle-right molecule was transformed by two consecutive voltage pulses of 2.0 V, and the upper molecule was transformed by a 2.6-V voltage pulse. The superposed grids in (B) indicate the Ag(110) surface lattice. STM imaging conditions: 0.1 V and 200 pA. (**E** and **F**) Constant-height AFM images and the corresponding Laplace-filtered images of species α, β, and γ. Quality factor $Q \approx 12{,}000$. (**G**) Line profiles obtained along the white dashed lines in (F), with numbers labeling the benzene rings. (**H**) Relative apparent size changes of the five benzene rings in α, β, and γ.

region (>2500 cm^{-1}), which provides a clear energy window with which to monitor the structure change related to C–H bonds (*31*). For species α, such a vibrational mode clearly appeared when the tip was placed at the middle of the molecule but disappeared when measured at the end site. Strong site dependence for other observed Raman modes was also observed. The disappearance of the C–H stretching mode for species γ measured at the middle site seems to confirm the assumption that the C–H bond could be broken during the structure transformation.

The most convincing evidence of C–H bond breaking should come from Raman maps of specific vibrational modes (*16*, *31*). However, it was found that during the continuous Raman mapping measurements, the transformation from α to γ could be easily triggered by the confined excitation light in a few seconds (see the supplementary text and figs. S7 and S8), making it too short to obtain a panoramic Raman map using a charge-coupled device (CCD) spectrometer. Alternatively, we used a high-speed single-photon avalanche photodiode (APD) with an edge-tunable band-pass filter to record the TERS maps (see the materials and methods and fig. S9). Figure 2B shows the simultaneously recorded STM images and Raman maps of the different species, with the photons in the wave-number window of ~2800 to 2900 cm^{-1} corresponding to the C–H stretching mode recorded with a duration time of 25 ms per pixel. Raman maps of the C–H stretching mode showed distinct differences among the species: Species α had two pronounced spots precisely located at both sides of the central benzene ring, and species β had only one spot left at the one side of the central ring; no signal could be detected for species γ. The disappearance of the C–H stretching mode in Raman maps from α to γ could be associated with the disappearance of the protrusions at the central ring in the AFM images (Fig. 1E). Thus, the major difference among the three pentacene species can be categorized by the number of C–H bonds at the central ring, confirming the breaking of C–H bonds in the structural transformation. The simulated Raman maps of C–H stretching mode of species α and β, which are based on C–H bond breaking at the central benzene ring, are in good agreement with the experimental results (Fig. 2C). Here, the two C–H bonds at the central benzene ring showed quite different features in both the AFM images and the TERS signals compared with other C–H bonds at noncentral benzene rings, which could be ascribed to the specific adsorption configuration of pentacene on Ag(110), where the middle two C–H bonds were located more freely above the hollow site than the others (Fig. 1A).

The spatial distributions of the C–H stretching mode were further analyzed by the line

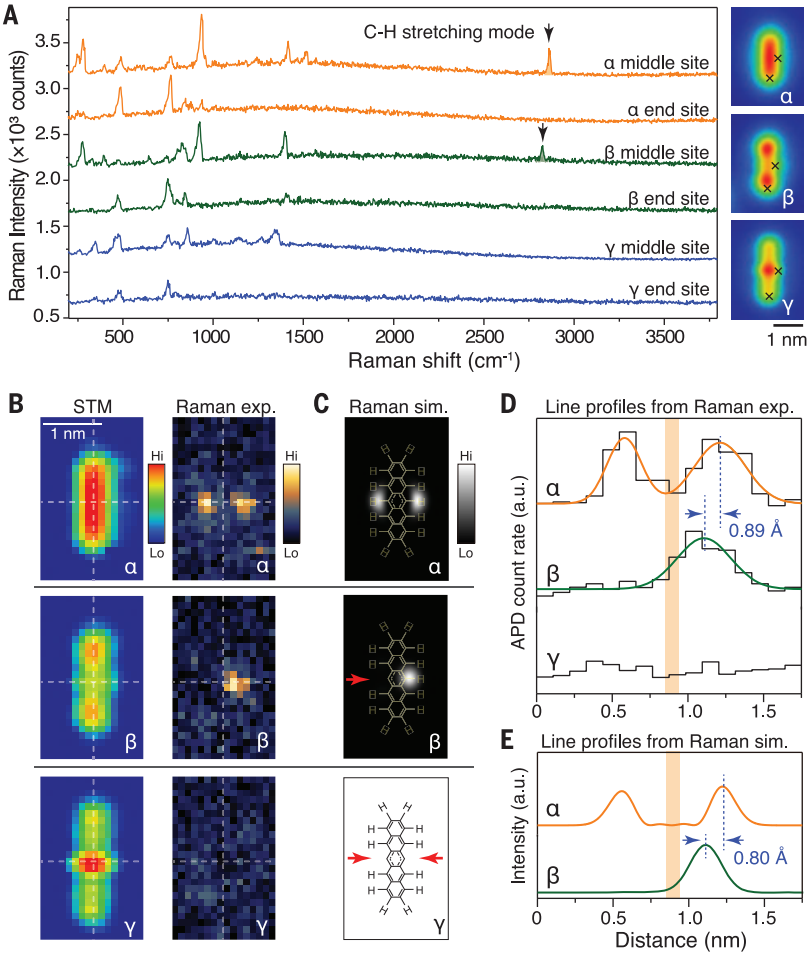

Fig. 2. Determining C–H breaking by Raman spectra and maps. (**A**) Typical Raman spectra obtained at the middle and end sites marked by the crosses over the species of α, β, and γ in the right panel. Parameters for tip-sample nanocavity: 0.1 V and 8 nA. Excitation light: 532 nm and 0.2 mW. CCD spectrometer integration time: 5 s. The spectra are shifted by a separation of 500 counts for clarity. (**B**) Simultaneously obtained STM topographic images and Raman maps for the C–H stretching mode of the pentacene species α, β, and γ. Vertical and horizontal lines indicate the long and short molecular axes, respectively. STM imaging conditions: 0.05 V and 8 nA. Raman maps were collected by introducing the photons in the ~2800 to 2900 cm^{-1} wave-number window to the APD detector, with a duration time of 25 ms per pixel (see fig. S9). (**C**) Simulated Raman maps of the C–H stretching mode for the three pentacene species. Red arrows indicate C–H bond breaking at the central benzene ring in β and γ. (**D** and **E**) Line profiles obtained along the short molecular axis in the experimental and simulated Raman maps, respectively, vertically shifted for clarity. The orange and green curves in (D) are the Gaussian fitting of the peaks.

profiles obtained along the short molecular axis in Raman maps. It can be seen that in the experimental Raman maps, there is a lateral shift of ~0.89 Å for the intensity spot of the C–H stretching mode from α to β (Fig. 2D). This shift could be also reproduced in the line profiles obtained from the simulated Raman maps (Fig. 2E). The observed changes of C–H stretching modes in the three pentacene species support dehydrogenation processes at the central benzene ring.

Nanocavity plasmons with a threshold energy of ~1.5 to 1.6 eV are close to the optical gap of molecular pentacene of ~1.7 eV (*37*), which implies that the light-induced plasmons, as well as the tip-induced plasmons mentioned above, were responsible for the excitation of pentacene on the Ag(110) surface (see the supplementary text). Similar plasmonic excitation was also observed in the dissociation of dimethyl disulfide molecules by the optically excited plasmon at the STM junction (*38*). For pentacene on Ag(110), the calculated relative energies for the three species were found to be 0, 3.01, and 6.01 eV for α, β + H, and γ + 2H, respectively (fig. S10). Such an ~3-eV energy difference thus requires the involvement of two quanta of plasmons for each C–H bond break. This two-photon process could be supported by the experimentally obtained exponent $N \sim 2$ in the power law dependence of reaction rate under 532-nm illumination (fig. S8D).

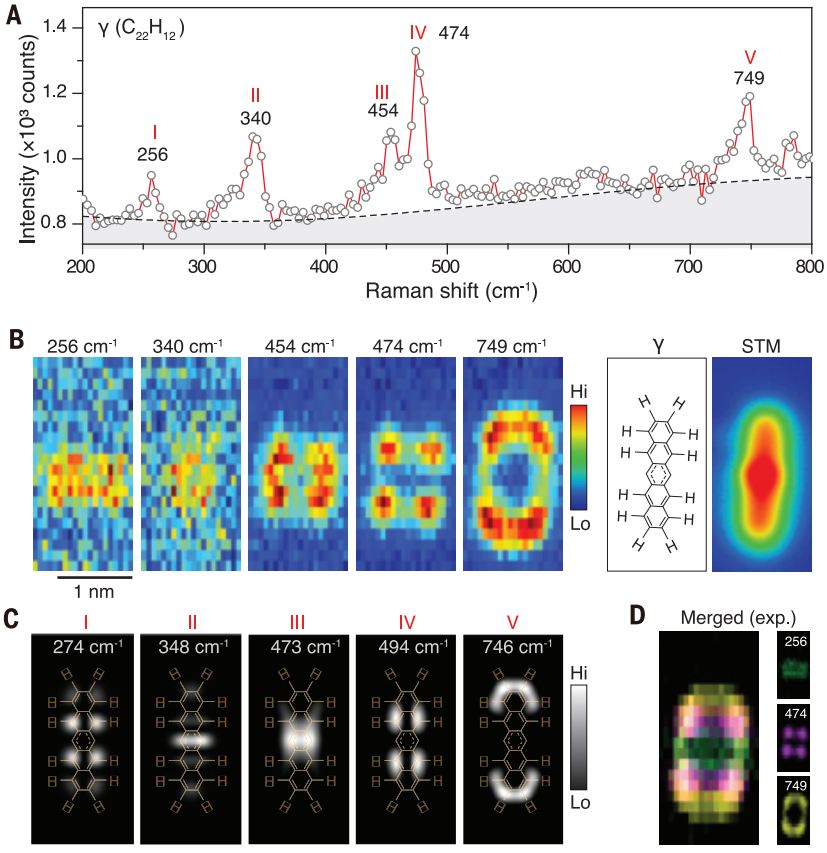

Fig. 3. Raman spectra and maps of the characteristic vibrations in the molecular skeleton. (**A**) Typical Raman spectra recorded around the central benzene ring of species γ ($C_{22}H_{12}$). The five peaks are denoted as the vibrations "I" to "V" in the low-wave-number range. The dashed line indicates the background counts extracted from the baseline correction method. (**B**) Raman maps of γ recorded by integrating the signals at the corresponding peaks in (A) with background subtracted (see fig. S11). The corresponding STM topographic images and the structure are shown in the right panels. (**C**) Simulated Raman maps of the corresponding vibrations of the γ species (see fig. S12). (**D**) Merged image of the experimental Raman maps of 256, 474, and 749 cm^{-1} with different colors.

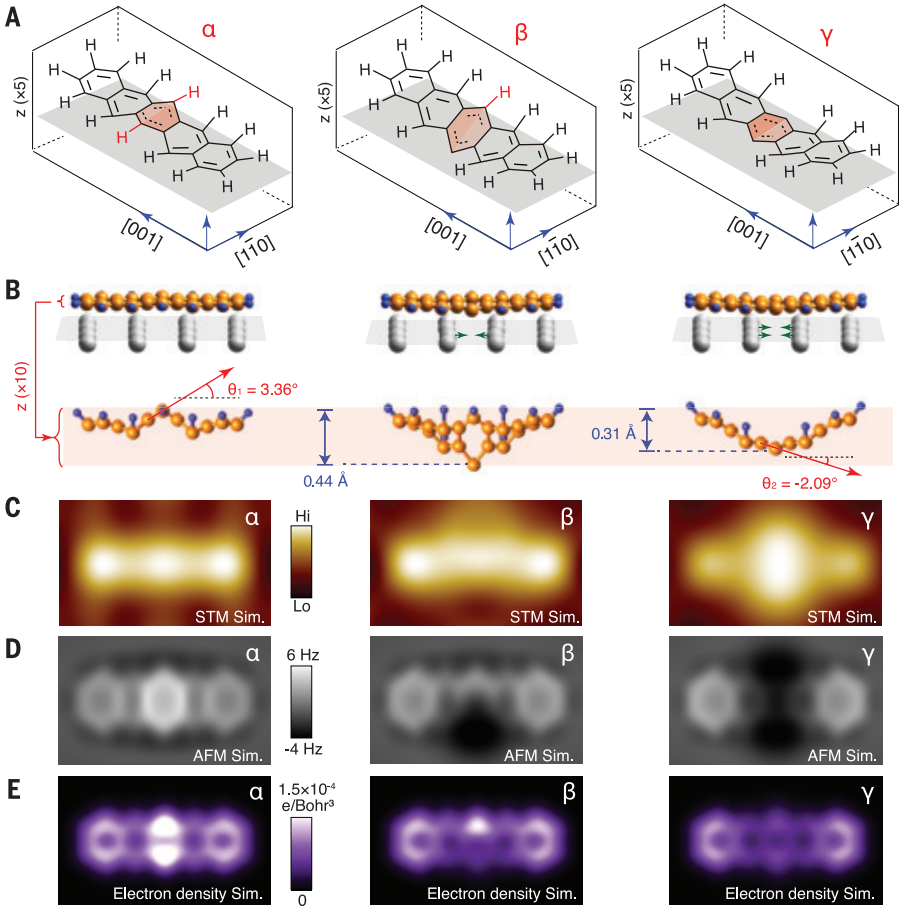

Fig. 4. Optimized structures and simulated images. (**A**) Optimized 3D geometries of the pentacene species α, β, and γ, with enlarged scale (×5) along the surface normal. (**B**) Top panel is a side view of the optimized geometries. The slight displacement of Ag atoms along the [001] direction is indicated by the green arrows under β and γ. Bottom panel is a side view of the distorted skeletons with enlarged scale (×10) in the surface normal. θ_1 and θ_2 denote the distortion of the central benzene ring in α and γ, respectively, with respect to the surface plane. d = 0.44 Å, and 0.31 Å labels the displacement of central C atom along the surface normal direction from α to γ. (**C**) Simulated constant current STM images with integrated DOSs in the range from 0.2 to 0.3 V. The images have been processed with Gaussian smoothing with an SD of 1.33 Å (see fig. S13). (**D** and **E**) Simulated AFM images and electron density maps of α, β, and γ. AFM images are simulated with the effective lateral stiffness k = 0.5 $N \cdot m^{-1}$ and q = 0.2e.

After the transformations of pentacene, the γ species was found to be stable, enabling us to conduct extensive measurements. The Raman spectrum of the γ species at the frequency region associated with the molecular skeleton is given in Fig. 3A, with five well-resolved spectral features located at 256 (I), 340 (II), 454 (III), 474 (IV), and 749 (V) cm^{-1}, respectively. The full Raman maps were recorded using the CCD spectrometer (Fig. 3B and fig. S11). One important observation is that all vibrational modes demonstrated highly localized features. The TERS signals were located either at the central ring or the outer rings of the species, implying that the highly conjugated pentacene became only partially conjugated. The image of the vibrational mode at 454 cm^{-1} could be used as strong evidence to rule out the possible ring opening for the central benzene ring in the γ species. The small intensity variation along two separated chains at the center of the molecule suggests similar local Raman polarizabilities over the chains. In other words, the electronic density over each chain was likely to be polarized together because of their conjugating nature. The image for the mode at 749 cm^{-1} could thus reveal that the skeleton of outer rings also contains conjugating carbon chains. It was further revealed that the experimentally measured Raman modes could be well described by the theoretical simulations for the suggested molecular structure (Fig. 3C, fig. S12, and movies S1 to S5). To fully construct the chemical structure of the γ species, a merged Raman image was obtained by adding the three modes that represented three regions of the species, which clearly showed the key features of the γ skeleton in real space (Fig. 3D). By combining the chemical components obtained by the TERS and the geometric deformations obtained by AFM, the possible chemical structures of γ species could thus be verified, i.e., the break of the C–H bond resulted in the bending of the molecule with the central ring coming closer to the substrate.

The combined STM-AFM-TERS measurements enabled us to unambiguously determine the structural and chemical heterogeneities among the three pentacene species. The importance of the specific local interaction between pentacene and the Ag(110) surface has been clearly demonstrated. The experimentally determined structures of the pentacene species could be further verified by the optimized structures from density functional theory (DFT), which allows more detailed structural information to be obtained (Fig. 4A). For instance, after structural optimizations, the distortion angle with respect to the surface was found to be 3.36° for the central benzene ring of the α species and −2.09° for the γ species (Fig. 4B). Moreover, the bending of the molecule pushed the central benzene ring downward to the surface, with an ~0.31-Å displacement of the C atoms in the γ species (Fig. 4B). A slight lateral displacement of 0.11 and 0.06 Å for the Ag atoms underneath the central benzene ring of the β and the γ species, respectively, was also suggested, which may extrude the central benzene ring and stretch the second and fourth rings along the long molecular axis.

These combined STM-AFM-TERS experimental results can provide a better reference for parameter selection in DFT simulations. For example, it was observed that by integrating the density of states in the voltage window from 0.2 to 0.3 V, the simulated STM images could reproduce the characteristic rod-like, dumbbell-like, and spindle-like features for α, β, and γ, respectively (Fig. 4C and fig. S13), although the experimental images were obtained at 0.1 V (i.e., integrated from 0 to 0.1 V). This discrepancy may have been caused by the inaccuracy of the DFT-calculated unoccupied states. Similarly, considering the effective charge q at the CO-decorated AFM tip apex (*25*, *39*, *40*), it was found that the experimentally observed size change of benzene rings could be better reproduced in the simulated AFM images by using q = 0.2e (Fig. 4D and fig. S14). Obviously, without the reliable structural information obtained from the combined STM-AFM-TERS measurements, the discrepancy between the theory and the experiment would remain disputable. Moreover, the contrast around the central two C–H bonds in AFM images mainly reflected the electron density distribution, in agreement with the simulated charge density maps (Fig. 4E). Electron density accumulation at the central two C–H bonds in α is also responsible for the enhanced polarizability for Raman intensity compared with the other C–H bonds at the noncentral rings.

Our study provides the first demonstration of the capacity offered by the combination of modern tip-based techniques. We have shown that at this stage it becomes possible to use the joint STM-AFM-TERS strategy to experimentally determine the interrelated structural and chemical heterogeneities of surface species, such as the three pentacene species on the Ag(110) surface observed here. The suggested experimental protocol can thus be widely applied for studying surface chemistry and catalysis at the single-bond limit.

REFERENCES AND NOTES

1. S. Titmuss, A. Wander, D. A. King, *Chem. Rev.* **96**, 1291–1306 (1996).
2. E. C. H. Sykes *et al.*, *Acc. Chem. Res.* **36**, 945–953 (2003).
3. G. A. Somorjai, Y. Li, *Proc. Natl. Acad. Sci. U.S.A.* **108**, 917–924 (2011).
4. W. Ho, *Acc. Chem. Res.* **31**, 567–573 (1998).
5. H. J. Lee, W. Ho, *Science* **286**, 1719–1722 (1999).
6. S. W. Hla, K. H. Rieder, *Annu. Rev. Phys. Chem.* **54**, 307–330 (2003).
7. G. A. Somorjai, Y. M. Li, *Introduction to Surface Chemistry and Catalysis* (Wiley, ed. 2, 2010).
8. J. G. Hou *et al.*, *Nature* **409**, 304–305 (2001).
9. A. Zhao *et al.*, *Science* **309**, 1542–1544 (2005).
10. S. W. Hla, L. Bartels, G. Meyer, K. H. Rieder, *Phys. Rev. Lett.* **85**, 2777–2780 (2000).
11. E. I. Altman, M. Z. Baykara, U. D. Schwarz, *Acc. Chem. Res.* **48**, 2640–2648 (2015).
12. M. Richard-Lacroix, Y. Zhang, Z. Dong, V. Deckert, *Chem. Soc. Rev.* **46**, 3922–3944 (2017).
13. M. Ternes, C. P. Lutz, C. F. Hirjibehedin, F. J. Giessibl, A. J. Heinrich, *Science* **319**, 1066–1069 (2008).
14. L. Gross *et al.*, *Science* **337**, 1326–1329 (2012).
15. D. G. de Oteyza *et al.*, *Science* **340**, 1434–1437 (2013).
16. R. Zhang *et al.*, *Nature* **498**, 82–86 (2013).
17. A. Riss *et al.*, *Nat. Chem.* **8**, 678–683 (2016).
18. Z. Han *et al.*, *Science* **358**, 206–210 (2017).
19. J. Lee, K. T. Crampton, N. Tallarida, V. A. Apkarian, *Nature* **568**, 78–82 (2019).
20. F. J. Giessibl, *Science* **267**, 68–71 (1995).
21. L. Gross, F. Mohn, N. Moll, P. Liljeroth, G. Meyer, *Science* **325**, 1110–1114 (2009).
22. J. Zhang *et al.*, *Science* **342**, 611–614 (2013).
23. C. L. Chiang, C. Xu, Z. Han, W. Ho, *Science* **344**, 885–888 (2014).
24. L. L. Patera, F. Queck, P. Scheuerer, J. Repp, *Nature* **566**, 245–248 (2019).
25. R. Ma *et al.*, *Nature* **577**, 60–63 (2020).
26. K. F. Domke, D. Zhang, B. Pettinger, *J. Am. Chem. Soc.* **128**, 14721–14727 (2006).
27. S. Jiang *et al.*, *Nat. Nanotechnol.* **10**, 865–869 (2015).
28. S. Duan *et al.*, *J. Am. Chem. Soc.* **137**, 9515–9518 (2015).
29. P. Liu, X. Chen, H. Ye, L. Jensen, *ACS Nano* **13**, 9342–9351 (2019).
30. N. Chiang *et al.*, *Nano Lett.* **16**, 7774–7778 (2016).
31. Y. Zhang *et al.*, *Natl. Sci. Rev.* **6**, 1169–1175 (2019).
32. W. H. Soe, C. Manzano, A. De Sarkar, N. Chandrasekhar, C. Joachim, *Phys. Rev. Lett.* **102**, 176102 (2009).
33. J. Repp, G. Meyer, S. Paavilainen, F. E. Olsson, M. Persson, *Science* **312**, 1196–1199 (2006).
34. N. Moll, L. Gross, F. Mohn, A. Curioni, G. Meyer, *New J. Phys.* **12**, 125020 (2010).
35. S. Fatayer *et al.*, *Science* **365**, 142–145 (2019).
36. N. Pavliček *et al.*, *Phys. Rev. Lett.* **108**, 086101 (2012).
37. S. Sharifzadeh, A. Biller, L. Kronik, J. B. Neaton, *Phys. Rev. B Condens. Matter Mater. Phys.* **85**, 125307 (2012).
38. E. Kazuma, J. Jung, H. Ueba, M. Trenary, Y. Kim, *Science* **360**, 521–526 (2018).
39. J. Peng *et al.*, *Nat. Commun.* **9**, 122 (2018).
40. M. P. Boneschanscher, S. K. Hämäläinen, P. Liljeroth, I. Swart, *ACS Nano* **8**, 3006–3014 (2014).
41. J. Xu *et al.*, Data for: Determining structural and chemical heterogeneities of surface species at the single-bond limit, Dryad (2021); 10.5061/dryad.d51c5b02c.

ACKNOWLEDGMENTS

We thank J. Zhao, Y. Zhang, and C. Ma for discussions. **Funding:** This work was supported by the Ministry of Science and Technology of China (2016YFA0200603), the Strategic Priority Research Program of Chinese Academy of Sciences (XDB36020200), the National Natural Science Foundation of China (21972129), and the Anhui Initiative in Quantum Information Technologies (AHY090000). **Author contributions:** J.G.H., B.W., and S.T. designed the experiments. J.X., X.Z., and S.T. performed the experiments and analyzed the data. Y.Z. performed the theoretical vibrational analysis and simulations. B.L. and Y.T. performed the DFT calculation and simulations. H.S., X.C., and A.Z. helped with the STM and AFM measurements. All authors discussed the results. Y.L., S.T., B.W., and J.G.H. wrote the manuscript with input from Z.D. and J.Y. **Competing interests:** The authors declare no competing interests. **Data and materials availability:** All data needed to evaluate the conclusions in the study are present in the main text or the supplementary materials. All data have also been uploaded to the Dryad database (*41*).

SUPPLEMENTARY MATERIALS

science.sciencemag.org/content/371/6531/818/suppl/DC1
Materials and Methods
Supplementary text
Figs. S1 to S14
References (*42*–*63*)
Movies S1 to S5

6 June 2020; resubmitted 7 December 2020
Accepted 14 January 2021
10.1126/science.abd1827

CORONAVIRUS

Broad and potent activity against SARS-like viruses by an engineered human monoclonal antibody

C. Garrett Rappazzo[1]*, Longping V. Tse[2]*, Chengzi I. Kaku[1], Daniel Wrapp[3], Mrunal Sakharkar[1], Deli Huang[4], Laura M. Deveau[1], Thomas J. Yockachonis[5], Andrew S. Herbert[6,7], Michael B. Battles[1], Cecilia M. O'Brien[6,7], Michael E. Brown[1], James C. Geoghegan[1], Jonathan Belk[1], Linghang Peng[4], Linlin Yang[4], Yixuan Hou[2], Trevor D. Scobey[2], Dennis R. Burton[4,8,9,10], David Nemazee[4], John M. Dye[6], James E. Voss[4], Bronwyn M. Gunn[5], Jason S. McLellan[3], Ralph S. Baric[2,11]†, Lisa E. Gralinski[2]†, Laura M. Walker[1,12]†

The recurrent zoonotic spillover of coronaviruses (CoVs) into the human population underscores the need for broadly active countermeasures. We employed a directed evolution approach to engineer three severe acute respiratory syndrome coronavirus 2 (SARS-CoV-2) antibodies for enhanced neutralization breadth and potency. One of the affinity-matured variants, ADG-2, displays strong binding activity to a large panel of sarbecovirus receptor binding domains and neutralizes representative epidemic sarbecoviruses with high potency. Structural and biochemical studies demonstrate that ADG-2 employs a distinct angle of approach to recognize a highly conserved epitope that overlaps the receptor binding site. In immunocompetent mouse models of SARS and COVID-19, prophylactic administration of ADG-2 provided complete protection against respiratory burden, viral replication in the lungs, and lung pathology. Altogether, ADG-2 represents a promising broad-spectrum therapeutic candidate against clade 1 sarbecoviruses.

The COVID-19 pandemic, caused by the β-coronavirus severe acute respiratory syndrome coronavirus 2 (SARS-CoV-2), presents an urgent global health crisis. Although two vaccines and two monoclonal antibody (mAb) therapies have been authorized for emergency use by the U.S. Food and Drug Administration, it is unknown whether these vaccines and treatments will provide broad protection against newly emerging SARS-CoV-2 strains that originate in humans or animal reservoirs (*1*). Furthermore, the recurrent zoonotic spillover of CoVs into the human population, along with the broad diversity of SARS-like CoVs circulating in animal reservoirs (*2*), suggests that new pathogenic CoVs are likely to emerge in the future and underscores the need for broadly active countermeasures.

As in other CoVs, the SARS-CoV-2 spike (S) protein mediates viral entry and is the only known target for neutralizing antibodies (nAbs). Although SARS-CoV and SARS-CoV-2 share 76% amino acid identity in their S proteins, only a limited number of cross-neutralizing antibodies have been described to date (*3*–*6*). These rare broadly neutralizing antibodies (bnAbs) represent an attractive opportunity for therapeutic drug stockpiling to prevent or mitigate future outbreaks of SARS-related CoVs, but their limited neutralization potency may translate into suboptimal protective efficacy or impractical dosing regimens. In this study, we show that such bnAbs can be engineered for improved neutralization potency while retaining neutralization breadth, and we demonstrate that these bnAbs can provide broad protection in vivo.

Affinity optimization of SARS-CoV-2 antibodies

We isolated several antibodies from the memory B cells of a 2003 SARS survivor that cross-neutralize multiple SARS-related viruses with relatively modest potency (*3*). Although breadth and potency are often opposing characteristics, we sought to engineer these bnAbs for improved neutralization potency against SARS-CoV-2 while maintaining or improving neutralization breadth and potency against other SARS-like viruses. Because binding affinity and neutralization potency are generally well correlated (*7*), we employed yeast surface display technology to improve the binding affinities of three of the bnAbs (ADI-55688, ADI-55689, and ADI-56046) for a prefusion-stabilized SARS-CoV-2 S protein (*3*, *8*–*10*).

Yeast display libraries were generated by introducing diversity into the heavy- and light-chain-variable genes of ADI-55688, ADI-55689, and ADI-56046 through oligonucleotide-based mutagenesis and transformation into *Saccharomyces cerevisiae* by homologous recombination (*8*). After four rounds of selection with a recombinant SARS-CoV-2 S1 protein, improved binding populations were sorted, and 20 to 50 unique clones from each lineage were screened for binding to SARS-CoV-2 S (*10*) (Fig. 1, A and B, and fig. S1). The highest-affinity binders from each of the three lineages bound to the S protein with monovalent equilibrium dissociation constants (K_Ds) in the picomolar range, representing 25- to 630-fold improvements in binding relative to their respective parental clones and surpassing the affinities of several clinical-stage nAbs (S309, REGN10987, REGN10933, and CB6/LY-CoV16) (Fig. 1B and fig. S2A) (*4*, *11*, *12*). To determine whether the improvements in SARS-CoV-2 S binding affinity translated to enhanced neutralization potency, we selected 9 to 14 affinity-matured progeny from each lineage and evaluated them for SARS-CoV-2 neutralizing activity in a murine leukemia virus (MLV) pseudovirus assay (*13*). All of the affinity-matured antibodies showed improved neutralizing activity relative to that of their parental clones, and the most-potent neutralizers from each lineage (ADG-1, ADG-2, and ADG-3) displayed neutralization half-maximal inhibitory concentrations (IC_{50}s) that were comparable to or lower than those observed for the clinical SARS-CoV-2 nAb controls (Fig. 1B). Notably, however, we observed no correlation between the binding affinities and neutralization potencies of ADG-1, -2, and -3 and the clinical-stage antibodies, suggesting that neutralization potency is more tightly linked to fine epitope specificity than binding affinity to prefusion S (fig. S2B).

Because in vitro engineering can lead to polyreactivity with potential risks of off-target binding and accelerated clearance in vivo (*14*), we evaluated ADG-1, ADG-2, and ADG-3 in a polyreactivity assay that is predictive of serum half-life in humans (*15*). All three antibodies lacked polyreactivity in this assay, indicating a low risk for poor pharmacokinetic behavior (fig. S3). The three antibodies also showed low hydrophobicity, a low propensity for self-interaction, and thermal stabilities within the range observed for clinically approved antibodies (fig. S3). Thus, the process of in vitro engineering appeared not to negatively affect biophysical properties that are often linked to characteristics such as serum half-life, ease of

[1]Adimab, LLC, Lebanon, NH 03766, USA. [2]Department of Epidemiology, The University of North Carolina at Chapel Hill, Chapel Hill, NC 27599, USA. [3]Department of Molecular Biosciences, The University of Texas at Austin, Austin, TX 78712, USA. [4]Department of Immunology and Microbiology, The Scripps Research Institute, La Jolla, CA 92037, USA. [5]Paul G. Allen School of Global Animal Health, Washington State University, Pullman, WA 99164, USA. [6]U.S. Army Medical Research Institute of Infectious Diseases, Frederick, MD 21702, USA. [7]The Geneva Foundation, Tacoma, WA 98402, USA. [8]IAVI Neutralizing Antibody Center, The Scripps Research Institute, La Jolla, CA 92037, USA. [9]Consortium for HIV/AIDS Vaccine Development (CHAVD), The Scripps Research Institute, La Jolla, CA 92037, USA. [10]Ragon Institute of Massachusetts General Hospital, Massachusetts Institute of Technology, and Harvard, Cambridge, MA 02139, USA. [11]Departments of Microbiology and Immunology, The University of North Carolina at Chapel Hill, Chapel Hill, NC 27599, USA. [12]Adagio Therapeutics, Inc., Waltham, MA 02451, USA.
*These authors contributed equally to this work.
†Corresponding author. Email: rbaric@email.unc.edu (R.S.B.); lgralins@email.unc.edu (L.E.G.); laura.walker@adimab.com (L.M.W.)

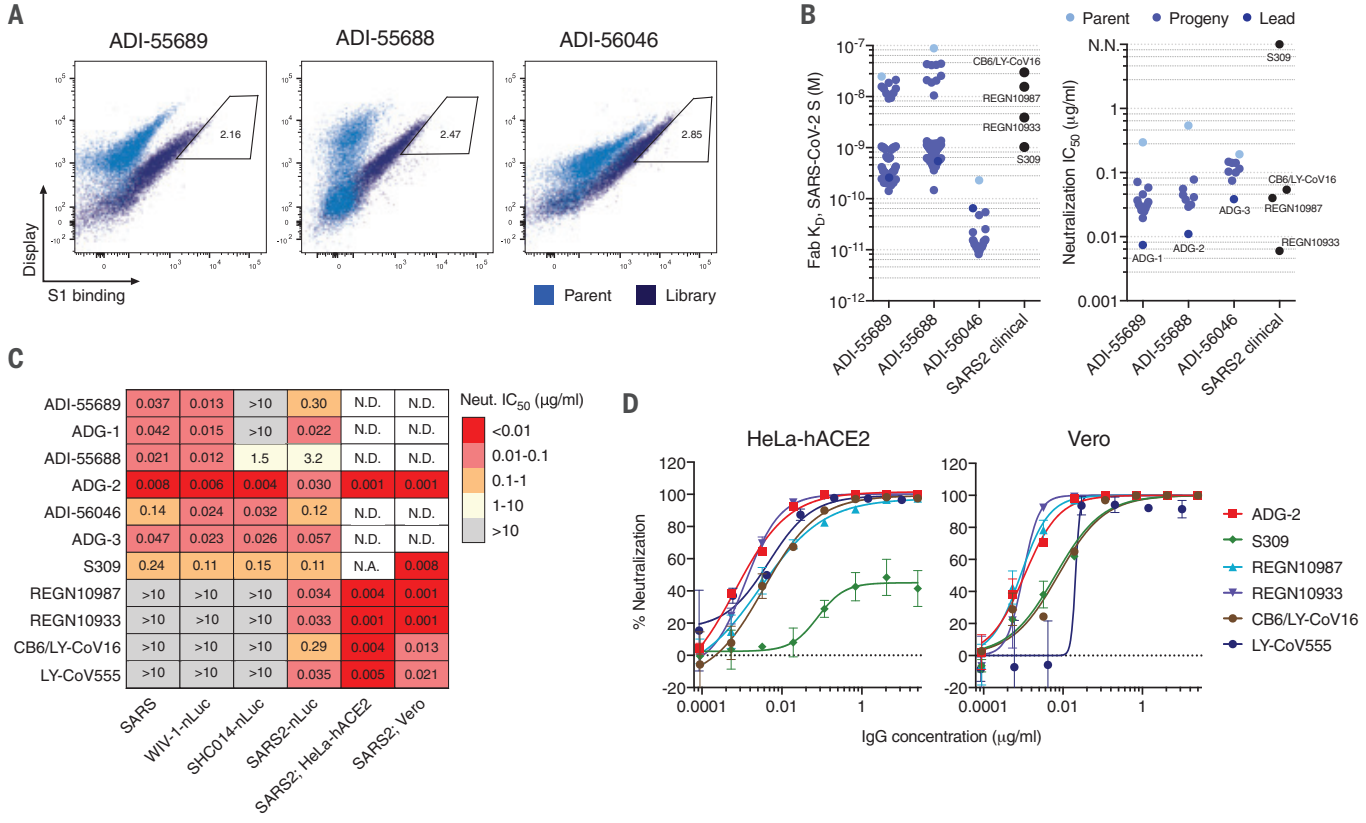

Fig. 1. Engineering SARS-CoV-2 antibodies for enhanced neutralization breadth and potency. (**A**) Flow cytometry plots from the terminal round of selection, showing binding of parental antibodies (light blue) and affinity maturation library antibodies (dark blue) to the SARS-CoV-2 S1 protein at 1 nM. Gates indicate the yeast populations sorted for antibody sequencing and characterization. (**B**) Dot plots of Fab binding affinities (left) and MLV–SARS-CoV-2 pseudovirus neutralization IC_{50}s (right) of parental antibodies and affinity-matured progeny. Clinical-stage SARS-CoV-2 antibodies are shown for comparison. (**C**) Heatmap showing the neutralization IC_{50}s of the indicated antibodies against authentic SARS-CoV, WIV-1-nLuc, SHC014-nLuc, SARS-CoV-2-nLuc, and SARS-CoV-2 on either HeLa-hACE2 or Vero target cells. SARS-CoV, WIV-1-nLuc, SHC014-nLuc, and SARS-CoV-2 nLuc assays were performed on Vero target cells. N.D., not determined; N.A., not applicable due to maximal neutralization plateau at <50% neutralization. (**D**) Authentic SARS-CoV-2 neutralization titrations performed using either HeLa-hACE2 (left) or Vero (right) target cells. The curves were fit by nonlinear regression. Error bars represent SD. All data are representative of at least two independent experiments.

manufacturing, ability to formulate to high concentrations, and long-term stability.

Neutralization breadth and potency of down-selected antibodies

To determine whether the process of affinity engineering affected neutralization breadth, we evaluated ADG-1, ADG-2, and ADG-3, as well as their respective parental antibodies, for neutralizing activity against a panel of representative clade 1 sarbecoviruses (SARS-CoV, SHC014-nLuc, SARS-CoV-2-nLuc, and WIV-1-nLuc). SHC014 and WIV-1 were selected because these two bat SARS-like viruses readily replicate in primary human airway cells, suggesting the potential for direct transmission to humans (*16*, *17*). Consistent with the MLV–SARS-CoV-2 assay results, ADG-2 displayed highly potent neutralizing activity against authentic SARS-CoV-2-nLuc, with an IC_{50} comparable to or lower than those observed for clinical-stage SARS-CoV-2 nAbs (*4*, *11*, *12*, *18*) (Fig. 1C and fig. S4). Furthermore, in contrast to the benchmark nAbs, ADG-2 displayed high neutralization potency against authentic SARS-CoV and the two bat SARS-related viruses, with IC_{50}s between 4 and 8 ng/ml (Fig. 1C and fig. S4). ADG-3 and the clinical nAb S309 also cross-neutralized all four sarbecoviruses but with markedly lower potency than that of ADG-2.

On the basis of its potent cross-neutralization and favorable biophysical properties, we selected ADG-2 as a lead therapeutic candidate and confirmed its potent neutralizing activity in an alternative authentic SARS-CoV-2 neutralization assay (IC_{50} ~ 1 ng/ml) (Fig. 1, C and D, and fig. S4). Because SARS-CoV-2 D614→G (D614G) has emerged as the dominant pandemic strain (*19*), we also performed neutralization studies with MLV–SARS-CoV-2 D614G and confirmed that ADG-2 retains potent neutralizing activity against this strain (fig. S5).

ADG-2 displays broad binding activity to clade 1 sarbecovirus RBDs

We further assessed the breadth of sarbecovirus recognition by ADG-2 by measuring its apparent binding affinity (K_D^{App}) to a panel of 17 representative sarbecovirus receptor binding domains (RBDs) expressed on the surface of yeast (*20*). Thirteen viruses were selected from clade 1—representing the closest known relatives of SARS-CoV-2 (GD-Pangolin and RaTG13) to the most divergent (SHC014 and Rs4231)—as well as four viruses from the distantly related clades 2 and 3, which do not use ACE2 as a host receptor (*21*) (Fig. 2A). Recombinant hACE2-Fc and the benchmark SARS-CoV-2 nAbs described above were included as controls. In agreement with prior reports (*10*, *20*), hACE2 recognized only clade 1 RBDs and bound with

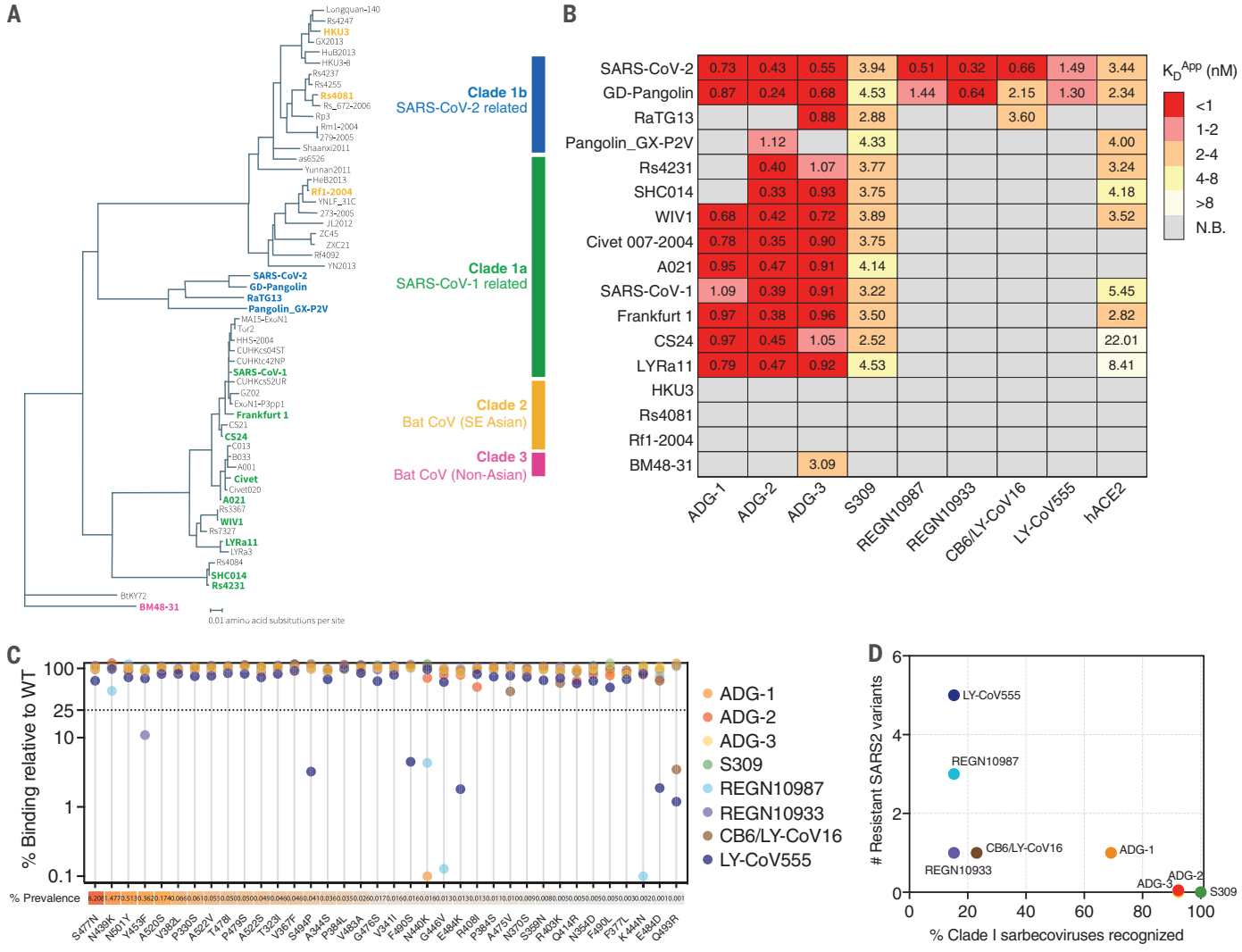

Fig. 2. Breadth of antibody binding to diverse sarbecoviruses and circulating SARS-CoV-2 variants. (**A**) Phylogenetic tree of 57 sarbecoviruses constructed via MAFFT (Multiple Alignment using Fast Fourier Transform) and maximum likelihood analysis of RBD subdomain 1 amino acid sequences extracted from the European Nucleotide Archive and GISAID database. Representative sarbecovirus RBDs selected for further study are denoted in bold and colored according to their canonical phylogenetic lineages. (**B**) Heatmap of antibody and recombinant hACE2 binding to yeast-displayed RBDs from 17 representative sarbecoviruses, grouped by phylogenetic lineages. K_D^{App} values were calculated by normalized nonlinear regression fitting. N.B., nonbinder under the conditions of this assay. (**C**) Antibody binding to naturally occurring SARS-CoV-2 RBD variants displayed on the surface of yeast. SARS-CoV-2 sequences were retrieved from the GISAID database on 14 July 2020 (n = 63,551 sequences). Antibody binding signal was normalized to RBD expression and calculated as percent binding of the variant relative to the WT SARS-CoV-2 RBD, assessed at their respective K_D^{App} concentrations for the WT construct. The prevalence of each variant, calculated from deposited GSAID sequences on 9 December 2020 (n = 211,539 sequences), is shown as a percentage of the total number of sequences analyzed. (**D**) Correlation between the number of resistant SARS-CoV-2 variants and percentage of clade 1 sarbecovirus RBDs recognized. All data are representative of two independent experiments.

higher affinity to SARS-CoV-2 than to SARS-CoV (Fig. 2B).

Consistent with their broadly neutralizing activities, S309, ADG-2, and ADG-3 displayed broad binding reactivity to clade 1 sarbecovirus RBDs, with ADG-2 and ADG-3 strongly binding 12 of 13 viruses and S309 binding all 13 (Fig. 2B). Notably, ADG-2 bound with high affinity (K_D^{App} = 0.24 to 1.12 nM) to every clade 1 sarbecovirus RBD that exhibited detectable hACE2 binding, supporting the high degree of ADG-2 epitope conservation among sarbecoviruses that can use hACE2 as a receptor. By contrast, ADG-1 bound to only 9 of 13 viruses, and CB6/LY-CoV16, LY-CoV555, REGN10987, and REGN10933 bound to only the closest evolutionary neighbor(s) of SARS-CoV-2, consistent with their narrow neutralization profiles (Figs. 2B and 1C).

Prior studies have shown that RBD mutants that are resistant to commonly elicited SARS-CoV-2 nAbs are circulating in the human population (*19*, *22*–*24*). We therefore sought to assess the breadth of ADG-2 binding to naturally circulating SARS-CoV-2 variants that contain single amino acid substitutions in the RBD. ADG-1, ADG-3, and the benchmark SARS-CoV-2 nAbs were included as comparators. Using the yeast surface display platform, we

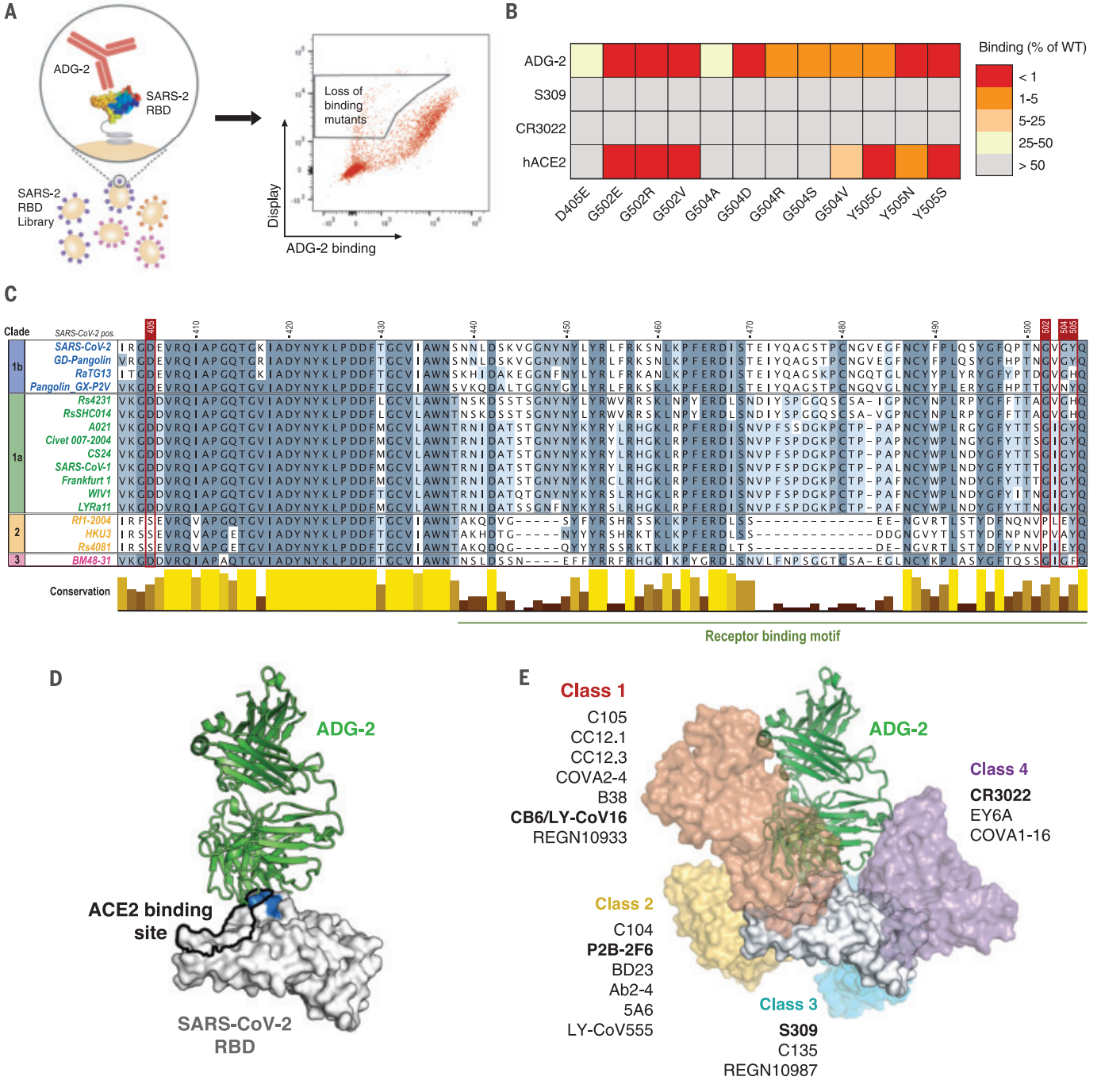

Fig. 3. ADG-2 binds to a conserved RBD epitope overlapping the hACE2 binding site. (**A**) Schematic showing the generation and selection of a mutagenized, yeast surface–displayed SARS-CoV-2 RBD library to identify mutations that knock down ADG-2 binding. (**B**) Heatmap showing mutations that abrogate binding of ADG-2 to the SARS-CoV-2 RBD. S309 and CR3022, which bind nonoverlapping epitopes distinct from the ADG-2 binding site, are included to control for mutations that globally disrupt the conformation of the RBD. Values indicate percent antibody or recombinant hACE2-Fc binding to the mutant SARS-CoV-2 RBD relative to the WT SARS-CoV-2 RBD, assessed at their respective EC_{80} concentrations (80% effective concentrations) for the WT RBD construct. (**C**) Protein sequence alignment of representative sarbecovirus RBDs, with sequences colored by percentage sequence identity and conservation shown as a bar plot. Positions delineating the receptor binding motif are based on the SARS-CoV-2 RBD. Residues determined to be important for ADG-2 binding, on the basis of the data shown in (B), are denoted in red. Single-letter abbreviations for the amino acid residues are as follows: A, Ala; C, Cys; D, Asp; E, Glu; F, Phe; G, Gly; H, His; I, Ile; K, Lys; L, Leu; M, Met; N, Asn; P, Pro; Q, Gln; R, Arg; S, Ser; T, Thr; V, Val; W, Trp; and Y, Tyr. (**D**) Cryo-EM reconstruction of the SARS-CoV-2 RBD bound by ADG-2, with ADG-2 knockdown mutations (blue) and the hACE2 binding site (black outline) highlighted. (**E**) Structures of previously reported antibodies (bold), representing frequently observed SARS-CoV-2 nAb classes 1 to 4, are overlaid on the ADG-2 structure (D), with additional representative SARS-CoV-2 nAbs listed.

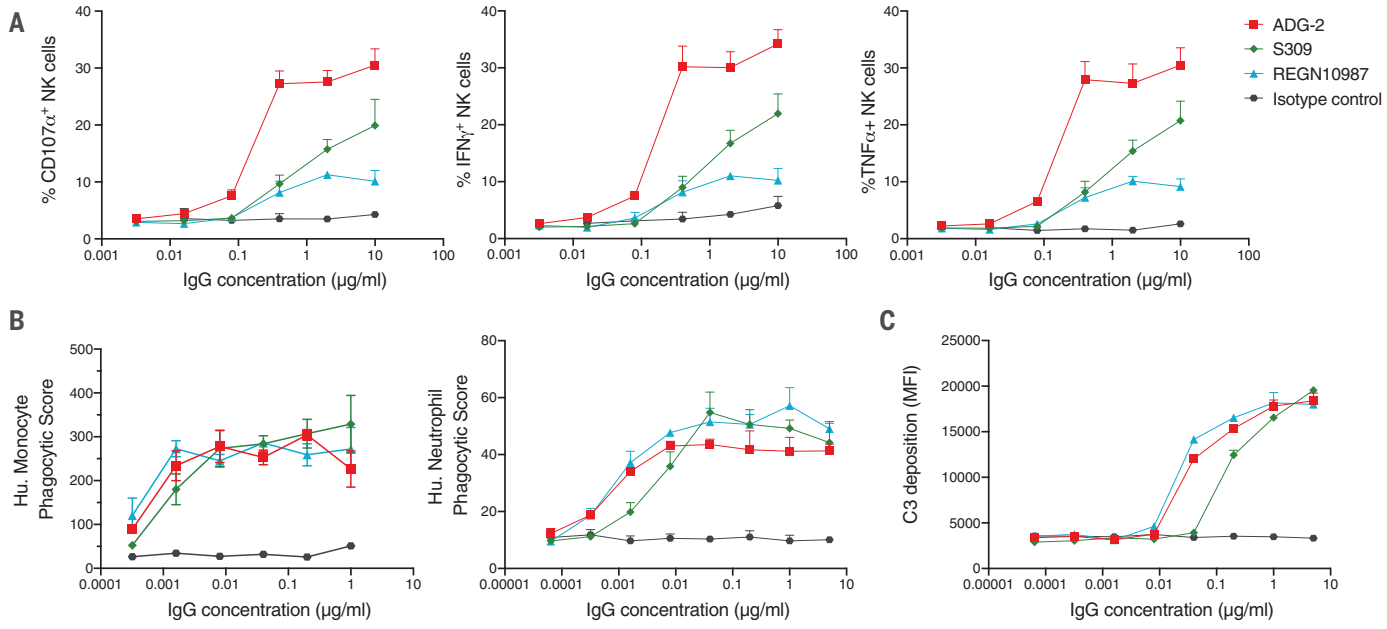

Fig. 4. ADG-2 triggers Fc-mediated effector functions. The indicated antibodies were assessed for the ability to induce Fc-mediated effector functions against RBD-coated targets at varying concentrations. (**A**) Primary human NK cells were analyzed for surface expression of CD107a, indicating degranulation (left), and the production of interferon-γ (IFNγ) (middle) or tumor necrosis factor–α (TNFα) (right) after incubation with antibody-RBD immune complexes for 5 hours. IgG, immunoglobulin G. (**B**) Antibody-mediated phagocytosis of RBD-coated fluorescent beads by differentiated THP-1 monocytes (left) or HL-60 neutrophils (right) was measured after incubation with immune complexes for 18 hours. Hu., human. (**C**) Antibody-mediated complement deposition was measured by detection of complement component C3 onto RBD-coated fluorescent beads after incubation of guinea pig complement with immune complexes for 20 min. MFI, mean fluorescence intensity. Error bars represent SD. All data are representative of two independent experiments.

expressed the 30 most frequently observed SARS-CoV-2 RBD variants reported in the GISAID database as well as 6 naturally circulating SARS-CoV-2 variants reported to be resistant to certain SARS-CoV-2 nAbs (*19*, *22*, *25*). One or more of the 36 SARS-CoV-2 variants exhibited loss of binding to ADG-1, CB6/LY-CoV16, LY-CoV555, REGN10987, and REGN10933, as defined by >75% loss relative to the wild-type (WT) construct (Fig. 2C). Notably, the loss-of-binding variants identified for REGN10987 and REGN10933 partially overlapped with those identified in previous in vitro neutralization escape studies, validating the use of RBD display for the prediction of antibody escape mutations (*26*). By contrast, ADG-2, ADG-3, and S309 bound to all 36 variants at levels ≥50% of those for WT SARS-CoV-2 (Fig. 2C). This result, combined with the substantial neutralization breadth observed for these three mAbs (Figs. 1C and 2, B and D), indicates a potential link between epitope conservation and resistance to viral escape. Finally, all of the antibodies retained high-affinity binding to the N501Y variant, which is the only RBD mutation present in the rapidly spreading B.1.1.7 lineage (*27*), suggesting that this newly emerging SARS-CoV-2 strain is likely susceptible to neutralization by these antibodies.

ADG-2 binds to a conserved neutralizing epitope overlapping the hACE2 binding site

To gain further insight into the antigenic surface recognized by ADG-2, we generated a mutagenized yeast surface display RBD library and performed rounds of selection to identify RBD variants that exhibited loss of binding to ADG-2 relative to the WT construct (Fig. 3A and fig. S6, A and B). To exclude mutations that globally disrupt the conformation of the RBD, a final round of positive selection was performed using a mixture of recombinant hACE2-Fc and two RBD-directed mAbs (S309 and CR3022) that target nonoverlapping epitopes distinct from the ADG-2 binding site (*4*, *28*) (figs. S6B and S7). Selected RBD mutants were individually tested for binding to ADG-2, recombinant hACE2-Fc, CR3022, and S309 to confirm site-specific knockdown mutations (fig. S6C). Substitutions at only four RBD positions—D405E, G502E/R/V, G504A/D/R/S/V and Y505C/N/S—specifically abrogated ADG-2 binding (Fig. 3B). These four residues are highly conserved among the clade 1 sarbecovirus subgenus and invariant among SARS-CoV-1, SARS-CoV-2, SHC014, and WIV1 viruses (Fig. 3C), providing a molecular explanation for the breadth of binding and neutralization exhibited by ADG-2. Consistent with the conservation of these residues among clade 1 sarbecoviruses, none of the substitutions that affected ADG-2 binding were present in full-length SARS-CoV-2 sequences deposited in the GISAID database at a frequency >0.001% as of 9 December 2020. In addition, three of the four identified mutations that abrogate ADG-2 binding lie within the hACE2 binding site (*29*), and at least one mutation at each position (G502E/R/V, G504V, and Y505C/N/S) also abrogated hACE2 binding (Fig. 3B), likely accounting for their absence among circulating SARS-CoV-2 isolates. These results suggest that the evolutionary conservation of the ADG-2 epitope is likely directly linked to ACE2 binding.

To support the results of this experiment, we performed low-resolution cryo–electron microscopy (cryo-EM) of the complex of ADG-2 bound to prefusion-stabilized SARS-CoV-2 S. This yielded a ~6-Å resolution three-dimensional reconstruction that clearly had at least one ADG-2 Fab bound to an RBD in the up conformation and allowed us to dock in previously determined high-resolution models of the SARS-CoV-2 spike and a homologous Fab (Fig. 3D; fig. S8, A to D; and table S1). Consistent with our fine epitope mapping experiments (Fig. 3B and fig. S7C), the epitope recognized by ADG-2 overlaps the

hACE2-binding site and each position identified by epitope mapping clustered to the cleft between the heavy and light chains of ADG-2 (Fig. 3D). This epitope also partially overlaps with those recognized by frequently observed "class 1" SARS-CoV-2 nAbs (*30*) (Fig. 3E). However, in contrast to previously reported nAbs in this class, ADG-2 binds with a divergent angle of approach and displays broadly neutralizing activity (*30*) (Figs. 3E and 1C and fig. S8E). Thus, ADG-2 binds to a highly conserved motif through a distinct angle of approach.

ADG-2 potently triggers Fc-mediated effector functions in vitro

Because Fc-mediated effector functions can contribute to protection independently of viral neutralization, we assessed the ability of ADG-2 to induce antibody-dependent natural killer (NK) cell activation and degranulation, antibody-dependent cellular phagocytosis mediated by monocytes and neutrophils, and antibody-mediated complement deposition using in vitro effector function assays (*31*). Benchmark SARS-CoV-2 nAbs S309 and REGN10987 were included as comparators. Notably, though ADG-2, S309, and REGN10987 showed comparable recruitment of phagocytosis (Fig. 4B), these antibodies differed with respect to complement deposition and NK cell activation (Fig. 4, A and C): S309 showed reduced complement deposition compared with ADG-2 and REGN10987, and ADG-2 showed superior NK cell activation to both S309 and REGN10987 (Fig. 4). In summary, ADG-2 robustly triggers diverse Fc-mediated effector activities with potencies comparable or superior to those of current SARS-CoV-2 clinical antibodies.

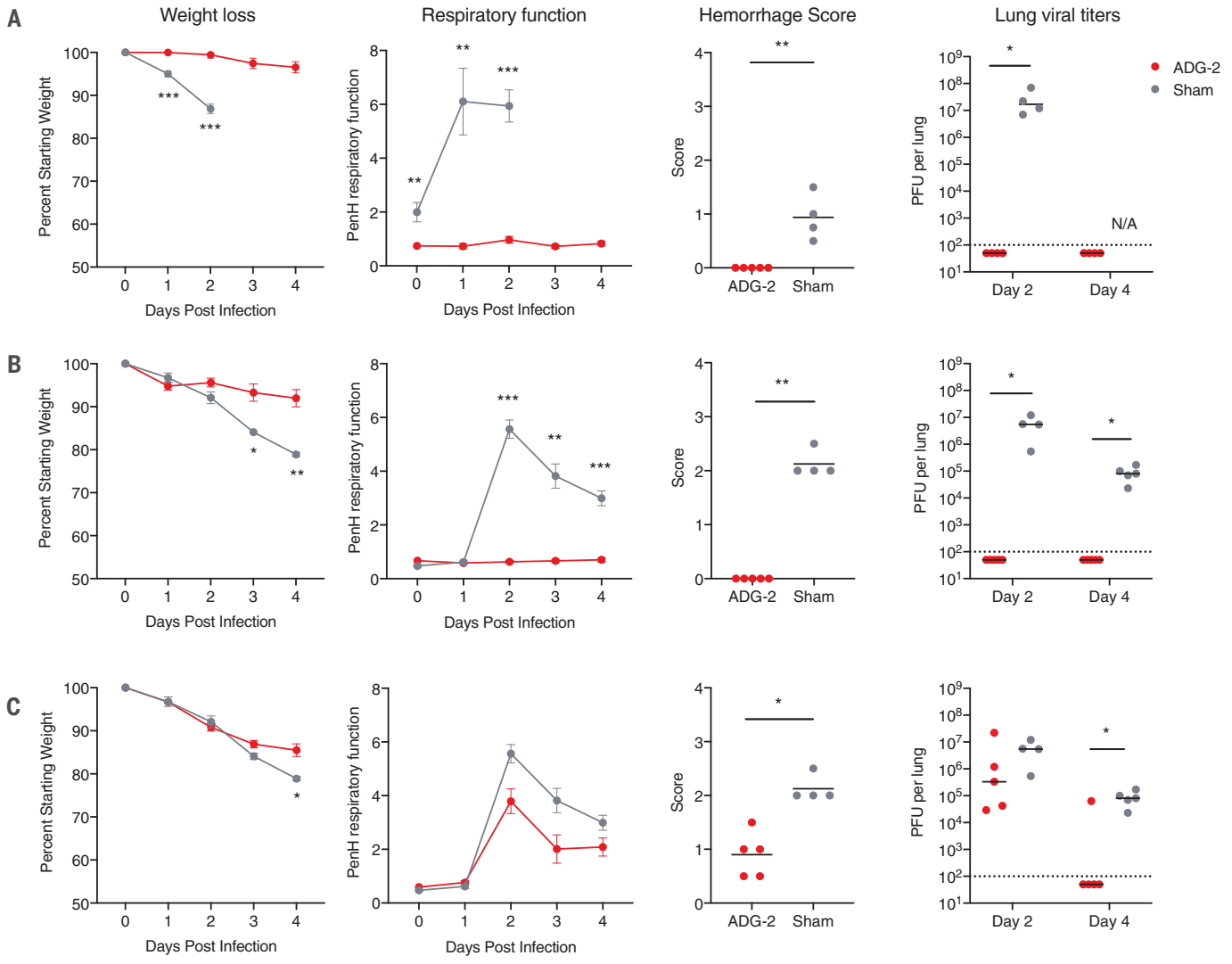

Fig. 5. Prophylactic and therapeutic administration of ADG-2 protects mice from SARS-CoV– and SARS-CoV-2–associated disease. Efficacy of prophylactic treatment with ADG-2 in (**A**) SARS-CoV–MA15 and (**B**) SARS-CoV-2–MA10 challenge models. A single dose of ADG-2 or sham treatment was delivered intraperitoneally 12 hours before infection. Mouse body weight and respiratory function were monitored for 4 days. Gross lung hemorrhage scores were determined on day 2 (MA15) or day 4 (MA10) after infection, and lung viral titers were measured on days 2 and 4 after infection. (**C**) Therapeutic treatment with ADG-2 or sham treatment 12 hours after SARS-CoV-2–MA10 infection. Mouse body weight, respiratory function, gross hemorrhage scores (day 2), and lung viral titers (days 2 and 4) were assessed as described above. Statistical comparisons were made using Mann-Whitney *U* tests or two-sided *t* tests with Holm-Sidak corrections for multiple comparisons (*$P < 0.05$, **$P < 0.01$, ***$P < 0.001$). Dotted lines indicate the limit of detection. Horizontal bars indicate mean or geometric mean.

ADG-2 broadly protects in murine models of SARS and COVID-19

Finally, we tested the ability of ADG-2 to provide broad in vivo protection in immunocompetent mouse models of SARS and COVID-19 using mouse-adapted SARS-CoV (MA15) and SARS-CoV-2 (MA10), respectively (*32*, *33*). Balb/c mice were prophylactically treated with either 200 μg of ADG-2 or phosphate-buffered saline (PBS) via intraperitoneal injection 12 hours before intranasal challenge with an MA15 or MA10 dose of 10^3 plaque-forming units (PFU). All mice were monitored daily for weight loss and changes in respiratory function, and groups of mice were euthanized at day 2 or 4 postinfection to allow for measurement of virus replication in the lung and analysis of lung histopathology. We observed substantial, progressive weight loss in sham-treated mice infected with both viruses along with increases in enhanced pause (Penh), a calculated measure of airway resistance (*33*). By contrast, mice treated prophylactically with ADG-2 demonstrated minimal weight loss, no change in Penh, and no signs of gross pathology at the time of harvest (Fig. 5, A and B). Furthermore, prophylactic antibody treatment prevented viral replication in the lungs at both 2 and 4 days postinfection (dpi). We next investigated the ability of ADG-2 to act antivirally against SARS-CoV-2 MA10 in a therapeutic setting. Mice were treated with 200 μg of ADG-2 or PBS 12 hours after intranasal challenge with a 10^3-PFU dose of MA10. Mice given therapeutic ADG-2 had intermediate levels of weight loss, moderate respiratory function changes, and some gross lung pathology—significantly more than prophylactically treated mice but significantly less than sham-treated mice (Fig. 5C). Therapeutic antibody treatment also resulted in a significant reduction in lung viral loads at 4 dpi, but not at 2 dpi, relative to sham-treated mice. We conclude that ADG-2 treatment can reduce disease burden in mice infected with both SARS-CoV MA15 and SARS-CoV-2 MA10.

Discussion

Since the beginning of the COVID-19 pandemic, a plethora of potently neutralizing SARS-CoV-2 antibodies have been isolated, and some have rapidly advanced to clinical trials (*34*). However, the epitopes recognized by most of these nAbs are highly variable among other clade 1 sarbecoviruses, hence limiting their neutralization breadth and increasing their susceptibility to antibody escape mutations (*22*). Here, we describe an engineered antibody that neutralizes SARS-CoV-2 with a potency that rivals current lead SARS-CoV-2 clinical nAbs but also broadly neutralizes other clade 1 sarbecoviruses, potently triggers Fc-mediated effector functions, and provides significant protection against SARS and COVID-19 in mouse models. Thus, ADG-2 represents a promising candidate for the prevention and treatment of not only COVID-19, but also future respiratory diseases caused by pre-emergent SARS-related CoVs. Furthermore, our fine epitope mapping and structural studies demonstrate that ADG-2 employs a distinct angle of approach to recognize a highly conserved epitope that overlaps the receptor binding site. This epitope represents an Achilles' heel for clade 1 sarbecoviruses and hence is an attractive target for the rational design of "pan-SARS" vaccines that aim to elicit similar broadly protective antibodies.

REFERENCES AND NOTES

1. B. B. Oude Munnink *et al.*, *Science* **371**, 172–177 (2021).
2. J. Cui, F. Li, Z. L. Shi, *Nat. Rev. Microbiol.* **17**, 181–192 (2019).
3. A. Z. Wec *et al.*, *Science* **369**, 731–736 (2020).
4. D. Pinto *et al.*, *Nature* **583**, 290–295 (2020).
5. C. Wang *et al.*, *Nat. Commun.* **11**, 2251 (2020).
6. H. Liu *et al.*, *Immunity* **53**, *1272–1280.e5 (2020)*.
7. P. W. Parren, D. R. Burton, *Adv. Immunol.* **77**, 195–262 (2001).
8. A. Z. Wec *et al.*, *Cell Host Microbe* **25**, 39–48.e5 (2019).
9. M. J. Feldhaus *et al.*, *Nat. Biotechnol.* **21**, 163–170 (2003).
10. D. Wrapp *et al.*, *Science* **367**, 1260–1263 (2020).
11. J. Hansen *et al.*, *Science* **369**, 1010–1014 (2020).
12. R. Shi *et al.*, *Nature* **584**, 120–124 (2020).
13. T. Giroglou *et al.*, *J. Virol.* **78**, 9007–9015 (2004).
14. S. A. Sievers, L. Scharf, A. P. West Jr., P. J. Bjorkman, *Curr. Opin. HIV AIDS* **10**, 151–159 (2015).
15. L. Shehata *et al.*, *Cell Rep.* **28**, 3300–3308.e4 (2019).
16. V. D. Menachery *et al.*, *Proc. Natl. Acad. Sci. U.S.A.* **113**, 3048–3053 (2016).
17. V. D. Menachery *et al.*, *Nat. Med.* **21**, 1508–1513 (2015).
18. B. E. Jones *et al.*, bioRxiv 2020.09.30.318972 [Preprint]. 9 October 2020. https://doi.org/10.1101/2020.09.30.318972.
19. B. Korber *et al.*, *Cell* **182**, 812–827.e19 (2020).
20. T. N. Starr *et al.*, *Cell* **182**, 1295–1310.e20 (2020).
21. M. Letko, A. Marzi, V. Munster, *Nat. Microbiol.* **5**, 562–569 (2020).
22. D. F. Robbiani *et al.*, *Nature* **584**, 437–442 (2020).
23. Y. Weisblum *et al.*, *eLife* **9**, e61312 (2020).
24. A. J. Greaney *et al.*, *Cell Host Microbe* **29**, 44–57.e9 (2021).
25. Y. Shu, J. McCauley, *Euro Surveill.* **22**, 30494 (2017).
26. A. Baum *et al.*, *Science* **369**, 1014–1018 (2020).
27. K. Leung, M. H. H. Shum, G. M. Leung, T. T. Y. Lam, J. T. Wu, medRxiv 2020.12.20.20248581 [Preprint]. 23 December 2020. https://doi.org/10.1101/2020.12.20.20248581.
28. M. Yuan *et al.*, *Science* **368**, 630–633 (2020).
29. J. Lan *et al.*, *Nature* **581**, 215–220 (2020).
30. C. O. Barnes *et al.*, *Nature* **588**, 682–687 (2020).
31. B. M. Gunn *et al.*, *Cell Host Microbe* **24**, 221–233.e5 (2018).
32. A. Roberts *et al.*, *PLOS Pathog.* **3**, e5 (2007).
33. S. R. Leist *et al.*, *Cell* **183**, 1070–1085.e12 (2020).
34. A. Renn, Y. Fu, X. Hu, M. D. Hall, A. Simeonov, *Trends Pharmacol. Sci.* **41**, 815–829 (2020).

ACKNOWLEDGMENTS

We thank T. Boland for assistance with SARS-CoV-2 sequence analysis; C. Williams for assistance with figure preparation; E. Krauland, J. Nett, and M. Vasquez for helpful comments on the manuscript; and J. Ludes-Meyers for assistance with cell transfection. All IgGs were sequenced by Adimab's Molecular Core and produced by the High Throughput Expression group. Biolayer interferometry binding experiments were performed by Adimab's Protein Analytics group. Opinions, conclusions, interpretations, and recommendations are those of the authors and are not necessarily endorsed by the U.S. Army. The mention of trade names or commercial products does not constitute endorsement or recommendation for use by the Department of the Army or the Department of Defense. **Funding:** This work was funded in part by National Institutes of Health (NIH)/National Institute of Allergy and Infectious Diseases (NIAID) grants awarded to J.S.M. (R01-AI12751), D.N. (R01-AI132317 and R01-AI073148), and R.S.B. (R01-AI132178 and U54 CA260543). J.E.V. was also supported by the Bill and Melinda Gates Foundation (OPP 1183956). B.M.G. and J.M.D. were supported by NIH/NIAID grant 5U19AI142777. **Author contributions:** L.M.W., L.E.G., and R.S.B. conceived and designed the study. L.M.D. and J.B. performed the directed evolution experiments. L.V.T., D.H., A.S.H., C.M.O., L.P., L.Y., T.D.S., D.R.B., D.N., J.M.D., J.V., and R.S.B. developed, designed, and performed neutralization assays. M.E.B. and J.C.G. designed and supervised developability and biolayer interferometry assays. C.G.R., C.I.K., M.S., and M.B.B. designed and performed the yeast surface display RBD experiments. D.W. and J.S.M. designed and performed Biacore surface plasmon resonance and structural assays. T.J.Y. and B.M.G. designed and performed Fc-effector functional assays. L.E.G. designed and performed the animal challenge studies. C.G.R., L.V.T., C.I.K., D.W., M.S., D.H., L.M.D., A.S.H., M.B.B., B.M.G., L.E.G., and L.M.W. analyzed the data. C.G.R., L.V.T., C.I.K., D.W., M.S., D.H., B.M.G., L.E.G., and L.M.W. wrote the manuscript, and all authors reviewed and edited the paper. **Competing interests:** C.G.R., C.I.K., M.S., L.M.D., M.B.B., M.E.B., J.C.G., and L.M.W. are employees of Adimab, LLC, and may hold shares in Adimab, LLC. L.M.W. is an employee of Adagio Therapeutics, Inc., and holds shares in Adagio Therapeutics, Inc. D.R.B. is on the scientific advisory board of Adimab, LLC, and Adagio Therapeutics, Inc., and holds shares in Adimab, LLC. L.M.W. and J.B. are inventors on a patent application submitted by Adagio Therapeutics, Inc., describing the engineered SARS-CoV-2 antibodies. **Data and material availability:** Antibody sequences have been deposited in GenBank under accession codes MW417369 to MW417400. The ADG-2 cryo-EM density map has been deposited into the Electron Microscopy Data Bank under accession code EMD-23160. All other data are available in the manuscript or supplementary materials. IgGs are available from L.M.W. under a material transfer agreement (MTA) from Adagio Therapeutics, Inc. The MA15 (SARS-CoV) challenge virus is available from BEI Resources as NR-44006; the MA10 (SARS-CoV-2) virus has been deposited but is not yet shipping while BEI confirms the sequence. MA10 is available from The University of North Carolina at Chapel Hill through a standard MTA agreement as we wait for BEI to be ready for orders. The hACE2 cell lines and constructs for pseudoviruses and proteins are available from D.N. under an MTA with The Scripps Research Institute. We gratefully acknowledge the authors from the originating laboratories and the submitting laboratories, who generated and shared via GISAID genetic sequence data on which this research is based (table S2). This work is licensed under a Creative Commons Attribution 4.0 International (CC BY 4.0) license, which permits unrestricted use, distribution, and reproduction in any medium, provided the original work is properly cited. To view a copy of this license, visit https://creativecommons.org/licenses/by/4.0/. This license does not apply to figures/photos/artwork or other content included in the article that is credited to a third party; obtain authorization from the rights holder before using such material.

SUPPLEMENTARY MATERIALS

science.sciencemag.org/content/371/6531/823/suppl/DC1
Materials and Methods
Figs. S1 to S8
Tables S1 and S2
References (*35*–*50*)

MDAR Reproducibility Checklist

30 October 2020; accepted 19 January 2021
Published online 25 January 2021
10.1126/science.abf4830

REPORTS

THERMOELECTRICS

High-entropy-stabilized chalcogenides with high thermoelectric performance

Binbin Jiang[1]*, Yong Yu[1,2]*, Juan Cui[1]*, Xixi Liu[1], Lin Xie[1], Jincheng Liao[3], Qihao Zhang[3], Yi Huang[1], Shoucong Ning[2], Baohai Jia[1], Bin Zhu[1], Shengqiang Bai[3], Lidong Chen[3], Stephen J. Pennycook[2], Jiaqing He[1,4]†

Thermoelectric technology generates electricity from waste heat, but one bottleneck for wider use is the performance of thermoelectric materials. Manipulating the configurational entropy of a material by introducing different atomic species can tune phase composition and extend the performance optimization space. We enhanced the figure of merit (*zT*) value to 1.8 at 900 kelvin in an n-type PbSe-based high-entropy material formed by entropy-driven structural stabilization. The largely distorted lattices in this high-entropy system caused unusual shear strains, which provided strong phonon scattering to largely lower lattice thermal conductivity. The thermoelectric conversion efficiency was 12.3% at temperature difference ΔT = 507 kelvin, for the fabricated segmented module based on this n-type high-entropy material. Our demonstration provides a paradigm to improve thermoelectric performance for high-entropy thermoelectric materials through entropy engineering.

Conversion processes waste more than two-thirds of the energy in the world, which can be potentially collected by technology that captures waste heat (*1*). Thermoelectric technology is an attractive option because it can be easily adopted for many situations as a result of its small size and lack of rotating parts or gas emissions (*2*, *3*). One major obstacle to using thermoelectric technology for real applications is the low conversion efficiency. The efficiency is directly determined by the dimensionless figure of merit [$zT = S^2\sigma T/(\kappa_e+\kappa_L)$] of thermoelectric materials (*4*, *5*), where S, σ, T, κ_e, and κ_L are the Seebeck coefficient, electrical conductivity, absolute temperature, carrier thermal conductivity, and lattice thermal conductivity, respectively. All of these parameters can be optimized by tuning band structures, microstructures, and bond states with a range of proposed strategies such as band convergence (*6*), resonant level (*7*), alloying (*2*), nanostructure (*8*), anharmonicity (*4*), and liquid-like ions (*9*). Although these efforts are named with different physical terminologies, the general strategy is to improve electrical transport properties and destroy the thermal transport path. In general, high-entropy alloys (HEAs) should provide a good way to improve thermoelectric performance by strengthening phonon scattering because of their disorder and distorted lattice. Manipulating the electronic properties to maintain electron transport can then be accomplished by trying to use the wide range of chemical compositions to vary phase composition and band structure (*10*).

HEAs are typically defined as a solid solution with more than five principal elements, each in a 5 to 35% molar ratio (*11*) (Fig. 1A). This concept has been extended into creating entropy-stabilized functional materials (*10*). The first reported entropy-stabilized high-entropy functional material was (Mg,Co,Ni,Cu,Zn)O oxide (*12*), which was followed by perovskites, fluorite, spinels, carbides, and silicides (*10*). For a given system, the configurational entropy will increase with increasing element species, leading to the decreased Gibbs free energy and stabilized crystal structure when the increase of entropy is larger than that of enthalpy (*10*, *12*). The change of energy manifests as the extended solubility limits of alloying elements or the entropy-driven structural stabilization effect (*13*, *14*). More accurately, a new phase formed by using entropy as the driving force, contributing to the extended phase space for performance optimization. The stabilized structure can keep

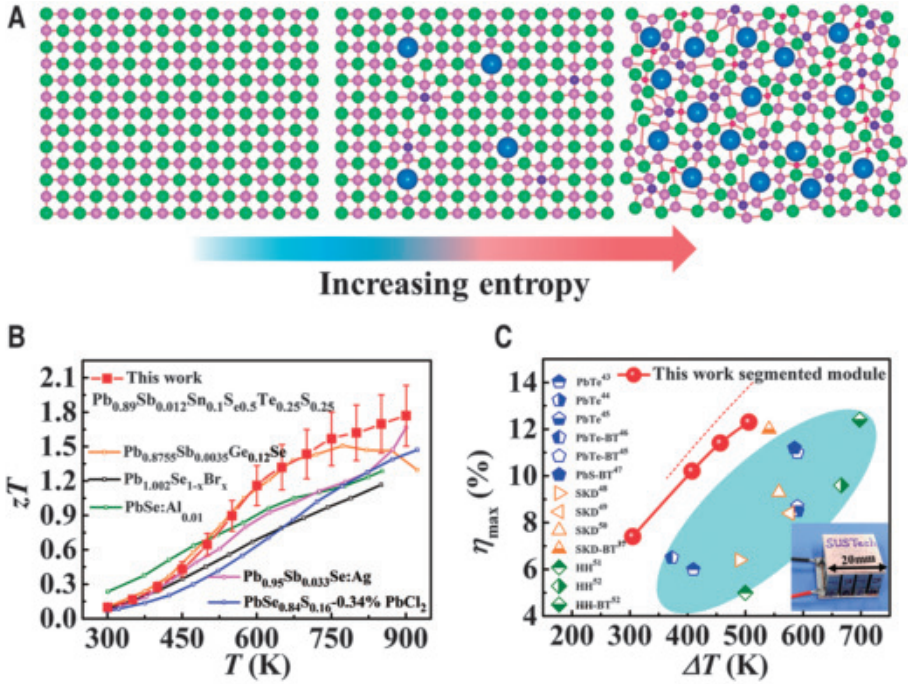

Fig. 1. Improving the performance of thermoelectric materials and modules through entropy engineering. (**A**) Diagram of lattice distortion with increasing entropy. The pink, red, green, blue, and purple spheres represent Pb, Sn, Se, Te, and S atoms, respectively. (**B**) *zT* values as a function of temperature for the high-entropy n-type PbSe-based materials in this work. Some reported *zT* values for traditional n-type PbSe-based materials are also included for comparison (*38*–*42*). (**C**) Maximum conversion efficiencies (η_{max}) as a function of temperature difference (ΔT) for the high-entropy segmented thermoelectric module in this work and some reported results from the literature, as indicated by the superscript [PbTe, skutterudites (SKD), and half-Heusler (HH)] (*37*, *43*–*52*). The red dashed line denotes the simulated values, the blue-shaded area indicates the previously reported results, and the inset is a photograph of the fabricated thermoelectric module.

[1]Shenzhen Key Laboratory of Thermoelectric Materials, Department of Physics, Southern University of Science and Technology, Shenzhen 518055, China. [2]Department of Materials Science and Engineering, National University of Singapore, Singapore 117575, Singapore. [3]State Key Laboratory of High Performance Ceramics and Superfine Microstructure, Shanghai Institute of Ceramics, Chinese Academy of Sciences, Shanghai 200050, China. [4]Guangdong-Hong Kong-Macao Joint Laboratory for Photonic-Thermal-Electrical Energy Materials and Devices, Southern University of Science and Technology, Shenzhen 518055, China.
*These authors contributed equally to this work.
†Corresponding author. Email: hejq@sustech.edu.cn

the long-range order of atomic arrangement, thereby maintaining the electrical transport framework. Meanwhile, short-range disorder in high-entropy materials exists because of the severe lattice distortion from the mismatch of ionic mass, size, and bond state (*15*). The distorted lattice strongly scatters heat-carrying phonons and largely lowers the lattice thermal conductivity of high-entropy materials (*16*, *17*), yielding low thermal transport properties to keep the temperature difference in the thermoelectric module.

Enhanced thermoelectric performance has been reported in $(Cu/Ag)_8Ge(Se/Te)_6$, (Cu/Ag)(In/Ga)Te_2, and (Sn/Ge/Pb/Mn)Te high-entropy materials (*14*, *18*–*20*). Though the thermoelectric performance was enhanced by increasing the configurational entropy in these materials, we have a poor understanding about the relationship between configurational entropy, microstructure, and thermoelectric properties. This is because microstructural investigations are usually focused on dislocations and nanoprecipitates rather than the high-entropy matrix. Additionally, the previous high-entropy thermoelectric materials may actually have been stabilized because of the negative formation enthalpy, with compositions within the solubility limit. We increased the configurational entropy by alloying Sn to form a cubic phase of n-type high-entropy (Pb/Sn)(Se/Te/S) materials over the solubility limit. This may prove to be an effective strategy for developing high-entropy thermoelectric systems using the entropy-driven structural stabilization effect. The manipulated entropy contributed to an ultrahigh zT value of 1.8 at 900 K in an n-type $Pb_{0.89}Sb_{0.012}Sn_{0.1}Se_{0.5}Te_{0.25}S_{0.25}$ high-entropy material (Fig. 1B). The optimized thermoelectric performance translated to an exceptionally high conversion efficiency of 12.3% at ΔT = 507 K in the fabricated segmented thermoelectric module (Fig. 1C), which is notable for the temperature range.

Solubility in alloys is limited by the size and mass differences between solute and solvent atoms, making it challenging to realize high-entropy alloys by increasing alloying content (*10*, *21*). When the contents of S and Te were each less than 0.2, we determined, using x-ray diffraction (XRD) patterns, that the samples had single-phase rock-salt structure (Fig. 2). Increasing S and Te content to 0.25 resulted in the (200) peak splitting into several peaks, which we attributed to multiple phases with different fractions of S, Se, and Te. We used energy dispersive spectroscopy (EDS) mapping (fig. S3) to verify that we formed separate phases rather than a phase transition to lower symmetry. Introducing Sn into the alloy results in the split peaks converging into a single (200) peak, which displayed a typical structural stabilization effect. We calculated the configurational entropy, enthalpy, and Gibbs free energy (Fig. 2B) and found that the structural stabilization effect could be well explained by the competition between entropy and enthalpy. The dependence of the Gibbs free energy (ΔG) on enthalpy (ΔH) and entropy (ΔS) is defined as $\Delta G = \Delta H - T\Delta S$. We calculated ΔH using density functional theory (DFT) and ΔS by the following equation (*22*):

$$\Delta S = -R\left[\left(\sum_{i=1}^{N} x_i \ln x_i\right)_{\text{cation}} + \left(\sum_{j=1}^{M} x_j \ln x_j\right)_{\text{anion}}\right] + \Delta S_{\text{vib}}$$

where R, N, M, x_i, and x_j are the gas constant, atomic species at the cation and anion sites, and the alloyed contents, respectively. We calculated the vibrational entropy (ΔS_{vib}) using DFT (fig. S2). Our calculated curves of the entropy, enthalpy, and Gibbs free energy clearly showed that the Pb(Se/Te/S) system should separate into the multiphase mixture with high S and Te content because of enthalpy-driven phase separation. With the introduction of another element Sn, the increase in entropy is faster than that of enthalpy, resulting in entropy-driven structural stabilization and the high-entropy range with a negative Gibbs free energy. The translation from the multiphase mixture to single phase through increasing configurational entropy in the (Pb/Sn)(Se/S/Te) system clearly shows that the entropy-driven structural stabilization effect can be an effective strategy for forming different high-entropy materials whose composition is over the solubility limit. The benefit of seeking out materials with compositions over the solubility limit is that it provides a more varied range that may be helpful for optimizing performance.

To further verify our single-phase identification in $Pb_{0.89}Sb_{0.012}Sn_{0.1}Se_{0.5}Te_{0.25}S_{0.25}$ (Fig. 2A and fig. S1), we also conducted high-angle annular dark field (HAADF) and atomic x-ray EDS analysis using scanning transmission electron microscopy (STEM) at different scales and in different areas (Fig. 2, C to H, and figs. S4 and S5) to investigate the homogeneity of this material. We found that the distribution of all elements was homogeneous from the micrometer to nanometer scales. Moreover, in

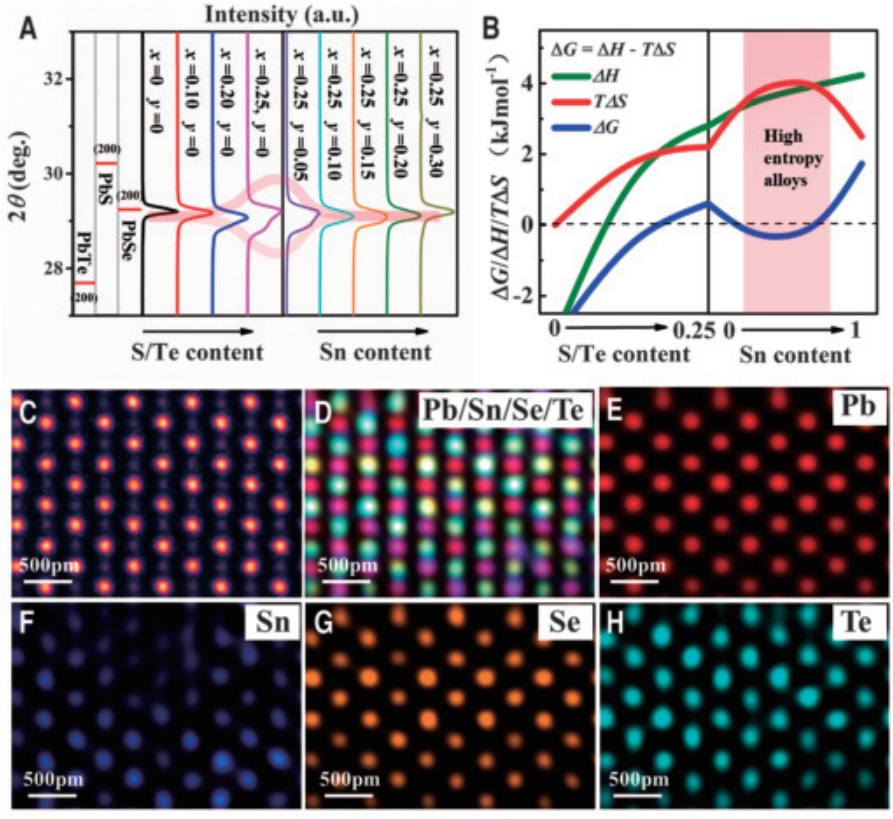

Fig. 2. Stabilizing single-phase structure by increasing the entropy. (**A**) XRD patterns of PbSe-based materials with increasing S/Te and Sn content ($Pb_{0.99-y}Sb_{0.012}Sn_ySe_{1-2x}Te_xS_x$, where x changes from 0 to 0.25 and y changes from 0 to 0.3). The red-shaded area indicates entropy-stabilized high-entropy composition. a.u., arbitrary units. (**B**) Entropy, enthalpy, and Gibbs free energy as a function of S/Te and Sn content. (**C** to **H**) Shown are a (C) HAADF image along the [110] zone axis; (D) Pb, Sn, Se, and Te total EDS mapping; and (E) Pb, (F) Sn, (G) Se, and (H) Te partial EDS mapping of a high-entropy $Pb_{0.89}Sb_{0.012}Sn_{0.1}Se_{0.5}Te_{0.25}S_{0.25}$ sample. S element mapping is not shown because of the weak signal and the overlapped peak with Pb, as shown in fig. S6.

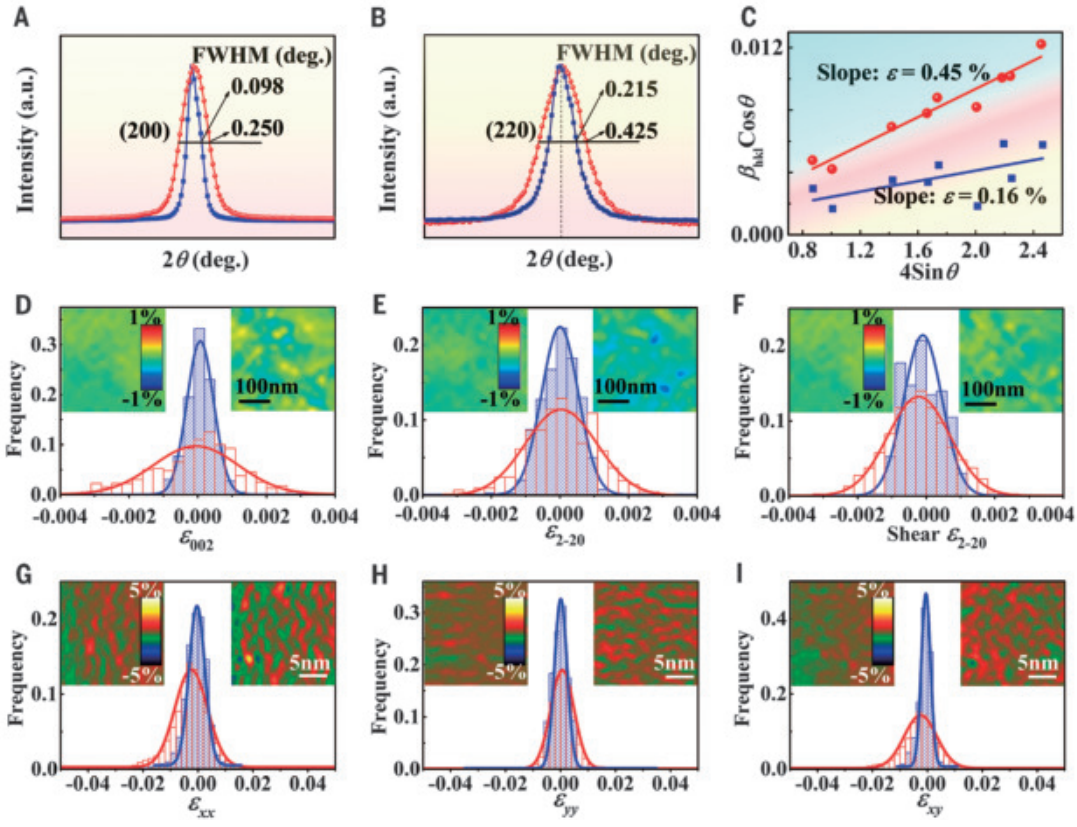

Fig. 3. Strain analysis at different scales. (**A** and **B**) Enlarged (A) (200) and (B) (220) peaks of powder XRD results for a high-entropy $Pb_{0.89}Sb_{0.012}Sn_{0.1}Se_{0.5}Te_{0.25}S_{0.25}$ sample (red). A traditional low-entropy $Pb_{0.99}Sb_{0.012}Se$ sample (blue) is also included for comparison. (**C**) Calculated lattice strains (ε) based on Williamson-Hall analysis. Statistical and spatial distribution of normal and shear strains measured by NBED and GPA. Red and blue represent the same samples as defined in (A) and (B). β_{hkl}, the FWHM of the (hkl) peak. (**D** to **I**) Normal strains along the (D) (002) and (E) (2-20) directions and shear strains along the (F) (2-20) direction based on NBED results are shown. Normal strains along the (G) *xx* and (H) *yy* directions and shear strains along the (I) *xy* direction based on GPA results are shown. The blue lines and left insets are from a low-entropy $Pb_{0.99}Sb_{0.012}Se$ sample. The red lines and right insets are from a high-entropy $Pb_{0.89}Sb_{0.012}Sn_{0.1}Se_{0.5}Te_{0.25}S_{0.25}$ sample.

the ultrahigh-resolution EDS mappings (Fig. 2, D to H), the atomic lattices and positions of every element were very clear, demonstrating that the atomic arrangement order stabilized by increasing entropy even though many atom species were introduced into one structure. The homogeneous distribution of the five elements across all scales distinguishes a high-entropy material from low-entropy and multiphase materials. The well-defined atomic arrangement is distinct from amorphous materials.

The entropy-driven stabilization allowed for a well-maintained atomic arrangement, but the strong mismatch of atomic size severely distorted the lattice and should strongly affect the thermal transport process (*13*, *16*, *17*). To visualize the distorted lattice, we measured the strains of low-entropy ($Pb_{0.99}Sb_{0.012}Se$) and high-entropy ($Pb_{0.89}Sb_{0.012}Sn_{0.1}Se_{0.5}Te_{0.25}S_{0.25}$) samples at different scales (Fig. 3). The broadened peaks [the (200) peak in Fig. 3A and the (220) peak in Fig. 3B] in our XRD data clearly demonstrate the increased strains from these distorted lattices. Based on a typical Williamson-Hall analysis (*23*), we calculated the strain using the full width at half maximum (FWHM) of all the peaks (Fig. 3C and fig. S7). The change from low to high entropy tripled the lattice strains from 0.16 to 0.45%.

Although our XRD analysis showed the macroscopic existence of lattice strains, their type and statistical and spatial distributions were unclear. We used nanobeam electron diffraction (NBED) to detect the lattice strains in a 350-nm–by–350-nm area (*24*) (Fig. 3, D to F, and fig. S8). In these measurements, we used a transmission electron beam with a diameter of 4 nm to measure the lattice parameters and orientations in the beam area. We plotted the normal strain by mapping in two perpendicular directions, [002] and [2-20], which revealed the spatial distribution of the normal strains at the nanoscale (insets of Fig. 3, D and E). We saw that the high-entropy sample had higher strain intensity and stronger strain fluctuation at a scale of around 10 nm, whereas those in the low-entropy sample were much lower and weaker. By counting hundreds of diffraction spots, we plotted frequency histograms (Fig. 3, D and E). The results illustrated the broader strain distribution in the high-entropy sample relative to the low-entropy sample. We conducted similar operations for shear strains along the [2-20] orientation (Fig. 3F) and showed similar large strain fluctuations in the high-entropy sample.

In addition, we further investigated the strain at the atomic scale through STEM-HAADF imaging. We chose a 20-nm–by–20-nm area randomly in both low- and high-entropy samples (fig. S8) and performed geometric phase analysis (GPA) based on STEM-HAADF images to calculate the atomic strains (*25*) (Fig. 3, H and I). We observed that the strain had a short-range strain fluctuation (below 1 nm) because impurity atoms usually affect the nearest and the second nearest atoms (*26*). Similar to the NBED results, the strain distribution fluctuations by GPA in the high-entropy sample were also much larger than those in the low-entropy sample because of the large mass and size differences. The differences in normal strains between low- and high-entropy samples are notably smaller than that of shear strains. This is because normal strains in GPA are calculated from the change of unit cell volume, whereas the shear strains reflect the deformation of the unit cell (*27*). The mismatch of atomic sizes can be easily released by a change of cell volume in low-entropy materials, whereas the atomic off-centering from potential and distribution asymmetry in high-entropy materials were responsible for the deformed unit cell and the large shear strains, which is the key difference between low- and high-entropy materials (*28*). Owing to the asymmetric potential difference and probability distribution functions, the equilibrium positions of atoms in high-entropy material

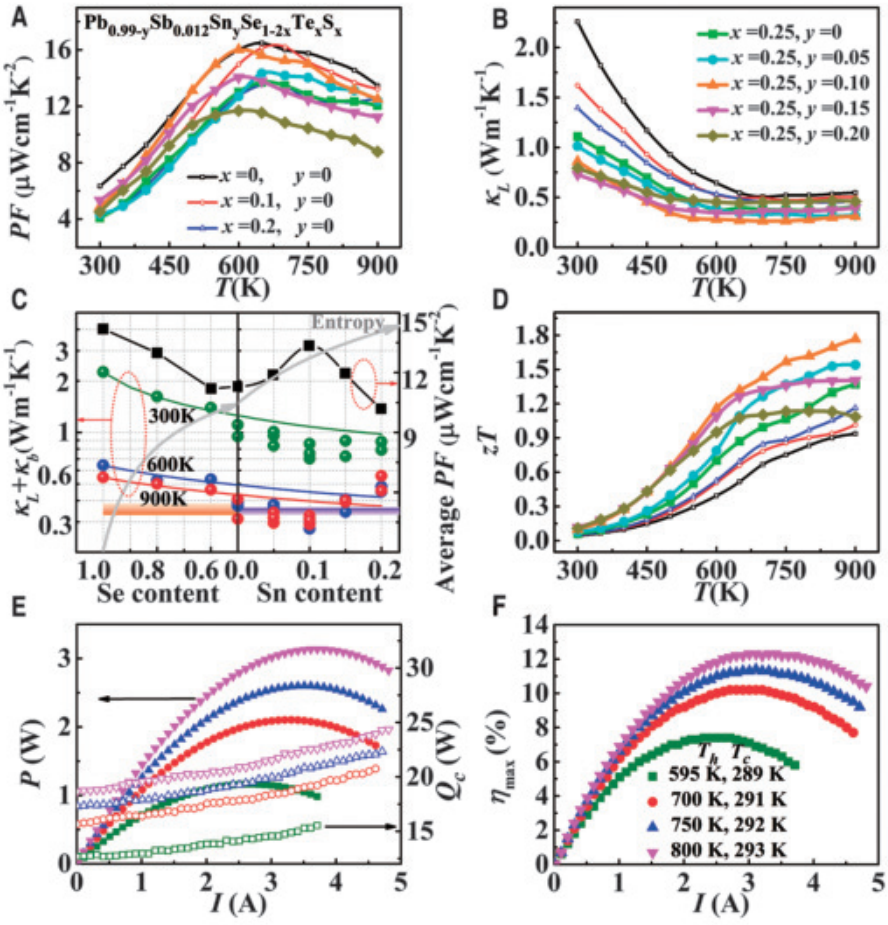

Fig. 4. Thermoelectric properties of $Pb_{0.99-y}Sb_{0.012}Sn_ySe_{1-2x}Te_xS_x$. *x* was changed from 0 to 0.25 and *y* from 0 to 0.2 for the samples. (**A**, **B**, and **D**) Temperature dependences of (A) power factor (*PF*), (B) lattice thermal conductivity ($\kappa_L + \kappa_b$), and (D) *zT* values. κ_b, bipolar thermal conductivity. (**C**) Composition dependence of $\kappa_L + \kappa_b$ and average *PF*. The solid lines are predictions based on the alloy model. The black line represents the experimental average *PF* (right red arrow). The green, blue, and red circles represent experimental lattice thermal conductivity (left red arrow). The orange-purple line represents theoretical minimum lattice thermal conductivity. (**E** and **F**) Shown are (E) output power (*P*, left black arrow) and heat flow at the cold side (Q_c, right black arrow) and (F) maximum conversion efficiency (η_{max}) as a function of the current (*I*) under different operating temperatures for the fabricated segmented thermoelectric module. T_h, temperature at the hot side; T_c, temperature at the cold side.

should deviate from the uniform distribution (figs. S9 to S11). The theoretical lattice strains of high-entropy material (fig. S11) that we calculated showed large shear strains and were consistent with the measured result (Fig. 3).

The entropy-driven structural stabilization and the severely distorted lattice should work together to effect the electrical and thermal transport properties. We measured the thermoelectric properties of n-type Sb-doped (Pb/Sn)(Se/Te/S) materials to evaluate the effect of this high-entropy concept (Fig. 4 and figs. S12 to S14). The electron mobility was well maintained after introducing Sn (fig. S18 and table S3), illustrating that the atomic lattice was well defined even when the system disorder (entropy) was increased. As a result, the power factors of high-entropy samples were well retained owing to the maintained electron mobility. To evaluate the effect of entropy-driven structural stabilization on power factors, we plotted the composition dependence of average power factors for all the samples (Fig. 4C and fig. S15A). The average power factor initially decreased with increasing entropy owing to electron scattering, but the power factor increased when further increasing the entropy because this eliminated phase-boundary electron scattering in the entropy-stabilized structure. The average power factor of 13.4 μW cm^{-1} K^{-2} in the single-phase $Pb_{0.89}Sb_{0.012}Sn_{0.1}Se_{0.5}Te_{0.25}S_{0.25}$ sample is larger than that of 11.2 μW cm^{-1} K^{-2} in the multiphase $Pb_{0.99}Sb_{0.012}Se_{0.5}Te_{0.25}S_{0.25}$ sample, which clearly demonstrates the positive effect of entropy-driven structural stabilization on electrical transport properties. The decreased power factor in the sample with the high Sn content was due to the decreased bandgap rather than high entropy, which resulted in the intrinsic excitation at high temperature (figs. S17 and S18A).The more exciting effect of high entropy was the largely depressed lattice thermal conductivity (κ_L) (Fig. 4B). To make clear the effect of composition and entropy on κ_L, we calculated the composition dependence of κ_L (Fig. 4C). The solid lines were predicted based on a widely accepted alloy model in which the differences in atomic mass and radius were included (table S4) (*29*, *30*). The experimental data for low-entropy samples were consistent with the predicted lines, indicating the suitability of the model. However, the experimental data for the high-entropy samples were lower than the predicted values. The κ_L for the high-entropy sample was largely depressed to an ultralow value of ~0.3 W m^{-1} K^{-1} over a large temperature range (550 to 900 K), which was close to the amorphous limit (*30*, *31*). We confirmed these results by reproducing the observation on three high-entropy samples (Fig. 4C).

Considering the absence of second phases and nanostructures in high-entropy samples, the similar Grüneisen parameters (table S1), and the high relative densities of all the samples (table S2), the reason for the ultralow κ_L in high-entropy samples should be the large lattice strains distributed at all the scales. The phonon dispersion for a one-dimensional single-atom harmonic chain can be written as (*32*)

$$\omega = 2\sqrt{\frac{F}{M}}\sin\left(\frac{\pi}{2}\frac{k}{k_c}\right)$$

where k, k_c, F, and M are the Boltzmann constant, cut-off wave vector, force constant, and atomic mass, respectively. F and M can be tuned by changing a materials' components, which should result in a fluctuation in phonon dispersion ($\Delta\omega$). Because the lifetime (τ_p) of phonons is proportional to $(\Delta\omega)^{-1}$, the large fluctuation of the force constant (ΔF) and atomic mass (ΔM) should shorten τ_p and depress κ_L, which is written as $\kappa_L \propto \tau_p \propto \frac{1}{\Delta\omega}$ (*33*). In the traditional alloy model, ΔF and ΔM are included to calculate the effect of constituent fluctuations on κ_L (*29*). However, the ΔF from $\Delta r/r_{avg}$, where r is atomic radius, in the model only includes the contribution from the volume variation of the unit cell, called the normal strain (*29*). Therefore, the large fluctuation in the force constant ($\Delta F \propto \varepsilon_{normal} + \varepsilon_{shear}$) from normal and shear strains should result in an ultralow κ_L in high-entropy materials, which is lower than the predicated value that only includes normal strains and is close to the theoretical minimum value (*30*). In addition, a nanoscale strain wave will induce the localization-like behavior of low-frequency phonons, contributing to an ultralow κ_L, as the results show in the superlattice structure and distorted graphene (*34*, *35*).

Owing to the well-maintained high electrical transport properties (*PF*) and the largely depressed κ_L, the zT values can be enhanced from 0.9 to 1.8 at 900 K when the composition changes from n-type low-entropy $Pb_{0.99}Sb_{0.012}Se$ to high-entropy $Pb_{0.89}Sb_{0.012}Sn_{0.1}Se_{0.5}Te_{0.25}S_{0.25}$. Not only was the peak value largely enhanced, but the zT values across the whole temperature range were also tremendously improved, making the average zT increase from 0.45 to 1.02 when the composition changed from low entropy to high entropy (fig. S15B). As of now, because the energy conversion efficiency of lead chalcogenide thermoelectric modules is limited by the low zT value of n-type material (*36*), our enhanced average zT value in n-type PbSe-based material should certainly push forward the applications of thermoelectric modules. Therefore, we used typical p-type Sb-doped Bi_2Te_3, p-type Na-doped PbTe, n-type Se-doped Bi_2Te_3, and our n-type high-entropy PbSe to fabricate a segmented thermoelectric module (fig. S19A). Based on a finite element analysis (*37*), the simulated highest conversion efficiency of our segmented module reached 13.9% at a temperature difference ΔT = 513 K when the ratio of $PbTe/Bi_2Te_3$ and $PbSe/Bi_2Te_3$ was optimized (Fig. 1C). The simulation results and the temperature fields that result from changing the ratio of $PbTe/Bi_2Te_3$ and $PbSe/Bi_2Te_3$ are shown in fig. S19, B to D. We fabricated an eight-couple segmented module (20 mm by 20 mm by 12.5 mm) with a ratio of 2.6 (inset of Fig. 1C) and measured its output properties (Fig. 4, E and F, and fig. S20). At ΔT = 507 K and current I = 3.7 A, we measured the internal resistance as 230 milliohms and the power output (P) reached a maximum value of 3.1 W. By measuring the heat flow on the cold side (Fig. 4E) (*37*), the maximum conversion efficiency (η_{max}) reached 12.3%. The deviation of experimental data from simulated data was from the contact resistance of interfaces and the heat emissivity of radiative heat flow. Thus, further improvements could be achieved by optimizing the contact interface and geometrical configuration.

We demonstrate that different high-entropy thermoelectric materials can be formed by entropy-driven structural stabilization, with electrical transport properties that are well maintained by the stabilized structure. Meanwhile, the large strains from the severely distorted lattice in this high-entropy material provide strong scattering for heat-carrying phonons, contributing to an ultralow κ_L. As a consequence, a high zT value (1.8 at 900 K, n-type) and conversion efficiency (12.3% at ΔT = 507 K) in the high-entropy material and module were realized in the experiments. Our demonstration provides insight into entropy engineering for high-performance thermoelectric materials and modules, which we expect to be an attractive pathway for developing high-performance functional materials.

REFERENCES AND NOTES

1. J. Mao *et al.*, *Science* **365**, 495–498 (2019).
2. G. Tan, L. D. Zhao, M. G. Kanatzidis, *Chem. Rev.* **116**, 12123–12149 (2016).
3. J. He, T. M. Tritt, *Science* **357**, eaak9997 (2017).
4. G. J. Snyder, E. S. Toberer, *Nat. Mater.* **7**, 105–114 (2008).
5. C. Chang *et al.*, *Science* **360**, 778–783 (2018).
6. Y. Pei *et al.*, *Nature* **473**, 66–69 (2011).
7. J. P. Heremans, B. Wiendlocha, A. M. Chamoire, *Energy Environ. Sci.* **5**, 5510–5530 (2012).
8. B. Poudel *et al.*, *Science* **320**, 634–638 (2008).
9. H. Liu *et al.*, *Nat. Mater.* **11**, 422–425 (2012).
10. N. Dragoe, D. Bérardan, *Science* **366**, 573–574 (2019).
11. J. W. Yeh *et al.*, *Adv. Eng. Mater.* **6**, 299–303 (2004).
12. C. M. Rost *et al.*, *Nat. Commun.* **6**, 8485 (2015).
13. A. Sarkar *et al.*, *Adv. Mater.* **31**, e1806236 (2019).
14. L. Hu *et al.*, *Adv. Energy Mater.* **8**, 1802116 (2018).
15. J. L. Braun *et al.*, *Adv. Mater.* **30**, e1805004 (2018).
16. C. M. Rost *et al.*, *Acta Mater.* **196**, 231–239 (2020).
17. D. Bérardan, A. K. Meena, S. Franger, C. Herrero, N. Dragoe, *J. Alloys Compd.* **704**, 693–700 (2017).
18. R. Liu *et al.*, *Adv. Mater.* **29**, 1702712 (2017).
19. B. Jiang *et al.*, *J. Mater. Chem. C* **5**, 943–952 (2017).
20. B. Jiang *et al.*, *Mater. Today Phys.* **5**, 20–28 (2018).
21. R. J. Korkosz *et al.*, *J. Am. Chem. Soc.* **136**, 3225–3237 (2014).
22. D. B. Miracle, O. N. Senkov, *Acta Mater.* **122**, 448–511 (2017).
23. G. K. Williamson, W. H. Hall, *Acta Metall.* **1**, 22–31 (1953).
24. A. Béché, J. L. Rouvière, J. P. Barnes, D. Cooper, *Ultramicroscopy* **131**, 10–23 (2013).
25. F. Hüe, M. Hÿtch, H. Bender, F. Houdellier, A. Claverie, *Phys. Rev. Lett.* **100**, 156602 (2008).
26. P. M. Fahey, P. B. Griffin, J. D. Plummer, *Rev. Mod. Phys.* **61**, 289–384 (1989).
27. A. L. Greer, Y. Q. Cheng, E. Ma, *Mater. Sci. Eng. Rep.* **74**, 71–132 (2013).
28. H. Song *et al.*, *Phys. Rev. Mater.* **1**, 023404 (2017).
29. J. Yang, G. P. Meisner, L. Chen, *Appl. Phys. Lett.* **85**, 1140–1142 (2004).
30. D. G. Cahill, S. K. Watson, R. O. Pohl, *Phys. Rev. B* **46**, 6131–6140 (1992).
31. L. D. Zhao *et al.*, *Appl. Phys. Lett.* **97**, 092118 (2010).
32. Y. Wu *et al.*, *Joule* **3**, 1276–1288 (2019).
33. E. Bouchbinder, E. Lerner, *New J. Phys.* **20**, 073022 (2018).
34. R. Venkatasubramanian, *Phys. Rev. B* **61**, 3091–3097 (2000).
35. L. Cui, X. Du, G. Wei, Y. Feng, *J. Phys. Chem. C* **120**, 23807–23812 (2016).
36. Y. Xiao *et al.*, *J. Am. Chem. Soc.* **139**, 18732–18738 (2017).
37. Q. Zhang *et al.*, *Energy Environ. Sci.* **10**, 956–963 (2017).
38. H. Wang, Y. Pei, A. D. LaLonde, G. J. Snyder, *Proc. Natl. Acad. Sci. U.S.A.* **109**, 9705–9709 (2012).
39. Q. Zhang *et al.*, *Energy Environ. Sci.* **5**, 5246–5251 (2012).
40. Z. Luo *et al.*, *Energy Environ. Sci.* **11**, 3220–3230 (2018).
41. Z. Chen *et al.*, *Nat. Commun.* **8**, 13828 (2017).
42. J. Androulakis *et al.*, *J. Am. Chem. Soc.* **133**, 10920–10927 (2011).
43. A. Singh *et al.*, *J. Phys. D Appl. Phys.* **42**, 015502 (2009).
44. P. Jood, M. Ohta, A. Yamamoto, M. G. Kanatzidis, *Joule* **2**, 1339–1355 (2018).
45. X. Hu *et al.*, *Energy Environ. Sci.* **9**, 517–529 (2016).
46. J. D'Angelo *et al.*, *J. Electron. Mater.* **40**, 2051–2062 (2011).
47. B. Jiang *et al.*, *Energy Environ. Sci.* **13**, 579–591 (2020).
48. D. Zhao *et al.*, *Mater. Sci. Semicond. Process.* **13**, 221–224 (2010).
49. P. Zong *et al.*, *Energy Environ. Sci.* **10**, 183–191 (2017).
50. Q. Zhang *et al.*, *Nano Energy* **41**, 501–510 (2017).
51. C. Fu *et al.*, *Nat. Commun.* **6**, 8144 (2015).
52. Y. Xing *et al.*, *Energy Environ. Sci.* **12**, 3390–3399 (2019).

ACKNOWLEDGMENTS

Funding: We acknowledge support from the leading talents of the Guangdong Province Program (grant no. 00201517), the Guangdong-Hong Kong-Macao Joint Laboratory (grant no. 2019B121205001), the National Natural Science Foundation of China (grant nos. 52002167, 11874194, 11934007, and 51632005), the Science and Technology Innovation Committee Foundation of Shenzhen (grant nos. KQTD2016022619565991 and ZDSYS20141118160434515), and a high level of special funds (G02206302). L.C. is grateful for support from the National Natural Science Foundation of China (grant no. 51632010).
Author contributions: Bi.J. and J.H. designed this work. Bi.J. synthesized the samples and carried out the transport property measurements. Y.Y., L.X., Y.H., and S.N. performed the transmission electron microscopy observations and analysis. J.C. performed the calculations. Bi.J., X.L., J.L., Q.Z., Ba.J., and B.Z. carried out the study on module fabrication and characterization. S.B., L.C., S.J.P., and J.H. analyzed the experimental data. Bi.J., Y.Y., J.C., and J.H. wrote and all authors edited this manuscript. **Competing interests:** None declared.
Data and materials availability: All data are available in the manuscript and supplementary materials.

SUPPLEMENTARY MATERIALS

science.sciencemag.org/content/371/6531/830/suppl/DC1
Materials and Methods
Supplementary Text
Figs. S1 to S20
Tables S1 to S4
References (*53*–*66*)

1 August 2020; accepted 18 January 2021
10.1126/science.abe1292

CONSERVATION

Human impacts on global freshwater fish biodiversity

Guohuan Su[1]*, Maxime Logez[2,3], Jun Xu[4,5], Shengli Tao[1], Sébastien Villéger[6]†, Sébastien Brosse[1]†

Freshwater fish represent one-fourth of the world's vertebrates and provide irreplaceable goods and services but are increasingly affected by human activities. A new index, Cumulative Change in Biodiversity Facets, revealed marked changes in biodiversity in >50% of the world's rivers covering >40% of the world's continental surface and >37% of the world's river length, whereas <14% of the world's surface and river length remain least impacted. Present-day rivers are more similar to each other and have more fish species with more diverse morphologies and longer evolutionary legacies. In temperate rivers, where the impact has been greatest, biodiversity changes were primarily due to river fragmentation and introduction of non-native species.

Rivers and lakes cover less than 1% of Earth's surface but represent substantial biodiversity, including nearly 18,000 fish species that constitute one-fourth of global vertebrates (*1*–*3*). These freshwater fishes support the functioning and stability of ecosystems through their contribution to biomass production and regulation of trophic networks and nutrient cycles (*4*). Freshwater fishes also contribute to human welfare as key food resources (*5*) and for recreative and cultural activities (*2*, *6*).

For centuries, human populations have directly affected fish biodiversity (*7*) through extraction and introduction of non-native species (*8*, *9*). Human activities have also modified the natural environment by changing land uses, altering flow regimes, fragmenting rivers by dams, polluting soil and waters, and altering climate; such actions indirectly favor extinction of native species and/or establishment of non-native species (*10*–*13*). Consequently, these direct and indirect anthropogenic impacts have led to modification of local species compositions (*8*, *9*). However, biodiversity is not restricted to purely taxonomic components but also includes functional and phylogenetic diversities. These two latter facets determine how organisms affect ecosystem functioning and stability (*14*–*18*) and are thus essential for conservation.

Here, we assess the extent to which six key facets of freshwater fish biodiversity—taxonomic, functional, and phylogenetic richness, plus the dissimilarity among river basins in each of these categories—have changed over the past two centuries in 2456 river basins, covering almost the entire continental surface of Earth (excluding deserts and poles) and hosting

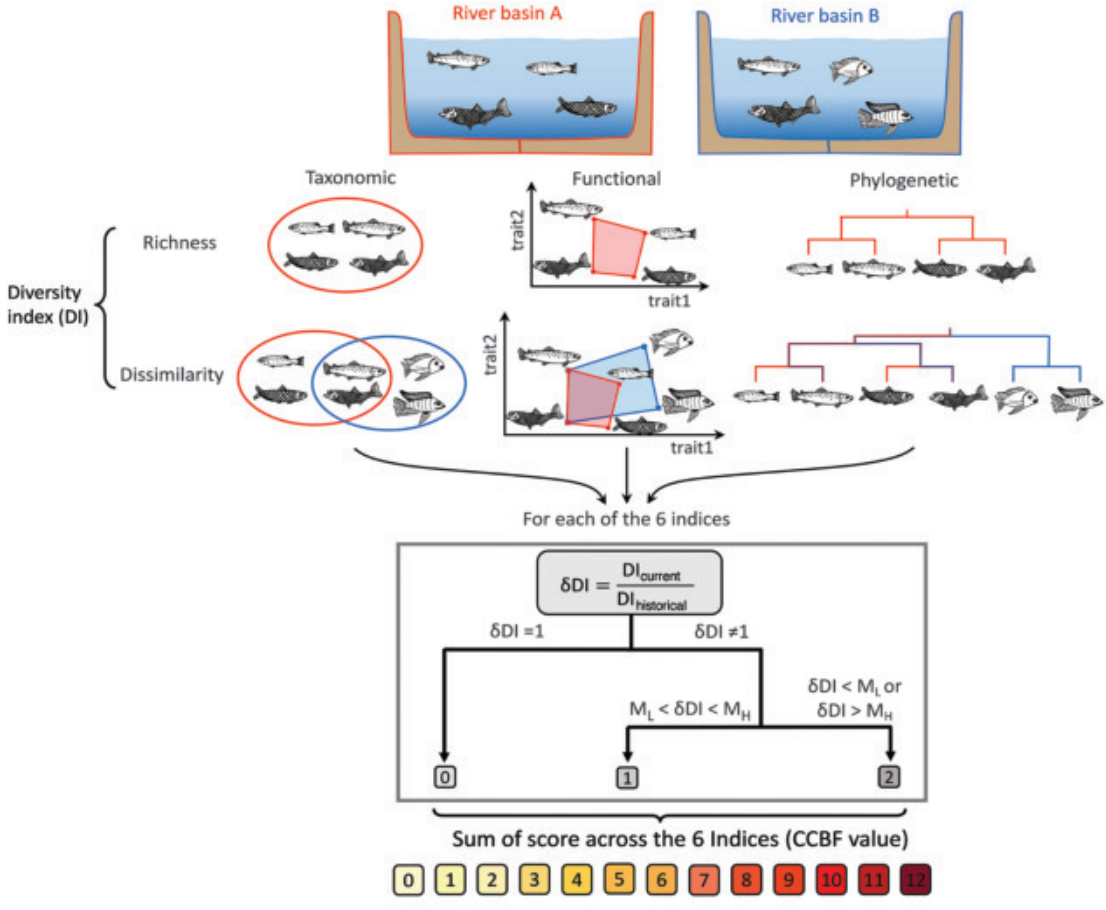

Fig. 1. Framework to measure the cumulative change in biodiversity facets (CCBF). δDI represents the change of a single diversity index among the six considered (taxonomic richness, functional richness, and phylogenetic richness within each river basin; taxonomic dissimilarity, functional dissimilarity, and phylogenetic dissimilarity between pairs of basins). M_L is the median of all the values lower than 1; M_H is the median of all the values higher than 1. The score is used to compute the CCBF index.

[1]Laboratoire Evolution et Diversité Biologique (EDB), UMR5174, Université Toulouse 3 Paul Sabatier, CNRS, IRD, Toulouse, France. [2]INRAE, Aix Marseille Univ, RECOVER, Aix-en-Provence, France. [3]Pôle R&D "ECLA," Aix-en-Provence, France. [4]Donghu Experimental Station of Lake Ecosystems, State Key Laboratory of Freshwater Ecology and Biotechnology of China, Institute of Hydrobiology, Chinese Academy of Sciences, Wuhan, P.R. China. [5]Laboratory for Marine Fisheries Science and Food Production Processes, Qingdao National Laboratory for Marine Science and Technology, Qingdao, P.R. China. [6]MARBEC, Univ Montpellier, CNRS, Ifremer, IRD, Montpellier, France.
*Corresponding author. Email: guohuan.su@gmail.com
†These authors contributed equally to this work.

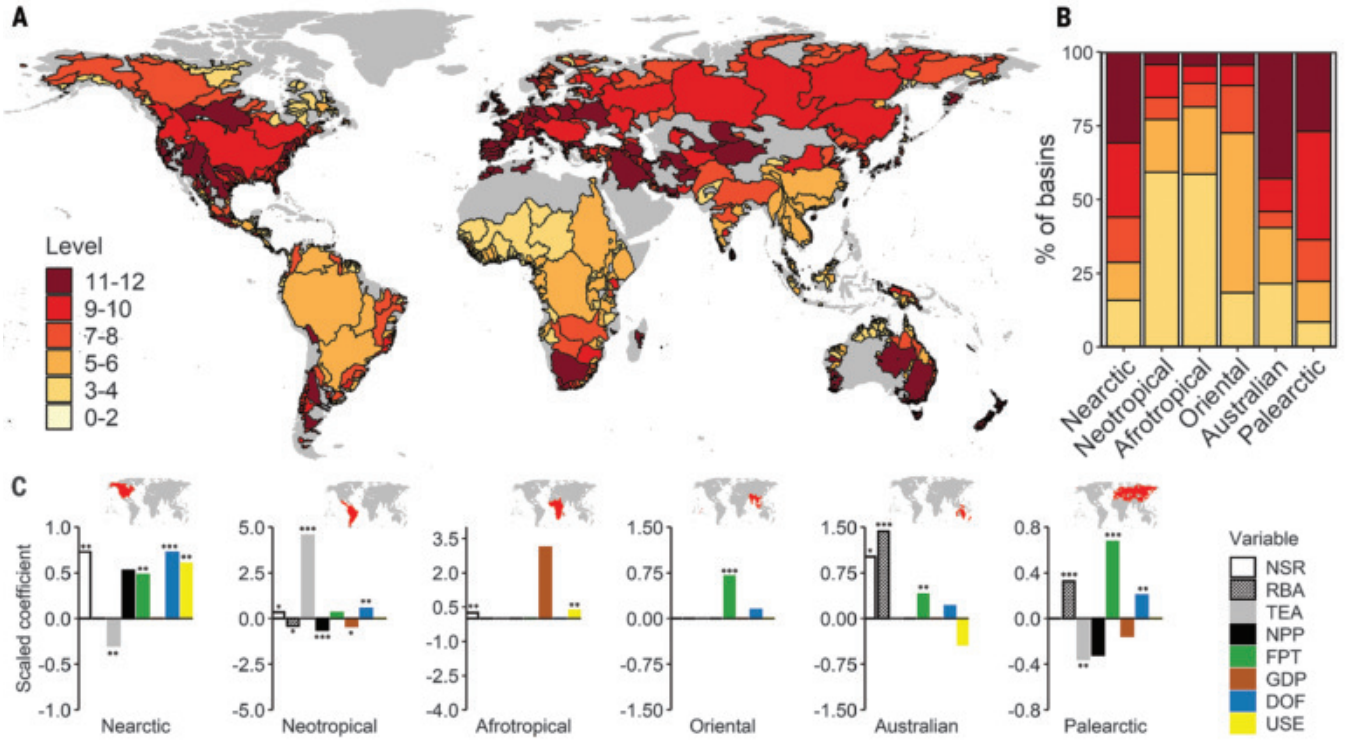

Fig. 2. Cumulative change in biodiversity of freshwater fish faunas. A cumulative index accounts for the sum of the changes in the six diversity indices: three facets (taxonomic, functional, and phylogenetic) measured at two scales (local and regional). (**A**) Map of the changes in 2456 river basins. (**B**) Percentage of river basins for six intensities of change in each biogeographic realm. (**C**) Scaled coefficient of the eight drivers of biodiversity change in an autoregressive error model in each realm (NSR, native species richness; RBA, river basin area; TEA, temperature anomaly since the last glacial maximum; NPP, net primary productivity; FPT, human footprint; GDP, gross domestic product; DOF, degree of fragmentation; USE, consumptive water use). Number of river basins used in the models: Afrotropical, n = 198; Australian, n = 525; Nearctic, n = 241; Neotropical, n = 350; Oriental, n = 292; Palearctic, n = 729. ***P < 0.001, **P < 0.01, *P < 0.05.

>14,000 species (>80% of the global freshwater fish pool) (*19*). We computed an index of Cumulative Change in Biodiversity Facets (CCBF), which ranges from 0 to 12, with higher scores depicting stronger changes across more facets. A score higher than 6 indicates either changes in all six biodiversity facets or changes higher than the median in more than three facets (Fig. 1) (*20*).

More than half of the river basins (52.8%; 1297 basins representing 40.2% of the world continental surface and 37.3% of the world river length) had CCBF scores higher than 6 (Fig. 2), revealing deep and spatially distributed anthropogenic impacts on fish biodiversity. In contrast, one-third of the river basins (35.7%; 878 rivers) did not experience changes in local richness but only changes in dissimilarity relative to assemblages from the same realm (fig. S1). Those least-impacted river basins were mostly small-sized, occupying only 13.4% of the world river basin surface, and supported 3876 species, or only 21.7% of the world fish fauna. Moreover, the least-impacted rivers were overrepresented in Afrotropical and Australian regions, whereas the Neotropics, although being the richest in species, functional, and phylogenetic diversity (*21*, *22*), accounted for less than 6% of the "least impacted" category (fig. S1).

Fish assemblages from the temperate regions of Nearctic, Palearctic, and Australian realms experienced the largest biodiversity changes, with more than 60% of the rivers reaching a CCBF score higher than 6 (Fig. 2, A and B). Overall biodiversity changes in temperate regions (CCBF = 8.6 ± 0.1, mean ± SE) were higher than in tropical rivers (CCBF = 5.1 ± 0.1). For instance, large temperate rivers such as the Mississippi, Danube, or Murray-Darling had CCBF scores higher than 8, whereas large tropical rivers, such as the Amazon, Congo, or Mekong, were less impacted (CCBF = 6, fig. S2). Such a spatial pattern is consistent with previous studies on changes in taxonomic richness and dissimilarity of freshwater fishes (*8*, *9*) and with historical reports on anthropogenic degradation of ecosystems (*23*) but is not consistent with changes observed in other taxa, for which changes in biodiversity were the highest in tropical regions [e.g., for marine biome (*24*) and forest (*25*)].

Mapping the patterns of changes across the six diversity components revealed discrepancies between richness facets (Fig. 3). Except for a few rivers in the northern part of the Palearctic and Nearctic realms, fish biodiversity did not decline in most of the rivers (Fig. 3, A to C). This markedly differs from recent results documenting the decline in freshwater living resources at the local scale (i.e., >1 to 10 km of river stretch) within some of these river basins (*12*, *26*). Interestingly, we report an inverse trend in freshwater fish for local taxonomic, functional, and phylogenetic richness in more than half of the world's rivers (Fig. 3, A to C, and Fig. 4). This increase in local diversity is primarily explained by anthropogenic species introductions that compensate for or even exceed extinctions in most rivers (*27*). Among the 10,682 fish species considered, 170 fish species went extinct in a river basin, but this number might be underestimated because of the time lag between effective extinction and published extinction reports (*28*). In addition, 23% of freshwater fish species are currently considered to be threatened (*29*), and some of these might become extinct in the near future (*26*).

In addition to the overall increase in richness of fish assemblages in river basins, biotic

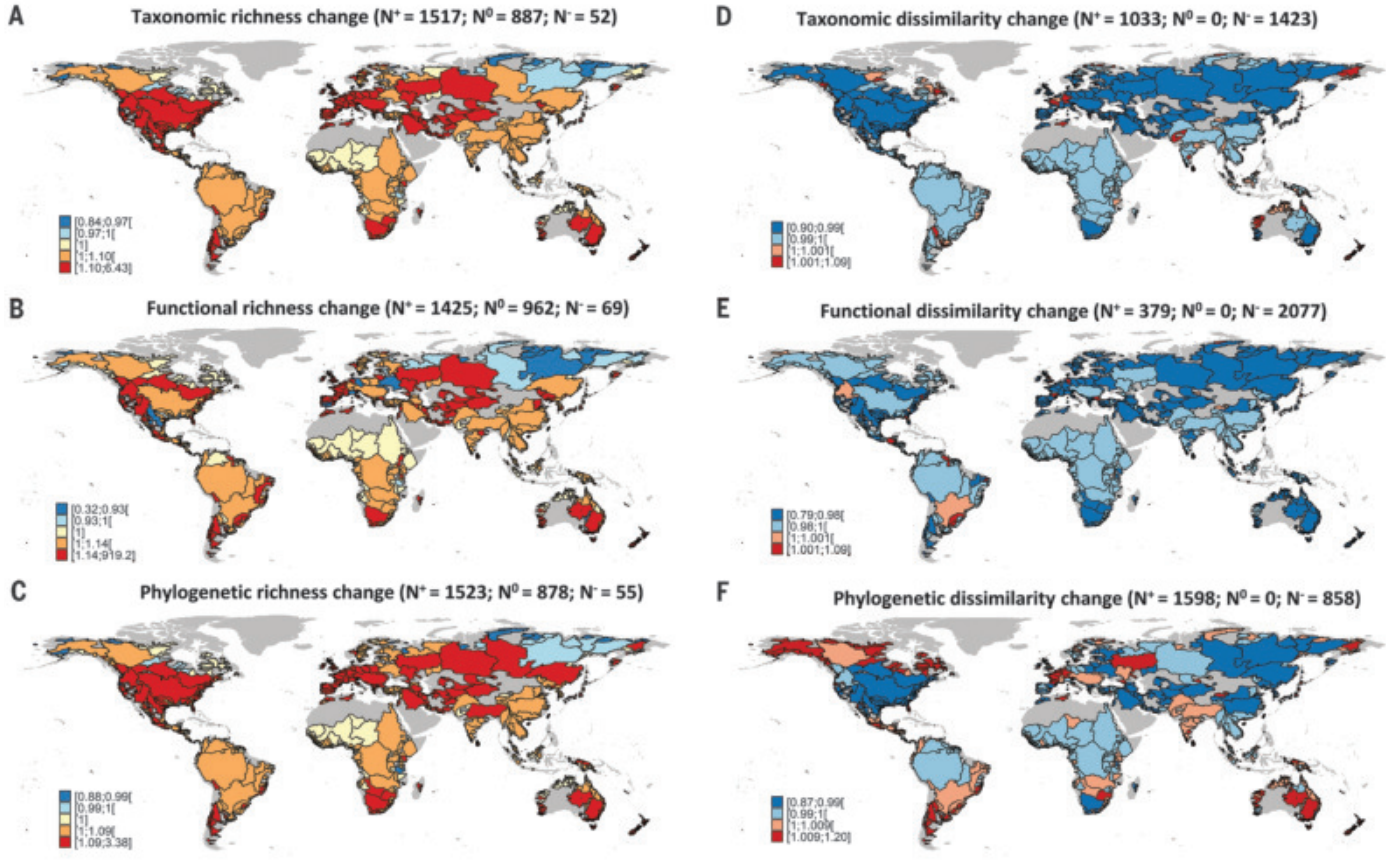

Fig. 3. Changes in each of the six biodiversity indices for the world freshwater fish assemblages (2456 river basins). (**A**) Taxonomic richness change; (**B**) functional richness change; (**C**) phylogenetic richness change; (**D**) taxonomic dissimilarity change; (**E**) functional dissimilarity change; (**F**) phylogenetic dissimilarity change. Legend values are the original ratio $DI_{current}/DI_{historical}$. Numbers of basins where fish diversity increased (N^+), remained unchanged (N^0), or decreased (N^-) are shown at the top of each panel.

homogenization—a general declining trend in biological dissimilarity between river basins—appears pervasive throughout the world's rivers (Fig. 3, D to F). Functional dissimilarity was the most impacted facet, with a decrease in 84.6% of the rivers, whereas taxonomic dissimilarity and phylogenic dissimilarity decreased in only 58% and 35% of the rivers, respectively (Fig. 3, D to F). The discrepancy between change in functional diversity and changes in taxonomic and phylogenetic diversity (Fig. 4) primarily stems from the origin of non-native species introduced into rivers. Species translocated from a river to nearby basins promote losses of dissimilarity because they often already occur as natives in many rivers of the realm and are often functionally and phylogenetically close to other native species (*9*, *30*). In contrast, exotic species (i.e., originating from other realms) are less frequently introduced, and their divergent evolutionary history with native species led to increased phylogenetic dissimilarity of their recipient rivers (*30*). For instance, the exotic species introduced in only a few rivers of Europe (e.g., the mosquitofish, *Gambusia affinis*, established in southwestern Europe, or the brook trout, *Salvelinus fontinalis*, established in cold-water ecosystems) (*30*), markedly enhanced the phylogenetic dissimilarity between those rivers. However, exotic species even from distinct evolutionary lineages could share functional traits with some native species, thereby leading to increased phylogenetic dissimilarity but decreased functional dissimilarity (Fig. 3). For instance, European trout (*Salmo trutta*) and Pacific salmon (*Oncorhynchus mykiss*) belong to an order (Salmoniformes) absent from the Australian realm, but those exotic salmonids are functionally similar to some native Australian fishes such as the spotted mountain trout (*Galaxias truttaceus*; Osmeriformes) (*31*).

The CCBF score was positively linked to human activities related to industrialization and economic development, such as human footprint [FPT (*23*)], with an increase of biodiversity changes with increased FPT in all the industrialized and populated realms. River fragmentation by dams, represented by the degree of fragmentation [DOF (*32*)] index, was also a widespread disturbance in the Nearctic and Palearctic realms (Fig. 2C) that experienced intensive damming for more than a century (*33*). Fragmentation by dams was also a significant driver of biodiversity change in the Neotropics, probably due to the rise of hydropower dam construction in this realm (*34*). Higher DOF values were reached in small- or medium-sized rivers, whereas the largest and most diverse rivers such as the Amazon, Orinoco, or Congo remain mostly free-flowing (*32*), although the current rise of dam construction on those rivers (*35*, *36*) will constitute a major threat to their biodiversity. Apart from river fragmentation, consumptive water use for agriculture and industry [USE (*32*)] was a significant driver of CCBF increase in the Nearctic realm, where water withdrawal for agriculture is intense (*32*, *37*) and acts in synergy with increasing DOF. In the Afrotropics, USE was the only significant human driver of CCBF, due to marked consumptive water use in regions with marked seasonal aridity (*32*, *37*). In addition, the CCBF score was positively correlated to richness in native species in most of the realms, indicating that the most speciose rivers are also the most impacted by biodiversity changes. Moreover, no negative associations

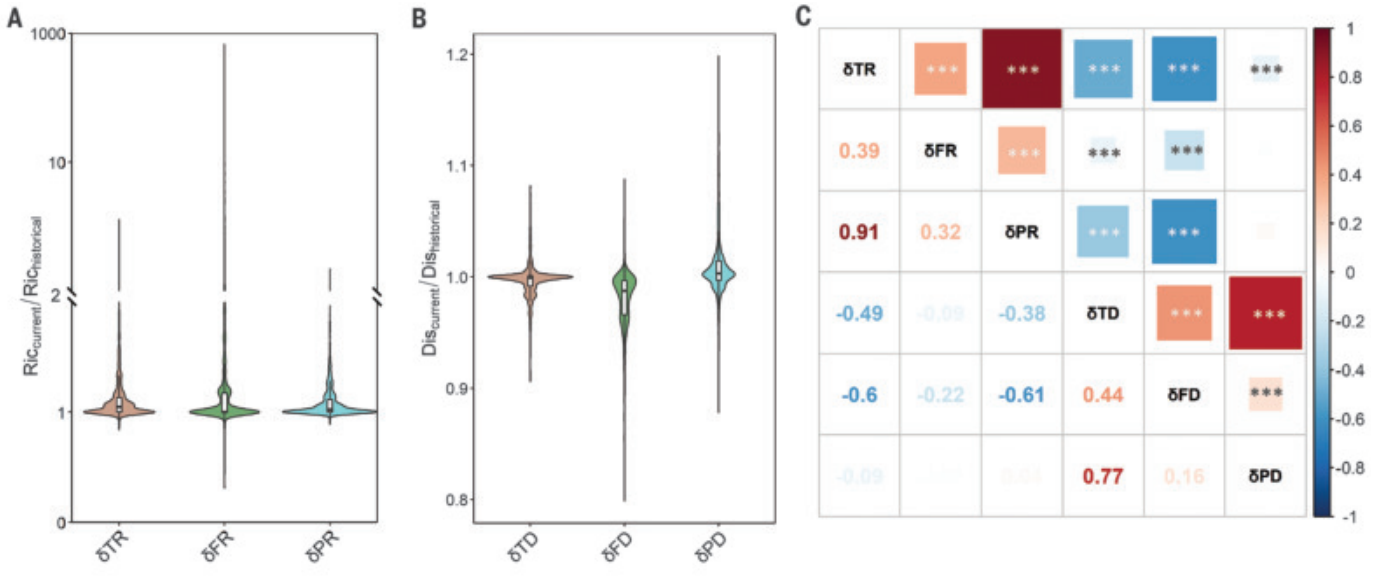

Fig. 4. Changes in biodiversity from historical period to current period. (**A** and **B**) Violin plots show the distribution of values of the three richness change indices (A) and the three dissimilarity change indices (B). (**C**) Pearson correlation between the changes in diversity indices (river basin number = 2456, ***P < 0.001).

between species richness and the CCBF were observed, providing little support for the hypothesis of biotic resistance that assumes a higher resistance of species-rich assemblages against disturbances (*38*–*40*).

Conserving freshwater fish diversity in the least-impacted rivers (accounting for 13.4% of the world basin surface) will remain below the target to protect at least 30% of Earth's surface by 2030, as proposed by a broad coalition of environmental organizations (*41*, *42*). This result suggests that reaching the freshwater fish target must involve consideration of not only the least impacted rivers but also areas where biodiversity has already been eroded by human activity. Moreover, conservation has moved toward systematically identifying regions in need of protection (*43*). The discrepancy in biodiversity erosion we report between freshwater ecosystems and marine and terrestrial ecosystems (*24*, *25*) demonstrates that current measures of biodiversity erosion, derived from marine and terrestrial organisms, do not apply to freshwaters, and thus underscores the need to develop freshwater-focused conservation priorities. In addition, the mismatches between changes in taxonomic, functional, and phylogenetic dissimilarities among the world freshwater fish fauna highlight the risk of evaluation based on change in a single facet as a surrogate of the changes in other facets. More important, our results highlight the need to consider the cumulative and synergistic effects of multiple human activities on the complementary facets of biodiversity. The CCBF index we propose presents a holistic measure of multiple measures of biodiversity change and offers potential for prioritizing and informing adaptive management and global conservation targets. Future studies and planning need to expand the focus from simple loss of species to integrated changes in facets of biodiversity resulting from interactions between synergetic human activities.

REFERENCES AND NOTES

1. G. H. Allen, T. M. Pavelsky, *Science* **361**, 585–588 (2018).
2. D. Dudgeon *et al.*, *Biol. Rev. Camb. Philos. Soc.* **81**, 163–182 (2006).
3. R. van der Laan, *Freshwater Fish List* (Almere, Netherlands, ed. 30, 2020).
4. S. Villéger, S. Brosse, M. Mouchet, D. Mouillot, M. J. Vanni, *Aquat. Sci.* **79**, 783–801 (2017).
5. R. Hassan, R. Scholes, N. Ash, *Ecosystems and Human Well-Being: Current State and Trends* (Island, 2005).
6. R. Arlinghaus *et al.*, *Proc. Natl. Acad. Sci. U.S.A.* **116**, 5209–5213 (2019).
7. R. C. Hoffmann, *Am. Hist. Rev.* **101**, 631–669 (1996).
8. F. Leprieur, O. Beauchard, S. Blanchet, T. Oberdorff, S. Brosse, *PLOS Biol.* **6**, e28 (2008).
9. S. Villéger, S. Blanchet, O. Beauchard, T. Oberdorff, S. Brosse, *Proc. Natl. Acad. Sci. U.S.A.* **108**, 18003–18008 (2011).
10. H. M. Pereira *et al.*, *Science* **330**, 1496–1501 (2010).
11. C. J. Vörösmarty *et al.*, *Nature* **467**, 555–561 (2010).
12. A. J. Reid *et al.*, *Biol. Rev. Camb. Philos. Soc.* **94**, 849–873 (2019).
13. D. Tickner *et al.*, *Bioscience* **70**, 330–342 (2020).
14. D. Mouillot, N. A. Graham, S. Villéger, N. W. Mason, D. R. Bellwood, *Trends Ecol. Evol.* **28**, 167–177 (2013).
15. S. Naeem, J. E. Duffy, E. Zavaleta, *Science* **336**, 1401–1406 (2012).
16. D. Craven *et al.*, *Nat. Ecol. Evol.* **2**, 1579–1587 (2018).
17. P. Brun *et al.*, *Nat. Commun.* **10**, 5691 (2019).
18. C. Pimiento *et al.*, *Sci. Adv.* **6**, eaay7650 (2020).
19. P. A. Tedesco *et al.*, *Sci. Data* **4**, 170141 (2017).
20. See supplementary materials.
21. A. Toussaint, N. Charpin, S. Brosse, S. Villéger, *Sci. Rep.* **6**, 22125 (2016).
22. D. L. Rabosky, *J. Biogeogr.* **47**, 1207–1217 (2020).
23. O. Venter *et al.*, *Sci. Data* **3**, 160067 (2016).
24. S. A. Blowes *et al.*, *Science* **366**, 339–345 (2019).
25. M. C. Hansen *et al.*, *Science* **342**, 850–853 (2013).
26. J. S. Albert *et al.*, *Ambio* **50**, 85–94 (2021).
27. A. Toussaint *et al.*, *Ecol. Lett.* **21**, 1649–1659 (2018).
28. S. T. Jackson, D. F. Sax, *Trends Ecol. Evol.* **25**, 153–160 (2010).
29. IUCN, *The IUCN Red List of Threatened Species* Version 2017-3 (2018); www.iucnredlist.org.
30. S. Villéger, G. Grenouillet, S. Brosse, *Glob. Ecol. Biogeogr.* **23**, 1450–1460 (2014).
31. S. Burgin, *Sustainability* **9**, 280 (2017).
32. G. Grill *et al.*, *Nature* **569**, 215–221 (2019).
33. B. Lehner *et al.*, *Front. Ecol. Environ.* **9**, 494–502 (2011).
34. C. Zarfl, A. E. Lumsdon, J. Berlekamp, L. Tydecks, K. Tockner, *Aquat. Sci.* **77**, 161–170 (2015).
35. E. P. Anderson *et al.*, *Sci. Adv.* **4**, eaao1642 (2018).
36. K. O. Winemiller *et al.*, *Science* **351**, 128–129 (2016).
37. P. Döll, K. Fiedler, J. Zhang, *Hydrol. Earth Syst. Sci.* **13**, 2413–2432 (2009).
38. J. E. Duffy, J. S. Lefcheck, R. D. Stuart-Smith, S. A. Navarrete, G. J. Edgar, *Proc. Natl. Acad. Sci. U.S.A.* **113**, 6230–6235 (2016).
39. M. Loreau *et al.*, *Science* **294**, 804–808 (2001).
40. J. M. Levine, *Science* **288**, 852–854 (2000).
41. E. Dinerstein *et al.*, *Sci. Adv.* **5**, eaaw2869 (2019).
42. S. L. Pimm, C. N. Jenkins, B. V. Li, *Sci. Adv.* **4**, eaat2616 (2018).
43. C. R. Margules, R. L. Pressey, *Nature* **405**, 243–253 (2000).

ACKNOWLEDGMENTS

We thank D. Mouillot and two anonymous reviewers for comments on the manuscript and A. Toussaint and N. Charpin for their help in data acquisition. **Funding:** Supported by CEBA, ANR-10-LABX-0025 and TULIP, ANR-10-LABX-41 projects; the China Scholarship Council (G.S.); a CNES postdoctoral fellowship (S.T.); and National Key R&D Program of China grant 2018YFD0900904 and International Cooperation Project of the Chinese Academy of Sciences grant 152342KYSB20190025 (J.X.). **Author contributions:** G.S., S.V., and S.B. designed the study, analyzed the data, and wrote the manuscript; G.S., J.X., and S.T. collected and compiled the data; G.S. and M.L. collaborated on the core data preparation and coding in R; and all authors contributed to revising the paper and preparing and approving it for publication. **Competing interests:** The authors declare no competing interests. **Data and materials availability:** All data needed to evaluate the conclusions in the paper are present in the paper and/or the supplementary materials. Additional data, scripts, and files related to this paper are available at https://doi.org/10.6084/m9.figshare.13383170.

SUPPLEMENTARY MATERIALS

science.sciencemag.org/content/371/6531/835/suppl/DC1
Materials and Methods
Figs. S1 to S4
Tables S1 to S3
References (*44*–*81*)

18 June 2020; accepted 14 January 2021
10.1126/science.abd3369

TISSUE REPAIR

Cholangiocyte organoids can repair bile ducts after transplantation in the human liver

Fotios Sampaziotis[1,2,3]*, Daniele Muraro[1], Olivia C. Tysoe[1,4], Stephen Sawiak[5], Timothy E. Beach[4], Edmund M. Godfrey[6], Sara S. Upponi[6], Teresa Brevini[1], Brandon T. Wesley[1], Jose Garcia-Bernardo[7], Krishnaa Mahbubani[4], Giovanni Canu[1], Richard Gieseck III[8], Natalie L. Berntsen[9,10,11], Victoria L. Mulcahy[2,12], Keziah Crick[13], Corrina Fear[13], Sharayne Robinson[13], Lisa Swift[13], Laure Gambardella[1,2], Johannes Bargehr[1,2,14], Daniel Ortmann[1], Stephanie E. Brown[1], Anna Osnato[1], Michael P. Murphy[15], Gareth Corbett[16], William T. H. Gelson[2,3], George F. Mells[2,3,12], Peter Humphreys[1], Susan E. Davies[17], Irum Amin[4,13], Paul Gibbs[4,13], Sanjay Sinha[1,2], Sarah A. Teichmann[7,18], Andrew J. Butler[4,13], Teik Choon See[6], Espen Melum[9,10,11,19,20], Christopher J. E. Watson[4,13,21,22], Kourosh Saeb-Parsy[4,13]†, Ludovic Vallier[1,4]*†

Organoid technology holds great promise for regenerative medicine but has not yet been applied to humans. We address this challenge using cholangiocyte organoids in the context of cholangiopathies, which represent a key reason for liver transplantation. Using single-cell RNA sequencing, we show that primary human cholangiocytes display transcriptional diversity that is lost in organoid culture. However, cholangiocyte organoids remain plastic and resume their in vivo signatures when transplanted back in the biliary tree. We then utilize a model of cell engraftment in human livers undergoing ex vivo normothermic perfusion to demonstrate that this property allows extrahepatic organoids to repair human intrahepatic ducts after transplantation. Our results provide proof of principle that cholangiocyte organoids can be used to repair human biliary epithelium.

Organoids have a particular potential for tissue repair as they retain key functions and characteristics of their tissue of origin. Nevertheless, their ability to repair native epithelia and restore their complexity after transplantation has not yet been established in humans, and organoid engraftment and survival in vivo has only been demonstrated in a limited number of animal studies (*1*).

The bile duct epithelium presents an archetypal and clinically important system for addressing this challenge and for developing proof-of-concept studies in humans for multiple reasons. Disorders of the biliary system, which transfers bile from the liver to the duodenum, account for 70% of pediatric and up to a third of adult liver transplantation (*2*), creating a pressing need for therapeutic alternatives, such as cell-based therapy. Furthermore, organoids suitable for regenerative medicine applications can be easily derived from biliary epithelial cells, known as cholangiocytes (*3*). Finally, the bile ducts also recapitulate the epithelial diversity found in other hollow-lumen organs (*4*). In particular, different regions along the biliary tree display distinct transcriptional profiles and functional properties, such as the chemical modification of bile (*5*, *6*) as well as variation in disease susceptibility between the intrahepatic ducts, extrahepatic ducts, and the gallbladder. Nevertheless, the impact of this regional variation on the characteristics and regenerative potential of the organoids derived from different regions of the biliary tree remains to be characterized.

To address these questions and demonstrate the value of organoids for regenerative medicine in humans, we first characterize cholangiocyte diversity in vivo using single-cell transcriptomics and confirm that different regions of the human biliary tree contain cells with distinct transcriptional profiles. We then show that cholangiocytes lose these differences in organoid culture and become interchangeable but that their regional identity can be restored in vitro by environmental stimuli. We subsequently use a biliary injury mouse model and a newly developed model for cell transplantation in human organs undergoing ex vivo normothermic perfusion (NMP) to prove that this plasticity allows cholangiocytes from one region to repair a different region of the biliary tree, thereby paving the way for cell-based therapy using organoids.

To characterize the cellular composition of the human biliary epithelium, cholangiocytes from different regions [intrahepatic bile ducts (IHD): 5 patients, 587 cells; common bile duct (CBD): 3 patients, 3006 cells; and gallbladder (GB): 3 patients, 3702 cells] were isolated using magnetic bead sorting, and their transcriptome was determined using droplet encapsulation single-cell RNA sequencing (scRNA-seq) (Fig. 1, A and B, and fig. S1, A to C). The isolated cells expressed key cholangiocyte markers, including KRT7, KRT19, SOX9, and GGT (fig. S2A). The transcriptomes of all three biliary cell populations shared a core transcriptional profile, illustrated by their proximity in uniform manifold approximation and projection (UMAP) space and high connectivity in partition-based graph abstraction (PAGA) analysis when compared with different liver cell types, such as stellate cells and liver sinusoidal endothelial cells (LSECs) (fig. S2, B to E). However, more detailed analysis after subclustering the cholangiocytes revealed nonoverlapping expression modules of the three populations (Fig. 1B), which suggests that, despite their similarities, cholangiocytes from different regions exhibit distinct gene expression signatures (*6*).

Differentially expressed gene (DEG) analysis (data S1) identified known region-specific markers, including aquaporins (*7*), mucins (*8*), *FGF19* (*9*), and *SOX17* (*10*) in the extrahepatic biliary tree; *JAG1* (*11*), *TACSTD2* (*12*), and YAP target genes in intrahepatic cholangiocytes (*13*, *14*); as well as previously unidentified markers including *DCDC2*, *TFF1-3*, and *SLC15A1* (Fig. 1, C and D, and fig. S3, A to D). Most of these genes correspond to functional markers such as bile acid receptors or channels modifying bile composition (fig. S3C). Thus, the transcriptional divergence among cholangiocytes from different regions could reflect adaptation to their microenvironment, such as the variation in

[1]Wellcome–MRC Cambridge Stem Cell Institute, Cambridge, Cambridgeshire, UK. [2]Department of Medicine, University of Cambridge, Cambridge, Cambridgeshire, UK. [3]Cambridge Liver Unit, Cambridge University Hospitals NHS Foundation Trust, Cambridge, Cambridgeshire, UK. [4]Department of Surgery, University of Cambridge and NIHR Cambridge Biomedical Research Centre, Cambridge, Cambridgeshire, UK. [5]Department of Clinical Neurosciences, University of Cambridge, Cambridge, Cambridgeshire, UK. [6]Department of Radiology, Cambridge University Hospitals NHS Foundation Trust, Cambridge, Cambridgeshire, UK. [7]Wellcome Sanger Institute, Wellcome Genome Campus, Hinxton, Cambridgeshire, UK. [8]Immunopathogenesis Section, Laboratory of Parasitic Diseases, National Institute of Allergy and Infectious Diseases, National Institutes of Health, Bethesda, MD, USA. [9]Norwegian PSC Research Center, Department of Transplantation Medicine, Division of Surgery, Inflammatory Diseases and Transplantation, Oslo University Hospital, Rikshospitalet, Oslo, Norway. [10]Research Institute of Internal Medicine, Division of Surgery, Inflammatory Diseases and Transplantation, Oslo University Hospital, Oslo, Norway. [11]Institute of Clinical Medicine, Faculty of Medicine, University of Oslo, Oslo, Norway. [12]Academic Department of Medical Genetics, University of Cambridge, Cambridge, Cambridgeshire, UK. [13]Department of Surgery, Cambridge University Hospitals NHS Foundation Trust, Cambridge, Cambridgeshire, UK. [14]Division of Cardiovascular Medicine, University of Cambridge, Cambridge, Cambridgeshire, UK. [15]MRC Mitochondrial Biology Unit, University of Cambridge, Cambridge, Cambridgeshire, UK. [16]Cambridge University Hospitals NHS Foundation Trust, Cambridge, Cambridgeshire, UK. [17]Department of Histopathology, Cambridge University Hospitals NHS Foundation Trust, Cambridge, Cambridgeshire, UK. [18]Cavendish Laboratory, Department of Physics, University of Cambridge, Cambridge, Cambridgeshire, UK. [19]Section for Gastroenterology, Department of Transplantation Medicine, Division of Surgery, Inflammatory Diseases and Transplantation, Oslo University Hospital, Rikshospitalet, Oslo, Norway. [20]Hybrid Technology Hub-Centre of Excellence, Institute of Basic Medical Sciences, Faculty of Medicine, University of Oslo, Oslo, Norway. [21]National Institute of Health Research (NIHR) Cambridge Biomedical Research Centre and the NIHR Blood and Transplant Research Unit (BTRU), Cambridge, Cambridgeshire, UK. [22]University of Cambridge in collaboration with Newcastle University and in partnership with NHS Blood and Transplant (NHSBT), Cambridge, Cambridgeshire, UK.

*Corresponding author. Email: fs347@cam.ac.uk (F.S.); lv225@cam.ac.uk (L.V.) †These authors contributed equally to this work.

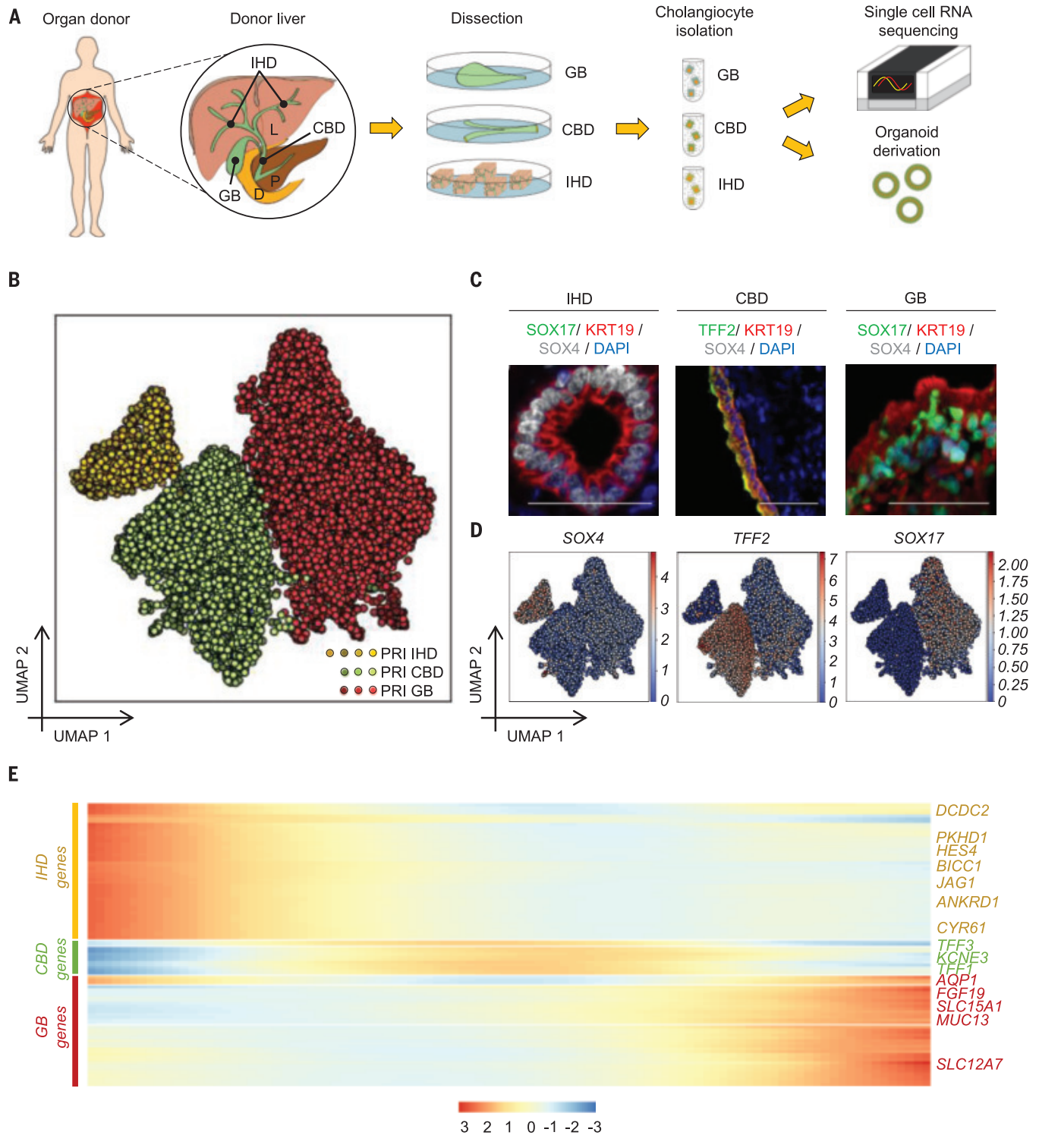

Fig. 1. Transcriptional profiling of primary cholangiocytes. (**A**) Schematic representation of the methodology used for scRNA-seq. (**B**) UMAP plot (7295 primary cells, *n* = 10 individuals) illustrating the distinct primary cholangiocyte populations in different regions of the biliary tree. (**C** and **D**) Immunofluorescence images (C) and UMAP representations (D) of normalized gene expression of primary cholangiocytes illustrating the differential expression of representative region markers. Scale bars, 50 μm. (**E**) Heatmap of top 100 DEGs in pseudotime (data S2) demonstrating a gradual transition in the transcriptional profile of cholangiocytes between different regions of the biliary tree. PRI, primary; IHD, intrahepatic ducts; CBD, common bile duct; GB, gallbladder; P, pancreas; D, duodenum; L, liver; DAPI, 4′,6-diamidino-2-phenylindole.

bile properties along the biliary tree (*15*). Accordingly, cholangiocytes from anatomically adjacent and therefore environmentally similar regions (e.g., IHD and CBD versus GB) displayed higher transcriptional similarity. This was illustrated by PAGA analysis (fig. S3, E and F) in agreement with results from diffusion pseudotime and single-cell consensus clustering (SC3) analyses (figs. S4 and S5). These results point toward a progressive change in the expression of region-specific markers (Fig. 1E and data S2) and a gradual transition in the transcriptional signature of cholangiocytes from adjacent regions (fig. S4, A to C) rather than the existence of distinct subpopulations (Fig. 1E and figs. S4 and S5). This gradient in gene expression likely indicates adjustment of the cells to environmental conditions, such as the gradual change in bile composition from the intrahepatic ducts to the gallbladder. Our results demonstrate that the human biliary epithelium is composed of cholangiocytes that display a gradual shift in their transcriptional profile along the biliary tree, which is likely imposed by region-specific microenvironments.

We subsequently used this single-cell map of the human biliary tree as a framework to characterize cholangiocyte organoids. To this end, a fraction of the primary cholangiocytes isolated for scRNA-seq from each region (IHD, CDB, and GB) were propagated as organoids using our established conditions (*3*, *16*). The resulting organoids expressed cholangiocyte markers (KRT7, KRT19, SOX9, HNF1B, and CFTR; fig. S6, A and B) and displayed comparable functionality (ALP, GGT activity; fig. S6, C and D) and similar expansion potential regardless of their region of origin (fig. S6E). To further explore these similarities, we performed scRNA-seq on these organoids (two lines per region; GB, 5859 cells; CBD, 5321 cells; and IHD, 6641 cells) (fig. S1, A to C). Principal components analysis (PCA) and UMAP analyses demonstrated that organoids exhibited overlapping transcriptomic profiles (Fig. 2A and fig. S7, A to D), which indicates that cholangiocytes grown in vitro assume a similar

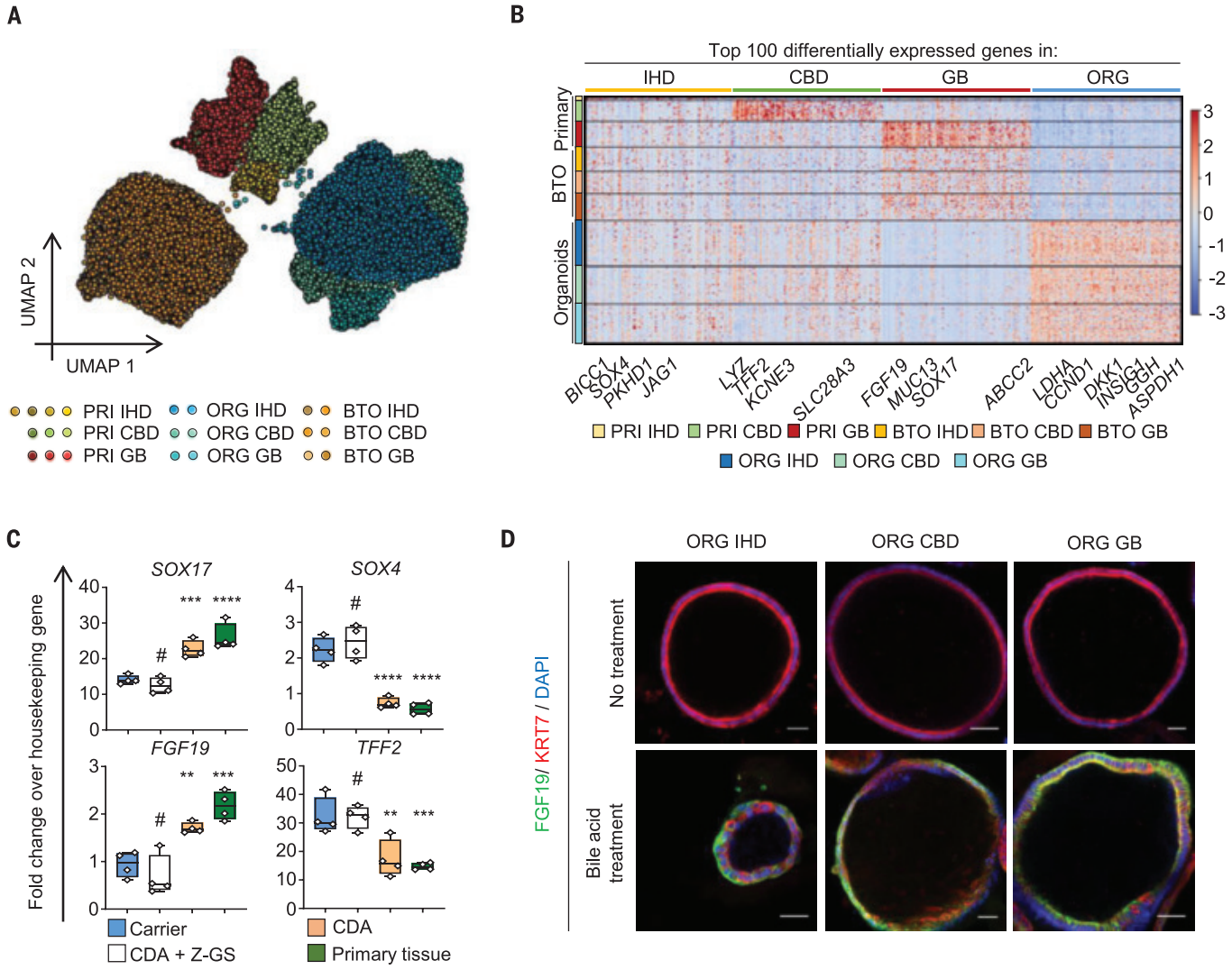

Fig. 2. Cholangiocyte organoid identity is controlled by niche stimuli. (**A**) UMAP (35,603 cells) of primary cholangiocytes and their corresponding organoids before and after gallbladder bile treatment showing the similarities between organoids from different regions and changes in their signature in response to bile. ORG, organoids; BTO, bile-treated organoids. (**B**) Heatmap of top 100 DEGs between primary regions, organoids, and BTOs (data S1 and S2) illustrating that organoids lose regional differences and up-regulate culture-related genes but reacquire gallbladder markers after bile treatment. (**C** and **D**) Quantitative real-time fluorescence polymerase chain reaction (QPCR) (C) [n = 4 samples per group; center line, median; box, interquartile range (IQR); whiskers, range; housekeeping gene, *HMBS*; $^{\#}P > 0.05$; $^{**}P < 0.01$; $^{***}P < 0.001$; $^{****}P < 0.0001$] and immunofluorescence (D) demonstrating the up-regulation of gallbladder markers and bile acid target genes after treatment with chenodeoxycholic acid (CDA) in the absence of the FXR inhibitor Z-GS. Z-GS, Z-guggulsterone. Scale bars, 50 μm.

transcriptional signature independent of their region of origin. Notably, regressing cell cycle–related genes did not change these observations, which excluded the possibility that a common proliferation signature could mask the differences between organoids of different spatial origins (fig. S7, A to C and E). Furthermore, we did not detect any cells coexpressing known somatic stem cell markers (*LGR5*, *PROM1*, *TACSTD2*, or *NCAM*), which excluded the possibility that organoid similarities reflect a common progenitor or stem cell identity (fig. S7F).

We then compared organoids from different regions with primary cholangiocytes to explore whether these similarities corresponded to the loss of their original regional identity in vitro (Fig. 2A). Organoids and primary cells after cell cycle regression shared a core transcriptional profile that reflected their common cholangiocyte nature, which was illustrated by their proximity in UMAP space and high PAGA connectivity when compared with different liver cell types, such as stellate cells and LSECs (fig. S7, C and D). However, DEG analyses highlighted down-regulation of region-specific markers such as *SLC13A1* and *SLC26A3* (Fig. 2B and fig. S7G), whereas gene ontology (GO) and gene set enrichment analyses (GSEA) identified these DEGs as factors facilitating the adaptation of cholangiocytes to their respective microenvironments—e.g., bile acid versus culture medium–processing genes (fig. S8, A to C). Furthermore, we confirmed the up-regulation of YAP target genes (data S3) in organoids, in accordance with previous studies (*14*). Therefore, primary cholangiocytes, propagated as organoids, adapted to their new microenvironment by maintaining their core transcriptional signature while losing the expression of markers specific to their region of origin.

To explore the mechanisms controlling cholangiocyte identity, we decided to add bile to our culture conditions as the principal determinant of the cholangiocyte microenvironment. Different organoids (IHD, CBD, and GB) were treated with human gallbladder bile for 72 hours and then characterized using scRNA-seq (Fig. 2A and fig. S1, A to C) (GB, 3815 cells; CBD, 3224 cells; and IHD, 3653 cells). UMAP and PCA revealed that treated organoids assumed a distinct but overlapping gene expression profile (Fig. 2A and fig. S9A), confirming a shared capacity to adapt to exposure to bile. Notably, PAGA and DEG analyses showed that this transcriptional profile was shifted toward a gallbladder identity (Fig. 2B and fig. S9, B and C). To characterize the factors controlling this transition, we interrogated DEGs in bile-treated organoids. GO, GSEA, and UMAP analyses (fig. S9, D to F) confirmed the induction of region-specific markers (SOX17, MUC13, and FGF19; Fig. 2B and fig. S9F) and revealed up-regulation of bile acid receptor pathways and downstream targets (*NR1H4/FXR*, *NR1I2*, *NR0B2*, *SLC51A*, *FGF19*, *ABCA1*, and *PPARG*; Fig. 2B and fig. S9, D to F). Notably, these results were validated through activation and inhibition of the farnesoid X receptor (FXR) using chenodeoxycholic acid and Z-guggulsterone, respectively (Fig. 2, C and D), which confirms that, regardless of their origin, cholangiocytes grown in vitro can respond and adapt to environmental stimuli. Together, these results suggest that cholangiocyte organoids could assume different regional identities when instructed by the appropriate niche factors.

To validate cholangiocyte plasticity and explore its functional implications, we decided to assess whether organoids from one region of the biliary tree could repair a different region after transplantation. For this, we induced cholangiopathy in immunodeficient mice using 4,4′-methylenedianiline (MDA) (*17*) (Fig. 3, A and B, and figs. S10 and S11) and attempted to rescue the phenotype with intraductal delivery (*18*) of human gallbladder organoids expressing red fluorescent protein (RFP). Control animals that received carrier medium without cells lost weight (fig. S10A) and died within 3 weeks (Fig. 3B and table S1), developing cholestasis (fig. S10B) and cholangiopathy demonstrated by immunofluorescence (IF) (fig. S10C), histology (fig. S10D), and magnetic resonance cholangiopancreatography (MRCP) (Fig. 3C; fig. S11, A to C; and movies S1 to S6). By contrast, animals that received organoids were electively culled at the end of the experiment and survived for up to 3 months, with resolution of cholangiopathy and normal serum biochemistry (Fig. 3, B and C; fig. S10, A, B, and D; fig. S11, B and C; and movies S3, S4, and S6). The transplanted gallbladder cholangiocytes engrafted in different size intrahepatic ducts (Fig. 3D; fig. S12, A to C; and movies S7 to S9) corresponding to ~25 to 55% of the regenerated biliary epithelium (fig. S12C), and they assumed an intrahepatic identity by losing gallbladder markers (SOX17) and expressing intrahepatic markers (SOX4, DCDC2, and BICC1) (Fig. 3D and fig. S12, A and B). Core biliary markers (KRT7, KRT19, and CFTR) were also expressed (fig. S12A), whereas we observed YAP activation in both engrafted and native cells (fig. S12, B and E), in accordance with previous studies (*13*). Notably, we never observed expression of other hepatic lineage markers such as albumin, which indicates that cholangiocyte organoid plasticity is likely to be limited to their biliary lineage of origin (fig. S12A). Furthermore, the engrafted cells expressed proliferation markers (fig. S12, B and D) at similar levels to those observed in native mouse cholangiocytes. Abnormal growth or tumor formation was never noticed in any of the analyses performed (Fig. 3, C and D; fig. S10D; and fig. S12, A and B), including the T1-weighted body magnetic resonance imaging (MRI) performed at the end of the experiment (movies S1 and S3). Thus, organoid transplantation appears to provide the healthy cells required to repair the damaged epithelium and rescue acute injury.

To ensure that animal rescue and resolution of cholangiopathy was specific to cholangiocyte organoids, we repeated the experiment using mesenchymal stem cells (MSCs)—a different type of cell known to provide anti-inflammatory effects after transplantation through paracrine signaling (fig. S13, A to C). This experiment allowed us to explore whether organoids are essential for duct regeneration and animal rescue and whether some of the observed effects could be attributed to paracrine signals that are not specific to our cells. MSCs failed to engraft (fig. S13C) and rescue the transplanted animals, which exhibited no difference in survival compared with controls ($P > 0.05$; fig. S13A) and no resolution of cholestasis on serum biochemistry (fig. S13B). Consequently, cholangiopathy resolution is specific to the engraftment of cholangiocyte organoids, and, although additional therapeutic effects of our cells through growth factor and cytokine secretion cannot be completely excluded, these effects are specific to cholangiocyte organoids.

We then explored whether organoid culture is required to unlock the plasticity of the cells or whether this reflects an inherent property of primary cholangiocytes. To achieve this, we transplanted primary gallbladder cholangiocytes (fig. S13, A to C) directly after isolation without in vitro culture. Under these conditions, very few primary cholangiocytes engrafted in the mouse bile ducts (fig. S13C), most likely because of the cumulative stress of isolation and transplantation, and the cholangiocytes failed to rescue the animals or resolve cholestasis (fig. S13, A and B). Nonetheless, the engrafted cells expressed intrahepatic markers and lost expression of gallbladder markers (fig. S13C). Thus, cholangiocyte plasticity is not limited to organoids grown in vitro; however, organoid culture is necessary for the cholangiocytes to recover from the stress of isolation and to achieve the large-scale expansion that provides the cell numbers required for engraftment and biliary repair.

To ensure that our results are not specific to the intrahepatic compartment or gallbladder organoids, we used our established methodology (*3*) to transplant common bile duct–derived cholangiocyte organoids in the gallbladder of immunocompromised mice. The engrafted cells exhibited loss of common bile duct markers and up-regulation of gallbladder markers (fig. S14), which confirms that our previous findings apply to different compartments of the biliary tree and to organoids of different

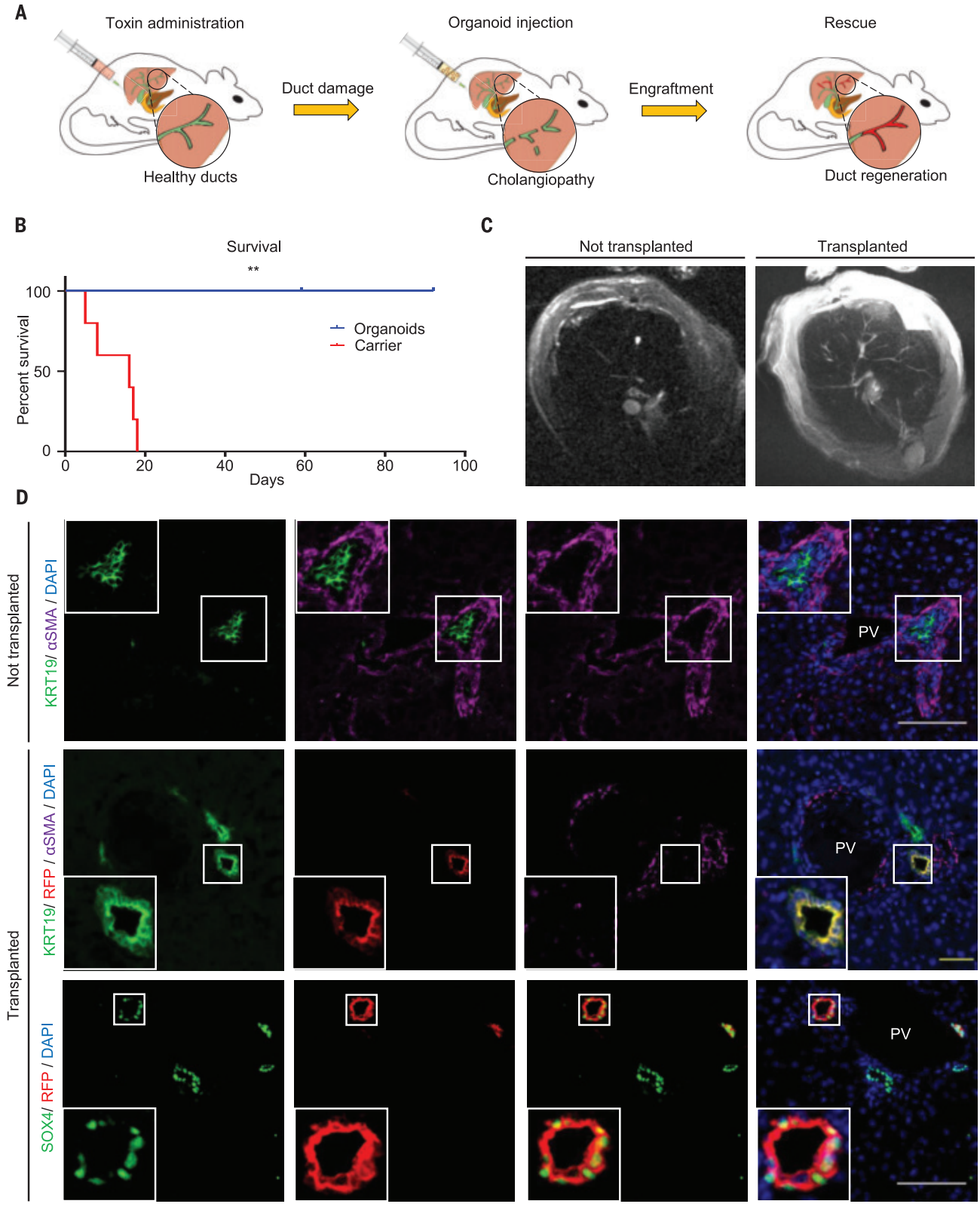

Fig. 3. Cholangiocyte organoids rescue cholangiopathy after transplantation and assume an identity corresponding to the site of engraftment. (**A**) Experimental outline schematic. (**B**) Kaplan-Meier curve (table S1: number of animals at risk) demonstrating animal rescue after gallbladder organoid injection. $^{**}P = 0.0018$; log-rank test. (**C**) MRCP demonstrating rescue of cholangiopathy after organoid injection. (**D**) Immunofluorescence demonstrating the engraftment of RFP-expressing gallbladder organoids in portal triads with the up-regulation of intrahepatic (SOX4) markers. Yellow scale bar, 50 μm; white scale bars, 100 μm. PV, portal vein.

origin. Taken together, these results establish that cholangiocytes from different regions of the biliary tree are interchangeable, and they suggest that extrahepatic cells can be used to repair acute intrahepatic duct injury.

Cell transplantation experiments in mouse models are extremely useful but are not always predictive of therapeutic outcomes (*19*). Furthermore, the mouse liver microenvironment is different from that of humans, which raises the possibility that our results may not translate between species. To address these challenges, we developed a model for cell-based therapy in humans utilizing ex vivo organ perfusion (*20*). Ex vivo NMP was developed to improve organ preservation and reduce ischaemia-reperfusion injury by circulating warm oxygenated blood through liver grafts before transplantation. Notably, the biliary tree is particularly susceptible to ischaemia, which results in duct damage (*21*, *22*). Low bile pH (<7.5) during NMP is used as a predictor of this type of cholangiopathy (*23*).

To assess the therapeutic potential of our cells for repairing human bile ducts, RFP-expressing gallbladder organoids were injected in the intrahepatic ducts of deceased human transplant donor livers ($n = 3$) with a bile pH <7.5 at the start of the experiment, which signified ischemic duct injury. The organs were

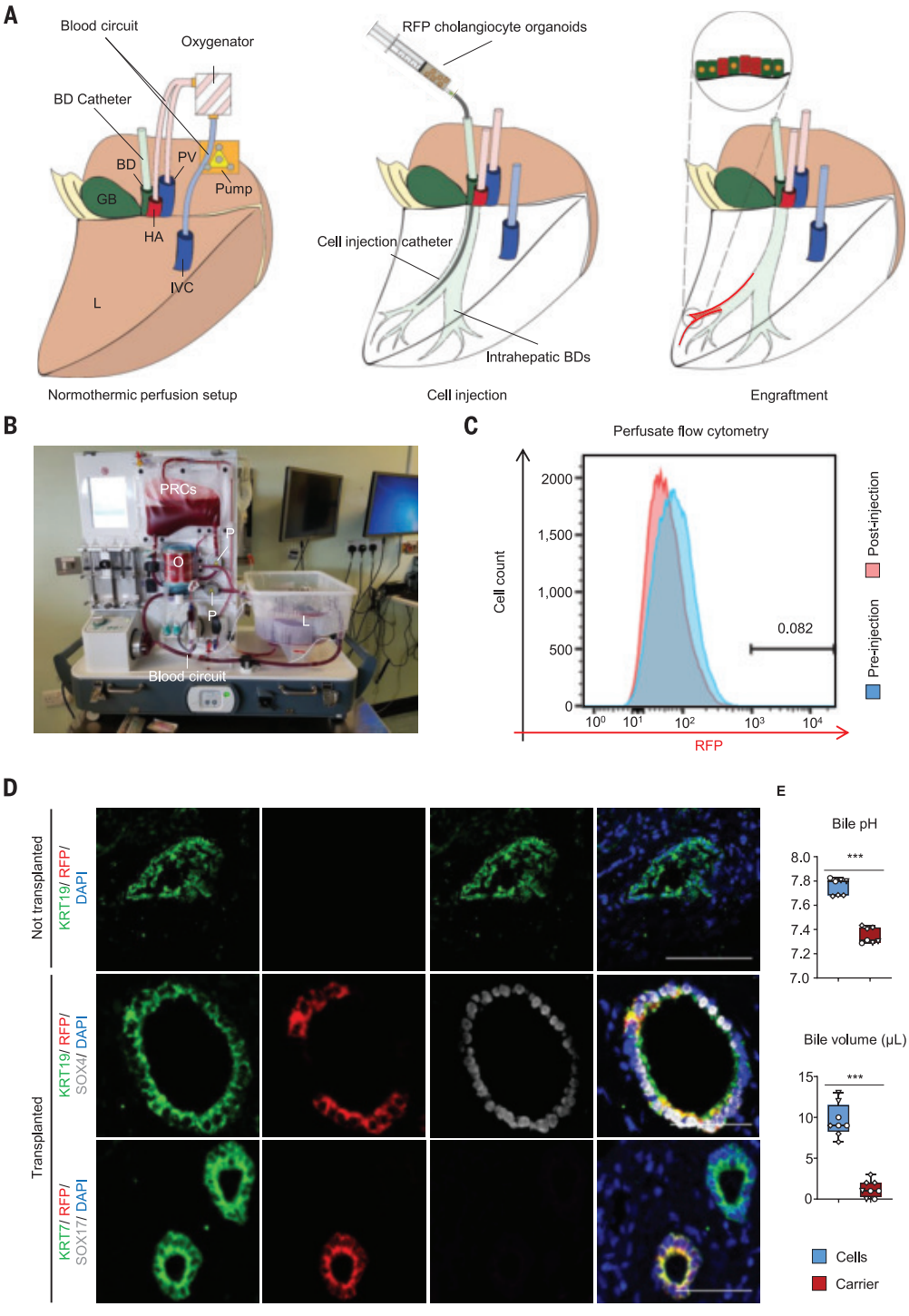

Fig. 4. Cholangiocyte organoids engraft in a human liver receiving NMP and improve bile properties. (**A** and **B**) Schematic representation of the technique for organoid injection (A) and photograph of the NMP circuit used (B). BD, bile duct; HA, hepatic artery; PV, portal vein; IVC, inferior vena cava; L, liver; P, pump; O, oxygenator; PRCs, packed red cells. (**C**) Flow cytometry revealing absence of RFP cells in the perfusate. (**D**) Immunofluorescence revealing the engraftment of RFP gallbladder organoids with upregulation of intrahepatic markers (SOX4) and loss of gallbladder markers (SOX17). Scale bars, 50 µm. (**E**) Organoid injection improves bile pH and choleresis. ***$P < 0.001$. $n = 3$ NMP livers. Each measurement is represented by a different data point, and each organ is represented by a different symbol.

perfused with oxygenated blood and nutrients at normal body temperature (*20*) (Fig. 4, A and B, and fig. S15A) for up to 100 hours to maintain a near-physiological microenvironment. Notably, the organoids were delivered in a terminal branch of the intrahepatic ducts under fluoroscopic guidance to minimize the area of distribution of the cells and maximize cell density (fig. S15B). At the end of the experiment, ultrasound imaging revealed no evidence of duct dilatation or obstruction (fig. S15C), and RFP-expressing cells were not detected in the perfusate by flow cytometry, which confirms that the injected cells remained in the biliary compartment (Fig. 4C). More importantly, the transplanted organoids engrafted in the intrahepatic biliary tree (Fig. 4D and figs. S15D and S16A), with RFP cells regenerating ~40 to 85% of the injected ducts (fig. S16B) and expressing key biliary markers (KRT7, KRT19, CFTR, GGT). Furthermore, engrafted gallbladder organoids exhibited loss of gallbladder markers (SOX17) and up-regulation of intrahepatic markers (SOX4, BICC1, DCDC2) without differentiation to other hepatic lineages (Fig. 4D; fig. S15D; and fig. S16A). Thus, at the end of the experiment, the injected ducts consisted of a mixture of native and transplanted cholangiocytes (fig. S16, A and B), with multiple transition points between donor and recipient cells and no evidence of cholangiopathy (Fig. 4D, fig. S15D, and fig. S16A).

Conversely, control ducts not receiving cells demonstrated evidence of ischemic injury with loss of epithelial continuity and sloughing of cells in the duct lumen (Fig. 4D). We subsequently characterized the impact of engraftment on organ function. Physiologically, cholangiocytes modify the composition and pH of bile through water transfer and bicarbonate secretion (*6*). Therefore, we compared the bile from organoid-injected versus carrier-injected ducts. Accordingly, bile aspirated from ducts injected with cells exhibited higher pH and volumes (Fig. 4E), which confirms that transplanted cholangiocytes retain their function to modify bile composition. Together, these results provide the first proof of principle that perfused organs can be used to ascertain functional engraftment of human cells, and they validate our mouse data by showing that cholangiocytes are interchangeable for transplantation in human organs.

Our results show that the biliary epithelium is composed of cholangiocytes with diverse transcriptional profiles that are determined by their local environments. This diversity is lost in organoid culture because of the lack of niche stimuli. However, organoids can adapt appropriately to local environmental cues both in vitro and after transplantation, restore the expression of region-specific markers, and assume different regional identities. Thus, organoids from a single region could potentially repair the entirety of the biliary tree. This plasticity could have substantial implications for regenerative medicine. Although autologous cell-based therapy potentially avoids the need for immunosuppression, its application for primary organoids is limited by the impact of disease on the epithelium. However, cholangiopathies belong to a family of localizing diseases that predominantly affect specific regions of an organ (*24*). Consequently, our results provide proof of concept that cholangiocytes from spared regions, such as the gallbladder, could be used for autologous cell-based therapy to repair human intrahepatic bile ducts, which constitute the most common site of injury in cholangiopathies.

Our model for cell engraftment in human perfused organs paves the way for the use of ex vivo cell-based therapy to improve graft function before transplantation, which could ultimately increase the number of useable organs and reduce pressure on the transplant waiting list. In this context, quality-controlled and readily available allogeneic cholangiocyte organoids from a cell bank could be used routinely in the future to prevent ischemic cholangiopathy in organs at risk of biliary injury (e.g., low bile pH), because the organ recipients will receive immunosuppression as part of their standard care. Our results provide proof of principle for the transplantation of organoids in human organs, which could expedite regulatory approval and fast-track first-in-human clinical trials. Ultimately, the same approach could also be applied to a variety of ex vivo perfused organs and cell types to validate functional cell engraftment, demonstrate safety, improve cell transplantation technique and efficacy, and accelerate the clinical translation of newly developed cell-based therapies.

REFERENCES AND NOTES

1. J. Drost, H. Clevers, *Development* **144**, 968–975 (2017).
2. R. H. Squires *et al*., *Hepatology* **60**, 362–398 (2014).
3. F. Sampaziotis *et al*., *Nat. Med.* **23**, 954–963 (2017).
4. K. Parikh *et al*., *Nature* **567**, 49–55 (2019).
5. C. A. Rimland *et al*., *Hepatology* 10.1002/hep.31252 (2020).
6. J. H. Tabibian, A. I. Masyuk, T. V. Masyuk, S. P. O'Hara, N. F. LaRusso, *Compr. Physiol.* **3**, 541–565 (2013).
7. A. I. Masyuk, N. F. LaRusso, *Hepatology* **43**, S75–S81 (2006).
8. K.-S. Yoo *et al*., *Gut Liver* **10**, 851–858 (2016).
9. S. J. L. B. Zweers *et al*., *Hepatology* **55**, 575–583 (2012).
10. Y. Zong, B. Z. Stanger, *Int. J. Biochem. Cell Biol.* **43**, 257–264 (2011).
11. K. Si-Tayeb, F. P. Lemaigre, S. A. Duncan, *Dev. Cell* **18**, 175–189 (2010).
12. N. Aizarani *et al*., *Nature* **572**, 199–204 (2019).
13. B. J. Pepe-Mooney *et al*., *Cell Stem Cell* **25**, 23–38.e8 (2019).
14. L. Planas-Paz *et al*., *Cell Stem Cell* **25**, 39–53.e10 (2019).
15. A. Lanzini, in *Encyclopedia of Food Sciences and Nutrition*, B. Caballero, Ed. (Academic Press, ed. 2, 2003), pp. 471–478.
16. O. C. Tysoe *et al*., *Nat. Protoc.* **14**, 1884–1925 (2019).
17. S.-B. Kwon *et al*., *Toxicol. Pathol.* **36**, 660–673 (2008).
18. N. L. Berntsen *et al*., *Am. J. Physiol. Gastrointest. Liver Physiol.* **314**, G349–G359 (2018).
19. C. Arber, M. K. Brenner, P. Reddy, *Semin. Hematol.* **50**, 131–144 (2013).
20. D. Nasralla *et al*., *Nature* **557**, 50–56 (2018).
21. A. I. Skaro *et al*., *Surgery* **146**, 543–553 (2009).
22. C. K. Enestvedt *et al*., *Liver Transpl.* **19**, 965–972 (2013).
23. C. J. E. Watson *et al*., *Am. J. Transplant.* **18**, 2005–2020 (2018).
24. R. G. Farmer, W. A. Hawk, R. B. Turnbull Jr., *Gastroenterology* **68**, 627–635 (1975).

ACKNOWLEDGMENTS

The authors would like to thank A. Petrunkina and the NIHR Cambridge BRC Cell Phenotyping Hub for their help with flow cytometry and cell sorting; K. Burling and the MRC MDU Mouse Biochemistry Laboratory [MRC_MC_UU_12012/5] for processing mouse serum samples; the Cambridge Biorepository for Translational Medicine for the provision of human tissue used in the study; P. Madrigal and C. Miau for bioinformatic support; C. Costa for his help with the NMP experiments; K. Reid and R. Clarke for their help with radiological imaging during the NMP experiments; and P. Humphreys, D. Clements, and S. McCallum for their help with confocal imaging. The monoclonal antibody TROMA-III developed by R. Kemler was obtained from the Developmental Studies Hybridoma Bank, created by the NICHD of the NIH and maintained at The University of Iowa, Department of Biology (Iowa City, IA). **Funding:** F.S. was supported by an NIHR Clinical Lectureship, the Academy of Medical Sciences Starter Grant for Clinical Lecturers, the Addenbrooke's Charitable Trust, and the Rosetrees Trust. T.B. was supported an EASL Juan Rodes fellowship. The L.V. laboratory is funded by the ERC advanced grant New-Chol, the Cambridge University Hospitals NIHR Biomedical Research Centre, and the core support grant from the Wellcome Trust and Medical Research Council of the Wellcome–MRC Cambridge Stem Cell Institute. L.G. and S.Si. were supported by a BHF Senior Research Fellowship (FS/18/46/33663). This research was supported by the NIHR Cambridge Biomedical Research Centre (BRC-1215-20014). The views expressed are those of the authors and not necessarily those of the NIHR or the Department of Health and Social Care. **Author contributions:** F.S. conceived and designed the study; performed experiments; acquired, interpreted, and analyzed the data; developed and validated the protocols described; performed bioinformatic analysis; generated the figures; and wrote and edited the manuscript. D.M. performed bioinformatics analysis. O.C.T. contributed to cell culture, harvesting and processing of tissue, scRNA-seq experiments, and animal experiments. T.E.B. contributed to animal experiments. S.Sa. performed the MRI experiments. E.M.G. performed the three-dimensional (3D) reconstruction of the mouse biliary tree from MRI images. E.M.G. and S.S.U. reviewed and reported the MRI images. T.B. contributed to tissue culture, QPCR, immunofluorescence, tissue clarification, and wholemount staining experiments. B.T.W. contributed to tissue dissociation and scRNA-seq experiments. J.G.-B. contributed to scRNA-seq experiments. K.M. contributed to primary tissue harvesting tissue. G.Ca. contributed to scRNA-seq experiments, flow cytometry, and magnetic-associated cell sorting. R.G. contributed to animal experiments, IF, and tissue histology. N.L.B. contributed to animal experiments. V.L.M. contributed to harvesting primary tissue. K.C., C.F., S.R., and L.S. contributed to ex vivo NMP experiments. J.B. contributed to imaging. L.G. contributed to tissue clarification and wholemount staining experiments as well as critical review of these data. D.O. and A.O. contributed to flow cytometry analyses and contributed to critical revision of the manuscript. P.H. contributed to 3D reconstruction and rendering of immunofluorescence images. S.E.B. contributed to experimental design and critical revision of the manuscript. G.Co. provided primary human samples. S.E.D. reviewed and reported the histology images and contributed to critical revision of the manuscript. I.A. contributed to bile aspiration using microdialysis catheters. A.J.B. and C.J.E.W. contributed to NMP experiments and critical revision of the manuscript. T.C.S. performed fluoroscopic cannulation of peripheral ducts in NMP experiments and contributed to critical revision of the manuscript. M.P.M., W.T.H.G., G.F.M., S.Si., S.A.T., P.G., and E.M. contributed to critical revision of the manuscript. K.S.-P. provided primary tissue, performed animal and ex vivo NMP experiments, contributed to the design and concept of the study, interpreted the data, and edited the manuscript. L.V. designed and conceived the study, interpreted the data, and wrote and edited the manuscript. All of the authors approved the manuscript. **Competing interests:** F.S., K.S.-P., and L.V. are founders and shareholders of BILITECH. L.V. is a founder and shareholder of DEFINIGEN. K.S.-P., F.S., and L.V. are inventors on the patent applications GB/19.96.17 and GBA 201709704 held by the University of Cambridge that cover the derivation and use of cholangiocyte organoids for regenerative medicine. The remaining

authors have no competing interests to disclose. **Data and materials availability:** All data are available in the main text or the supplementary materials. scRNA-seq data are available on ArrayExpress (accession no. E-MTAB-8495). Cholangiocyte organoids described in this publication are available from University of Cambridge under a material transfer agreement with the university.

SUPPLEMENTARY MATERIALS
science.sciencemag.org/content/371/6531/839/suppl/DC1
Materials and Methods
Figs. S1 to S16
Tables S1 to S3
References (*25*–*38*)
Movies S1 to S9
Data S1 to S3

10 November 2019; resubmitted 1 May 2020
Accepted 9 December 2020
10.1126/science.aaz6964

MITORIBOSOME

Mechanism of membrane-tethered mitochondrial protein synthesis

Yuzuru Itoh[1,2]*, Juni Andréll[1,2]*, Austin Choi[3]*, Uwe Richter[4,5,6]*, Priyanka Maiti[3], Robert B. Best[7], Antoni Barrientos[3]†, Brendan J. Battersby[4]†, Alexey Amunts[1,2]†

Mitochondrial ribosomes (mitoribosomes) are tethered to the mitochondrial inner membrane to facilitate the cotranslational membrane insertion of the synthesized proteins. We report cryo–electron microscopy structures of human mitoribosomes with nascent polypeptide, bound to the insertase oxidase assembly 1–like (OXA1L) through three distinct contact sites. OXA1L binding is correlated with a series of conformational changes in the mitoribosomal large subunit that catalyze the delivery of newly synthesized polypeptides. The mechanism relies on the folding of mL45 inside the exit tunnel, forming two specific constriction sites that would limit helix formation of the nascent chain. A gap is formed between the exit and the membrane, making the newly synthesized proteins accessible. Our data elucidate the basis by which mitoribosomes interact with the OXA1L insertase to couple protein synthesis and membrane delivery.

Proteins encoded in the human mitochondrial DNA (mtDNA) are essential for life, and aberrations in their synthesis are associated with clinical pathologies (*1*, *2*). Synthesis of these transmembrane proteins of the oxidative phosphorylation complexes occurs on dedicated mitochondrial ribosomes (mitoribosomes) that have a specialized exit tunnel and regulatory features (*3*). These mitoribosomes are tightly associated with the inner mitochondrial membrane for efficient protein delivery (*4*). Cotranslational membrane insertion is catalyzed by a putative mitochondrial insertase, the oxidase assembly 1–like (OXA1L) protein, a homolog of yeast Oxa1 and bacterial YidC (*5*–*7*). In yeast, Oxa1 is required for the assembly of the oxidative phosphorylation complexes (*8*), and its C terminus is associated with the mitoribosome (*9*, *10*). In human cells, depletion of OXA1L impairs the assembly of the complexes I, IV, and V (*11*, *12*), and biallelic *OXA1L* pathogenic mutations present with fatal encephalitis, hypotonia, and developmental delay (*12*). Mechanistically, the association of the mitoribosome with an insertase would likely protect the hydrophobic membrane proteins during their egression into the lipid bilayer. On the basis of studies of cotranslational folding of membrane proteins into an α-helical conformation in the ribosomal tunnel in bacteria (*13*), it has been postulated that such a secondary structure may also start forming within the mitoribosome tunnel. However, no structure of mitoribosome with a membrane insertase has been reported; thus, a mechanism of nascent-chain emergence remained unknown.

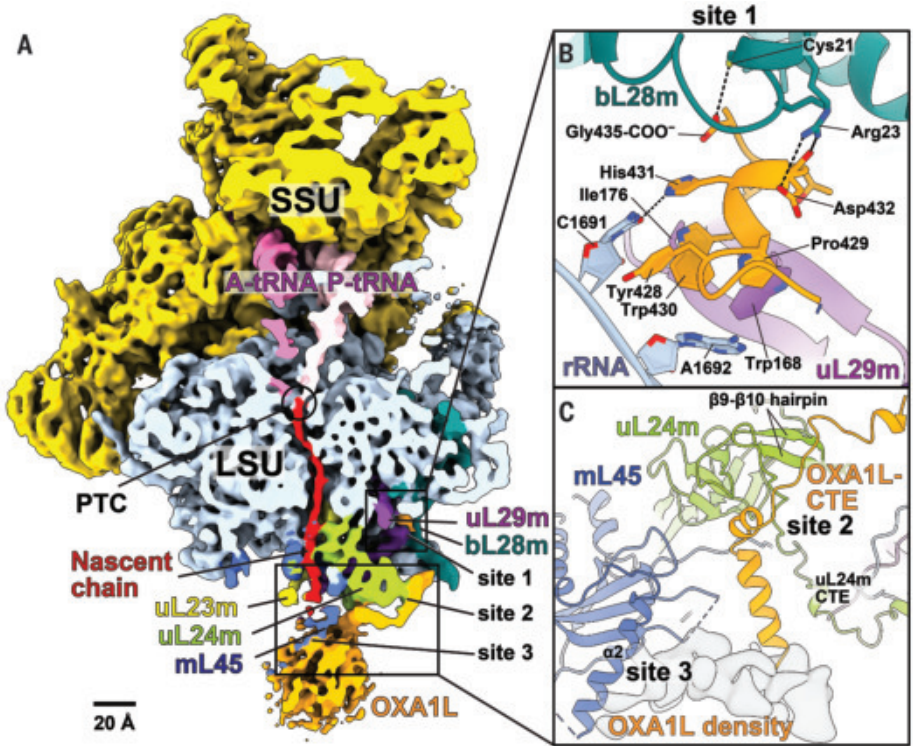

Fig. 1. Human mitoribosome:OXA1L complex. (**A**) Density of mitoribosome:OXA1L complex lowpass filtered to 6-Å resolution for clarity and cut through the tunnel. Contact sites 1, 2, and 3 are indicated. PTC, peptidyl transferase center; LSU, large subunit; SSU, small subunit. (**B**) Contact site 1 is formed by OXA1L C-terminal helix bound to bL28m, uL29m, and rRNA. Tyr^{428} is stacked on rRNA Cys^{1691} (C1691), and His^{431} hydrogen bonds with C1691. The backbone carbonyl and side chain of Asp^{432} form polar interactions with bL28m (Arg^{23}, Pro^{429}, and Trp^{430}) and hydrophobic interactions with uL29m (Trp^{168} and Ile^{176}) and rRNA A1692. (**C**) OXA1L-CTE interacts with uL24m (site 2), and the OXA1L core (shown with density) is associated with mL45-α2 (site 3).

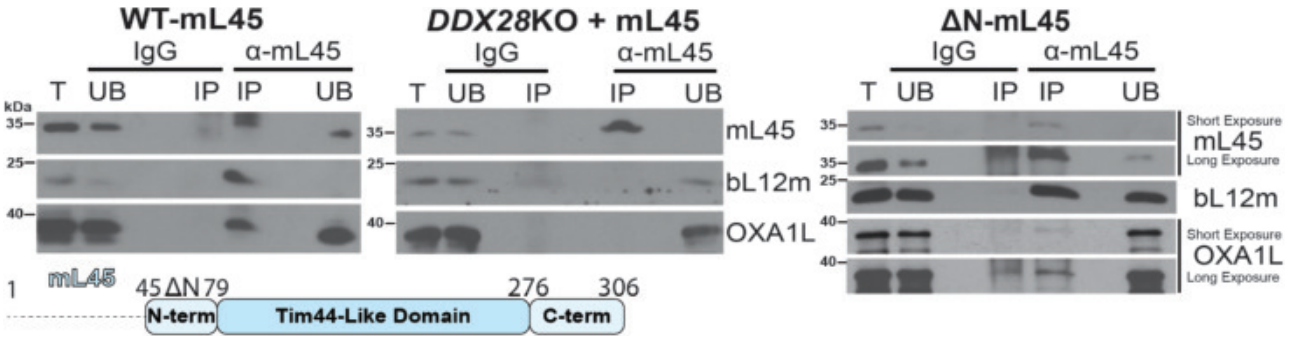

Fig. 2. Biochemical characterization of mL45 and OXA1L interaction. Immunoprecipitation of mL45 from mitochondrial extracts of T-Rex-293 cells expressing WT or Δ*N-mL45* and the *DDX28*-KO (knockout) cells overexpressing WT *mL45*. The cells were probed for mL45, OXA1L, or bL12m as an mtLSU marker, and immunoglobulin G (IgG) was used as a control. IP, immunoprecipitated; T, total input; UB, unbound.

To capture the interactions of a mitoribosomal exit tunnel with its substrate, we used the peptidomimetic actinonin, which structurally resembles formylmethionine, to induce a cotranslational accumulation of stalled mitoribosomes during nascent-chain synthesis (fig. S1) (*14*). To sort the particles corresponding to translating mitoribosomes, we collected six cryo–electron microscopy (cryo-EM) datasets and classified them on the basis of the presence of the small subunit after signal subtraction (*15*). Then, we performed a second step of signal subtraction and three-dimensional (3D) classification on the A-site tRNA and a third step on the insertase region (fig. S2A). Subsequent 3D refinement produced a reconstruction that showed a fragmented density extending from the tunnel exit. To reduce the flexibility of a putative insertase on the mitoribosome, we subjected the complex to amine-to-amine crosslinking and repeated the cryo-EM analysis with two additional datasets (fig. S2, B to F, and materials and methods). In silico sorting yielded a subset of 30,744 particles that, upon contrast transfer function refinement and Bayesian polishing (*15*), resulted in the 2.89-Å reconstruction, revealing densities for tRNAs in the A- and P-sites, continuous density from the peptidyl transferase center extending to the tunnel exit, and additional mass outside the exit correlating with the position of the inner mitochondrial membrane (*4*) (Fig. 1A and fig. S3). The position of the extra density and its overall dimensions were in agreement with the bacterial ribosome:YidC reconstructions (*16*, *17*) that accommodate a single copy of the insertase (fig. S4).

Although the local resolution for the additional density is 5 to 8 Å, reflecting intrinsic flexibility, by combining biochemical stabilization with targeted classification and polishing, we could improve the signal-to-noise ratio and trace ~50 amino acid residues that were docked to the surface of the mitoribosomal large subunit (mtLSU) (fig. S5). The quality of the side-chain densities was sufficient for modeling the C-terminal residues of OXA1L (fig. S5D), and mass-spectrometry analysis confirmed the presence of OXA1L (fig. S6). OXA1L binds to the mitoribosome through three distinct contact sites spanning the solvent-exposed side of the mtLSU (Fig. 1A and fig. S7). Together, the interface anchoring OXA1L involves three mitoribosomal proteins and ribosomal RNA (rRNA), comprising a total buried surface area of ~1500 Å^2.

Site 1 is found in the mitoribosomal cleft toward the L1 stalk, ~70 Å away from the membrane surface (Fig. 1, A and B). It comprises mitochondrial-specific protein extensions of bL28m, uL29m, and the rRNA bypass element H4-H8 (residues 1689 to 1695) that together form the binding pocket for the OXA1L C-terminal helix (YPWHDTLG-COO$^-$) (fig. S8, A and B). A series of interactions involve residues that are generally conserved in vertebrates and underlie a tight association that does not occur in bacteria (fig. S9).

Site 2 is separated from site 1 by 27 Å and consists solely of the mitoribosomal protein uL24m (Fig. 1C). Although the part of OXA1L linking the two contact sites is not well resolved, we could model 40 residues composed of an α helix, two short 3_{10}-helices, and a 10-residue loop. Together, it binds to the matrix-exposed surface, thus encompassing uL24m, and the loop is stabilized by the β9-β10 hairpin (residues 133 to 147) at the C-terminal domain of uL24m (Fig. 1C and fig. S9D). Consistent with the shape of uL24m, the OXA1L structure is bent in this region by ~80° (Fig. 1, A and C).

Site 3 is ~15 Å away from site 2 and formed by the core domain of mL45, where the globular density of the OXA1L membrane part is attached (Fig. 1C). Although no OXA1L model could be placed here because of the flexibility, continuous density can be traced from the α helix of OXA1L C-terminal extension (CTE) at site 2 (Fig. 1A). The contact is mostly through the α-helix mL45-α2 (residues 94 to 128) on top of the core β sheet of the mL45 Tim44-like domain. Overall, the observed interactions of OXA1L with the mitoribosome are consistent with super-resolution microscopy showing that the CTE truncation (Δ332–433) of OXA1L reduces, but does not completely abolish, the colocalization with the translating mitoribosome (*18*).

Consistent with the structure, we find that OXA1L forms a stable interaction with mL45 in vitro only when it is assembled into the mitoribosome (Fig. 2 and fig. S10). To demonstrate this, we used a cell line in which the mtLSU assembly helicase DDX28 has been deleted (*19*). We ectopically expressed mL45, which associates with the mitochondrial membranes despite the mtLSU assembly defect but does not interact with OXA1L (Fig. 2 and fig. S10). Thus, the interaction between OXA1L and mitoribosomes is mediated by mitoribosome-assembled mL45.

Next, we examined the cryo-EM data with respect to the exit tunnel interior and identified two distinct states, Class 1a* and Class 1b* (figs. S2B and S11). The particles in Class 1b* represent the OXA1L-unbound (inactive) state. The density in the upper tunnel is separated from the tRNA by 12 Å (fig. S11A). This density extends from mL45 and corresponds to its N-terminal sequence, consistent with a previous study (*20*). The previous study also proposed that the mL45 N-terminal tail acts to recruit the OXA1L insertase, implying a targeting

[1]Science for Life Laboratory, Department of Biochemistry and Biophysics, Stockholm University, 17165 Solna, Stockholm, Sweden. [2]Department of Medical Biochemistry and Biophysics, Karolinska Institutet, 17177 Stockholm, Sweden. [3]Department of Neurology, University of Miami Miller School of Medicine, Miami, FL 33136, USA. [4]Institute of Biotechnology, University of Helsinki, 00790 Helsinki, Finland. [5]Faculty of Biological and Environmental Sciences, University of Helsinki, 00790 Helsinki, Finland. [6]Wellcome Centre for Mitochondrial Research, Biosciences Institute, Newcastle University, Newcastle upon Tyne NE2 4HH, UK. [7]Laboratory of Chemical Physics, National Institute of Diabetes and Digestive and Kidney Diseases, National Institutes of Health, Bethesda, MD 20892-0520, USA.
*These authors contributed equally to this work.
†Corresponding author. Email: abarrientos@med.miami.edu (A.B.); brendan.battersby@helsinki.fi (B.J.B.); amunts@scilifelab.se (A.A.)

mechanism in mammalian mitochondria analogous to the signal recognition particle (*20*). In fungi, mL45 (Mba1) is not a structural component of the mitoribosome (*21*, *22*), whereas in ciliates, a homolog of the bacterial signal recognition particle binding protein Ffh was identified in the mitoribosomal tunnel (*23*). To investigate whether mL45 N terminus recruits OXA1L in human mitochondria, we expressed a variant with a shortened N terminus residues 45 to 74 (ΔN) and showed that although the relative amount of coimmunoprecipitated OXA1L is lower than for the wild type (WT), the truncation of mL45 does not entirely prevent interaction with OXA1L (Fig. 2).

In the inactive state, the basic residues in the mL45 N terminus form electrostatic interactions with the rRNA core that anchor the protein moiety inside the tunnel (Fig. 3A and fig. S11A). In the lower tunnel, mL45 Pro^{68} is stabilized by the mitochondria-specific rRNA A1804, mL45 Ile^{76}, and uL23m Leu^{126} (fig. S12A). We found that A1804 is an mtDNA insertion (fig. S8C), which is an unusual feature because only deletions in the mammalian mitochondrial rRNA have been reported to date (*24*–*28*). This stabilization allows mL45 Arg^{61} and Lys^{62} to point toward the rRNA interior (fig. S12A) so that the mL45 N-terminal tail is positioned directly on the nascent-polypeptide path (Fig. 3A). This is further correlated with two hydrophobic residues, Val^{66} and Ile^{67}, forming interprotein hydrophobic pairs with uL23m-α2 (fig. S12A). These interactions stabilize uL23m-α2 perpendicularly to the tunnel so that it fills the spacings at the exit site, blocking the path.

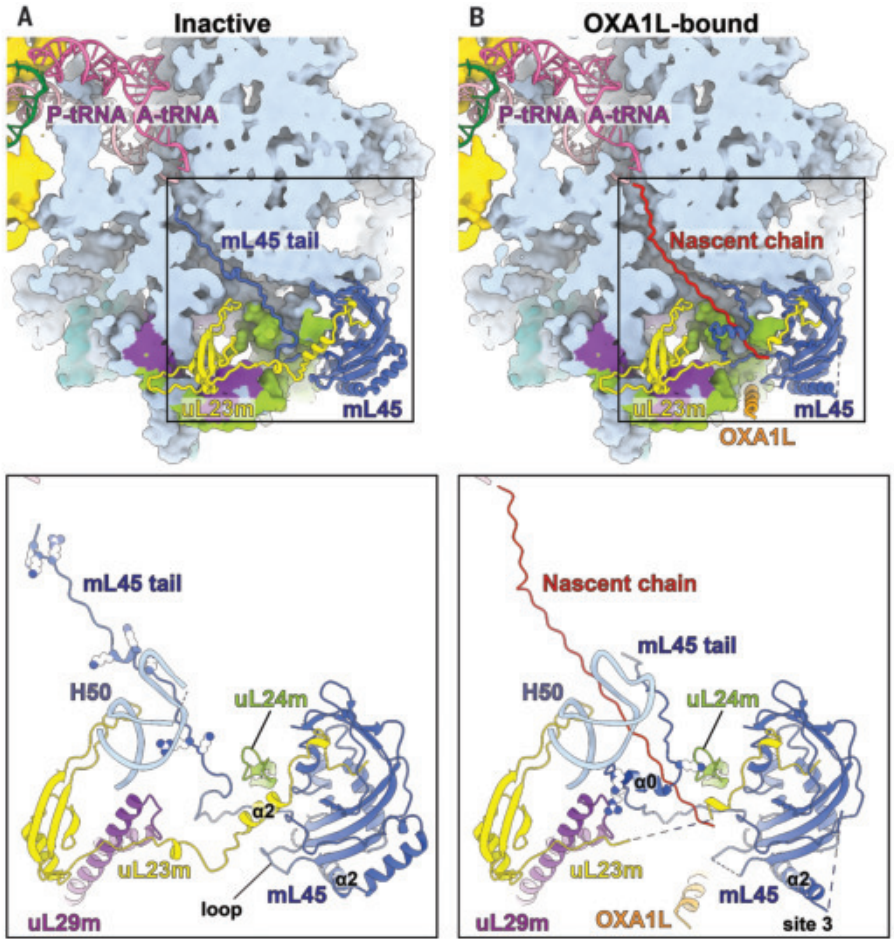

Fig. 3. Comparison between inactive and OXA1L-bound structures. (**A**) In the inactive state, the mL45 N-terminal tail occupies the tunnel. Basic residues in the tunnel are shown as spheres in the bottom panel. uL23m-α2 is stabilized by the mL45 tail and a loop (residues 200 to 208) of mL45. The tip of rRNA Helix 50 (H50) is disordered because of flexibility. (**B**) In the OXA1L-bound state, a nascent polypeptide occupies the tunnel. The mL45 tail is folded and stabilized by uL24m, uL29m, and rRNA H50. The basic residues participating in the stabilization are shown in the bottom panel. The tip of H50 is ordered, uL23m-α2 and the mL45 loop are disordered, and the path through the tunnel is open. The contact site 3 with OXA1L is formed through mL45-α2. The bottom panels show partial structures of uL23m (residues 37 to 153), uL24m (93 to 112), and uL29m (94 to 157).

Class 1a* represent the OXA1L-bound state. A continuous density connected to the P-tRNA is observed in the tunnel, corresponding to a nascent polypeptide of a mitoribosome engaged in protein synthesis and associated with OXA1L (fig. S11B). Glu^{70}-Lys^{71} of mL45 adopt a conformation related by ~100°, which results in the 12-Å and 17-Å displacement of the upstream Val^{66} and Ile^{67}, respectively. Therefore, the uL23m-α2 is released and destabilized (Fig. 3B and fig. S12). The loop from the mL45 Tim44-like domain also becomes disordered by losing its interaction with uL23m-α2. The lack of an internal protein scaffold allows the lower tunnel to accommodate a nascent chain. In the upper tunnel, the mL45 membrane-distal tail adopts a folded α helix (α0), stabilized by the mitochondria-specific insertion of uL29m, the β4-β5 hairpin of uL24m, and H50 of rRNA from the opposite sides (Figs. 3B and 4A and fig. S13). Thus, a continuous pathway is formed from the tunnel entrance to the mitoribosomal surface at the membrane-facing region that is available for nascent chain conduction (Fig. 4B and movie S1).

Once folded within the lower tunnel, mL45 forms two mitochondria-specific constriction sites with uL24m (Fig. 4C). The constrictions keep the tunnel width less than 8 Å (Fig. 4D). By contrast, in bacteria, the tunnel increases in diameter to greater than 15 Å, allowing nascent chains to fold in the exit tunnel (*29*). To assess whether mL45-induced geometry of the exit tunnel determines cotranslational protein folding, we used coarse-grained molecular dynamics simulations with WT and Δ*N-mL45* mitoribosomes. Our results show that the observed enclosure of the nascent chain by mL45 decreases helix formation at the constriction sites within the tunnel (fig. S14).

Our data further assign two additional functions to mL45: (i) directing the nascent polypeptide toward the tunnel exit by compensating for rRNA deletion and (ii) positioning the exit at a distance from the membrane surface. The former is achieved by the folded N terminus of mL45, which supports a specific extended-away conformation of the uL24m β4-β5 hairpin rather than extruding into the vestibule, as in bacteria (fig. S8D). As a result, the residues at the hairpin tip that were shown to be implicated in bacterial protein folding (*30*) are 17 Å away, outlining the tunnel walls. This architecture shields an unfolded nascent chain and prevents it from escaping the tunnel prematurely because of rRNA H24 deletion (fig. S8B and D). Then, the positioning of the exit relative to the membrane is mediated by the mL45 Tim44-like domain that allows a gap between the mitoribosomal surface and the insertase, as opposed to a closer association as seen in bacteria (fig. S15). This structural arrangement makes the newly synthesized mitochondrial proteins more accessible for peptidyl deformylase,

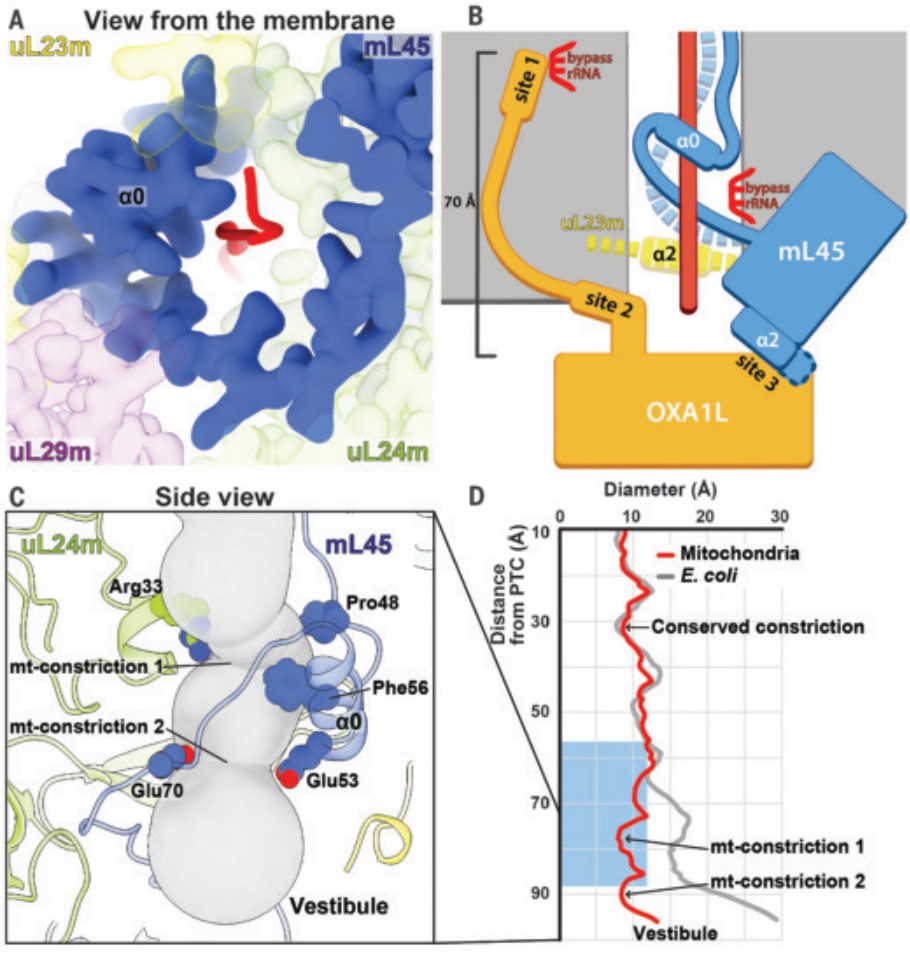

Fig. 4. Mechanism of membrane-tethered nascent-polypeptide emergence. (**A**) Folding of the mL45 tail stabilized by uL29m and uL24m, resulting in a continuous protein arch coating the interior with the nascent chain. (**B**) Side-view schematic of the gating mechanism. The folding of mL45-α0 (blue tube) leads to the detachment of its N terminus from rRNA (dashed blue) and destabilization of uL23m-α2 (dashed yellow) that together open the way for a polypeptide chain (red). OXA1L is docked to the extended mL45-α2 (site 3) for cotranslational insertion of the emerging polypeptide. Contact sites 1 and 2 are formed between the OXA1L-CTE and the mitoribosomal surface up to 70 Å away from the membrane surface. (**C**) Side view of the lower tunnel, shown as a gray tube. Mitochondria-specific constriction sites are formed by mL45-α0 and uL24m, and the involved residues are shown. (**D**) Tunnel diameter was calculated for the mitoribosome and *Escherichia coli* ribosome and plotted along the path. The blue rectangle indicates the position of an α-helical formation within the tunnel in bacteria.

methionine amino peptidase, and chaperones before the membrane insertion. In yeast, the deletion of mL45 (Mba1) is associated with membrane insertion defects (*31*).

The sequencing of the human mitochondrial genome 40 years ago (*32*) was a turning point in mitochondrial research, postulating a putative specialized mechanism for the synthesis of these 13 transmembrane proteins. Our discovery of mL45-induced conformational changes represents a gating mechanism of the mitoribosome without similarity in bacterial and cytosolic systems. It forms a cavity, secluding unfolded nascent chains and securing their delivery to the membrane. The gating is correlated with the association of the OXA1L insertase; however, secondary structure formation is not favored while a nascent chain is at the constriction sites. Together, the data offer a molecular insight into how proteins are synthesized in human mitochondria.

REFERENCES AND NOTES

1. D. De Silva, Y.-T. Tu, A. Amunts, F. Fontanesi, A. Barrientos, *Cell Cycle* **14**, 2226–2250 (2015).
2. A. Suomalainen, B. J. Battersby, *Nat. Rev. Mol. Cell Biol.* **19**, 77–92 (2018).
3. S. Aibara, V. Singh, A. Modelska, A. Amunts, *eLife* **9**, e58362 (2020).
4. R. Englmeier, S. Pfeffer, F. Förster, *Structure* **25**, 1574–1581.e2 (2017).
5. Y. Chen *et al.*, *Structure* **25**, 1403–1414.e3 (2017).
6. E. van Bloois, G. Jan Haan, J.-W. de Gier, B. Oudega, J. Luirink, *FEBS Lett.* **576**, 97–100 (2004).
7. M. van der Laan, P. Bechtluft, S. Kol, N. Nouwen, A. J. M. Driessen, *J. Cell Biol.* **165**, 213–222 (2004).
8. M. Hildenbeutel *et al.*, *J. Mol. Biol.* **423**, 590–599 (2012).
9. L. Jia *et al.*, *EMBO J.* **22**, 6438–6447 (2003).
10. G. Szyrach, M. Ott, N. Bonnefoy, W. Neupert, J. M. Herrmann, *EMBO J.* **22**, 6448–6457 (2003).
11. L. Stiburek *et al.*, *J. Mol. Biol.* **374**, 506–516 (2007).
12. K. Thompson *et al.*, *EMBO Mol. Med.* **10**, e9060 (2018).
13. M. Bañó-Polo *et al.*, *Nat. Commun.* **9**, 5246 (2018).
14. U. Richter *et al.*, *Curr. Biol.* **23**, 535–541 (2013).
15. J. Zivanov *et al.*, *eLife* **7**, e42166 (2018).
16. S. Wickles *et al.*, *eLife* **3**, e03035 (2014).
17. A. Kedrov *et al.*, *Cell Rep.* **17**, 2943–2954 (2016).
18. R. G. Lee *et al.*, *J. Cell Sci.* **133**, jcs240374 (2020).
19. Y.-T. Tu, A. Barrientos, *Cell Rep.* **10**, 854–864 (2015).
20. E. Kummer *et al.*, *Nature* **560**, 263–267 (2018).
21. A. Amunts *et al.*, *Science* **343**, 1485–1489 (2014).
22. Y. Itoh, A. Naschberger, N. Mortezaei, J. M. Herrmann, A. Amunts, *Nat. Commun.* **11**, 5187 (2020).
23. V. Tobiasson, A. Amunts, *eLife* **9**, e59264 (2020).
24. B. J. Greber *et al.*, *Nature* **515**, 283–286 (2014).
25. A. Amunts, A. Brown, J. Toots, S. H. W. Scheres, V. Ramakrishnan, *Science* **348**, 95–98 (2015).
26. B. J. Greber *et al.*, *Science* **348**, 303–308 (2015).
27. A. Brown *et al.*, *Nat. Struct. Mol. Biol.* **24**, 866–869 (2017).
28. A. S. Petrov *et al.*, *Mol. Biol. Evol.* **36**, 207–219 (2019).
29. M. Liutkute, E. Samatova, M. V. Rodnina, *Biomolecules* **10**, 97 (2020).
30. R. Kudva *et al.*, *eLife* **7**, e36326 (2018).
31. H. Bauerschmitt *et al.*, *Mol. Biol. Cell* **21**, 1937–1944 (2010).
32. S. Anderson *et al.*, *Nature* **290**, 457–465 (1981).

ACKNOWLEDGMENTS

We thank SciLifeLab for access to the cryo-EM facility (funded by the KAW, EPS, and Kempe foundations) and clinical proteomics mass spectrometry facility; Diamond Light Source for access to eBIC (funded by the Wellcome Trust, MRC, and BBSRC) under proposal EM19823-1 with assistance from Y. Chaban; and R. Kock Flygaard and N. Fluman for advice. **Funding:** Swedish Foundation for Strategic Research (FFL15:0325), Ragnar Söderberg Foundation (M44/16), Cancerfonden (2017/1041), European Research Council (ERC-2018-StG-805230), Knut and Alice Wallenberg Foundation (2018.0080), The Academy of Finland (307431 and 314706 to B.J.B.), Sigrid Juselius Foundation (to B.J.B), NIH-R35 grant (GM118141 to A.B.), and MDA Research Grant (MDA-381828 to A.B.) supported this work. R.B.B. was supported by the Intramural Research Program of the National Institute of Diabetes and Digestive and Kidney Diseases of the NIH. This work used the computational resources of the NIH HPC Biowulf cluster (https://hpc.nih.gov). Y.I. was supported by H2020-MSCA-IF-2017 (799399-Itohribo). P.M. is the recipient of a postdoctoral fellowship from the American Heart Association (19POST34450174). **Author contributions:** B.J.B., U.R., and A.A. designed the project. J.A., U.R., and A.A. prepared the sample for cryo-EM. J.A. and Y.I. collected and processed the cryo-EM data. Y.I. built the model. A.C., P.M., and A.B. performed biochemical analysis. R.B.B. performed molecular simulation. A.A., Y.I., and J.A. wrote the manuscript with contributions from all coauthors. **Competing interests:** The authors declare no competing interests. **Data and materials availability:** The atomic coordinates were deposited in the RCSB Protein Data Bank (PDB) under accession numbers 6ZM5 and 6ZM6. The cryo-EM maps have been deposited in the Electron Microscopy Data Bank (EMDB) under accession numbers EMD-11278, EMD-11279, EMD-11280, EMD-11281, EMD-11282, EMD-11283, EMD-11284, EMD-11285, EMD-11286, and EMD-11287.

SUPPLEMENTARY MATERIALS

science.sciencemag.org/content/371/6531/846/suppl/DC1
Materials and Methods
Figs. S1 to S15
Tables S1 to S5
References (*33*–*61*)
MDAR Reproducibility Checklist
Movie S1

29 July 2020; accepted 24 December 2020
10.1126/science.abe0763

CORONAVIRUS

Prospective mapping of viral mutations that escape antibodies used to treat COVID-19

Tyler N. Starr[1]*, Allison J. Greaney[1,2,3]*, Amin Addetia[1,4], William W. Hannon[1,4], Manish C. Choudhary[5], Adam S. Dingens[1], Jonathan Z. Li[5], Jesse D. Bloom[1,2,6]†

Antibodies are a potential therapy for severe acute respiratory syndrome coronavirus 2 (SARS-CoV-2), but the risk of the virus evolving to escape them remains unclear. Here we map how all mutations to the receptor binding domain (RBD) of SARS-CoV-2 affect binding by the antibodies in the REGN-COV2 cocktail and the antibody LY-CoV016. These complete maps uncover a single amino acid mutation that fully escapes the REGN-COV2 cocktail, which consists of two antibodies, REGN10933 and REGN10987, targeting distinct structural epitopes. The maps also identify viral mutations that are selected in a persistently infected patient treated with REGN-COV2 and during in vitro viral escape selections. Finally, the maps reveal that mutations escaping the individual antibodies are already present in circulating SARS-CoV-2 strains. These complete escape maps enable interpretation of the consequences of mutations observed during viral surveillance.

Antibodies are being developed as therapeutics to combat severe acute respiratory syndrome coronavirus 2 (SARS-CoV-2) (*1*). Antibodies against some other viruses can be rendered ineffective by viral mutations that are selected during treatment of infected patients (*2*, *3*) or that spread globally to confer resistance on entire viral clades (*4*). Therefore, determining which SARS-CoV-2 mutations escape key antibodies is essential for assessing how mutations observed during viral surveillance may affect the efficacy of antibody treatments.

Most leading anti–SARS-CoV-2 antibodies target the viral receptor binding domain (RBD), which mediates binding to the angiotensin-converting enzyme 2 (ACE2) receptor (*5*, *6*). We recently developed a deep mutational scanning method to map how all mutations to the RBD affect its function and recognition by antiviral antibodies (*7*, *8*). This method involves creating libraries of RBD mutants, expressing them on the surface of yeast, and using fluorescence-activated cell sorting and deep sequencing to quantify how each mutation affects RBD folding, ACE2 affinity (measured across a titration series), and antibody binding (fig. S1A). In this study, we used the duplicate mutant libraries described in (*7*), which consist of barcoded RBD variants that cover 3804 of the 3819 possible amino acid mutations. Our libraries were made in the genetic background of the RBD from the early isolate Wuhan-Hu-1, which still represents the most common RBD sequence, although several mutants are currently increasing in frequency (*9*, *10*). We mapped how the 2034 mutations that do not strongly disrupt RBD folding and ACE binding (*7*) affected binding by recombinant forms of the two antibodies in Regeneron's REGN-COV2 cocktail (REGN10933 and REGN10987) (*11*, *12*) and Eli Lilly's LY-CoV016 antibody (also known as CB6 or JS016) (*13*) (fig. S1B). REGN-COV2 was recently granted emergency use authorization for treatment of COVID-19 (*14*), whereas LY-CoV016 is currently in phase 3 clinical trials (*15*).

We completely mapped RBD mutations that escape binding by the three individual antibodies as well as the REGN-COV2 cocktail (Fig. 1, A and B, and zoomable maps at https://jbloomlab.github.io/SARS-CoV-2-RBD_MAP_clinical_Abs/). REGN10933 and REGN10987 are escaped by largely non-overlapping sets of mutations in the RBD's receptor binding motif (Fig. 1A), consistent with structural work showing that these antibodies target distinct epitopes in this motif (*11*). But unexpectedly, one mutation [$Glu^{406}\rightarrow$ Trp (E406W)] strongly escapes the cocktail of both antibodies (Fig. 1A). The escape map for LY-CoV016 also reveals escape mutations at a number of different sites in the RBD (Fig. 1B). Although some escape mutations impair the RBD's ability to bind ACE2 or be expressed in properly folded form, many come at little or no cost to these functional properties, according to prior deep mutational scanning measurements using yeast-displayed RBD (*7*) (color gradient in Fig. 1, A and B, indicates loss of ACE2 affinity and in fig. S2 indicates decrease in RBD expression).

To validate the antigenic effects of key mutations, we performed neutralization assays using spike-pseudotyped lentiviral particles and found concordance between the antibody binding escape maps and neutralization assays (Fig. 1C and fig. S3). As expected from the maps for the REGN-COV2 antibodies, a mutation at site 486 escaped neutralization only by REGN10933, whereas mutations at sites 439 and 444 escaped neutralization only by REGN10987—and so none of these mutations escaped the cocktail. But E406W escaped both individual REGN-COV2 antibodies and thus also strongly escaped the cocktail. Structural analyses and viral-escape selections led Regeneron to posit that no single amino acid mutation could escape both antibodies in the cocktail (*11*, *12*), but our complete maps identify E406W as a cocktail escape mutation. E406W affects the REGN-COV2 antibodies in a relatively specific way and does not grossly perturb the function of the RBD, given that it only mildly reduces neutralization by LY-CoV016 (Fig. 1C) and the titers of spike-pseudotyped lentiviral particles (fig. S3F).

To explore whether our escape maps are consistent with how the virus evolves under antibody selection, we first examined data from Regeneron's viral escape–selection experiments in which spike-expressing vesicular stomatitis virus (VSV) was grown in cell culture in the presence of either REGN10933, REGN10987, or the REGN-COV2 cocktail (*12*). That work identified five escape mutations from REGN10933, two from REGN10987, and none from the cocktail (Fig. 2A). All seven cell culture–selected mutations were prominent in our escape maps while also being accessible by just a single-nucleotide change to the wild-type codon in the Wuhan-Hu-1 RBD sequence (Fig. 2B), demonstrating concordance between the escape maps and viral evolution under antibody pressure in cell culture. Notably, E406W is not accessible by a single-nucleotide change, which may explain why it was not identified by the Regeneron cocktail selections despite being relatively well tolerated for RBD folding and ACE2 affinity.

To determine whether the escape maps could inform analysis of viral evolution in infected humans, we examined deep sequencing data from a persistently infected immunocompromised patient who was treated with REGN-COV2 at day 145 after diagnosis with COVID-19 (*16*). The late administration of the treatment allowed ample time for the patient's viral population to accumulate genetic diversity, some of which could have been driven by immune pressure, because the patient mounted a weak autologous neutralizing antibody response before treatment (*16*). Administration of REGN-COV2 was followed by rapid changes in the frequencies of five amino acid mutations in the RBD (Fig. 2C and fig. S4). Our escape maps showed that three of these mutations escaped REGN10933 and that one escaped REGN10987 (Fig. 2B). Notably, the mutations

[1]Basic Sciences and Computational Biology, Fred Hutchinson Cancer Research Center, Seattle, WA 98109, USA. [2]Department of Genome Sciences, University of Washington, Seattle, WA 98109, USA. [3]Medical Scientist Training Program, University of Washington, Seattle, WA 98109, USA. [4]Molecular and Cellular Biology Graduate Program, University of Washington, Seattle, WA 98109, USA. [5]Brigham and Women's Hospital, Harvard Medical School, Boston, MA 02115, USA. [6]Howard Hughes Medical Institute, Seattle, WA 98109, USA.
*These authors contributed equally to this work.
†Corresponding author. Email: jbloom@fredhutch.org

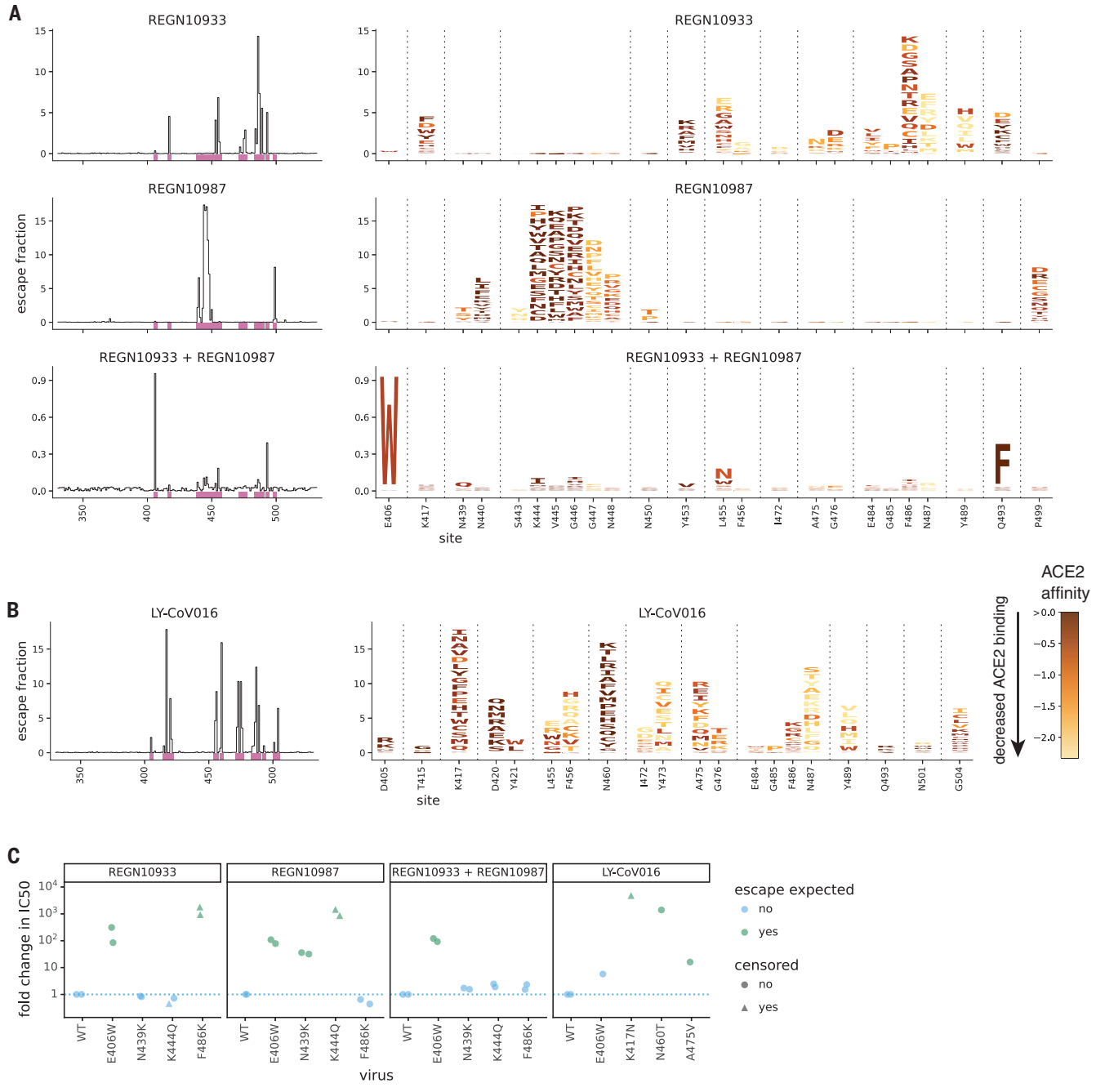

Fig. 1. Complete maps of mutations that escape binding by the REGN-COV2 antibodies and Ly-CoV016. (**A**) Maps for antibodies in REGN-COV2. Line plots at left show escape at each site in the RBD (summed effects of all mutations at each site). Sites of strong escape (purple underlines) are shown in logo plots at right. The height of each letter is proportional to how strongly that amino acid mutation mediates escape, with a per-mutation "escape fraction" of 1 corresponding to complete escape. The *y*-axis scale is different for each row, so, for instance, E406W escapes all REGN antibodies but is most visible for the cocktail as it is swamped out by other sites of escape for the individual antibodies. See https://jbloomlab.github.io/SARS-CoV-2-RBD_MAP_clinical_Abs/ for zoomable versions. Letters are colored according to how mutations affect the RBD's affinity for ACE2 as measured via yeast display (*7*), with yellow indicating poor affinity and brown indicating good affinity; see fig. S2, A and B, for maps colored by how mutations affect expression of folded RBD and fig. S2, C and D, for distribution of effects on ACE2 affinity and RBD expression across all mutations observed among circulating viral isolates. (**B**) Map, as in (A), for LY-CoV016. (**C**) Validation of key mutations in neutralization assays using spike-pseudotyped lentiviral particles. We chose to validate mutations predicted to have large effects or that are present at high frequency among circulating SARS-CoV-2 isolates (e.g., N439K). Each point indicates the fold increase in the median inhibitory concentration (IC_{50}) for a mutation relative to the unmutated wild-type (WT) spike, which contains D614G. The dotted blue line at 1 indicates WT-like neutralization, and values >1 indicate increased neutralization resistance. Point colors indicate whether escape was expected at that site from the maps. Point shapes indicate that the fold change is censored (an upper or lower limit) owing to the IC_{50} being outside the dilution series used. Most mutants were tested in duplicate and thus have two points. Full neutralization curves are shown in fig. S3. Single-letter abbreviations for the amino acid residues are as follows: A, Ala; C, Cys; D, Asp; E, Glu; F, Phe; G, Gly; H, His; I, Ile; K, Lys; L, Leu; M, Met; N, Asn; P, Pro; Q, Gln; R, Arg; S, Ser; T, Thr; V, Val; W, Trp; and Y, Tyr.

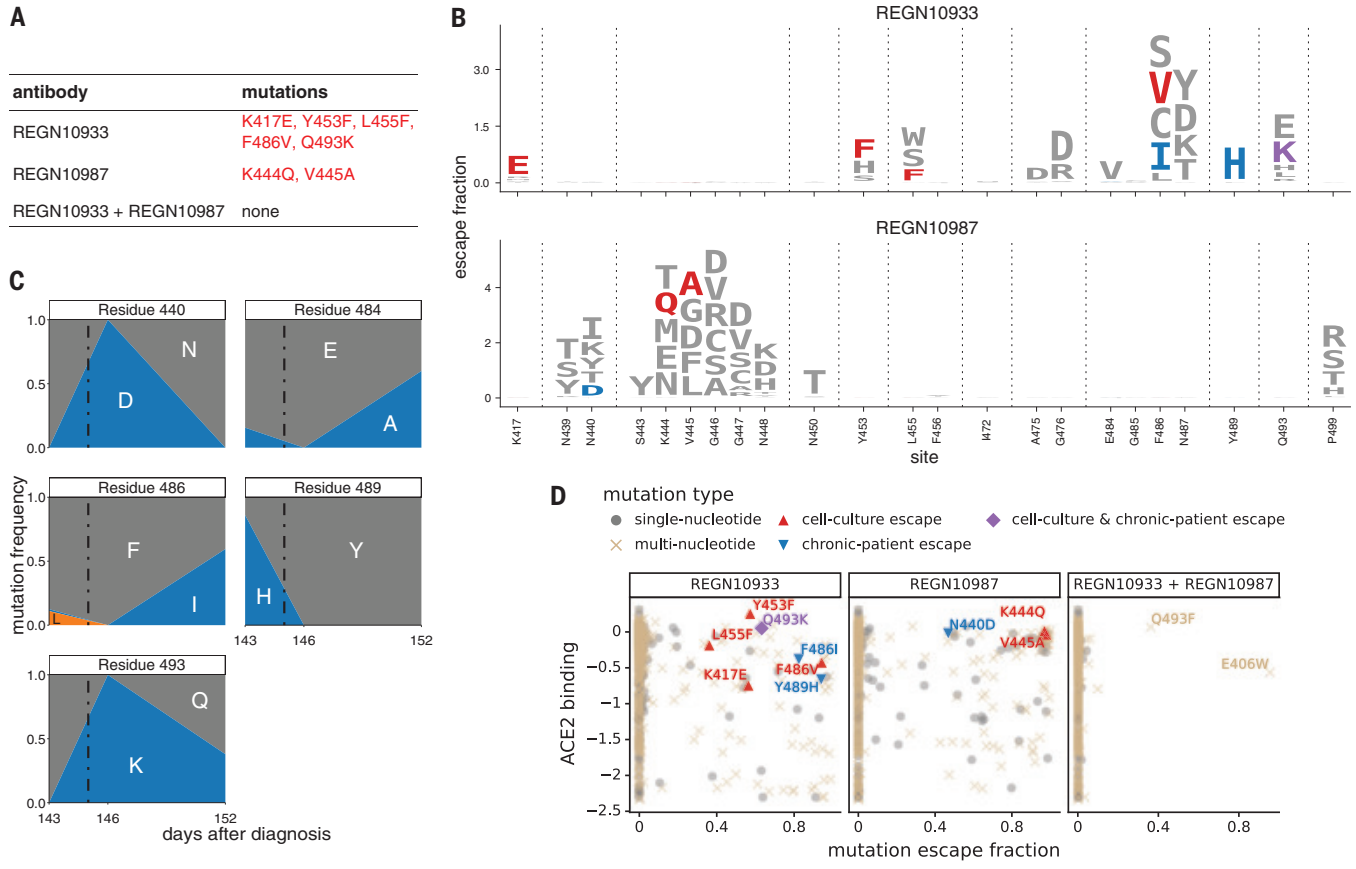

Fig. 2. Escape maps are consistent with viral mutations selected in cell culture and a persistently infected patient. (**A**) Viral escape mutations selected by Regeneron with spike-pseudotyped VSV in cell culture in the presence of antibody (*12*). (**B**) Escape maps like those in Fig. 1A, but showing only mutations accessible by single-nucleotide changes to the Wuhan-Hu-1 sequence, with nongray colors indicating mutations in cell culture (red), the infected patient (blue), or both (purple). Figure S5 shows these maps colored by how mutations affect ACE2 affinity or RBD expression. (**C**) Dynamics of RBD mutations in a patient treated with REGN-COV2 at day 145 of infection (black dot-dash vertical line). E484A rose in frequency in linkage with F486I, but because E484A is not an escape mutation in our maps, it is not shown in other panels. See also fig. S4. (**D**) The escape mutations that arise in cell culture and the infected patient are single-nucleotide–accessible and escape antibody binding without imposing a large cost on ACE2 affinity [as measured using yeast display (*7*)]. Each point is a mutation, with shape and color indicating whether it is accessible and selected during viral growth. Points farther to the right on the *x* axis indicate stronger escape from antibody binding; points higher up on the *y* axis indicate higher ACE2 affinity.

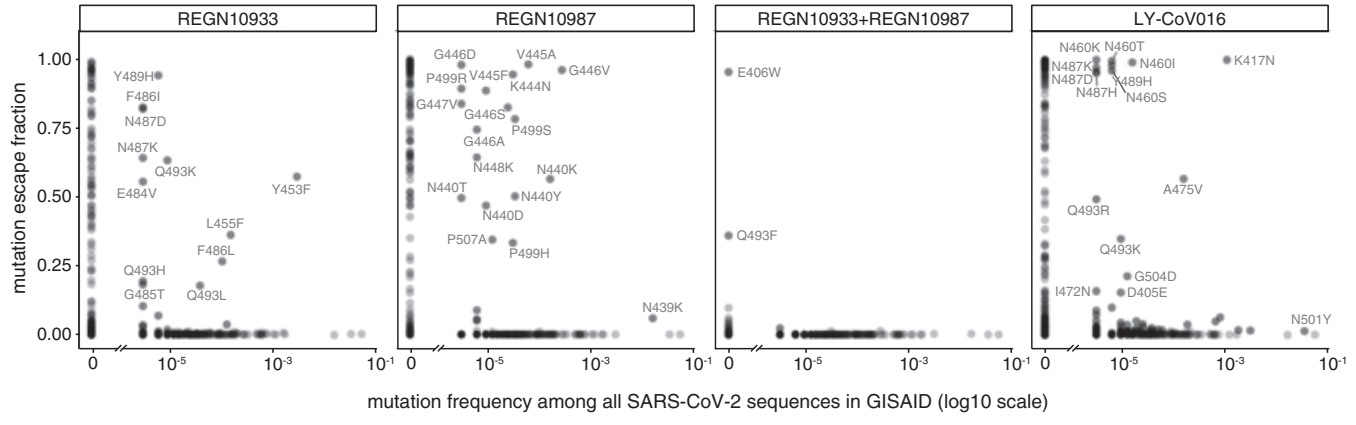

Fig. 3. Antibody escape mutations in circulating SARS-CoV-2. For each antibody or antibody combination, the escape score for each mutation is plotted versus its frequency among the 317,866 high-quality human-derived SARS-CoV-2 sequences on GISAID (*26*) as of 11 January 2021. Escape mutations with notable GISAID frequencies are labeled. The REGN-COV2 cocktail escape mutation E406W requires multiple nucleotide changes from the Wuhan-Hu-1 RBD sequence and is not observed among sequences in GISAID. Other mutations to residue E406 (E406Q and E406D) are observed with low frequency counts, but neither of these mutant amino acids is a single-nucleotide mutation away from W either.

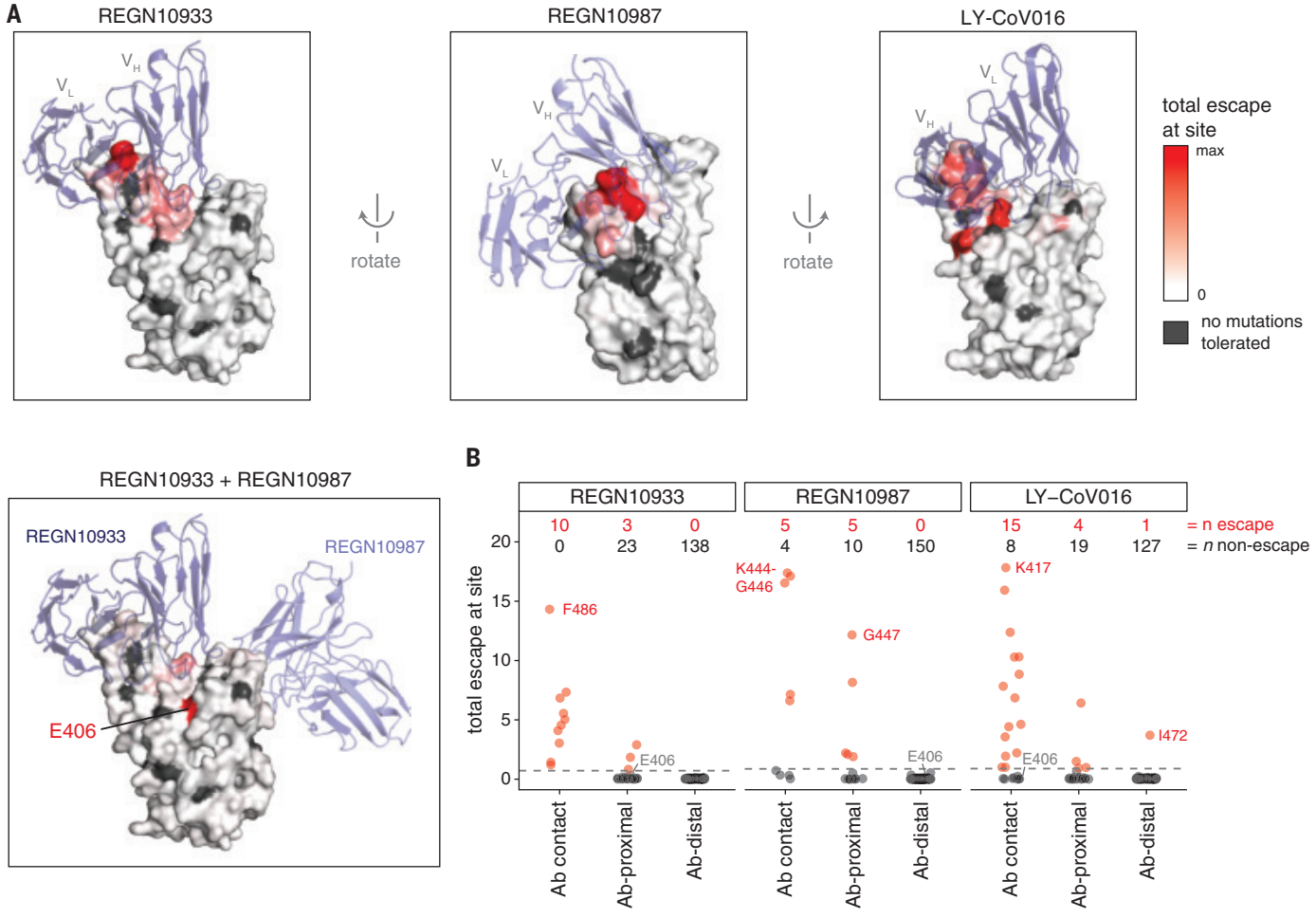

Fig. 4. Structural context of escape mutations. (**A**) Escape maps projected on antibody-bound RBD structures. [REGN10933 and REGN10987: Protein Data Bank (PDB) ID 6XDG (*11*); LY-CoV016: PDB ID 7C01 (*13*)]. Antibody heavy- and light-chain variable domains are shown as blue cartoons, and the RBD surface is colored to indicate how strongly mutations at that site mediate escape (white indicates no escape, red indicates strongest escape site for that antibody or cocktail). Sites where no mutations are functionally tolerated are colored gray. (**B**) For each antibody, sites were classified as direct antibody contacts (non-hydrogen atoms within 4 Å of antibody), antibody-proximal (4 to 8 Å), or antibody-distal (>8 Å). Each point indicates a site, classified as escape (red) or non-escape (black). The dashed gray line indicates the cutoff used to classify sites as escape or non-escape (see materials and methods for details). Red and black numbers indicate how many sites in each category are escape or non-escape sites, respectively. Interactive visualizations are at https://jbloomlab.github.io/SARS-CoV-2-RBD_MAP_clinical_Abs/, and hypothesized mechanisms of escape and additional structural details for labeled points are shown in fig. S6.

did not all sweep to fixation after antibody treatment; instead, there were competing rises and falls (Fig. 2C). This pattern has been observed in the adaptive within-host evolution of other viruses (*17*, *18*) and can arise from genetic hitchhiking and competition among viral lineages. Both these forces appear to be at play in the persistently infected patient (Fig. 2C and fig. S4C): E484A (not an escape mutation in our maps) hitchhikes with F486I (which escapes REGN10933) after treatment, and the viral lineage carrying N440D and Q493K (which escape REGN10987 and REGN10933, respectively) competes first with the REGN10933 escape-mutant Y489H and then with the lineage carrying E484A and F486I and the Q493K lineage.

Three of the four escape mutations in the REGN-COV2–treated patient were not identified in Regeneron's viral cell culture selections (Fig. 2B), illustrating an advantage of complete maps. Viral selections are incomplete in the sense that they only identify whatever mutations are stochastically selected in that particular cell culture experiment. In contrast, complete maps annotate all mutations, which could include mutations that arise for reasons unrelated to treatment but incidentally affect antibody binding.

Of course, viral evolution is shaped by functional constraints as well as pressure to evade antibodies. The mutations selected in cell culture and the patient consistently met the following criteria: They escaped antibody binding, were accessible via a single-nucleotide change, and imposed little or no cost on ACE2 affinity [as measured by prior deep mutational scanning using yeast-displayed RBD (*7*)] (Fig. 2D and fig. S5). Therefore, complete maps of how mutations affect key biochemical phenotypes of the RBD (e.g., ACE and antibody binding) can be used to assess likely paths of viral evolution. One caveat is that over longer evolutionary time frames, the space of tolerated mutations could shift as a result of epistatic interactions, as has been observed in viral immune and drug escape (*19*–*21*).

The complete maps enable us to assess what escape mutations are already present among circulating SARS-CoV-2. We examined all human-derived SARS-CoV-2 sequences available as of 11 January 2021 and found a substantial number of RBD mutations that escaped one or more of the antibodies (Fig. 3). However, the only escape mutations present in >0.1% of sequences were the REGN10933 escape-mutant Y453F [0.3% of sequences; see also (*12*)], the REGN10987 escape-mutant N439K

[1.7% of sequences; see also Fig. 1C and (*22*)], and the LY-CoV016 escape-mutant K417N (0.1% of sequences; see also Fig. 1C). Y453F is associated with independent outbreaks linked to mink farms in the Netherlands and Denmark (*23*, *24*); notably, the mink sequences themselves sometimes also contain other escape mutations, such as F486L (*24*). N439K is prevalent in Europe, where it has constituted a large percentage of sequences from regions including Scotland and Ireland (*22*, *25*). K417N is present in the B.1.351 lineage first identified in South Africa (*10*). Another mutation of current interest is N501Y, which is present in B.1.351 and also the B.1.1.7 lineage originally identified in the United Kingdom (*9*). Our maps indicate that N501Y has no effect on either of the REGN-COV2 antibodies and has only a modest effect on LY-CoV016 (Fig. 3).

To determine whether the escape maps could be rationalized from the structural interfaces of the antibodies and RBD, we projected the maps onto crystal or cryo–electron microscopy structures (Fig. 4A; interactive versions at https://jbloomlab.github.io/SARS-CoV-2-RBD_MAP_clinical_Abs/). As might be expected, escape mutations generally occur in the antibody-RBD interface. However, structures alone are insufficient to predict which mutations mediate escape. For example, LY-CoV016 uses both its heavy and light chains to bind a wide epitope overlapping the ACE2-binding surface, but escape is dominated by mutations at RBD residues that contact the heavy-chain complementarity-determining regions (Fig. 4A and fig. S6, E to G). In contrast, escape from REGN10933 and REGN10987 mostly occurs at RBD residues that pack at the antibody heavy- and light-chain interface (Fig. 4A and fig. S6, A to D). The E406W mutation that escapes the REGN-COV2 cocktail occurs at a residue not in contact with either antibody (Fig. 4, A and B). Although E406 is in closer structural proximity to LY-CoV016 (Fig. 4B and fig. S6H), the E406W mutation has a much smaller impact on this antibody (Fig. 1, B and C), suggesting a long-range structural mechanism specific to the REGN-COV2 antibodies (fig. S6I). Taken together, mutations at RBD residues that contact antibody do not always mediate escape, and several prominent escape mutations occur at residues not in contact with antibody (Fig. 4B and fig. S6, D and G).

In this study, we have completely mapped mutations that escape three leading anti–SARS-CoV-2 antibodies. These maps demonstrate that prior characterization of escape mutations was incomplete, having identified neither a single amino acid mutation that escapes both antibodies in the REGN-COV2 cocktail nor most mutations that arose in a persistently infected patient treated with the cocktail. Of course, our maps still do not answer the most pressing question: Will SARS-CoV-2 evolve widespread resistance to these antibodies? But certainly, it is concerning that so many escape mutations impose little cost on RBD folding or receptor affinity and that some are already present at low levels among circulating viruses. Ultimately, it will be necessary to wait and see what mutations spread as SARS-CoV-2 circulates in the human population. Our work will help with the "seeing," by enabling immediate interpretation of the effects of the mutations cataloged by viral genomic surveillance.

REFERENCES AND NOTES

1. A. Renn, Y. Fu, X. Hu, M. D. Hall, A. Simeonov, *Trends Pharmacol. Sci.* **41**, 815–829 (2020).
2. M. Caskey *et al.*, *Nature* **522**, 487–491 (2015).
3. J. R. Kugelman *et al.*, *Cell Rep.* **12**, 2111–2120 (2015).
4. E. A. F. Simões *et al.*, *Clin. Infect. Dis.* ciaa951 (2020).
5. D. Wrapp *et al.*, *Science* **367**, 1260–1263 (2020).
6. A. C. Walls *et al.*, *Cell* **181**, 281–292.e6 (2020).
7. T. N. Starr *et al.*, *Cell* **182**, 1295–1310.e20 (2020).
8. A. J. Greaney *et al.*, *Cell Host Microbe* **29**, 44–57.e9 (2021).
9. A. Rambaut *et al.*, "Preliminary genomic characterisation of an emergent SARS-CoV-2 lineage in the UK defined by a novel set of spike mutations," Virological.org (2020); https://virological.org/t/preliminary-genomic-characterisation-of-an-emergent-sars-cov-2-lineage-in-the-uk-defined-by-a-novel-set-of-spike-mutations/563.
10. H. Tegally *et al.*, medRxiv 2020.12.21.20248640 [Preprint]. 22 December 2020. https://doi.org/10.1101/2020.12.21.20248640.
11. J. Hansen *et al.*, *Science* **369**, 1010–1014 (2020).
12. A. Baum *et al.*, *Science* **369**, 1014–1018 (2020).
13. R. Shi *et al.*, *Nature* **584**, 120–124 (2020).
14. Regeneron Pharmaceuticals, Inc., "Regeneron's casirivimab and imdevimab antibody cocktail for COVID-19 is first combination therapy to receive FDA emergency use authorization," press release (21 November 2020); https://investor.regeneron.com/news-releases/news-release-details/regenerons-regen-cov2-first-antibody-cocktail-covid-19-receive/.
15. Eli Lilly and Company, "A phase 3 randomized, double-blind, placebo-controlled trial to evaluate the efficacy and safety of LY3819253 alone and in combination with LY3832479 in preventing SARS-CoV-2 infection and COVID-19 in skilled nursing and assisted living facility residents and staff; a NIAID and Lilly Collaborative Study" (Clinical trial registration NCT04497987, clinicaltrials.gov, 2020); https://clinicaltrials.gov/ct2/show/NCT04497987.
16. B. Choi *et al.*, *N. Engl. J. Med.* **383**, 2291–2293 (2020).
17. K. S. Xue *et al.*, *eLife* **6**, e26875 (2017).
18. A. F. Feder *et al.*, *eLife* **5**, e10670 (2016).
19. J. D. Bloom, L. I. Gong, D. Baltimore, *Science* **328**, 1272–1275 (2010).
20. L. I. Gong, M. A. Suchard, J. D. Bloom, *eLife* **2**, e00631 (2013).
21. T. H. Zhang *et al.*, *PLOS Genet.* **16**, e1009009 (2020).
22. E. C. Thomson *et al.*, *Cell* 10.1016/j.cell.2021.01.037 (2021).
23. European Centre for Disease Prevention and Control, Rapid Risk Assessment: Detection of new SARS-CoV-2 variants related to mink, ECDC, Stockholm, 12 November 2020; www.ecdc.europa.eu/en/publications-data/detection-new-sars-cov-2-variants-mink.
24. B. B. Oude Munnink *et al.*, *Science* **371**, 172–177 (2021).
25. A. T. Chen, K. Altschuler, S. H. Zhan, Y. A. Chan, B. E. Deverman, bioRxiv 2020.09.23.310565 [Preprint]. 28 September 2020. https://doi.org/10.1101/2020.09.23.310565.
26. S. Elbe, G. Buckland-Merrett, *Glob. Chall.* **1**, 33–46 (2017).
27. T. Starr, J. Bloom, A. Greaney, A. Addetia, jbloomlab/SARS-CoV-2-RBD_MAP_clinical_Abs: Science revision, Zenodo, (2021); https://doi.org/10.5281/zenodo.4443311.
28. W. Hannon, jbloomlab/SARS-CoV-2_chronic-infection-seq: Archived for publication, Version 1, Zenodo (2021); https://doi.org/10.5281/zenodo.4433185.

ACKNOWLEDGMENTS

We thank K. Crawford for help with neutralization assays; A. Feder, D. Veesler, N. King, and D. Ellis for helpful comments; and the Fred Hutch Flow Cytometry and Genomics facilities for assistance. **Funding:** This work was supported by the NIAID (R01AI127893 and R01AI141707 to J.D.B. and T32AI083203 to A.J.G.), the Gates Foundation (INV-004949 to J.D.B.), and the Massachusetts Consortium for Pathogen Readiness through grants from the Evergrande Fund (to J.Z.L.). Scientific computing at Fred Hutch is supported by ORIP grant S10OD028685. T.N.S. is a Washington Research Foundation Innovation Fellow at the University of Washington Institute for Protein Design and an HHMI Fellow of the Damon Runyon Cancer Research Foundation (DRG-2381-19). J.D.B. is an investigator of the Howard Hughes Medical Institute. **Author contributions:** T.N.S., A.J.G., A.S.D., and J.D.B. designed the study. T.N.S., A.J.G., A.A., and A.S.D. performed the experiments. T.N.S., A.J.G., and J.D.B. analyzed the experimental data. J.Z.L. and M.C.C. sequenced the persistent infection, and W.W.H. analyzed that data. T.N.S., A.A., W.W.H., and J.D.B. wrote the initial draft, and all authors edited the final version. **Competing interests:** J.Z.L. has consulted for Abbvie and Jan Biotech. The other authors declare no competing interests. **Data and materials availability:** Raw sequencing data are on the NCBI SRA under BioProject PRJNA639956/BioSample SAMN16850904 (escape mapping) and BioProject PRJNA681234 (patient sequencing). Computer code and processed data for the escape mapping are at (*27*) and https://github.com/jbloomlab/SARS-CoV-2-RBD_MAP_clinical_Abs. Code and data for the patient sequencing are at (*28*) and https://github.com/jbloomlab/SARS-CoV-2_chronic-infection-seq. The sequences of the antibodies are provided via citations in the materials and methods, the cells and plasmids for the neutralization assays are available in BEI Resources and AddGene (see materials and methods for details), and the yeast mutant libraries are available to academic researchers upon request with a completed material transfer agreement. We gratefully acknowledge the authors from the originating laboratories and the submitting laboratories, who generated and shared via GISAID genetic sequence data on which this research is based (all contributors listed at https://github.com/jbloomlab/SARS-CoV-2-RBD_MAP_clinical_Abs/blob/main/data/gisaid_hcov-19_acknowledgement_table_2021_01_11.pdf). This work is licensed under a Creative Commons Attribution 4.0 International (CC BY 4.0) license, which permits unrestricted use, distribution, and reproduction in any medium, provided the original work is properly cited. To view a copy of this license, visit https://creativecommons.org/licenses/by/4.0/. This license does not apply to figures/photos/artwork or other content included in the article that is credited to a third party; obtain authorization from the rights holder before using such material.

SUPPLEMENTARY MATERIALS

science.sciencemag.org/content/371/6531/850/suppl/DC1
Materials and Methods
Figs. S1 to S6
References (*29*–*39*)
MDAR Reproducibility Checklist
Data S1

1 December 2020; accepted 19 January 2021
Published online 25 January 2021
10.1126/science.abf9302

Arizona State University | The University of Arizona

LAUNCH OF A NEW JOINT UNIVERSITY VENTURE:

THE INSTITUTE FOR FUTURE HEALTH (IFH)

DOCTORAL LEVEL POSITIONS IMMEDIATELY AVAILABLE

DIRECTORS OF RESEARCH PROJECTS

- CARDIO-PULMONARY DISEASE
- MENTAL HEALTH
- INFECTIOUS DISEASE SURVEILLANCE

LEAD DATA SCIENTISTS

- REMOTE HEALTH MONITORING
- LARGE SCALE DATA ANALYTICS
- MACHINE LEARNING/ARTIFICIAL INTELLIGENCE

The IFH will be a research and clinical hub to integrate the convergence of biomedicine, engineering and computing for innovation in precision health and digital health and their dependence on proficient capture, analysis and use of rapidly expanding large-scale data. Inter-disciplinary project teams from both universities and clinical and corporate partners will develop new sensors, wireless platforms and biometrics for remote monitoring of health status, interactive telemedicine and the application of cognitive computing in patient care to improve diagnosis, monitor treatment adherence, reduce hospital readmissions and maintain wellness. The initial projects will focus on cardio-pulmonary diseases, mental health and infectious disease surveillance.

Detailed Specifications and Application Information Available at:
https://casi.asu.edu/

Apply by **March 8, 2021**

ScienceCareers online @sciencecareers.org

FIND YOUR HAPPIER PLACE.

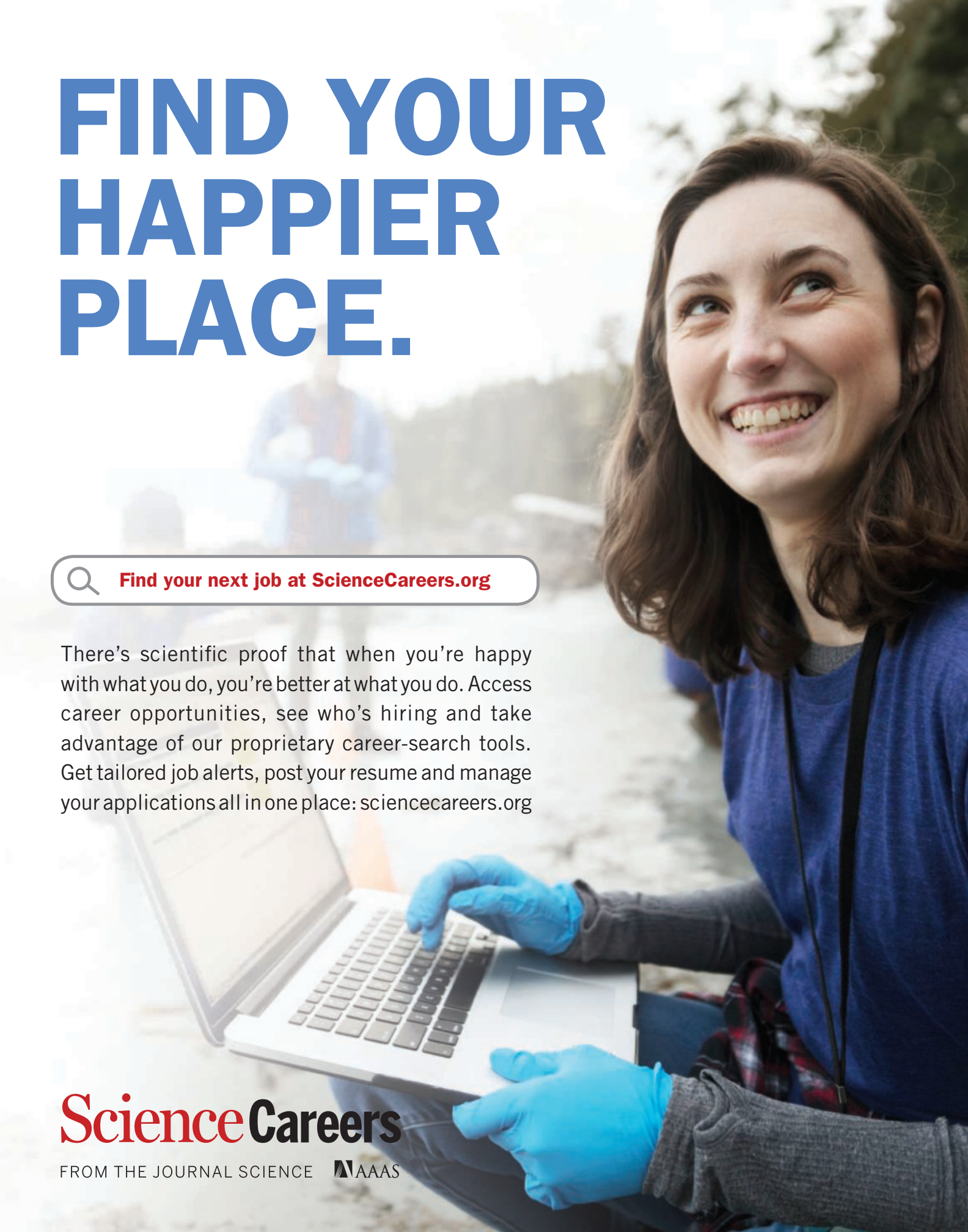

Find your next job at ScienceCareers.org

There's scientific proof that when you're happy with what you do, you're better at what you do. Access career opportunities, see who's hiring and take advantage of our proprietary career-search tools. Get tailored job alerts, post your resume and manage your applications all in one place: sciencecareers.org

ScienceCareers

FROM THE JOURNAL SCIENCE AAAS

ScienceCareers
FROM THE JOURNAL SCIENCE AAAS

Confused about your next career move?

Download Free Career Advice Booklets!

ScienceCareers.org/booklets

University of Nebraska Medical Center

CHAIR, DEPARTMENT OF PATHOLOGY & MICROBIOLOGY

Applications are invited from high-energy, customer-focused, entrepreneurial physician/scientist/educator to fill the position of **Chair, Department of Pathology & Microbiology for the University of Nebraska Medical Center** and **Nebraska Medicine in Omaha Nebraska.**

We are seeking a leader interested in shepherding a complex and fast-growing Midwest-leading department with a rich history into its next phase of development. With more than 70 fulltime physicians, clinical providers and basic scientists, the department is also supported by a large volunteer and emeritus faculty to provide a collaborative educational and scientific environment. A fully accredited ACGME residency program and five fellowship programs offer highly interactive opportunities for advanced training.

The subspecialty-based anatomic and clinical services provide consultation and testing through a large reference laboratory, Regional Pathology Services (RPS), with over 600 clients in 26 states that benefit from a digital imaging and advanced informatics strategy. For over 20 years the department-based Nebraska Public Health Laboratory (NPHL) has provided state-of-the-art support to the state and federal government leading to a global reputation in emerging infectious diseases.

Research funding for FY2019 was listed at number 30 by the Blue Ridge Institute for Medical Research with a world-class program in microbiology and virology. Additional areas of excellence include cancer biology and immunology and with considerable overlap between 23 cutting-edge laboratories supported by an interdisciplinary graduate program with over 70 Ph.D. students. Growing research opportunities exist in cellular therapy based on advanced clinical program and department directed GMP facility.

The successful Chair candidate will be an MD or MD/PhD or equivalent with national recognition as a leader in pathology and prior administrative experience with a history of innovative research with federal funding. The next chair will have a strategic vision for expanding research and clinical programs in cellular therapy and continuing the growth of an interactive basic/translational research program in the department that bridges multiple departments and Institutes. They will guide the department's teaching programs and provide strong research mentorship to clinical and research faculty.

For consideration, please submit CV and letter of interest in confidence to:
Eileen Blake
Alexander, Wollman & Stark
eblake@AlexanderWollmanStark.com
610.399.5284

The University of Nebraska Medical Center is an Equal Opportunity Affirmative Action Employer. Individuals from diverse backgrounds are encouraged to apply.

By **Eric Wengert**

Mentor as you'd want to be mentored

In my first undergraduate research position, I imagined I'd design creative experiments, collect interesting data, and engage in thought-provoking discussions about science. Then reality set in. I spent most of my summer washing glassware, making solutions, and completing basic protocols while my postdoc mentor caught up on email. On the rare occasions when I was instructed to do a real experiment, my brief "training" left me feeling woefully unprepared. But although I learned little science, I learned valuable lessons about mentoring.

During my college neuroscience classes, I had been captivated by the complexity of the brain and drawn to a field that addressed some of life's big questions: Who am I? What is consciousness? But my summer research experience left me with serious doubts about whether I was cut out for a career in science. One Saturday, I attempted an experiment my mentor had demonstrated a few days earlier—only to realize I had no idea what I was doing. I did the best I could. When I finished, I was mortified to discover I hadn't used one of the treatment tubes my mentor had prepared.

I worked in another lab later in college. The experience wasn't much better and my self-doubts persisted. However, to my surprise, my mentors—along with my teachers—encouraged me to apply to graduate school. I'm grateful, because I might not have had the confidence to carry on otherwise.

I'm also grateful because my former mentors, in demonstrating what *not* to do, showed me how to be a better mentor myself. When I became a graduate student, I made a point of treating the undergraduates I supervised the way I wish I'd been treated. Here are three keys to my approach:

MAKE IT INDIVIDUAL. My first mentor never asked me about my career goals—and because they never asked, I assumed they didn't care. I've since learned that in order to mentor effectively, it is critical to start with some simple questions: "Why do you want to do this research? What are you most interested in?" Only then can you form a mutually beneficial plan, forging a connection between the students' goals and your project. It's also helpful to pay attention to the conditions under which your students do their best work. For example, some may appreciate real-time support, but others may feel nervous if you're constantly looking over their shoulder.

"A student's first taste of research can cement their enthusiasm for science."

INVEST TIME. I know it's tempting to relegate tedious tasks to undergraduates and cut corners in training to save valuable time. But investing time up front to explain and demonstrate scientific techniques will benefit everyone: The students will learn more and you'll have more capable assistants. I spend time training my students at the outset. I also supervise them regularly when they first set out to perform experiments on their own, gradually giving them more independence as they grow in ability. This allows me to correct missteps in real time, helping them gain good habits before bad ones develop.

DON'T IGNORE THE BIG PICTURE. Colleagues who view undergraduates as "just a pair of hands" often give their students a series of tasks without explaining the big-picture goals of the research. I think that's a big mistake. Students will get much more out of a research experience if they have "aha!" moments—if they can see their tasks in the context of broad scientific concepts and questions. You also stand to benefit because knowledgeable students will be more invested in your work, and they will be better able to troubleshoot experiments if problems arise. For everyone's sake, treat your students as you'd like to be treated: as a valued scientific colleague, not a pair of hands.

I'm glad I persisted in science despite lackluster early research experiences. But I worry others won't be so lucky. A student's first taste of research can cement their enthusiasm for science or discourage them for good, so it's important to make it rewarding. ■

Eric Wengert is a Ph.D. student at the University of Virginia.
Send your career story to SciCareerEditor@aaas.org.

ILLUSTRATION: ROBERT NEUBECKER

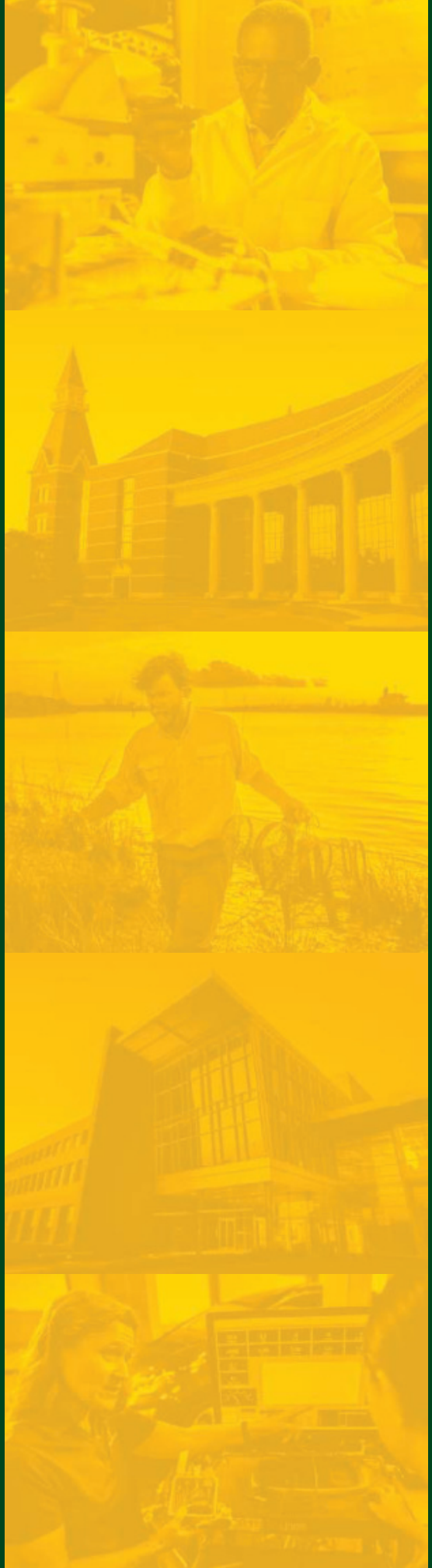

Bold vision. Sustained investment.

Baylor University has made a visionary commitment to research that addresses significant global challenges and provides faculty with the flexibility and resources to broaden and sustain the impact of their research. On a path to preeminence as a Christian research university and guided by a strategic roadmap for systemic growth, Baylor's current fundraising focus has established 12 pivotal, newly endowed academic chair positions.

Baylor seeks visionary researchers to fill five newly funded, endowed chairs in:

- **Biomedical Engineering**
- **Materials Science**
- **Water and Health**
- **Molecular/Cellular Biology and Health**
- **Data Science/Cybersecurity**

These chairs will be supported by Baylor's sustained investment in transformational research growth and university-wide R1 research commitment.

Learn more at **baylor.edu/research/grow**.

Baylor University

Share **Your Robotics Research** with the **World**.

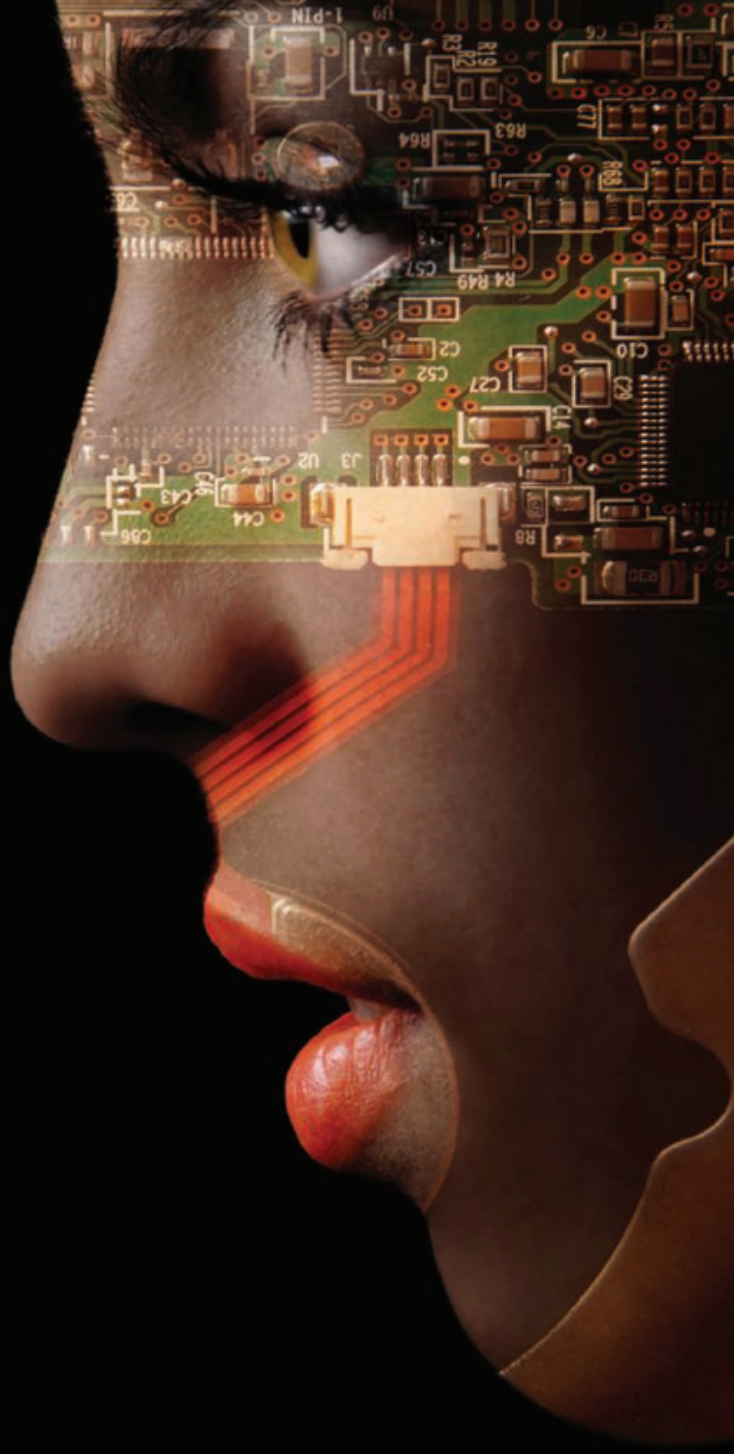

Shaping the future of robotics with high impact research!

As a multidisciplinary online-only journal, *Science Robotics* publishes original, peer-reviewed, research articles that advance the field of robotics. The journal provides a central forum for communication of new ideas, general principles, and original developments in research and applications of robotics for all environments.

Submit your research today. Learn more at: **robotics.sciencemag.org**

Twitter: @SciRobotics
Facebook: @ScienceRobotics

Science Robotics
AAAS